Scuola Universitaria Superiore IUSS Pavia

DEVELOPMENT OF A DISCRETE CRACK PLASTICITY MODEL FOR THE CRACK-BASED ASSESSMENT OF EARTHQUAKE-DAMAGED REINFORCED-CONCRETE STRUCTURES

A Thesis Submitted in Partial Fulfillment of the Requirements for the Degree of Doctor of Philosophy in

EARTHQUAKE ENGINEERING AND ENGINEERING SEISMOLOGY

Obtained in the framework of the Doctoral Program in

Understanding and Managing Extremes

by

William D. Galik

May 2026

Scuola Universitaria Superiore IUSS Pavia

DEVELOPMENT OF A DISCRETE CRACK PLASTICITY MODEL FOR THE CRACK-BASED ASSESSMENT OF EARTHQUAKE-DAMAGED REINFORCED-CONCRETE STRUCTURES

A Thesis Submitted in Partial Fulfillment of the Requirements for the Degree of Doctor of Philosophy in

EARTHQUAKE ENGINEERING AND ENGINEERING SEISMOLOGY

Obtained in the framework of the Doctoral Program in

Understanding and Managing Extremes

by

William D. Galik

Supervisor: Prof. Paolo M. Calvi

May 2026

Abstract

After an earthquake, the decision to repair or replace a damaged structure is influenced by crack width observations, which are used to classify component damage levels. However, empirical crack width limits are inconsistent across current guidelines. For instance, a residual crack width is classified as "Severe" by the JBDPA guidelines if it exceeds 1 mm, whereas the same classification is triggered in the FEMA 306 guidelines only for a residual crack width surpassing 9.5 mm. Clearly, empirical definitions of crack severity lead to some confusion. In some cases, improperly diagnosed crack damage has led to catastrophic failure. Logically, a rational approach to defining crack-width guidelines is sought, both to evaluate the existing guidelines and to give insight into the parameters that might play a role in the next generation of guidelines.

To this end, a case study was undertaken to assess the ability to model, with existing tools, cracking damage after an earthquake, and to assess the consequences of such damage. The popular structural analysis tool OpenSees was used to model a series of squat RC walls and to develop a framework for identifying when a crack width exceeds a safe level. While the proposed framework identifies potential areas of improvement in existing crack-width guidelines and measures peak strength and peak damage accurately, the analysis shows that existing simplified models struggle to replicate residual (i.e., post-EQ) crack widths. This is the case even when the EQ excitation is known precisely. The poor match of experimental residual crack widths and predicted numerical crack widths comes from the over-simplification of the crack mechanics in existing macro-elements for walls, which seek only to match the load-deformation response of walls, using few simple parameters, while treating local mechanisms in little detail. As residual cracks widths are one of few pieces of information that can be reliably measured on site, a new, more accurate crack model is

needed. The bulk of this thesis is spent to satisfy this need by developing a new model, one that strives for maximum accuracy while preserving simplicity. In the end, the intended audience is earthquake engineers who need to perform already time-intensive nonlinear time history analyses.

A crack model is developed in this PhD work that is valid for any crack type (e.g., shear, flexure, crushing), and as such can be a basis for developing simulation-based, crack-width guidelines for any number of structural components. The proposed material model is a path-dependent, crack-width-based plasticity model for arbitrary cyclic loading of RC cracks. The form of the stress-space yield surface and the plasticity flow rule are interpreted from experimental data from cyclic testing of individual cracks under generalized load conditions. Elastic crack behavior follows empirically defined rules for the elastic stiffness of a crack. The crack plasticity model, which is defined for general excitations, recovers well-known behaviors in pure opening and pure closing, so that it forms a basis for analysis of general cracks. The material description is implemented in the widely used structural analysis software OpenSees, to define the 2-dimensional response of zero-length node-to-node elements that are commonly used by earthquake engineers.

Validation of the crack model is performed for a variety of cracks: unreinforced, reinforced, sliding, and crack systems. Two applications are then studied in further detail. First, the recently proposed double-beam coupling beam system, which deliberately promotes crack formation for predictable nonlinear behavior and energy dissipation, is studied. However, the system's current design procedures are overly conservative in the absence of detailed knowledge of the crack's contribution to the coupling beam's seismic performance. By using the new crack model, design of such systems is made more reliable and efficient (i.e., less reinforcement = saved money and easier construction.

Base-sliding shear walls are another system that will benefit from this thesis. Unanticipated crack-sliding has recently been observed in a full-scale shake-table test of a 4-story, seismically-designed RC building at the E-Defense facility, where wall sliding was noted to amplify the global drift and deformation demands. In the test aftermath, current state-of-the-art models failed to replicate the overall structural response, partly due to no suitable interface element to control wall sliding. This thesis fills this gap by providing an easy-to-mesh crack element. To further aid analysts,

a macro-element for wall base sliding is currently under development for use with the beam-column elements that abound in OpenSees. The work has broader implications for the family of slip-susceptible structures, from precast connections to external retrofits with short anchorages.

Sommario

La decisione di riparare o sostituire una struttura danneggiata, dopo un terremoto, è influenzata dalle osservazioni sulla larghezza delle crepe, le quali vengono utilizzate per classificare i livelli di danno dei componenti. Tuttavia, i limiti empirici dello spessore di una crepa sono incoerenti tra le linee guida attuali. Ad esempio, una larghezza residua di una crepa è classificata come "Grave" dalle linee guida JBDPA se supera 1 mm, mentre la stessa classificazione viene applicata secondo le linee guida FEMA 306 solo per una larghezza residua delle fessure superiore a 9,5 mm. Chiaramente, le definizioni empiriche di gravità delle crepe creano una certa confusione. In alcuni casi, una diagnosi errata di danni causati da crepe ha portato a cedimenti catastrofici. Logicamente, si cerca un approccio razionale alla definizione delle linee guida per la larghezza delle crepe, sia per valutare le linee guida esistenti sia per fornire informazioni sui parametri che potrebbero svolgere un ruolo nella prossima generazione di linee guida.

A tal fine, è stato condotto un caso studio per valutare la capacità di modellare, con gli strumenti esistenti, il danno da crepe dopo un terremoto e per valutarne le conseguenze. Lo strumento popolare di analisi strutturale OpenSees è stato utilizzato per modellare una serie di pareti in cemento armato basse e per sviluppare un framework per identificare quando la larghezza di una crepa supera un livello di sicurezza. Mentre il framework proposto identifica potenziali aree di miglioramento nelle linee guida esistenti sulla larghezza delle crepe e misura accuratamente la resistenza massima e il danno massimo, l'analisi mostra che i modelli semplificati esistenti faticano a replicare le ampiezze residue delle crepe (ovvero, post-EQ). Questo accade anche quando la scossa EQ è nota con precisione. La scarsa corrispondenza tra le larghezze residue sperimentali delle crepe e le larghezze numeriche previste deriva dall'eccessiva semplificazione della meccanica delle crepe nei macro-elementi esistenti per le

pareti, i quali cercano solo di riprodurre la risposta carico-deformazione delle pareti utilizzando pochi semplici parametri e trattando i meccanismi locali con scarso dettaglio. Poiché la larghezza residua delle crepe è una delle poche informazioni che può essere misurata in modo affidabile in loco, è necessario un nuovo modello di fessurazione più accurato. La maggior parte di questa tesi è dedicata a soddisfare questa esigenza sviluppando un nuovo modello che punta alla massima accuratezza pur preservando la semplicità. In definitiva, il pubblico a cui si rivolge questo lavoro è costituito da ingegneri sismici che devono eseguire analisi non lineari nel tempo, già di per sé impegnative in termini di tempo.

In questo lavoro di dottorato viene sviluppato un modello di crepa valido per qualsiasi tipo di fessura (ad esempio, taglio, flessione, schiacciamento) e, di conseguenza, può costituire la base per lo sviluppo di linee guida basate sulla simulazione per la larghezza delle crepe, per un numero qualsiasi di componenti strutturali. Il modello di materiale proposto è un modello di plasticità dipendente dal percorso e basato sulla larghezza della crepa, per carichi ciclici arbitrari di crepe in cemento armato. La forma della superficie di snervamento nello spazio degli sforzi e la regola del flusso di plasticità vengono interpretate a partire da dati sperimentali ottenuti da prove cicliche di singole crepe in condizioni di carico generalizzate. Il comportamento elastico della crepa segue regole definite empiricamente per la rigidezza elastica di una crepa. Il modello di plasticità della crepa, definito per excitations generali, recupera comportamenti ben noti in apertura e chiusura pura, in modo da costituire una base per l'analisi di crepe generali. La descrizione del materiale è implementata nel software OpenSees, ampiamente utilizzato, per definire la risposta bidimensionale di elementi nodo-a-nodo di lunghezza zero, strumenti comunemente utilizzati dagli ingegneri sismici.

La validazione del modello di crepe viene eseguita per una varietà di crepe: non rinforzate, rinforzate, scorrevoli e crack systems. Vengono poi studiate più in dettaglio due applicazioni. In primo luogo, viene studiato il sistema di travi di accoppiamento a doppia trave recentemente proposto, che promuove deliberatamente la formazione di crepe per un comportamento non lineare prevedibile e una dissipazione di energia. Tuttavia, le attuali procedure di progettazione del sistema sono eccessivamente conservative in assenza di una conoscenza dettagliata del contributo della crepa alle prestazioni sismiche della trave di accoppiamento. Utilizzando il nuovo

modello di crepa, la progettazione di tali sistemi risulta più affidabile ed efficiente (ovvero, meno armatura = risparmio di denaro e costruzione più semplice).

Le pareti di taglio scorrevoli alla base sono un altro sistema che trarrà beneficio da questa tesi. Uno scorrimento imprevisto delle crepe è stato recentemente osservato in un test su tavola vibrante a grandezza naturale di un edificio in cemento armato di quattro piani, progettato secondo normative antisismiche, presso la struttura E-Defense, dove si è notato che lo scorrimento delle pareti amplificava le richieste globali di spostamento e deformazione. In seguito al test, gli attuali modelli all'avanguardia non sono riusciti a replicare la risposta strutturale complessiva, in parte a causa della mancanza di un elemento di interfaccia idoneo a controllare lo scorrimento delle pareti. Questa tesi colma questa lacuna fornendo un elemento di fessurazione facile da incastrare. Per facilitare ulteriormente gli analisti, è attualmente in fase di sviluppo un macro-elemento per lo scorrimento alla base delle pareti da utilizzare con gli elementi trave-colonna presenti in OpenSees. Il lavoro ha implicazioni più ampie per la famiglia di strutture suscettibili allo scorrimento, dalle connessioni prefabbricate agli adeguamenti esterni con ancoraggi corti.

Acknowledgements

First, I want to thank my primary advisor, Paolo Calvi, who took a gamble and hired me (at the time, a fresh mechanical engineering graduate) as a master's research assistant in Seattle. I am grateful that he stuck with me after I finished my master's degree at the University of Washington (UW) and helped bring me to Pavia, Italy to round out my structural engineering studies within the context of this PhD in earthquake engineering. Throughout the six years spent with Prof. Calvi, he has been unconditionally supportive, even in moments when I have felt least deserving.

During the last four years in Pavia, I have tried to retain some of the philosophy acquired at UW. I hope to have replicated, if only partially, the elegance and creativity applied to research problems by my UW instructors Richard Wiebe, John Stanton and Peter Mackenzie-Helnwein. Any failure to do so is certainly a reflection on me, and not them.

I am also grateful for the influence of Guido Andreotti at IUSS Pavia, who guided the initial phase of my research and introduced me to plasticity theory, without which this Thesis would have taken a much altered path.

Beyond research, my transition from the U.S. to Pavia would have been much more isolating were it not for the kindness of the Stivella family, the Pezzano family, Winna Chang Hing He, Paolo Bianchi, the G.S. Olmo family and the Sanmaurense family. A heartfelt thanks also goes out to all the friends who have stuck by my side, despite the probably significant effort often required to do so: Matt Jenkins, Tanakij Hanmongkolpipat, Tatsu Sweet, David Tyus, Yealemnegus Fufa Waktola, Deniz Akan, Giammaria Gabbianelli, Enrico Stivella and Marco Belli.

Finally, thank you to my ever-supportive and patient parents, as well as my two super brothers.

Contents

List of Figures

List of Tables

Nomenclature

List of abbreviations
List of symbols

Nomenclature

α	tangent dilation angle
α_b	exponent in bond stress-slip law
α_d	ad-hoc factor accounting for dowel action within FSAM panel model
α_{sec}	secant dilation angle, using current width and current slip measurements
$\bar{\sigma}$	average stress in reinforcement cross section
$\bar{\varepsilon}$	average strain in reinforcement cross section
$\bar{n}$	modular ratio
β	parameter used to describe parabolic family of displacement paths experimentally imposed at pre-formed cracks
β_{ops}	parameter of `hysteretic` material in OpenSees that controls unloading stiffness damage
$\boldsymbol{\Delta\varepsilon}^{\boldsymbol{e,tr}}$	trial elastic strain increment during plastic step

$\boldsymbol{\nu_{,\varepsilon}}$ strain gradient of crushing strain

$\boldsymbol{\tilde{\omega}_{,\varepsilon}}$ strain gradient of effective crack opening $\tilde{\omega}$

$\boldsymbol{\varepsilon}$ crack total strain vector

$\boldsymbol{D^{ep}}$ elasto-plastic crack stiffness tensor

$\boldsymbol{D^{e}}$ elastic crack stiffness tensor

$\boldsymbol{D^{unl}}$ crack stiffness tensor during unloading

$\boldsymbol{D}$ crack stiffness tensor

$\boldsymbol{f_{,\sigma}}$ stress gradient of yield surface F

$\boldsymbol{g_{,\sigma}}$ stress gradient of plastic potential surface G

χ^{j} collapse scale factor for j^{th} ground motion

χ_{act} ratio of c_{act} / v_{cimax}

χ_{lok} ratio of c_{lok} / v_{cimax}

χ^{r}_{lok} value of χ corresponding to "rough" parabola

χ^{s}_{lok} value of χ corresponding to "smooth" parabola

$\Delta\lambda$ increment of plastic flow multiplier during a plastic displacement step

$\delta_{\perp}$ sliding displacement at crack centerline, used in beam on elastic foundation analysis ($\delta_{\perp} = s/2$)

δ_{peak} bond slip that develops peak bond stress

δ_{sc} bond slip

η series of modification factors for bearing stiffness of concrete subgrade

γ load ratio, $\gamma = \frac{f_x}{v}$

γ^{int} internal load angle, σ_n/v_{ci}

$\hat{\beta}$ root of characteristic equation that governs the transverse displacement of a beam on elastic foundation

$\hat{\rho}$ dilation-proportionality factor for combined interlock behavior

$\hat{F}$ combined yield surface for aggregate interlock, consisting of individual yield surfaces for tensile-dominated, shear-dominated and compression dominated surfaces, F^t, F^{lok} and F^c, respectively

$\hat{G}$ plastic potential surface for combined interlock behavior

$I\hat{M}$ mean collapse intensity

κ rate parameter controlling the effective crack roughness parameter r

κ_{col} mean collapse intensity ratio

κ_{safe} collapse intensity ratio corresponding to safe future performance

μ concrete friction coefficient

μ^{act} effective concrete friction coefficient during frictional unloading

ν crushing strain (strictly non-positive)

ϕ curvature

ψ traction ratio at the crack, σ_n/v_{ci}

ρ^{act} dilation-proportionality factor for activation reversal

ρ_h horizontal reinforcement ratio

ρ_l longitudinal reinforcement ratio

ρ_s reinforcement ratio

ρ_{cd} contact density function

σ_n crack normal stress (tension positive)

σ_n^{prev} previous converged value of crack normal stress

σ_{pu} yield strength of concrete paste

σ_{sC} bar stress at crack

σ_{sy} reinforcement yield stress

τ_b bond stress

$\tau_{b,avg}$ average bond strength between reinforcement and concrete

$\tau_{b,max}$ peak bond stress, which occurs at bond slip δ_{peak}

θ micro contact angle at a point along crack interface

$\tilde{\omega}$ effective crack width, i.e., equivalent strain used for damage calculations

$\tilde{\theta}$ effective contact angle (rad) that contributes to sliding damage within the effective crack width term $\tilde{\omega}$

ε_{cs} shrinkage strains in concrete

a_g maximum aggregate diameter

A_{cr} nominal crack area

b_w beam width

c cohesive stress

c_{act} cohesion intercept of activation yield surface F^{act}

c_{lok} cohesion intercept of combined interlock yield surface $\hat{F}$

d a derived shape parameter for F^{lok}, as a function of h, k and χ_{lok}

d_b reinforcement diameter

D_{ns} component of elastic crack stiffness contributing to normal stress due to change in crack slip

D_{nw} component of elastic crack stiffness contributing to normal stress due to change in crack width

$D_{ts,0}$ initial crack stiffness in shear

D_{ts} component of elastic crack stiffness contributing to shear stress due to change in crack slip

D_{tw} component of elastic crack stiffness contributing to shear stress due to change in crack width

E_s reinforcement Young's modulus

F crack yield function (generic)

f'_c compression strength (magnitude) for undamaged crack

$f'_{c,\nu}$ compression strength (magnitude) for crack after crushing damage

$f'_{c,res}$ residual compressive strength (magnitude)

F^c semi-elliptical yield surface for crushing behavior

F^t partial elliptical yield surface for decohesion behavior

F^{lok} parabolic yield surface for shear-dominated crack behavior

F^{tr} trial yield function evaluation

f_s reinforcement stress

f_t crack tensile strength

f_x external load normal to the crack (positive in tension)

f_{cl} closure stress magnitude required to fully close a crack

G^c plastic potential surface for compression-dominated interlock behavior

G^t plastic potential surface for tensile-dominated interlock behavior

G^{lok} plastic potential surface for shear-dominated interlock behavior

g_c toggle function to check for crushing accumulation

g_d toggle function for yield function shape change

G_f^I mode-I fracture energy

G_f^{II} mode-II fracture energy

g_s toggle function to check for s_{max}

g_w toggle function to check for crack surface overlap

h size parameter for F^{lok}, describing the normalized horizontal coordinate at the parabola vertex (negative valued)

h_b beam height

I_s moment of inertia of reinforcement bar

k size parameter for F^{lok}, describing the normalized vertical coordinate at the parabola vertex

k^r value of k corresponding to "rough" parabola

k^s value of k corresponding to "smooth" parabola

K_a contact reduction factor used in the contact density model

k_c subgrade stiffness of concrete being borne upon by rebar

l span of double-beam coupling beam

l' length of cracked portion of double-beam coupling beam, approximately $0.9l$

L_c length of curvature influence zone

L_p length of plastic hinge region

l_{ch} characteristic length

L_{unb} reinforcement unbonded length

M inclination of critical state line

M_{pr} probable moment

n crack-normal direction vector

q rate parameter controlling crack closure behavior

r	effective crack roughness, calculated during sub-critical loading
s	crack slip
s^e	elastic component of crack slip
s^p	plastic component of crack slip
s_t^{cr}	critical value of plastic slip corresponding to crack decohesion due to particle abrasion
s_θ	crack slip aligned with micro-plane inclination
s_{brk}	crack re-engagement slip
$s_{m\theta}$	crack spacing parameter
s_{max}	history variable for maximum slip magnitude (i.e., in either direction) experienced by a crack during a load history
s_{max}^+	maximum slip experienced in positive loading direction
s_{max}^-	maximum slip experienced in negative loading direction
t	crack-tangential direction vector
t_w	wall thickness
v	applied shear stress
V_F	flexural contribution to shear strength
V_n	nominal shear strength
v_{cimax}	maximum shear that can be supported by a crack, as a function of the current crack width
v_{ci}	crack shear stress
v_{ci}^{prev}	previous converged value of crack shear stress
v_{ucs}	shear stress at crack of double-beam coupling beam

V_{UC}	contribution of crack shear to shear capacity of double-beam coupling beam
w	crack opening
w^e	elastic component of crack width
w^p	plastic component of crack width
W^{cr}	work spent on crack fracture process
w_0	residual crack width
w_θ	crack opening aligned with micro-plane inclination
w_{lim}	limiting crack width corresponding to onset of unsafe collapse risk
w_{max}	history variable for maximum width experienced by a crack during a load history
x_c	horizontal coordinate of the center of the tensile-dominated yield surface F^t

Chapter 1

Introduction

1.1 Motivation

Reinforced Concrete (RC) structures are expected to deform inelastically during strong seismic events in order to meet basic design objectives (e.g., avoid collapse under strong ground shaking). If, after an earthquake (EQ), a damaged structure does not satisfy desired post-EQ performance levels, the structure's capacity may be restored either by repair or replacement. The decision to repair or replace relies on an accurate estimate of a structure's residual capacity; hence, reliable guidelines for post-EQ assessment play a crucial role in decision making.

Among possible damage indicators, visual crack information—such as the location, number, size, and direction of cracks—is commonly used by engineers (and included in damage assessment guidelines) to determine the health of concrete structures. Additionally, crack information can be used to infer the condition of steel reinforcement, which is hidden from plain sight but is vital in providing necessary strength and ductility. Decisions on post-EQ occupancy status, based on tagging frameworks [22, 101] that require accurate post-event damage state identification, can be aided by incorporating crack-based algorithms [10] for damage state estimation. In the case of retrofitting, crack widths drive the optimal repair method [72], which in turn dictates repair costs [129].

Despite the ostensible utility of crack width as a damage indicator, substantial variation exists from guideline to guideline about what crack width levels represent a severe threat to the stability of a structure [24]. Previous

works have focused on the consistency of bridge inspection manuals, with Calvi, et al. [24] demonstrating signifcant inconsistencies in crack-width grading rules of adjacent jurisdictions within the United States, leading to the comical question: *does a crack know which guideline it should adhere to?* The root of the inconsistencies lies in the generic crack-based assessment approach available in current guidelines, that, though simple and easy to deploy, ignores fundamental structural aspects that determine whether a crack will be innocuous or sinister.

Crack-width guidelines for EQ applications take a similar broad-strokes approach. Post-EQ damage is graded based on crack widths [59, 81] as well as on the presence of concrete crushing and indications of reinforcement buckling. Roughly, a wider crack implies more damage, although, in reality, the damage severity for a given crack width may additionally depend on crack type [24], crack-pattern density [119], crack orientation [47], axial load level [25], component size [147], component aspect ratio [48], reinforcement configuration [4] reinforcement fatigue life [54], corrosion levels [66] and concrete strength [48]. Crack-width guidelines do not consider most of these effects, the omission of which can be particularly dangerous and can lead to mis-assessment of structural capacity.

Mis-assessments of a building's post-EQ condition are potentially disastrous. False red tags can lead to unnecessary and prolonged downtime while false green tags belie increased collapse risk and potential loss of life. Elwood [53] reports an incident following the 2010 Canterbury earthquake in which a heavily cracked RC wall building was deemed safe to occupy – despite previous concerns that a primary shear wall was susceptible to shear cracking and crushing – only to collapse in an aftershock, killing 18. In a similar instance, a viaduct on the railway line connecting Dublin and Belfast collapsed just a week after passing an inspection with "no visible structural issues" [145]. Since damage is permitted by building codes in the name of collapse prevention, consonant attention must be devoted to accurate damage assessment.

It is evident that a methodology is needed that can reliably link visual damage measurements with expected structural performance. Rational approaches for providing this link have been come to be called Crack-Based Assessment.

1.2 Challenges with Crack-Based Assessment

At its core, crack-based assessment is a reformulation of typical forward-analysis procedures. In forward analysis, an analyst starts with a model of an undamaged structure, applies the expected loads, and evaluates the capacity (force or deformation) that can be expected for the chosen configuration. Crack-based assessment, on the other hand, starts with an already damaged structure and seeks to quantify the existing damage (damage for now is loosely defined) based on the available observations, often where the prior loading history is not precisely known. Once this arduous task is performed, the future performance of the damaged structure can be evaluated following standard forward-analysis techniques. Crack-based assessment falls into the class of inverse problems, sketched schematically in Fig. 1.1.

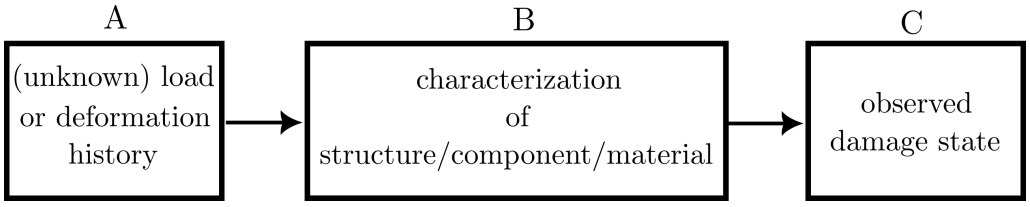

Figure 1.1. Outline of crack-based assessment inverse problem

For the difficult problem of crack-based earthquake damage assessment, identifying the load history at any particular crack (box A) from the observed damage state (box C) and the known structural behavior (box B) is rather difficult. The difficulty is accentuated by the fact that the 'known' boxes B and C are, at best, approximations: box B (structural behavior) can only be approximated by models, and box C (current state) is only partially observed because damage to internal reinforcement is largely inferred.

To alleviate some difficulty, crack-based assessment has been traditionally framed within the realm of monotonic problems, which is a reasonable approximation of bridge loading. Attempts to extend available monotonic methodologies to the assessment of reversed-cyclic cracking damage are few. The development of a general mechanics-based crack-based assessment routine would require sophisticated material models for cyclic crack behavior,

which are currently limited, or wholly unavailable. Furthermore, available crack constitutive models do not have inputs that are directly related with crack measurements, nor are many models able to unify shear cracks and flexure cracks.

1.3 Objectives of This Document

The primary objective of this Thesis is to advance the abilities of engineers to directly include cracks into finite-element models, without unduly increasing the modeling complexity. This aim was borne out of the surprising observation that few analysis models are equipped to handle crack data as direct inputs (though some indirect approaches are available), rendering difficult the engineer's task to determine the current state of health of an arbitrarily cracked structure and to forecast how it will perform over time.

The primary task toward achieving the objective of this Thesis is the development and implementation of a novel constitutive model for reinforced-concrete crack interfaces. The crack model seeks to unify shear cracks, flexure cracks and crushing damage, and is fully parameterized by the crack width, which is measured on site after buildings have been damaged by earthquakes. These features, along with the implementation of the proposed crack model into a popular finite element software, simplify the pre-processing phase of crack-based assessment routines.

1.4 Scope and Limitations

First, it is noted that this Thesis deals with assessment of already damaged structures. An equally important aspect of the problem that is not dealt with is how to effectively design new structures to avoid the tricky business of assessing cracks. Work on the design for damage limitation is being undertaken, for example, by Opabola and Elwood [127].

Within earthquake engineering, simplified models with few degrees of freedom tend to prevail (e.g., [6]), aligned with the earthquake engineering community's preference for a simplified toolkit to support time-sensitive decisions. Here, a more detailed approach to crack-based assessment is undertaken by directly modeling individual cracks. This approach provides a direct translation from damage measurements to numerical model

development. While a scaled-back modeling approach may eventually prove more numerically efficient – mimicking the debate between smeared and discrete approaches to nonlinear finite-element crack analysis [151] – the discrete crack approach is undertaken herein because of its straightforward physical interpretation. Ultimately, this approach may form the basis for simplified methods, or augment existing methods that "panelize" structures [153, 86, 27].

This Thesis focuses on cracks that are fully formed and does not deal with crack propagation. The eventual forecasting analysis of arbitarily cracked structures could be done by (i) pre-defining many potential crack planes (though this method has generally been rejected due to its numerical cost and sensitivity to mesh boundaries), or (ii) by adopting efficient smeared crack material laws (e.g., [136]) in the uncracked regions.

The crack model proposed in this Thesis has been developed for cyclically loaded rough interfaces crossed by well-embedded reinforcement, as these conditions are most representative of EQ damage to RC structures. The model framework is general, however, and its applicability could eventually be extended to unreinforced cracks, smooth cracks and keyed cracks (common in precast applications). Analysis of cracks subject to very high-cycle fatigue, such as may occur in traffic loading of bridges, requires additional considerations.

Significant attention is given to cracks carrying shear, partly because this behavior is less well-understood than cracks carrying pure axial tractions, but also because the consequences for misinterpreting shear cracks are higher.

Although the motivation for this thesis has been presented on the structural scale, much of the work is at the level of a single crack. This is to ensure that a valid and robust crack description is available for eventual implementation into full-scale assessments of damaged structures. What's more, the proposed crack model is immediately applicable to a variety of structural systems that are controlled by a single, dominant crack or interface. Examples include deep beams [111], RC walls that slide at the construction joint [172, 1], precast concrete interfaces [123], external retrofit layers [131], bridge deck overlays [88, 63], concrete dam lift joints [143], certain ductile beams [126], a novel coupling beam solution [39], the interfaces between 3D printed concrete layers [13], and novel sliding-rocking column joints [155].

1.5 Layout of This Thesis

Chapter 2 reviews aspects of previous works that align with the aim of this thesis: that is, to develop a framework for incorporating existing cracks into nonlinear finite-element simulations of damaged RC structures. Hence, existing approaches for crack-based assessment are reviewed, noting a lack of direct, yet general approaches. In response to this need, a detailed review of individual crack behavior is provided, along with modeling approaches for individual interfaces.

Chapter 3 assesses, through a case study of diagonally cracked squat RC walls, the ability of currently available numerical methods to forecast the effects of existing cracking damage on future EQ performance. The Chapter also demonstrates how detailed crack modeling can be integrated into risk frameworks for informed decision making.

Chapter 4 describes a novel plasticity-based material model for describing rough, damaged interfaces that are typical of naturally formed cracks in reinforced concrete. The model for crack behavior captures pressure-dependency, sliding-induced dilation, stiffness degradation due to shearing of aggregate particles, strength reduction due to crack widening and loss of effective contact, and configuration-dependent dissipation mechanisms. Additionally, the crack model is parameterized by crack-width, is valid for any load configuration and is formulated for arbitrary cyclic loading, making the model ideal for crack-based assessment of earthquake-damaged RC structures.

Chapter 5 describes the finite element implementation of the material model described in Chapter 4.

Chapter 6 demonstrates the versatility of the crack plasticity model, using a popular open-source finite element framework. A large number of aggregate interlock specimens, both monotonic and cyclic, are simulated and compared with the reported experimental data. Based on the best-fit numerical simulations, recommendations are made for selecting the parameters of the crack-plasticity model based on residual crack widths. Finally, a crack-sensitive structural component is simulated to demonstrate

the use of the crack model in medium-scale simulations.

Chapter 7 is a reaction to and conclusion of the Thesis, discussing the steps still needed in order to realize a general-purpose crack-based-assessment routine.

Chapter 2

Literature Review

This Chapter reviews existing approaches for crack-based assessment in Section 2.1, noting a lack of discrete-crack approaches. Then, in Section 2.2, the experimental behavior of individual cracks is comprehensively reviewed. Finally, in Section 2.3, existing mathematical models for individual crack behavior are summarized.

2.1 Existing Approaches for Crack-Based Assessment

As post- World War II infrastructure is nearing the end of its design life, it is crucial to allocate limited resources to the bridges and buildings most in distress. This need has been highlighted by the collapse of numerous aging bridges in recent decades, including the Laval overpass in 2006 [117], the Petrulla viaduct in 2014 [16], the Lecco overpass in 2016 [140], the Fossano Bridge in 2017 [62], the Morandi Bridge in 2018 [23] and the Caprigliola Bridge in 2020 [157]. Techniques for crack-based assessment have been developed, in part, to respond to this need, and represent a promising approach both for detailed and rapid assessments of bridges. In the realm of earthquake engineering, crack-based assessment is more prominent for the analysis of masonry structures while remaining little-explored for reinforced concrete. Approaches for crack-based assessment are summarized in Sections 2.1.1, 2.1.2 and 2.1.3, representing various schools of thought for crack-based assessment: Section 2.1.1 summarizes mechanics-based theories, Section 2.1.2 summarizes risk approaches and Section 2.1.3

describes the use of advanced visual inspections for developing new damage predictors.

2.1.1 Mechanics-Based Approaches to Crack-Based Assessment

Mechanics-based approaches for crack assessment seek to apply the principles of equilibrium and compatibility to establish the residual strength of cracked structural components. Many crack assessment approaches have come from the Toronto school of models that are rooted in the Modified Compression Field Theory [174]. The MCFT represents an advanced constitutive model for cracked reinforced concrete; however, alternative constitutive laws have also been adopted for crack-assessment studies, discussed below.

2.1.1.1 Shear-Critical Components

Many analytical crack-based assessment studies focus on shear-critical structures, as these structures tend to fail suddenly without warning, thus making them good candidates for rapid inspection. Shear-critical structures tend to develop a single, main crack. This feature simplifies the geometry and permits the cracked component to be idealized, e.g., as a cracked panel [27], which enables the use of MCFT-like theories.

Calvi, et al. [27] proposed a cracked membrane approach for assessing shear cracks that treats a cracked panel element subject to biaxial stresses. Because a biaxial membrane element is representative of many structural components, this method is applicable to a wide range of assessment problems. Central to the approach of Calvi, et al. [27] is an empirically derived relationship between crack secant angle and local crack stresses, based on biaxially loaded crack experiments [25]. This relationship, though limited to monotonic loading, permits local crack stresses to be estimated from visual observations of crack width and crack slip. Also derived (empirically) from width and slip measurements are the strains in crack-crossing reinforcement. Reinforcement is assumed to resist no dowel action and behave according to a monotonic elastic-perfectly-plastic constitutive law. From the above simplifications and assumptions, plus the assumption that the external stresses acting on the panel can be estimated with

some accuracy, the Calvi assessment model provides analysts a series of health indicators, including safety factors against failure of concrete struts and crack-crossing reinforcement. The procedure has been successfully implemented in the analysis of a drop-in bridge span [24].

Zaborac, et al. [181] also proposed a fixed-crack smeared panel approach for crack-based assessment, after performing an extensive review of residual shear capacity versus maximum diagonal crack width [180] and noting that diagonal crack width measurements alone (as suggested from a simplified CBA schematic in Fig. 2.1) are not sufficient to estimate the residual shear capacity of shear-critical members. The panel approach allows for structural geometry and reinforcement to be incorporated into the assessment. The approach uses observations of width and spacing (crack slips are not used because their measurement is difficult to precisely obtain and generally unavailable, even in controlled laboratory settings) to derive the average strain state of the idealized panel. In deriving the element stress state, sectional normal stresses are related to the sectional shear stresses. For a given crack observation and loading condition, the crack-based residual capacity curve is incrementally calculated assuming the orientation of the effective crack remains fixed. The crack-based approach predicts remaining strength well for plane-stress elements with well-distributed reinforcement subject to known monotonic load patterns.

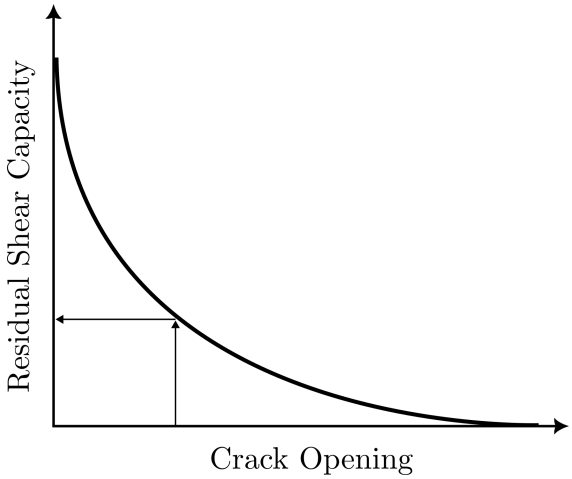

Figure 2.1. Simple crack-based assessment schematic, image adapted from [113]

Diverging from the panel approaches, Mihaylov has developed a series of kinematic theories to analyze shear-dominant structures such as deep beams [112, 115] and squat walls [114]. The kinematic theories describe the displacement field over the entire structural component, based on the assumption that deformations are concentrated in a dominant diagonal crack and that a fanned pattern of radial struts emanates from the loading point to the tensile face. A rigid block occupies the region outside the critical crack and rotates and translates based on two distinct deformation modes, characterized by the strain in the tensile reinforcement and the deflection of the loading zone. The displacement of the rigid block determines the width of the main diagonal crack. Model predictions for crack width correspond well with experimental data [112]. Having characterized the overall deformation field, the main crack width is used to predict the shear resistance due to aggregate interlock and the shear resistance of stirrups [170]. Crack spacing affects the calculated dowel action contribution. A final strength contribution is provided by the critical loading zone, which can also be estimated from crack measurements [113]. An important feature of the kinematic theories is that strength contributions are calculated from the geometry of the main crack, which is calculated as a function of crack angle and strain of longitudinal reinforcement across the crack, both of which are measurable. The kinematic theories can thus be transformed into crack-based assessment routines.

Trandafir, et al. [168] have adapted the kinematic theory by directly including crack local-geometry into the kinematic descriptions, allowing them to predict residual shear strength of lightly reinforced deep beams based on crack width measurements. Their so-called crack-based kinematic theory takes advantage of the ever-increasing availability of digital crack measurements, which allow for a detailed discretization of crack width, slip and inclination. The point-by-point crack description is coupled with a version of the contact density model [89] that has been re-calibrated against wide-crack experiments [25]. The inclusion of crack shape results in the ability to predict strength differences in nominally-identical beams due to random variations in crack pattern: the effect of crack shape on shear strength has been observed experimentally for unreinforced deep beams [111] and for plain mixed-mode cracks [78], and has been used in other crack descriptions [166]. The crack-based assessment framework of Trandafir, et al. [168] analyses the member including the detailed geometry of different

potentially critical cracks, taking the true critical crack as the one that results in the lowest residual capacity. This approach has proven successful in predicting the response of a 4-m deep beam [170].

Mihaylov, et al. [113] have simplified the crack-based kinematic theory, based on observations that failure of deep beams is triggered by crushing in the loading zone. Fathalla and Mihaylov [57] have similarly developed a crack-based assessment approach for squat shear walls, noting that damage in the compression toe can be used to assess the remaining shear strength.

2.1.1.2 Pseudo Crack Approach

The mechanical approaches for crack-based assessment in Section 2.1.1 are limited in that they generally require knowledge of the external load pattern or are restricted to a particular structural configuration, such as four-point bending. Arbitrarily oriented cracks may be difficult to handle with such approaches. This limitation can be overcome by the "pseudo-crack" modeling approach in which crack measurement data are transformed into equivalent strain fields that can easily be applied as nodal loads in continuum finite element models. The pseudo-crack approach is summarized in Fig. 2.2.

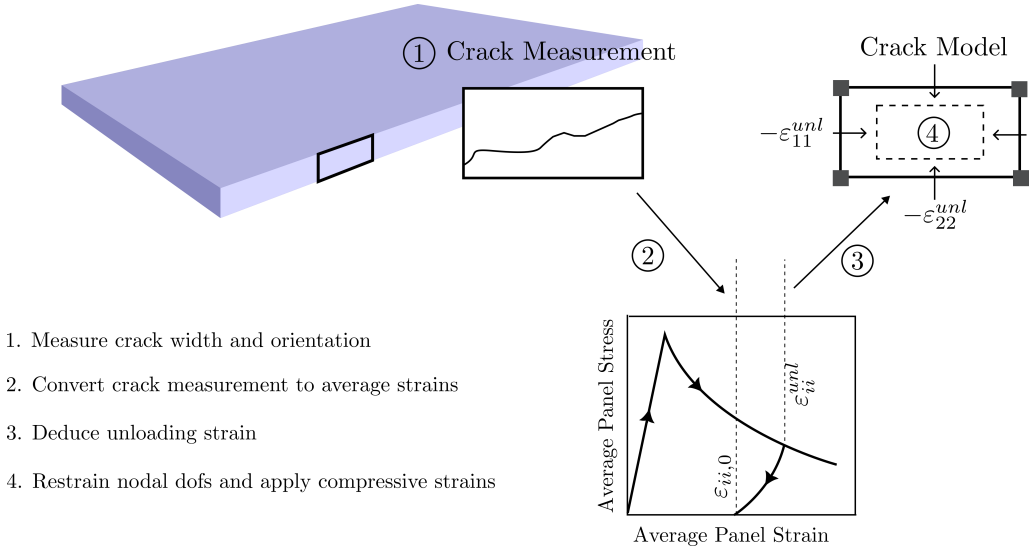

Figure 2.2. pseudo-crack modeling scheme, image adapted from [65]

One prominent example of the pseudo-crack approach is the model

developed by Fujiyama et al. [65] for fatigue analysis of cracked RC bridge decks, and later extended to horizontal cracks that form in bridge deck slabs at reinforcement layers [178]. The method smears crack measurements into an average residual strain field and back-calculates the peak panel strains that would have unloaded to the smeared residual strains. The unloading strains are imposed at the nodes of a finite element model to represent prior damage. The pseudo-crack approach has shown promise for high-cycle fatigue analysis of bridge decks, but is limited by the assumptions of non-reversed loading and zero residual crack stress at the measured state.

A similar approach was employed by Zaborac, et al. [182] in the assessment of a diagonally-cracked bent cap, with some trial and error required on the location and amount of prestraining to apply. Zaborac, et al. [182] recommend a prestrain value of about $\Delta\varepsilon_c = -1.5w_{cr}/s_{cr}$ to be applied narrowly along the damage plane.

Rather than apply prestrains to represent pre-exisiting cracks, Bahnamiri and Hrynyk [12] replace crack width and crack inclination observations with an effective stress vector that would reproduce the observed crack. Their process is iterative. The crack-producing stress is kept constant in forecasting analyses to represent the pre-existing cracking damage. The approach of Bahnamiri and Hyrnyk was preliminarily validated against monotonic, pure shear panel tests, for which the crack-based model generally underestimates the residual shear stress.

2.1.1.3 Weakened Elements Method

Similar to the pseudo-crack approach just described, the so-called weakened-elements method modifies a finite element model during the pre-processing stage to reflect the presence of existing cracking damage. In the weakened-elements approach, material properties of cracked elements are adjusted to reflect reduced properties, as sketched in Fig. 2.3.

Blomfors et al. [20] overlayed a field-measured crack pattern onto a finite element discretization of a tensile-cracked beam. Elements that were intersected by the crack overlay were assigned reduced mode-I fracture energy via strain offsets. The strain offsets are chosen based on the measured crack width so that the remaining fracture energy, according to a standard bilinear cohesion curve, is reproduced in the weakened element. In this case, the weakened-elements approach aligns with the pseudo-crack method, but

provides a more rational method for selecting the prestrain to apply to the cracked elements. Blomfors, et al. [20] used a shear-retention factor of 0.01 (i.e., cracked shear modulus reduced by 99% in cracked elements).

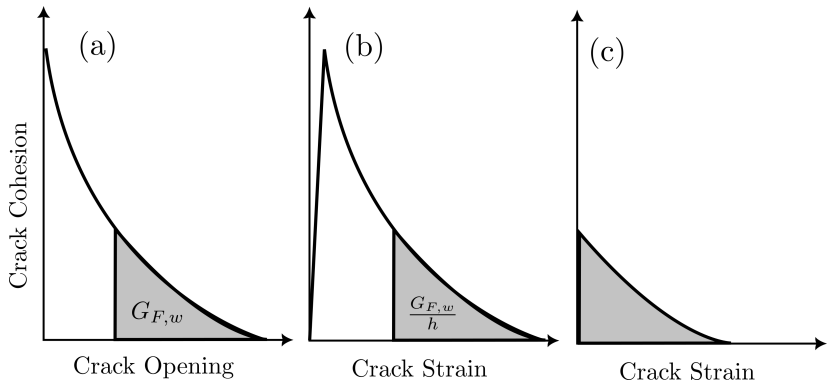

Figure 2.3. weakened-element modeling scheme: (a) residual fracture energy based on measured crack width; (b) stress-strain relationship based on element size h; (c) weakened element stress-strain law in crack-perpendicular direction (image adapted from [20])

Blomfors et al. [20] also modeled the pre-cracked specimen with discrete interface elements, noting significant pre-processing effort to include interfaces in the finite element mesh. Their crack geometries were simplified to avoid convergence problems for more realistic tortuous crack patterns. The cracked beam was tested in 4-point bending, and simulated with the weakened elements method and the discrete interface approach: overall, Blomfors, et al. [20] reports better predictions using the weakened-elements method.

A recent work by Alashmi and Oudah [3] extends the weakened-elements method by incorporating random fields into the material properties of cracked elements, useful for analysing corroded reinforced concrete members in a computationally efficient way.

2.1.2 Risk-Based Approaches to Crack-Based Assessment

Risk-forward approaches for crack-based assessment are conceptually similar to traditional crack-based assessment frameworks, save that the output of a risk approach is a building performance objective, which is often presented in probabilistic terms. The probabilistic output, e.g., collapse risk or expected losses, may be preferable for stakeholders compared with the traditional deterministic approach summarized in Fig. 2.1 for which residual strength is the output.

2.1.2.1 FEMA 306 Relative Performance Assessment

The concept of relative performance was introduced by FEMA 306 [59] (which deals with wall components) to quantify the effect of a damaging earthquake on the future earthquake performance of a wall-structure. In particular, FEMA 306 evaluates whether a performance objective (e.g., collapse prevention for rare ground motion) is met for a wall structure, both in its undamaged condition and after enduring EQ-induced damage. FEMA 306 measures performance as the ratio of displacement capacity inherent in the structure to the displacement demand of the expected shaking. A displacement capacity-to-demand ratio, or performance index, exceeding 1.0 indicates that the performance objective is met. The ratio of the performance index for the damaged building (d'_c/d'_d) to that of the undamaged building (d_c/d_d), i.e. the *relative performance index*, describes how EQ damage has reduced the structural capacity. A relative performance index less than 1.0 indicates a reduction in performance due to the existing damage.

$$RPI = \frac{d'_c/d'_d}{d_c/d_d} \tag{2.1}$$

In the FEMA 306 procedure, displacement demand is estimated by nonlinear-static procedures (e.g., displacement-coefficient method or capacity-spectrum method) and displacement capacity is defined as the displacement corresponding to the exceedance of any component displacement limit. Displacement limits are defined based on the structural component of interest and the desired performance level from ASCE-41 [6]. For a damaged structure, displacement demand and displacement

capacity calculations account for reduction in component strength, stiffness and displacement capacity via "component modification factors" tabulated in FEMA 306. The reduction factors are empirically defined for each wall behavior mode (e.g., diagonal tension) and various crack width bins representing damage severity. Following this procedure, it is possible to approximate whether a crack-damaged RC-wall structure (with each component characterized by a certain crack type and crack width) will satisfy the target performance objective(s).

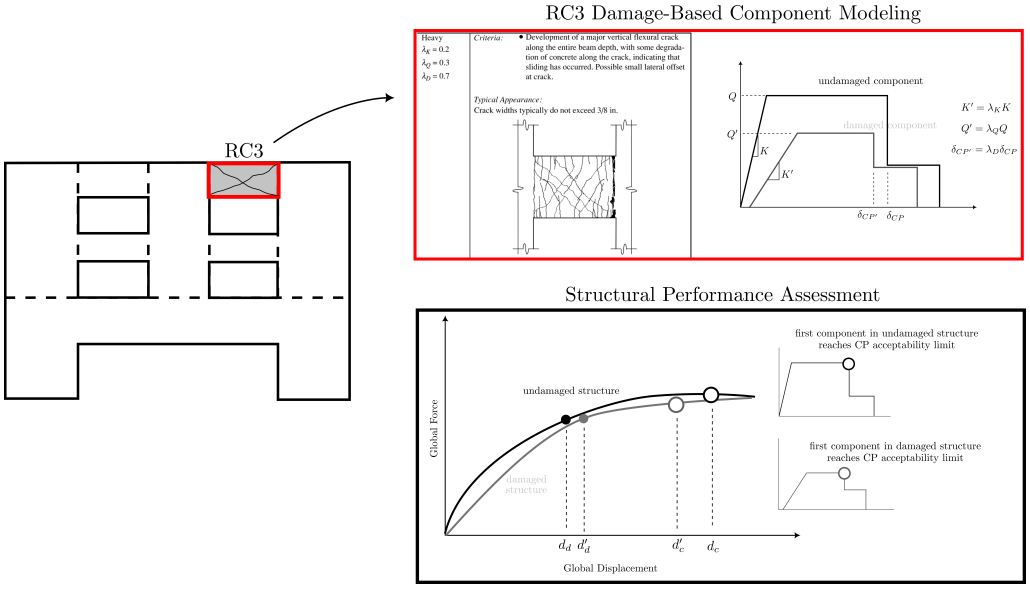

Figure 2.4. FEMA306 component-based approach to crack-based assessment, images adapted from [59]

The FEMA 306 approach was an early framework that can be used to derive a structure's performance, and *remains unique in that it permits a relationship between performance and crack width measurements.* The framework also distinguishes between wall types and failure modes. Despite its pioneering nature, the crack-width framework is of a preliminary nature (not accounting for the many effects that may alter crack width) and its precise outputs are subject to question, as the recommended crack widths in FEMA 306 have been called into question [121, 137].

2.1.2.2 FEMA P-58 and Crack-Width-Based Fragilities

The FEMA P-58 *Methodology for Seismic Performance Assessment of Buildings* [60] represents a "next-gen" approach for seismic performance assessment. FEMA P-58 seeks to build on first generation risk frameworks (such as ASCE 41) to: incorporate the uncertainty inherent in seismic design via a layered probabilistic approach; and communicate the desired performance for design of new buildings and assessment of damaged buildings, enabling stakeholders to use risk in their decision making processes. Performance can be measured through casualties, repair cost, repair time, environmental impacts and unsafe placarding, depending on the building use.

The assessment methodology of FEMA P-58 involves: (i) probablistic representation of seismic hazard at a site; (ii) assessment of building response (in terms of appropriate global demand parameters), given a ground motion intensity; (iii) identification of structural component damage, given a global demand value; and (iv) calculation of losses, measured through consequence functions that correspond to the damage state.

FEMA P-58 is not presented as a crack-based assessment framework, but is flexible and permits the use of appropriate demand parameters, as long as those parameters "*...predict(s) the occurrence of the potential damage states with the least uncertainty*". FEMA P-58 goes on to say that "*when considered necessary or appropriate, it is possible to use other demand parameters (e.g., ...local component actions)*". Thus, the FEMA P-58 could be adapted into a crack-based assessment methodology by adopting crack width as a demand parameter, assuming the following conditions are met:

- crack widths are demonstrated to be superior at predicting component damage states than commonly used global demand parameters such as story drift ratio;
- crack widths can be reliably and efficiently predicted for seismic inputs;

The framework could be used either to: (i) assess the state-of-health of an earthquake-damaged structure, or its performance under future earthquakes to determine is repair action is necessary to return the structure to the desired performance level and if occupancy restrictions are called

for; (ii) assess the likely performance of various retrofit solutions. This Thesis is primarily concerned with the first case. For the assessment of an earthquake-damaged structure, the relevant performance measures are collapse risk, repair time, repair cost and unsafe placarding. Of these, collapse risk and unsafe placarding are most directly related with structural performance, while repair time and repair cost are influenced heavily by material procurement, obtainment of permits, lead times and site cleanup.

A crack-forward approach could reduce the dependence of performance assessments on engineering judgment. The results of FEMA P-58 performance assessments of existing buildings are, in the words of the FEMA document, sensitive to "*the interpretation of visible evidence of damage by inspectors performing post-earthquake safety investigations*". This may be because visual damage markers – among them crack width – are merely supplementary to the framework for damage assessment; some guidance is given regarding the visual markers corresponding to each damage level, but engineering judgment is still relied on to bin the damage. If component damage states are mis-interpreted, the measured performance may not reflect the true risk posed by the damaged building. The need to reduce engineering judgment is apparent for the case of placarding: unsafe placards are required if a prescribed ratio of fragility components (e.g., shear walls or beam-column joints) exceed a damage level. An example could be that a red tag is assigned if 20% of shear walls exceed damage level 3. The reliance on inspector judgment is amplified by the fact that the global demand parameters – such as story drift ratio, peak drift and residual drift – that are directly related with discrete damage levels are not trivial to measure in the field.

Since the publication and subsequent adoption of FEMA P-58 by the seismic risk community, some research works have explored direct relationships between crack width and component damage levels. Yurdakul, et al. [179] developed crack-width-based damage fragilities for beam column joints based on high-fidelity numerical modeling and proposed to use residual crack width measurements as a direct indicator of the economic feasibility of joint repair. Aydin, et al. [9] use fiber-based numerical models to propose a relationship between cumulative crack width in the plastic hinge region of flexurally-dominated reinforced concrete columns and the maximum sustained drift demand. They also proposed fragility-type curves relating the probability of having exceeded certain drift demands, given a

crack width. While the analyses of Aydin, et al. are limited to flexural cracks, the work highlights the practical need for using crack-forward assessment approaches. Marder, et al. [104], explored relationships between crack measures and rotation demands of beam plastic hinge regions, noting that maximum crack width should be augmented by a measure of crack density or number to get a more meaningful damage index. Marder, et al. then proposed empirical predictions for plastic hinge rotation demand based on either the maximum-width-to-cumulative-width ratio or the number of cracks in the plastic hinge region.

Relationships between crack width and global demand parameters, such as those mentioned above, can be incorporated into risk assessments following a damage-dependent fragility approach. A case for damage-dependent fragility functions has been made by de Quevedo Iñarritu, et al. [144], who argue that buildings with existing damage are more vulnerable to future quakes and that seismic fragilities should reflect pre-existing damage in order to arrive at accurate loss estimations. Additionally, de Quevedo Iñarritu, et al. demonstrate that non-cumulative global damage indices (e.g., story drift ratio, stiffness degradation) tend to underpredict the accumulation of damage during sequential seismic analyses relative to using component-based damage indices. In principle, crack width and crack density could form the seed for a promising local damage index.

2.1.3 Fractal Approaches to Crack-Based Assessment

Building on the discussion in the previous subsection, this subsection reviews research that relates crack-width measurements to damage levels in structural components, with the aim to reduce subjectivity in structural damage assessments. These methods are based on visual markers such as crack width, crack density and crack orientation, and provide a promising set of tools for damage characterization in the field. Possibilities for incorporation into risk frameworks was discussed previously.

2.1.3.1 Crack Mono-fractal Damage Indices

Farhidzadeh, et al. [56] use a simple box-counting method to classify the fractal dimension of cracks, that is, the tortuosity (between 1 and 2) of crack surfaces. The box-counting method covers a visual area with an overlay grid

and counts how many boxes are crossed by at least 1 crack. In this way, the complexity of the cracking pattern is estimated. By counting the number of boxes N of size r and plotting the relationship in log-log space, the fractal dimension D is practically estimated.

$$\log(N(r)) = D\log(1/r) + C \tag{2.2}$$

It should be noted that the range of box sizes used to obtain the experimental estimation of D is related to a material characteristic length, and some care should be taken in selecting an appropriate range.

Farhidzadeh, et al. [56] proposed a simple damage index, based on the crack pattern fractal dimension D from Eq. (2.2), that rescales the fractal dimension D from its original range (between 1 and 2) to a more practical range between 0 and 1, where 1 represents maximum crack density.

Remarkably, for the two shear walls tested by Farhidzadeh, et al. [56], the proposed damage index provided a near-perfect estimation of the relative stiffness loss $1-\frac{K}{K_0}$ throughout the reversed-cyclic loading protocol.

Farhidzadeh, et al. [56] related values of the proposed damage index to damage grades (based on crack width) from the IAEA guidelines [76] for nuclear vessel assessments. While the proposed damage index gave a smoother transition between damage grades I-III than using residual cracks, the crack width at peak deformation gave comparable results as the damage index. This suggested that, if a simple crack measure is used in lieu of a fractal measure, the peak width is a more reliable predictor of damage than the residual crack width.

Woods, et al. [177] incorporate the damage index of Farhidzadeh, et al [56] into an automated inspection routine, and propose a correlations between the damage index and the damage grade based on tests of shear-dominant RC walls: A DI from 0.0-0.2 indicates minor cracks; a DI from 0.2-0.6 indicates moderate cracking and onset of steel yielding; a DI between 0.6-1.0 indicates critical damage such as heavy cracking, extensive steel yielding, concrete crushing and spalling.

Modifications have been proposed to the Farhidzadeh damage index by Carillo, et al. [30] who rescale the damage index so that a damage index of 1 corresponds to loss of lateral load-carrying capacity.

Finally, it should be noted that the fractal approach is built upon the underlying assumption that structures are properly designed and can adequately redistribute damage so that a uniform and distributed crack

pattern forms. The approach does not predict an increase of damage if existing cracks widen, which is a limitation. This approach is also insufficient for shear-critical structures that are dominated by a single, wide crack.

2.1.3.2 Crack Multi-Fractal Damage Indices

Multi-fractal analysis extends the box-counting method and the mono-fractal dimension to consider the density of cracks within each box, from which a generalized fractal dimension D_q is obtained [28, 50]. The parameter q allows for the self-similar fractal pattern to be analyzed at different scales by weighting boxes with a certain crack density. Negative values of q are useful for identifying hairline cracks, while positive values of q are useful for identifying crushing or spalling damage [119]. A representative picture of damage to RC components can be sketched by considering fractal characteristics for q values of -1, 0 and 1 [119, 28]. Values of the fractal dimension can be plotted against various local scalings to produce a *singularity spectrum* that is useful for identification of crack trends [37]. Ebrahimkhanlou, et al. [50] show that evolution of the singularity spectrum (which is a convex parabola in the case of self-similar crack patterns) can indicate both formation of new cracks and growth of existing cracks.

Multi-fractal crack indices have also been utilized as predictors for maximum drift ratios [119, 73]. Momeni and Dolatshahi [119] predict peak drift levels of RC shear walls based on visual multi-fractal crack measurements, and suggest that the predicted drift ratios can be used in conjunction with already existing fragility functions to establish the probability of exceeding certain damage levels. Momeni and Dolatshahi [119] also develop new fragility functions based directly on the visual crack measurements of a large database of damaged shear walls. Hamidia, et al. [73] mimic the study of Momeni and Dolatshahi [119] to provide predictive equations for the peak sustained drift of RC moment frames. Interestingly, the drift prediction equations proposed by Hamidia, et al. [73] only include fractal dimensions with orders (i.e., q values) below or equal to 1, indicating that — for the considered database — crack pattern and density are more important than crack width for predicting peak sustained drift. Zamani, et al. [183] propose a routine for including the multi-fractal indices obtained from visual crack inspections into the FEMA P-58 framework for loss

estimation.

Taking the crack fractal prediction one step further, Azhari and Hamidia [10] augment the multi-fractal index by succularity and lacunarity to develop fragility curves relating ASCE 41 seismic performance levels to crack fractal indices. Despite the mathematical sophistication, the developed fragility curves assume that the current acceptance limits of ASCE 41 represent "truth" damage state, which may not be perfectly accurate.

2.1.4 Comments on Existing Crack-Based Assessment Routines

Current strategies for crack-based assessment are largely limited to applications for which loads are monotonically increasing or held constant. While some crack assessment has been considered for cyclic applications (e.g., cyclically loaded bridge decks) there remains a need for a mechanics-based crack-description that can be used as model inputs for high-fidelity numerical modeling of existing cracking damage, when said damage was sustained due to reversed-cyclic loading such as might be expected from an earthquake. To provide a direct crack representation – contrasted with the indirect pseudo-crack method – the remainder of this Thesis is concerned with discrete crack modeling and the eventual implementation of such a model into a finite element framework for the analysis of full-scale damaged structures.

To establish the true behavior of a crack under general loading, Section 2.2 summarizes empirical evidence of cyclically loaded cracks, with emphasis on cyclic, mixed-mode behavior.

Then, Section 2.3 reviews some successful approaches available in the literature for modeling cyclic interface behavior.

2.2 Experimental Observations of Crack Behavior

The approach of this Section is to collect and present experimental data that covers the full range of expected crack behavior. These observations, properly packaged together, will provide evidence for a unified crack model that describes both flexure cracks and shear cracks, and can be used as

a basis for an interface element that represents existing cracking damage within a finite element framework.

First, monotonic shear transfer is treated in Section 2.2.1. Monotonic shear friction is a vast topic and cannot be treated in full – rather, Section 2.2.1 seeks only to review shear strength trends and to collect observations of crack dilation. Experimental shear strength results are distilled onto a normalized strength surface and crack dilation data is compared to an empirical expression common in design codes. More extensive reviews of shear-friction behavior can be found in the numerous summary papers and databases available in the literature [133, 46, 156].

Section 2.2.2 reviews available evidence from cyclic shear crack experiments, with priority given to fully reversed behavior. For select high-quality data, the effect of load reversals is plotted in stress coordinates (shear stress versus clamping stress), in displacement coordinates (crack width versus crack slip) and in the crack-tangential space (crack shear versus crack slip) to give a full picture of cyclic crack response. The discussion focuses on fully reversed cycles, but brief comments are also made for single-sided cyclic shear in Section 2.2.3. Together with the monotonic experiments reviewed in Section 2.2.1, the cyclic experimental observations form the basis of a material model that is formulated later in Chapter 4. It will be shown in Chapter 4 that crack shear behavior can be unified with existing tension and compression descriptions to arrive at a general model of an arbitrarily loaded crack.

Finally, the interactions between crack and the reinforcement crossing the crack is reviewed in Section 2.2.4.

An overview of testing setups exploited in the literature – either for aggregate interlock or dowel action – is shown in Fig. 2.5. A sheared gray panel is shown in the Figure to schematically represent the deformation mode of each interface, which is represented by a bold green line.

2.2.1 Shear Friction Response to Monotonic Loading

Shear Strength Monotonic shear transfer across reinforced concrete interfaces has been studied experimentally since the 1960s via nearly one thousand experiments [133]. Most expressions for interface shear strength recognize the cohesive-frictional nature of shear-friction, which is separated into its constituent parts in Eq. (2.3):

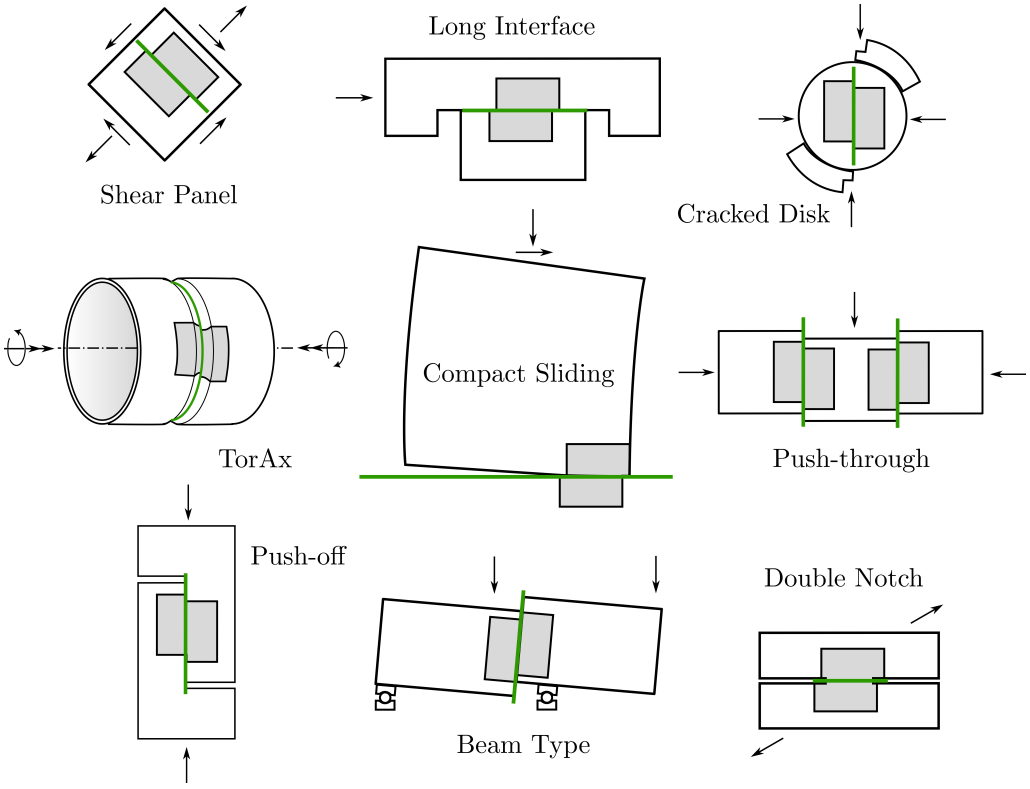

Figure 2.5. Various experimental configurations for testing individual cracks: TorAx [18], Shear Panel [25], Compact Sliding [171], Long Interface [125, 130], Beam Type [99], Push Through [165, 184], Double Notch [78, 166, 74, 161], Push-off [63], Cracked Disk [49]

$$v_{ci} = c + \mu(-f_x + \rho_s \sigma_{sy}) \tag{2.3}$$

where v_{ci} is the crack shear strength, c is the cohesive stress, μ is the concrete friction coefficient, f_x is the applied stress across the crack (tension positive, hence the minus sign for clamping stress), ρ_s is the reinforcement ratio of the crack-perpendicular reinforcement, and σ_{sy} is the reinforcement yield stress. Equation (2.3) is one of many functional forms that have been proposed for shear-friction strength, though it is the simplest and most common. An extensive survey of other shear frictional strength equations can be found in the summary paper by [156].

Regardless of the chosen form for shear-friction strength, it is recognized that reinforcement passively contributes to the effective clamping stress. That is, crack opening activates the reinforcement, which in turn resists opening. For interface strength calculations, full reinforcement tensile strength is often assumed to develop, though ACI 318-19 [2] limits the usable strength to 420 MPa. The achievable clamping stress has also been noted to decrease for large crack slips due to localized bar curvatures (kinking) at the cracked section. Kinking effects will be discussed in Section 2.2.4. Alternative versions of Eq. (2.3) include a strength contribution from dowel action, commonly proportional to $\sqrt{\sigma_{sy} f'_c}$, with Tanaka and Murakoshi [164] proposing a "dowel index" $d_b^2 \sqrt{\sigma_{sy} f'_c}$ to approximate the peak dowel resistance. In the interest of separating the interface resistance from the reinforcement resistance (necessary for the eventual finite element implementation of Chapter 5), the two are reviewed independently in this work.

Crack topology also affects crack shear strength. Surface roughness -- related to concrete strength and maximum aggregate diameter [166] -- improves strength and stiffness and is often lumped into the friction coefficient, which can range from $\mu = 0.6$ for smooth surfaces to $\mu = 1.0$ for rough surfaces [2]. Rougher surfaces interlock better, leading to increased cohesion. High contact stresses lend the cohesion term sensitive to concrete strength [154]. The importance of local contact conditions is emphasized by [174], who calibrated an expression for the peak transferable interface shear stress (v_{cimax}) based on monotonic experiments by Walraven [176]. The expression for v_{cimax}, reported in Eq. (2.4) with units of MPa and mm, is a function of crack width (w), maximum aggregate diameter (a_g) and the concrete strength (f'_c).

$$v_{cimax} = \frac{\sqrt{f'_c}}{0.31 + \frac{24w}{a_g + 16}} \tag{2.4}$$

While Eq (2.4) does not satisfy the conceptual limit that the shear capacity should vanish as w approaches a_g, the phantom residual stress is low, and this does not seem to hinder the predictive power of the model for more realistic crack widths: the equation has been validated repeatedly in the four decades since the original MCFT publication [174]. In a later publication, Vecchio suggests that stresses are transferred across crack faces

up to widths of about 5 mm [173].

[174] proposed a parabolic strength envelope, normalized by v_{cimax}, for interlocking cracks under combined shear and compression. As shown in Eq. (2.5), the mixed-mode crack retains a non-zero cohesion c that scales as $0.18v_{cimax}$. The peak interface shear strength is attained at the parabola vertex $(-v_{cimax}, v_{cimax})$ termed herein the *critical stress*. Notably, the secant slope to the vertex is 1.0, which corresponds to a rough ACI crack. Clamping stresses beyond the critical point shift the failure mode to a crushing-type, for which Eq. (2.5) is not valid.

$$\frac{v_{ci}}{v_{cimax}} = 0.18 + 1.64\left(\frac{-\sigma_n}{v_{cimax}}\right) - 0.82\left(\frac{-\sigma_n}{v_{cimax}}\right)^2 \tag{2.5}$$

The parabolic strength surface of Eq. (2.5) is a convenient alternative to Eq. (2.3) because its normalizing parameter v_{cimax} is a function of crack width. This feature will prove useful for crack-based assessment, undertaken in later chapters of this Thesis. The parabolic surface is plotted in Fig. 2.8

Force-displacement curves Equations (2.3) and (2.5) indicate the pressure sensitivity of shear strength but give no insight into the force-displacement behavior of a crack (though it can be intuited that force-displacement behavior also depends on the applied normal pressure).

To better characterize the role of clamping pressure, a definition is first provided for the *critical clamping pressure* as the pressure that completely prevents crack opening during sliding. Cracks with mild (i.e., sub-critical) clamping pressure are *dilatative* and open during sliding, while cracks with super-critical clamping pressures are *contractive*.

Dilatative cracks exhibit increasing force-displacement curves. This is because, in the absence of extreme clamping pressure, adjacent aggregate particles slide vertically across each other and activate reinforcement clamping which effectively strengthens the shear-friction resistance. Critically-clamped cracks and super-critical (contractive) cracks, on the other hand do not engage reinforcement confinement, and degrade rapidly with sliding because the aggregates are prevented from overriding. Essentially, aggregates are forced to plough through the adjacent concrete matrix.

Constant-width boundary conditions have commonly been adopted experimentally, possibly inspired by the numerical scheme proposed by Walraven (discussed in Section 2.3) in which shear-slip curves are generated for

a variety of constant crack widths then spliced together for more realistic dilation paths. It is unclear whether the "splicing" approach is tenable for generic dilation paths, given the strongly path-dependent behavior of concrete.

Dilatative cracks experiments are typically performed for either the special case of constant clamping stress or for the more *natural* conditions in which reinforcement passively confines the slip-attendant crack opening. Critically-clamped cracks or cracks subject to forced (un-natural) dilation paths often exhibit a clear peak strength. In fact, Tirassa et al [166] proposed a dependence of peak shear stress on secant dilation angle ($\alpha_{sec} = \arctan w/s$). However, "natural" crack paths are characterized by a gradual hardening behavior and do not exhibit a unique peak shear. In effect, the peak of the shear-slip responses for imposed linear dilation paths is an artifact of the unnatural, forced ploughing of aggregate particles through the concrete matrix. Thus, any relationship between peak strength and α_{sec} may be unreliable for cracks in applications with well-clamped (or reinforced) cracks (though such a relationship would be useful for direct crack-based assessment).

Dilation behavior Due to reinforcement restraint, the interface normal stress (σ_n) in Eq. (2.3) becomes increasingly compressive for slip-attendant crack opening. In turn, large clamping stresses promote local aggregate crushing, thereby shifting the deformation mode from overriding to sliding. Experimentally, the sensitivity of crack opening on clamping stress is most apparent for interfaces crossed by unbonded reinforcement [176]. For cracks crossed by bonded reinforcement, on the other hand, Walraven proposed a dilation relationship that is independent of clamping stress, suggesting that crack closure is impeded by an accumulation of rubble particles at the interface. This assertion has not been proven elsewhere and contradicts evidence that a crack – even if filled with rubble – closes under sufficient clamping stress [153]. Despite the apparent discrepancy, the form of Walraven's [176] dilation law has been influential, and a similar equation has appeared in the CEB-FIP Model Code (MC), provided in Eq. (2.6) with units of mm.

$$w = 0.6 s^{2/3} \tag{2.6}$$

Equation (2.6) is compared in Fig. 2.6 with crack paths from various

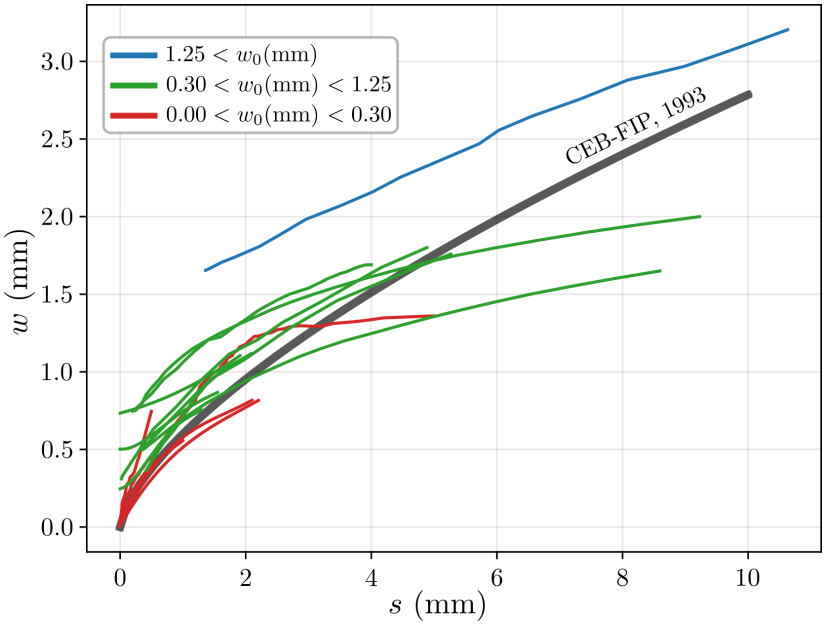

Figure 2.6. Monotonic crack paths of rough cracks with various initial crack widths, compared to 1993 Model Code

experiments, containing both bonded and unbonded reinforcement [25], [165], [176], [71], [116], [51]. The MC equation closely follows the monotonic crack trajectories of small initial cracks ($w_0 < 0.30$ mm). Paths for medium ($0.30 < w_0 < 1.25$ mm) and large ($w_0 > 1.25$ mm) cracks follow flatter trajectories but seem to approach the MC curve. However, the continued dilation for large sliding displacements predicted by the MC equation is not supported by experimental results; crack overriding is theoretically limited by the aggregate size [15].

Though Eq. (2.6) fits many experiments well, the equation does not functionally capture the dependence of crack normal stress, aggregate size, concrete strength, load conditions, or initial crack width. The Author has not found any simplified dilation relationship with better predictive power, which is a gap in the literature, particularly as more complicated load scenarios are considered.

Path-dependency In a small number of interface tests, a pre-defined crack dilation relationship was imposed and maintained throughout the test

[78], [166], [18], [74]. Jacobsen [78] and Tirassa, et al. [166] both imposed linear crack paths ($\Delta w = \tan\alpha\,\Delta s$) on narrow cracks having initial crack widths less than 0.1 mm. The imposed dilation angles (α) were varied between 40 and 60 degrees. Hassanzadeh [74] explored a similar set of linear paths as well as a parabolic family of crack displacement paths ($w = \beta\sqrt{s}$) which he deemed more natural than the linear path. Most recently, [18] tested a single specimen under a controlled crack opening, where the crack opening was scaled proportional to the applied shear stress. This resulted in a nonlinear path in displacement space. Becks and team also tested four constant-width cracks. Each path is plotted in Fig. 2.7, noting that only the cracks paths starting at 0.1 mm are shown for the Tirassa and Jacobsen experiments.

The hypothesis of path-independence, implicity assumed by multiple authors [165], [176], would dictate that two cracks with the same net deformation (w, s) should resist identical shear. This can be tested by comparing crack states at various intersection points in Fig. 2.7.

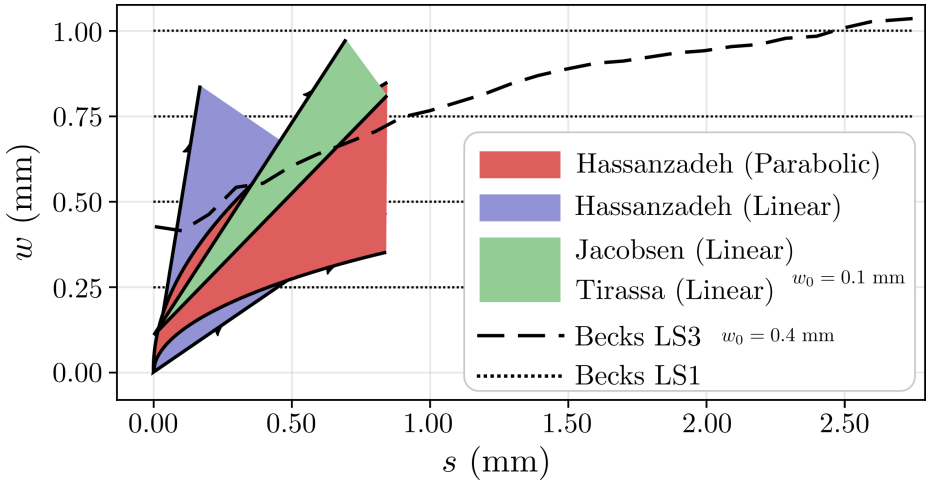

Figure 2.7. Crack path spaces for controlled dilation paths [78], [166], [18], [74]

Both Hassanzadeh and Becks performed simple path-dependence checks by comparing the crack stresses at displacement intersection points of different paths. Becks' constant-width test series intersects the controlled Becks path in three locations, as shown in Fig. 2.7. In the shear-slip plot, however, the intersections are offset, or in one case missing entirely.

Despite this, Becks and team do not wholly reject the path-idependent hypothesis. Hassanzadeh, on the other hand, tests path-dependency more thoroughly and is less forgiving. Hassanzadeh tests a stair-stepping crack path that alternates between linearly increasing paths (purple family of paths in Fig. 2.7) and parabolic paths (red family of paths in Fig. 2.7). In this way Hassanzadeh creates multiple intersection points. He observes that the crack normal stress is similar at the intersection points, but the shear stress is strongly path-dependent. Hassanzadeh also tested paths that differed initially but that eventual merged, noting that the crack stresses had a memory of the initial path and did not likewise merge.

Work conjugate plot The preceding discussion suggests that absolute crack width and absolute crack stress cannot be directly related, in light of crack path-dependence. Inspired by soil mechanics, the Author plots the instantaneous dilation angle ($\alpha = \Delta w/\Delta s$) onto the work-conjugate stress-deformation plot of Fig. 2.8. Natural experiments by Walvraven are overlayed on the v_{cimax}-normalized stress parabola along with marker orientation lines to indicate the tangent dilation angle. Remarkably, the instantaneous dilation angle aligns with the normal vector to the strength envelope. The dilation angle flattens as shear approaches the parabola vertex, eventually flattening completely when shear saturates.

Critically-clamped constant-width experiments are added to the plot with triangular markers, where it is observed that cracks of this type follow a flatter stress path with no apparent cohesion.

2.2.2 Cyclic Shear Behavior of Individual Cracks

This Section describes the fundamental features of cyclic, mixed-mode crack behavior through a review of twelve relevant experimental campaigns summarized in Table 2.1. The test protocols apply fully-reversed cyclic shear loads via push-off tests, panel tests and a novel torsional rig, among other test setups summarized in Fig. 2.5. In addition to shear, axial loads are applied as either shear-proportional (ratio from -1 to 1), constant compression, or not at all. All specimens are initially cracked or mated in the case of cold joints (initial crack widths up to 0.70 mm), crossed by reinforcement (either bonded or unbonded) and undergo fully reversed cyclic loading (either load control or displacement control).

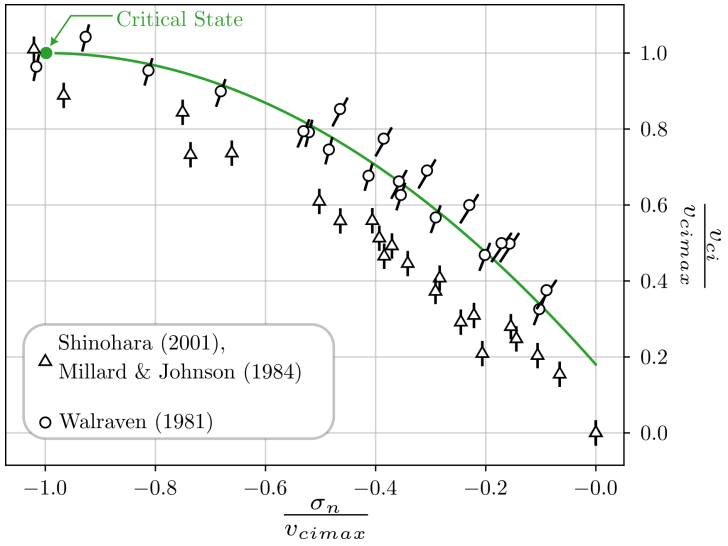

Figure 2.8. Combined stress-dilation chart with experimental data [161], [176], [116] (displacement axes are illustrative)

Each of the considered tests reports data for at least shear stress, crack slip and crack dilation. Additionally, some tests [25, 18] directly report crack normal stress or report data such as reinforcement strain that allows for crack normal stress to be calculated from equilibrium considerations [125]. On the whole, the dataset provides a broad picture of interfaces under fully reversed cyclic loads.

Cyclic Shear Strength Reduction Shear strength of a cyclically loaded crack is not clear-cut as it was for monotonically loaded cracks. While Mattock [108] proposed a generic 20% strength reduction for cyclic loading, it has since been established that the cyclic shear strength reduction depends on both number and type of cycles. Cattaneo, et al. [33] suggests a 30% strength reduction after 3 repeated cycles at a given slip amplitude, on top of the 20% Mattock knockdown. [125] measures a similar reduction and finds that rougher surfaces weaken faster than smooth surfaces. Figueira et al. [63] proposed $S-N$ curves for the strength loss per cycle, but consider only specific stress ranges. In reality, cycles-to-failure might vary by orders of magnitude depending on the loading sequence [14] and whether the stress range changes sign or not; fully reversed cycles are more damaging than

partially reversed cycles with the same stress range. Directional asymmetry further complicates strength characterization. [165] – followed by others [25, 171, 87, 132] – observed that sliding resistance in the second direction is pre-impaired by sliding in the first direction.

Table 2.1. Summary of reversed-cyclic interface experiments

Researcher	No.	Type	BC's	A_{cr}	f'_c	w_0	a_g	Reinf.
Tassios [165]	2	LOK	const. clamp $\sigma_n = -0.5$	300x150	16 - 40	< 0.1	N/R	
Fronteddu [64]	18[2]	LK	const. clamp dynamic load	500x250	28	0.0	20	none
Kono [87]	2	LK + DWL		400x160	45-110	0.0	20	bonded
Gebreyouhannes [71]	2	LK	repeated cycles const. shear amp.	280x150	32.0	0.5-0.7	20	unbonded
Puntel [143]	5	LK	const. clamp	900x300	22	≈ 0.0	N/R	none
Calvi [25]	8	LK	load control shear-prop. tens.	890x70	29-110	0.1-0.3	14	unbonded $L_{unb} = 700$ $\rho_s = 0.01085$
Trost[1] [171]	11	LK + DWL	slip control	420x120	30.3	0.3-1.4	16	bonded
Palieraki [130]	2	LK + DWL	slip control	500x100	24.3/31.9	0.0	N/R	bonded
Cattaneo [33]	1	LK + DWL	slip control	500x200	28.4/32.1	0.0	N/R	bonded
Oikonomopoulou [125]	3	LK + DWL	slip control	1200x300	22-27	0.0	32	short embed notable pullout
Li[1] [90]	9	LK + DWL	slip control	900x200	44	0.0		grouted sleeve
Becks [18]	1	LK	constant width	700x46	HSC	0.25-1.0	4	none

[1] crack dilation measurement includes cracks in the continuum

[2] reports cyclic crack dilation data for only 1 specimen

Cyclic strength reduction can partially be explained by crack path kinematics. Upon reversal, some crack opening is typically irrecoverable, either by rubble buildup, bar pullout or aggregate mismatch. This lends fewer contacting aggregates available to resist subsequent shearing cycles. The protruding aggregates progressively fracture and crush during continued sliding. If sliding damage is incremental and load reversals occur often and evenly, the aggregate fracturing may develop evenly in each direction. If, instead, sliding progresses significantly in one direction before reversing direction, the aggregate shear-failure plane may reduce the effective contact area in the reverse direction, thereby accounting for response asymmetry. Asymmetric response can also be partially explained by high clamping pressures, since crushing damage is uniform across an aggregate particle and affects interlocking behavior in both directions equally.

Scans of concrete surfaces have been compared before and after experimental testing, verifying that rough surfaces degrade significantly during frictional processes. But due to the practical difficulties of directly measuring aggregate erosion during loading no empirical relationships have been proposed relating surface roughness and shear strength, nor for predicting how surface roughness will evolve during sliding, to the Author's knowledge.

Cyclic Crack Dilation The intuitive argument that cyclic shear strength is related with crack-face deformation invites an investigation of crack width versus slip behavior. Experimental crack trajectories are shown in Fig. 2.9 for select experimental programs from Table 2.1. It is seen that reversed-cyclic crack paths follow two distinct behavioral modes: (i) interlock (i.e., loading) branches for which $|s_{t+1}|-|s_t| > 0$, and (ii) reversal (i.e., unloading) branches for which $|s_{t+1}| - |s_t| < 0$. The distinction between loading and unloading leads to cracks being classified as a "configuration-dependent" material [143].

Interlock dilation generally follows the monotonic MC curve for small shear slip magnitudes. However, crack paths flatten significantly for large slip offsets and after multiple cycles. This effect is not captured by the empirical model-code equation Eq. (2.6) for which crack width increases indiscriminately with slip. In fact, maximum crack widths tend to not exceed 2 mm in the reversed-cyclic experiments – much less than even the 5 mm limit suggested by Vecchio [173] for monotonic loading (note that experiments with partially reversed cycles are less damaging and may

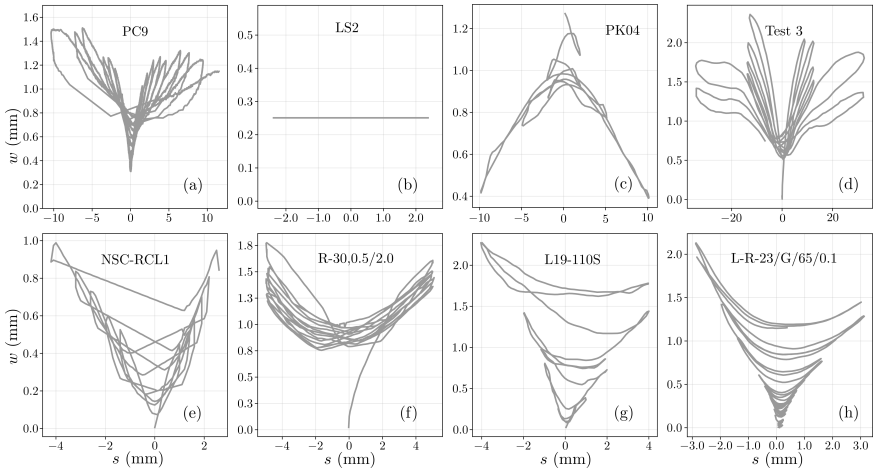

Figure 2.9. Reversed-cyclic crack paths: (a) [25], (b) [18], (c) [171], (d) [143], (e) [71], (f) [165], (g) [87], (h) [125]

develop larger crack openings). Inspection of Fig. 2.9 makes it clear that the monotonic dilation path of Eq. (2.6) is not valid generally for reversed-cyclic cracks, particularly those subject to large slips. The specimens of [143] were pushed to 40 mm of lateral offset and showed significant flattening of the dilation curve with each repeated cycle. Large increases in crack width from the campaign of Oikonomopoulou were attributed to reinforcement pullout.

Upon unloading, slip reversal is initially suppressed by friction and clamping forces. Simultaneously, rubble particles consolidate and aggregates willingly "reseat" from their laterally offset position [162]. Thus, crack closure initially outpaces slip reversal, resulting in characteristic butterfly-shaped unloading loops (see Fig. 2.9a and 2.9d). At the point of zero slip, a permanent crack width remains. For continued slip reversal, aggregates engage in the opposite direction at the break point, or *engagement slip*, which tends to increase with additional cycles.

While the trends of the crack trajectory seem to generally hold true, a notable exception to the rule is reported by Trost [171], who observed crack closure to accompany increases in sliding magnitude. Partly, this result can be attributed to the presence of high clamping stresses crossing the interface. This result highlights the complexity of cyclic crack path response, and should elicit caution against using simple, unjustified rules, which are likely calibrated only for specific boundary conditions, materials,

and load protocols.

Crack Hysteresis The eight crack paths from Fig. 2.9 correspond to the shear-slip responses in Fig. 2.10, which consist of three regimes: (i) interlocking branches for which aggregates are in contact; (ii) stiff unloading branches; and (iii) activation branches for which slip reverses rapidly once reinforcement clamping friction is overcome.

Interlock resistance weakens for repeated cycles at a single slip amplitude, and the shape of the loading branch grows increasingly concave with repeated cycles. Most damage occurs in the first cycle, which is apparent in Fig. 2.10f.

For repeated shear-amplitude cycles (see examples at a medium-amplitude shear Fig. 2.10a and 2.10e) there also exists a convex-to-concave transition of the hysteresis loops, and the secant stiffness decreases approximately linearly with each cycle [25]. [26] relate the corresponding increment in shear slip with the total sliding energy via an experimentally calibrated power law. While this approach represents a step forward toward a rational approach for characterizing crack damage, Calvi et al. do not clarify whether there should be an upper limit on the sliding energy that can be absorbed by a crack. Others [31, 67] posit the existence of a mode-II fracture energy in sliding without clearly establishing its expected value.

Comparing Figs. 2.10a and 2.10e, it is noted that the protocol of Calvi in Fig. 2.10a leads to a symmetric response because the shear amplitude increases gradually, with many cycles along the way to larger shears. This is contrasted with the result in Fig. 2.10e for which small amplitude cycles are skipped. It can be surmised, then, that strength asymmetry follows early cycles that approach peak strength.

Unloading stiffness does not appear to degrade significantly throughout loading. Stiff unloading continues until slip reverses suddenly, sometimes called the “free slip” or “breakaway” stage, but called in this Thesis reversal “activation”. The shear stress that activates free slip may increase or decrease based on the net effect of clamping stress and interface friction: reinforcement clamping increases as a crack widens while friction decreases. Stress pairs corresponding to the onset of activation are plotted in normalized stress space in Fig. 2.12b.

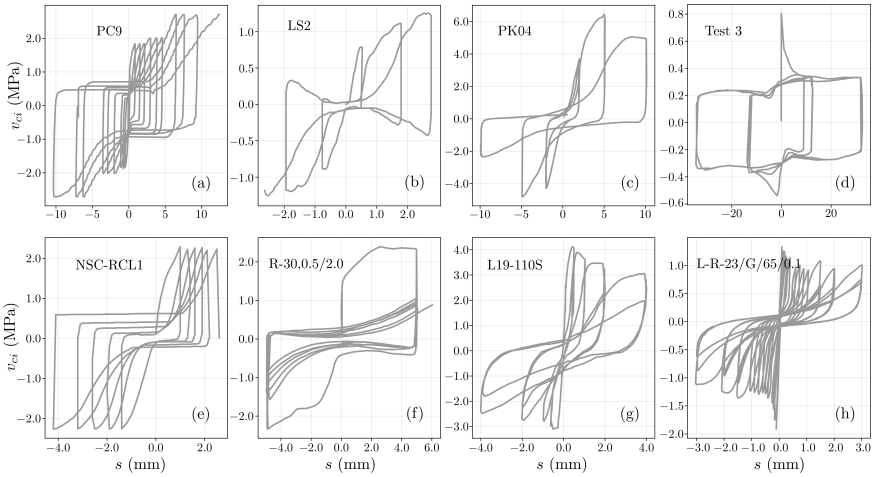

Figure 2.10. Reversed-cyclic shear-slip response: (a) [25], (b) [18], (c) [171], (d) [143], (e) [71], (f) [165], (g) [87], (h) [125]

Cyclic Strength Surface Reversed-cyclic stress path histories are plotted in normalized stress space in Fig. 2.11 for 6 representative test specimens chosen from Table 2.1. For none of the considered experiments does the peak cyclic shear approach the monotonic expression for v_{cimax} from Eq. (2.4). In part, this can be attributed to the boundary conditions adopted by [165] and [143], who imposed constant clamping stresses of only 0.5 MPa and 0.37 MPa across the test interface. Similarly, the achievable clamping stress in the tests of [125] was hampered by significant bar pullout. However, tests that saw higher clamping stress across the crack (e.g., test PC13 of Calvi in Fig. 2.11b) appear to follow a parabolic envelope similar to the MCFT normalized strength equation of Eq. (2.5).

The validity of Eq. 2.5 for cyclic strength estimation is tested in Fig. 2.12a by plotting experimental load stages in Fig. 2.11 on top of Eq. (2.5). Load stages are measured at stress peaks in the load histories (see circular markers in Fig. 2.11), and while they don't correspond to shear failure, they do correspond to onset or progression of material non-linearities. Figure 2.12 shows that Eq. (2.5), which was calibrated originally against monotonic tests, provides an upper bound to the collection of cyclic load stage data from Fig. 2.11. A lower bound to the same data can be derived by constructing a "damaged" counterpart to Eq. (2.5). The damaged parabola in Fig. 2.12a is constructed herein to represent a cohesion-less interface

with a secant friction coefficient of 0.6 (loosely based on ACI smooth crack provisions).

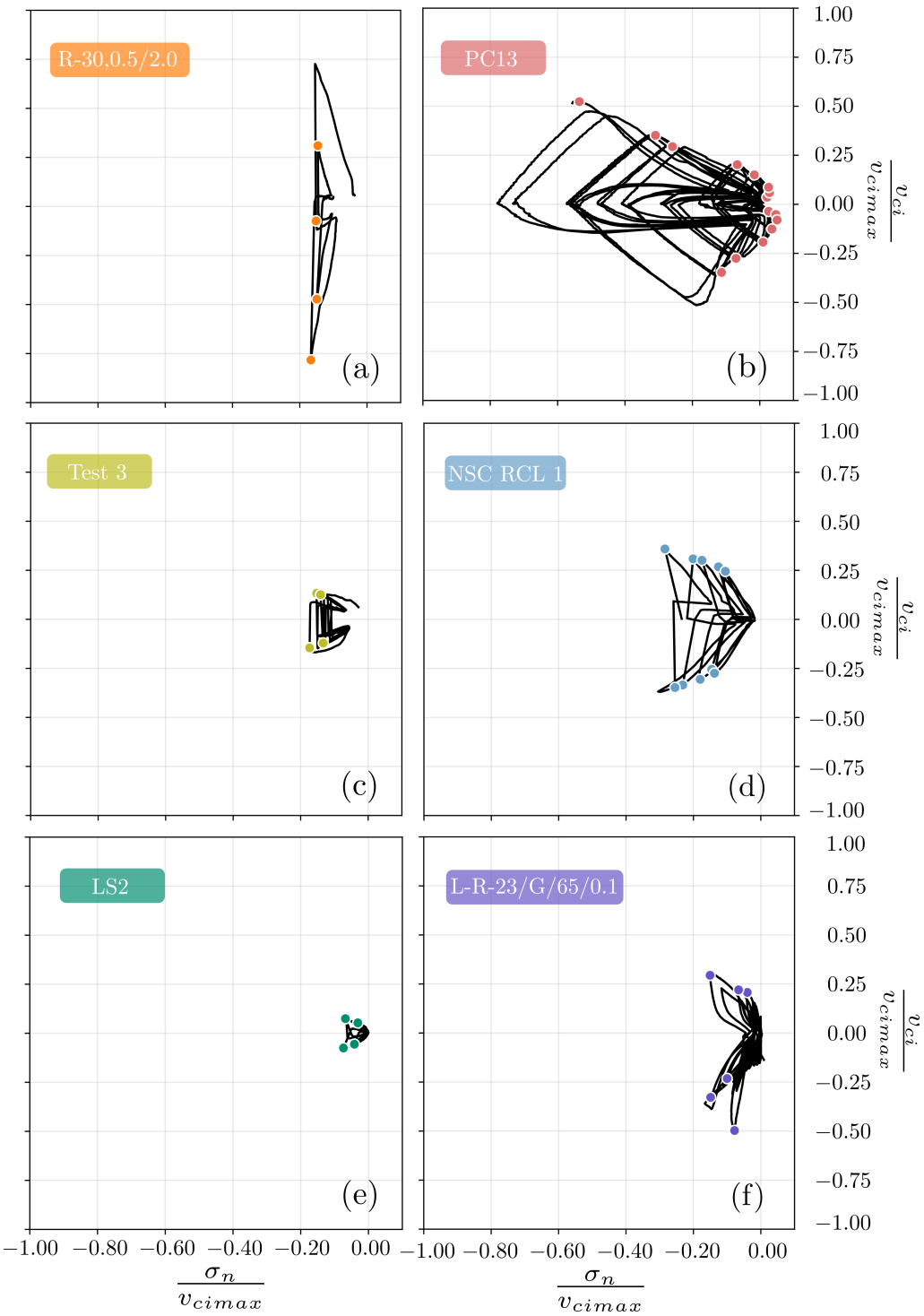

Figure 2.11. Reversed-cyclic response in stress space: (a) [165], (b) [25], (c) [143], (d) [71], (e) [18], (f) [125]

Figure 2.12b highlights the frictional nature of slip reversal by plotting various "activation"-onset load stages that were manually identified from the six experiments in Fig. 2.11. The activation points are subject to some error, as the transition from elastic unloading to plastic reversal is not always sudden (see Fig. 2.11b). But the linear frictional trend remains clear, and to a first approximation the activation shear is proportional to the clamping stress via a friction coefficient μ_{act}. A shaded region is plotted in Fig. 2.12b that bounds the experimental activation points between friction coefficients $\mu_{act} = 0.2$ and $\mu_{act} = 0.6$. The relatively low values of reversal friction align with observations of Fronteddu [64] that reversal friction is lower than traditional concrete-to-concrete friction results, hence the subscript to distinguish activation friction.

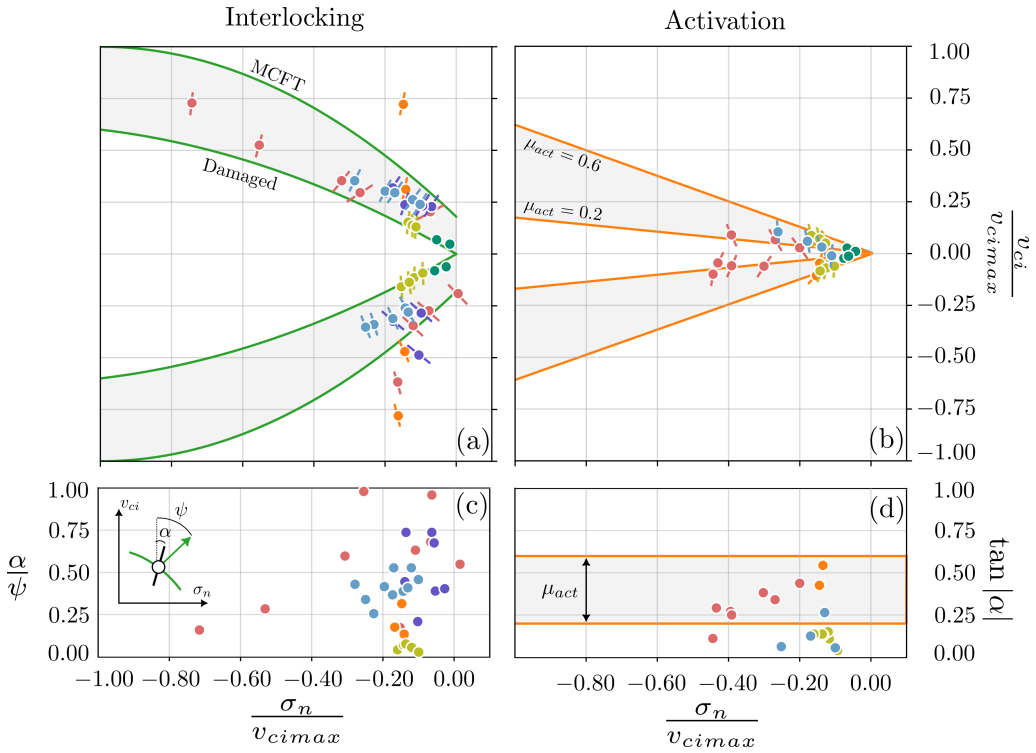

Figure 2.12. All reversed-cyclic data plotted in normalized stress space: (a) interlock load stages, (b) activation load stages (colors correspond to specific experiments plotted in Fig. 2.11)

Generalized Dilation Rules As was done for monotonic loading, some researchers have proposed methods for predicting crack stresses based on observable crack measurements (e.g., width, slip and inclination angle). Prominent among these are the rules proposed by Calvi [26] for relating secant dilation angle ($\alpha_{sec} = w/s$) with the traction ratio at the crack ($\tan\psi = \sigma_n/v_{ci}$). The first-principles relation proposed by Calvi is:

$$\tan\psi = \frac{\sigma_n}{v_{ci}} = \frac{\cos\alpha_{sec} \mp \mu\sin\alpha_{sec}}{\sin\alpha_{sec} \pm \mu\cos\alpha_{sec}} \tag{2.7}$$

where the analyst must know the crack configuration (i.e., loading or unloading) to determine which algebraic operators to use in Eq. (2.7). The fit of Eq. (2.7) onto Calvi's own experimental data is very good, using a friction coefficient of 0.8 for both loading and unloading. However, the expression does not truly consider path-dependency even though it distinguishes loading from unloading. To see this, the reader is referred to the previously discussed path-dependency test of Hassanzadeh [74] who showed that path-dependency effects can be significant even for one-way loading.

In light of deficiencies in simple dilation rules, the experimental data of Table 2.1 and Fig. 2.11 have been plotted in an incremental framework in Fig. 2.12. Each load stage stress pair in Fig. 2.12a-b is accompanied by an inclined marker that indicates the instantaneous dilation angle, $\alpha = \Delta w/\Delta s$ (extracted from the experimental data).

Figure 2.12c compares the dilation angle α with the instantaneous load angle $\Delta\psi$ for each interlock data point in Fig. 2.12a. Graphically, $\Delta\psi$ represents the angle between the the vertical axis and failure surface normal (the normal to the "damaged" surface is used to obtain $\Delta\psi$ in Fig. 2.12c). The ratio $\alpha/\Delta\psi$ is less than 1 across the board, with an average "knockdown" ratio of 0.37 (which reduces to 0.31 if the normal to the original MCFT parabola is used for calculating $\Delta\psi$). It can be further seen that within each test (load stages of a single test are plotted in the same color), the dilation knockdown decreases as clamping stress increases. More data is needed in the high clamping range to clarify what form such a law would take.

Figure 2.12d is the "activation" analog to Fig. 2.12c. The figure directly plots the tangent dilation angle during free-slip breakway. Interestingly, the dilation angle during activation is mirrored about the vertical axis with

respect to the normal to the friction surface. Yet, the magnitude of the dilation angle is remarkably similar to the reversal friction angle. Thus, a first approximation may be to take the reversal dilation angle equal to the breakaway friction.

2.2.3 Single-Sided Cyclic Shear Behavior

Reversed-cyclic tests of reinforced-concrete panels – representative of plane stress elements such as beams, walls, columns and beam-column joints – have shown that the individual cracks within diffuse crack systems undergo single-sided actions, not fully reversed actions [152]. This effect arises from the formation of two orthogonal crack sets, one for each principle direction. Experimentally, when a panel was loaded positively, a positive crack set was engaged, aligned with the principal loading direction. Upon load reversal, the positive cracks closed and a negative crack set opened, oriented with the principal direction in the negative loading direction. For continued load reversals, the two cracks sets see-sawed between open and closed, between active and inactive. Thus, single-sided crack cycling may arise in earthquake applications.

Various researchers have explored the single-sided cyclic behavior of concrete interfaces (both plain and reinforced). Only a brief review is presented here, as single-sided cycling is just a special case of fully reversed cycling. In fact, for very low-cycle fatigue, the single-sided cyclic loading does not differ significantly from the monotonic backbone [25, 71]. Given that the monotonic crack response has already been discussed in detail, the following comments treat the high-cycle fatigue response, though this is done in minimal detail as high-cycle fatigue applications exceed the primary scope of this Thesis.

Figueira et al [63] investigated the high-cycle fatigue performance of untreated interfaces cast at different times, crossed by reinforcement with a reinforcement ratio of 1.07%. The interfaces were representative of the connection between a precast beam and a cast-in-place deck, common in railway bridges. Figueira developed a simple $S - N$ curve to related the number of cycles that can be resisted at various stress amplitudes. He also investigated the effect of the minimum shear amplitude during cycling on the fatigue performance. For the most extreme case tested by Figueira (a peak cyclic load of 80% the monotonic strength and a minimum cyclic load of 5%

the monotonic strength), the average number of cycles to failure was 2820. While this number of cycles is of little interest in seismic applications, it is useful to note that Figueira observed a significantly flatter dilation response for high-cycle fatigue than for monotonic loading, indicating that sliding damage accumulates for repeated sub-critical loading. Gebreyouhannes [71] observed a similar phenomenon and developed expressions for the reduction of shear stiffness with number of cycles. Based on the strong sensitivity on boundary conditions discussed previously, it is doubtful that a relationship calibrated from the results of a single test campaign is generally applicable to other boundary conditions and reinforcement details.

Some attempts have been made to establish design-focused limit states. Zewdie et al [184] performed low-cycle fatigue tests on interfaces reinforced with various bar arrangements, confinement and load amplitude. Based on the results of the test, they proposed a serviceability limit state of $s = 0.5$ mm and an ultimate limit state of $s = 0.9$ mm for the accumulated slip at the joint. They also note that permanent slip accumulation closely follows bond failure between reinforcement and the concrete of the joint.

In terms of design for strength, Liu et al [92] show that fatigue cycles have little effect on the residual strength of an interface.

An extensive testing program has been undertaken in recent years by the team at RWTH Aachen University to unify the characterization of concrete fatigue behavior. In particular, the group has focused on multi-axial fatigue characterization, interaction of reinforcement bond fatigue with concrete crack initiation, and the effect of load sequence on concrete fatigue life. The focus of the Aachen group on intact concrete is slightly out of scope for this Thesis, which is concerned with individual crack interfaces. However, the Aachen group does perform various reversed cyclic tests on pre-formed cracks [18] as well as a series of high-compression, post-peak shear-fatigue tests during which a clear interface forms [17]. These latter tests provide rare data for highly-compressed shear crack behavior.

2.2.4 Reinforcement Behavior at a Crack

Another important aspect for interface resistance is the contribution of – and interaction with – reinforcement at the crack. Nominally, the effect of reinforcement is to clamp the interface together and resist crack opening. This has been written in Eq. 2.3. The ability of reinforcement to provide

the expected clamping force depends on:

- sufficient embedment to prevent bar pullout;
- dowel action, which may cause premature bar yielding in curvature;
- local bond failure at the crack;

Each of the aforementioned effects may either directly reduce the reinforcement confinement pressure or will reduce the clamping stiffness, leading to crack width growth. The following paragraphs briefly summarize experimental characterizations of bar effects at a crack, with specific focus on works that estimate the state of reinforcement from crack measurements. In a later Chapter, these results will be utilized to accurately model the crack and reinforcement behavior together.

Consequences of Dowel Action Reinforcement dowel action is an important mechanism for resisting shear at a crack, and provides an increasing portion of the total sliding resistance as the crack slip grows. However, dowel action is accompanied by yielding of the extreme reinforcement fibers in flexure, which reduces the effectiveness of crack clamping [125, 99]. Maekawa and Qureshi [99] showed experimentally that bars under simultaneous pullout and dowel action activated less clamping pressure than would be predicted on the basis of uniaxial strength. Their experimental program showed that the portion of usable clamping stress was reduced to 50% of the uniaxial strength in some cases, depending on bar diameter and the imposed displacement path at the crack. Cyclic loading also reduced the reinforcement effectiveness.

Various authors have proposed axial-shear interaction diagrams to estimate reinforcement yield or fracture under multi-axial actions [100, 134, 45, 175, 146]. Such diagrams are useful for strength design but give no insight into the bar deformations during combined loading processes.

If, in the context of crack-based assessment, crack measurements are to be used as predictors of the residual reinforcement state, it is helpful to investigate bar deformations under combined loads. To this end multiple researchers have idealized dowel action as a beam-on-elastic-foundation, or variation thereof. Analytical solution of the governing equation provides insight into the parameter groupings influencing the “real” (i.e., messy

nonlinear response) deformation profile along the length of the bar in the wake of a crack. The governing equation for a beam on elastic foundation is:

$$E_s I_s \frac{d^4 \delta_\perp}{dx^4} + k_c d_b \delta_\perp = 0 \tag{2.8}$$

where E_s is the reinforcement modulus, I_s is the reinforcement moment of inertia, k_c is the subgrade stiffness and $\delta_\perp$ is the sliding displacement at the crack centerline, $\delta_\perp = s/2$. Solving Eq. (2.8) for $\delta_\perp$, then applying the displacement condition and the moment-free condition at the crack results in the following elastic dowel shear, as a function of crack slip:

$$V_{dowel} = \hat{\beta}^3 E_s I_s s \tag{2.9}$$

where $\hat{\beta} = \frac{2}{d_b}\left(\frac{k_c d_b}{\pi E_s}\right)^{1/4}$ is the root of the characteristic equation of 2.8. The solution of the beam-on-elastic-foundation problem also foresees the position of maximum moment along the bar, enabling the calculation of peak bar stress (which occurs at some distance from the crack plane).

Maekawa and Qureshi [98] use the beam-on-elastic foundation model to estimate the"curvature influence zone", or the length of bar influenced by sliding at the crack, as three times the location of maximum bending moment:

$$L_c = \frac{3\pi}{4}\left(\frac{4E_s I_s}{k_c d_b}\right)^{1/4} \tag{2.10}$$

A simpler rule of thumb, based on experimental measurements, also proposed by Maekawa and Qureshi [98] is to take the curvature influence zone as 5 bar diameters on either side of the crack.

The analytical solutions for the beam-on-elastic foundation problem bear out the importance of properly estimating the bearing stiffness of bar against concrete (k_c). Experimentally calibrated expressions for k_c have been developed in the literature as a function of concrete strength, bar diameter, bar orientation and crack slip [98, 135, 120]. Experiments show that nonlinearity of the bearing stiffness kicks in at crack slips exceeding roughly $0.02d_b$ [135]. The experiments by Pejatovíc and Muttoni [135] also proposed stiffness-reduction factors for cyclic actions, bar positioning within

the concrete body, and the coupling effect of bar pullout, culminating in the following proposed bearing stiffness expression:

$$k_c = 0.2\frac{E_c}{d_b}\eta_\theta\eta_\delta\eta_c\eta_{cast}\eta_{fc}\eta_{bond}\eta_{cyc} \tag{2.11}$$

Some of the bearing-stiffness-modification factors are discussed subsequently. For a full characterization of concrete bearing stiffness, see [135].

Dowel bearing stiffness k_c degrades as the lateral bar deformation grows. Physically interpreted, the concrete crushes locally, which reduces the effective bearing stiffness. Pejatovíc and Muttoni [135] model this with the η_δ factor:

$$\eta_\delta = \frac{1.5}{1 + 25\frac{\delta_\perp}{d_b}} \leq 1.0 \tag{2.12}$$

Dowel bearing stiffness k_c is also reduced under the simultaneous action of bar pullout [98, 135, 120]. Simply, the bond resistance to bar pullout produces inclined radial cracks in the concrete, leaving concrete cantilevered wedges to resist dowel bearing. Pejatovíc and Muttoni [135] measure the effect of bar pullout on bearing stiffness as:

$$\eta_{bond} = \left(\frac{1}{1 + w/0.2}\right)^{1/6} \tag{2.13}$$

where w is the crack opening. Certainly Eq. (2.13) is not perfect, as it weights the effect of bar pullout equally along the "curvature influence zone". However, the equation does recognize the multi-dimensional nature of the interaction between concrete and reinforcement at a crack. The interaction becomes more layered if the bar curvature – amplified as it is by bearing stiffness reduction from pullout – leads to yielding in the extreme fibers of the crack-crossing bar. Flexural yielding reduces the axial bar stiffness (before reaching the nominal yield strength) and further amplifies the crack opening due to aggregate override. The effect is summarized in Fig. 2.13.

Cyclic dowel action results in a strength reduction (roughly half of monotonic strength lost [175]) and a reduction in bearing stiffness that stabilizes with number of cycles [135].

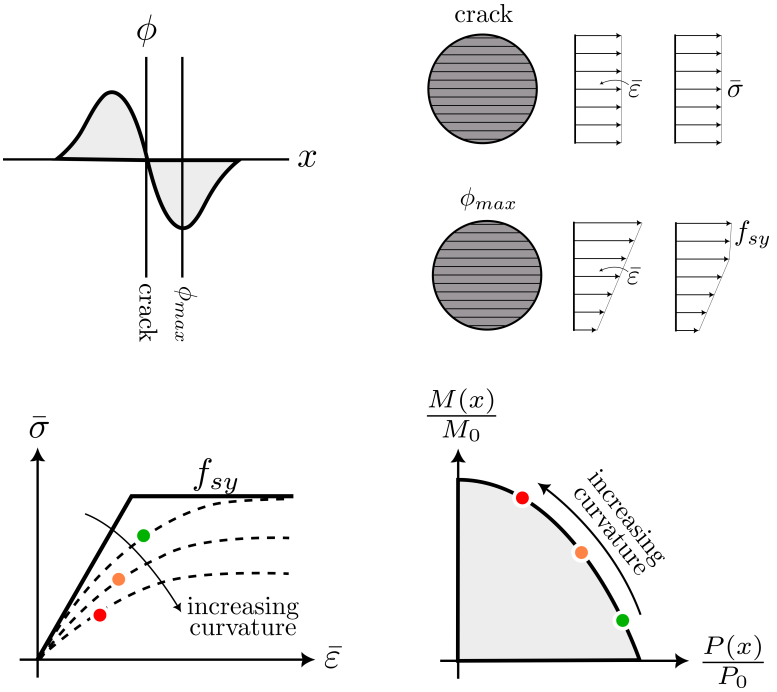

Figure 2.13. Effect of curvature ϕ on reinforcement clamping effectiveness, measured by cross-sectional average stress and strain ($\bar{\sigma}$ and $\bar{\varepsilon}$): adapted from [99]

Consequences of Reinforcement Bond Slip In addition to reducing dowel action stiffness, bond slip is important to be able to estimate so that bar stresses can be obtained from visual crack observations. To this end, a first-principles relationship has been developed by Corres and Muttoni [43] based on bar slip under monotonic loading:

$$w = \frac{s_{cr}}{E_s}\left[\sigma_{sC} - \frac{s_{cr}\tau_{b,avg}}{d_b}\frac{1+(\bar{n}-1)\rho_s}{1-\rho_s} - E_s\varepsilon_{cs}\right] \tag{2.14}$$

Equation (2.14) provides a relationship for bar stress at a crack σ_{sC} from the measurement of crack width (w) and crack spacing (s_{cr}). The expression relies on an accurate estimation of the average bond strength in the uncracked regions, $\tau_{b,avg}$ and also considers the effect of shrinkage strains (ε_{cs}), reinforcement ratio (ρ_s) and modular ratio ($\bar{n}$). Corres and Muttoni [43] devoted significant effort to deriving (via a multitude of experiments) an expression for $\tau_{b,avg}$ in terms of the local bond characteristics, but dealt

primarily with tension and flexure cracks in monotonic loading. In light of the path-dependency effects discussed in Section 2.2.1, and the lack of data from sliding cracks built into their proposed expressions, the relationship is not reviewed here. Instead, attention is given to the local bond-slip behavior, which is a more basic building block to eventually generalize Eq. (2.14) to arbitrary loading.

Various bond-slip expressions have been proposed in the literature [44, 95, 96, 52]. In general, bond exhibits an initial ascending branch followed by a short plateau and finally a linearly decaying strength for increasing slip. Various expressions have been proposed for the loading portion of the curve, but a common form is

$$\tau_b = \tau_{b,max} \left(\frac{\delta_{sc}}{\delta_{peak}} \right)^{\alpha_b} \tag{2.15}$$

where α_b is commonly taken as 0.4 and the peak bond strength $\tau_{b,max}$ is a function of confinement, bar diameter and concrete strength. A secant stiffness to the point of max bond stress has been proposed by Lowes, et al. [95] as 20 MPa/mm. Unloading and cyclic behavior have been characterized by the pioneering experimental campaign of Eligehausen, et al [52]. Unloading is characterized by a frictional resistance that decays with the maximum slip demand and the number of load cycles [95]. Frictional resistance is small relative to mechanical bond resistance in loading, and is taken between 5-20% of the unloading point from the monotonic curve by Lv, et al [96].

Reinforcement Unbonded Length Maekawa, et al. [97] also proposed a relationship between crack width and reinforcement strain, as follows:

$$w = 2d_b\varepsilon_{cs}(2 + 3500\varepsilon_{cs}) \left(\frac{20}{f'_c} \right)^{2/3} \tag{2.16}$$

When performing crack-based assessment (i.e., w is measured), Eq. 2.16 can be inverted for the bar strain at the crack ε_{cs}, which is an indicator of reserve capacity. Other expressions analagous to Eq. (2.16) have been proposed in the literature, e.g., for predicting stirrup rupture in deep beams [170].

For modeling purposes, it can be handy to estimate the length of reinforcement that is locally unbonded at the crack section [153] as this

determines the stiffness of the crack-crossing reinforcement. Simple compatibility considerations between crack opening and bar strain lead to an estimation of the unbonded length, L_{unb}, as w/ε_s. Ruggiero notes that the unbonded length is limited by the crack spacing, which can be directly measured. An estimation of a "bond degradation zone" has been proposed by Maekawa and Qureshi [99] as 5 bar diameters.

2.3 Previous Interface Constitutive Models

Some promising models for describing the behavior of interfaces are presented here. The wealth of information on interface modeling is enormous. Only the information that is directly applied to this thesis, or that helps tell the story of this thesis is reviewed. Mostly, this Section focuses on models that account in some way for the mechanical features of the crack interface, this way a direct interface (i.e., strong discontinuity) approach can be used.

2.3.1 Direct Equilibrium Approaches

Two Phase Model

Walraven [176] proposed a two-phase representation of concrete, consisting of concrete paste and spherical aggregate particles, to describe the mechanics of aggregate interlock. In the idealization, aggregate particles are stiffer and stronger than the matrix, and as such, plough through the concrete paste material without any deformation or degradation. For a given crack offset the transverse and normal stresses can be obtained from Eq. 2.17:

$$\begin{aligned} \tau &= \sigma_{pu}\left(A_y + \mu A_x\right) \\ \sigma &= \sigma_{pu}\left(A_x - \mu A_y\right) \end{aligned} \tag{2.17}$$

where A_x and A_y are projections of the contact area (summed for all aggregate particles over the entire crack plane), σ_{pu} is the yield strength of the concrete paste and μ is the concrete friction coefficient.

The heart of Walraven's model is to characterize the contact projections as functions of the crack offset vector so that Eq. 2.17 can be used to predict stress transfer across the crack for arbitrary crack displacements. Walraven adopts a probabilistic approach that involves:

1. assuming a particle volume ratio p_k and a distribution of aggregate sizes in the concrete volume;

2. consideration of an arbitrary cross-section: given that the crack intersects a particle of a given diameter D^*, determine the probability that the diameter of the intersection circle equals some arbitrary diameter D_0;

3. identification of the number of particles of each diameter D_0 that are crossed by a crack at an arbitrary section;

4. determination of the average contact projections for a single aggregate particle;

5. integration over all possible aggregate diameters.

The above steps give A_x and A_y. Walraven then produced a series of curves describing the contact area vs. crack slip for various fixed values of crack width. These curves are then transformed into stress-slip curves using Eq. 2.17. Though the model outputs are quite complicated, Walraven proposed the following simplified relationships:

$$\begin{aligned} \tau &= -\frac{f'_c}{30} + s\left[1.8w^{-0.80} + \left(0.234w^{-0.71} - 0.20\right)f'_c\right] \\ \sigma &= -\frac{f'_c}{20} + s\left[1.35w^{-0.63} + \left(0.19w^{-0.55} - 0.15\right)f'_c\right] \end{aligned} \tag{2.18}$$

Extensions of the original formulation have been proposed [141], along with variations on the simplified stress-slip curves [34].

Traditionally, the constant width stress-slip curves are used as backbones for arbitrary dilation paths. In other words, path independence is assumed. This thesis assesses the validity of path-independence in later Chapters.

Contact Density Model

The contact density model provides an early, clever approach to incorporate the roughness of a crack surface into a path-dependent model describing the crack dilatancy and interface contact stresses. As is typical, the model develops reasonable assumptions to characterize the kinematics of

deformation, constitutive behavior of the materials, and equilibrium of the resulting forces. As a note, in the description presented here, the sign convention of the original paper has been modified to align with that of the model presented in Chapter 4 of this thesis, wherein crack opening and crack tension are positive.

At the heart of the model is the so-called contact density function $\rho_{cd}(\theta)$ that describes the distribution of contact angles along a unit length of rough crack face. The contact density function respects the property that its integral over the full range of possible contact angles is unity:

$$\int_{-\pi/2}^{\pi/2} \rho_{cd}(\theta)\, d\theta = 1 \tag{2.19}$$

Thus, the area of a particular micro-plane with inclination θ^* is proportional to the area of the nominal crack area A_{cr} by the probability of finding that particular plane orientation in the distribution function $\rho_{cd}(\theta^*)$ times the infinitesimal angle slice $d\theta$. In other words:

$$dA_\theta = A_{cr}\rho_{cd}(\theta)\, d\theta \tag{2.20}$$

From a macroscopic point of view, the authors propose a reduction factor for contact area, based on the limit that crack contact is lost when the nominal crack width surpasses half the maximum aggregate size (assuming the aggregates pull out symmetrically from each side of the crack face):

$$K_a = 1 - \frac{w}{a_g/2} \tag{2.21}$$

With an estimation of the contacting areas as a function of crack width, an equilibrium expression can be written, aided by the assumption that the nominal stress components σ_n and v_{ci} are the resultants of the direct bearing contact σ_θ perpendicular to each micro-plane:

$$\begin{aligned} V &= \int_{-\pi/2}^{\pi/2} \sigma_\theta \sin\theta K_a\, dA_\theta \\ N &= \int_{-\pi/2}^{\pi/2} \sigma_\theta \cos\theta K_a\, dA_\theta \end{aligned} \tag{2.22}$$

The authors argue, logically, that the local contact stresses perpendicular to each micro-plane angle θ are a function of local crack slip and local crack width. In other words, steep adjacent crack segments will engage before shallow segments, and therefore bear a larger portion of the total tractions. Thus, the authors make use of a global-to-local transformation to obtain crack displacements in a local reference frame aligned with an arbitrary micro-plane angle θ:

$$\begin{Bmatrix} s_\theta \\ w_\theta \end{Bmatrix} = \begin{bmatrix} \cos\theta & \sin\theta \\ -\sin\theta & \cos\theta \end{bmatrix} \begin{Bmatrix} s \\ w \end{Bmatrix} \tag{2.23}$$

The final piece to the mechanics puzzle is the constitutive law for the local contact stresses σ_θ. The authors propose a compression-only, elasto-plastic behavior for each micro-plane as a function of the local crack closure $-w_\theta$. The constitutive law is:

$$\sigma_\theta = E_\theta(w_\theta - w_\theta^p) \tag{2.24}$$

where the superscript p indicates the plastic component of local crack closure, and E_θ is the stiffness of particle contact.

Plugging the local constitutive law into the equilibrium Equation (2.22), substituting also Eq. (2.20), Eq. (2.21) and Eq. (2.23), and differentiating, the nominal stress traction projections can be written as a linear mapping of the nominal crack face displacements:

$$\begin{Bmatrix} \Delta v_{ci} \\ \Delta\sigma_n \end{Bmatrix} = \begin{bmatrix} D_{ts} & D_{tw} \\ D_{ns} & D_{nw} \end{bmatrix} \begin{Bmatrix} \Delta s \\ \Delta w \end{Bmatrix} \tag{2.25}$$

As an interesting note, the off-diagonal stiffness terms D_{vw} and D_{ns} are investigated. The result of plugging into Eq. (2.22) is:

$$\begin{aligned} v_{ci} &= E_\theta \int_{-\pi/2}^{\pi/2} (w\cos\theta - s\sin\theta - w_\theta^p)\left(1 - \frac{w}{a_g/2}\right)\rho_{cd}\sin\theta\, d\theta \\ \sigma_n &= E_\theta \int_{-\pi/2}^{\pi/2} (w\cos\theta - s\sin\theta - w_\theta^p)\left(1 - \frac{w}{a_g/2}\right)\rho_{cd}\cos\theta\, d\theta \end{aligned} \tag{2.26}$$

and the derivative with respect to the nominal crack opening gives the coupling stiffness terms.

$$D_{tw} = E_\theta \int_{-\pi/2}^{\pi/2} \left[\left(1 - \frac{w}{a_g/2} \right) \rho_{cd} \sin\theta \cos\theta - \frac{\rho_{cd} \sin\theta}{a_g/2} (w \cos\theta - s \sin\theta - w_\theta^p) \right] d\theta \tag{2.27}$$

$$D_{ns} = E_\theta \int_{-\pi/2}^{\pi/2} - \left(1 - \frac{w}{a_g/2} \right) \rho_{cd} \sin\theta \cos\theta \, d\theta \tag{2.28}$$

The original proposal for the contact density function was $\rho_{cd}(\theta) = 0.5 \cos\theta$, which leads to D_{ns} vanishing due to the properties of odd functions ($\rho_{cd} \sin\theta \cos\theta$ is odd). Meanwhile, all products in D_{tw} are odd, save for the term $\rho_{cd} \sin^2\theta$, which is even and evaluates to a non-zero value when integrated. Performing the integration, $D_{tw} = \left(\frac{s}{a_g/2} \right) \left(\frac{E_\theta}{3} \right)$ is obtained. This means that each crack plane of the contact density model has a non-symmetric, elastic stiffness tensor (if any slip is present).

The contact modification function K_a can be modified such that a symmetric stiffness is obtained, for the choice:

$$K_a = 1 - \frac{w}{a_g/2} - \frac{8}{3\pi} \frac{s}{a_g/2} \sin\theta \tag{2.29}$$

The contact density model fails to capture the coupling term D_{ns} because it assumes that the crack roughness profile remains unchanged during sliding, because the crack displacements are smaller than the roughness magnitude. This assumption has been shown to be invalid by experimental methods [78]. As a final note, the issue of the non-symmetric elastic stiffness can be alleviated by adopting a rigid-plastic assumption, which is typically done with the CDM.

General Crack Component Model

The General Crack Component Model [153] introduces two novelties: (i) the idea that crack systems come in a pair of two cracks. One is active while the other is inactive, each undergoing only single-sided shear cycles; (ii) useful description of crack-closure behavior.

The crack closure law is particularly useful for crack-based assessment, because the unloaded state is what the engineer will observe. According to the crack closure law of Ruggiero, the crack normal stiffness is a function

of current crack width, maximum history crack width, crack closure stress, direction of loading (i.e., closing or opening) and a rate parameter. Letting w represent the current crack width, w_{max} the maximum history crack width, f_{cl} the compressive stress magnitude required to fully close the crack, σ_n the current crack stress (positive in tension) and q a rate parameter, the stress-displacement curve in opening or closing can be written as:

$$\sigma_n = q \ln(w + w^0) - f^0 \tag{2.30}$$

where two survival variables are defined:

$$w^0 = w_{max} \frac{\exp(-f_{cl}/q)}{1 - \exp(-f_{cl}/q)} \tag{2.31}$$

and

$$f^0 = q \ln \left[\frac{w_{max}}{1 - \exp(-f_{cl}/q)} \right] \tag{2.32}$$

Ruggiero notes that the closure stress magnitude f_{cl} should increase with maximum crack width w_{max}, according to a linear law (MPa,mm units):

$$f_{cl} = 1.0 w_{max} + 2.0 \tag{2.33}$$

Finally, distinct values of q are proposed for opening and closing to reflect the different nature of the two responses. In opening, the crack sheds any compressive stress rapidly (low q value ≈ 0.2), while in closure, the crack builds compression more gradually (higher q value ≈ 0.5).

2.3.2 Plasticity Approaches

Normal/Shear Cracking Model [31]

Carol, et al. [31] proposed a simple model for discrete crack analysis that couples the normal and shear crack behaviors. The model starts with an uncracked interface that forms a crack when a so-called cracking surface is exceeded in stress space. The cracking surface is a hyperbolic function that transitions between mode I tensile cracks and mode II shear cracks:

$$F = v_{ci}^2 - (c - \mu\sigma_n)^2 + (c - \mu\chi_t)^2 \tag{2.34}$$

After crack formation, the cracking surface shrinks, approaching a simple Mohr-Coulomb surface with no cohesion or tensile strength. The rate at which the cracking surface shrinks depends on the work spent on the fracture process, W^{cr}:

$$dW^{cr} = \begin{cases} \sigma_n dw + v_{ci} ds & \sigma_n > 0 \text{ (tension)} \\ \\ v_{ci} ds \left(1 - \left|\frac{\sigma_n \mu}{v_{ci}}\right|\right) & \sigma_n < 0 \text{(compression)} \end{cases} \tag{2.35}$$

According to the model, the tensile strength vanishes when W^{cr} approaches the mode I fracture energy (G_f^I) and the cohesion vanishes when W^{cr} approaches the mode II fracture energy (G_f^{II}).

Dilatancy, or slip-induced crack opening, is modeled by introducing a plastic potential surface G that controls the flow rule. Carol, et al. use an associated flow rule when the crack normal stress is tensile and a non-associated flow rule when the crack normal stress is compressive. The non-associativity is applied to the normal component of the yield surface gradient via two factors, f_σ^{dil} and f_c^{dil}:

$$\frac{\partial G}{\partial \sigma_n} = \frac{\partial F}{\partial \sigma_n} f_\sigma^{dil} f_c^{dil} \tag{2.36}$$

The knockdown factor f_σ^{dil} accounts for the presence of a critical clamping stress, which, if imposed across the crack will prevent dilation. The second knockdown factor f_c^{dil} describes the loss of dilation as cohesion, which can be described as micro-roughness, vanishes.

While the model is simple and elegant, it provides little basis for selection of the model parameters. Furthermore it is unsuitable for use with existing cracks for which the residual mode-II fracture energy would be difficult to establish. Finally, the lack of a compression cap on the cracking surface limits the model to use within a solid-meshed finite element framework.

Cam-Clay Model Incorporating Micro-Scale Effects [79]

Jacobsen, et al. [79] propose to use a Cam-Clay elliptical yield surface to characterize the plasticity criterion of plain concrete cracks. The elliptical yield surface mimics Mohr-Coulomb shear behavior, but also includes a compression cap. The yield surface is written as:

$$F = v_{ci}^2 + M^2\sigma_n(\sigma_n - f_t - f_c') + M^2 f_t f_c' \tag{2.37}$$

where M is the slope of the critical state line, i.e., the line connecting the uniaxial tensile strength with the peak of the elliptical yield surface. For simplicity, the authors adopt an associated flow rule to describe the development of plastic strains.

Hardening of the yield surface is described by two hardening variables, taken as the residual tensile strength and the actual compressive strength. The hardening functions are defined so that standard relationships for mode-I opening (fictitious crack model [75]) and closing (linear softening [80]) are reproduced, using plastic crack opening and closing, respectively. Decohesion is assumed irreversible.

Implemented as described above, Jacobsen, et al. [79] fail to represent experimental results of mixed-mode crack experiments. They attribute this failure to the insufficiency of a plane crack assumption to capture micro-roughness effects along the crack. To remedy this, Jacobsen, et al. [79] apply the Cam-Clay model to local, inclined segments of topograhic crack surface scans, then summing local tractions into an effective global response. Interestingly, the distribution of contact angles from the topographic scans resembles the contact density function proposed (and discussed previously in this Thesis) by Li and Maekawa [89]. Incorporation of the local roughness significantly improved the prediction of peak shear and normal tractions.

The model of Jacobsen, et al. [79], though promising, has not been tested for cyclic loading. It could possibly be used for the analysis of existing cracks if estimates of the maximum crack opening can be estimated from visual measurements.

Extended Coulomb Model with Granular Third Body [162]

Stupkiewicz and Mroz [162] build upon the simple Coulomb law, which forms a conical surface in stress space, to develop a qualitative model for cyclically loaded interfaces that captures: tension damage, effect of mismatched joints on normal stiffness, pressure effects on dilation, reversible dilation and degradation.

The basic Coulomb surface is written as:

$$F = |v_{ci}| + \mu\sigma_n \leq 0 \tag{2.38}$$

and a slip potential function G can be defined by replacing μ with $\tan\alpha$ where α is the dilation angle, to be specified by the user of the constitutive model. Under cyclic shearing, the simple Coulomb model produces excessive dilation. Stupkiewicz and Mroz [162] respond by applying an exponential decay evolution law to the dilation angle, requiring an additional parameter to control the rate of the decay of dilation angle with either work hardening or strain hardening.

The Coulomb surface is then extended to include a cohesion term that degrades with damage (between 0 and 1) where damage approaches 1 when the sum of the magnitude of plastic slip reaches a critical value

$$s_t^{cr} = \frac{2G_f}{v_{cimax}} \tag{2.39}$$

Stupkiewicz and Mroz [162] demonstrate that models of the Coulomb variety cannot reproduce cyclic interface behavior, though the monotonic results can be calibrated rather nicely.

To retrieve cyclic behavior, Stupkiewicz and Mroz [162] introduce the concept of "configurational dilatancy" and a dilation shape function that is based on the characteristic height and length of the aggregate particles. Configurational dilatancy recognizes that a crack will open when slip offset increases, but will close when slip offset decreases. Like other models, the configurational dilatancy can be transformed to global coordinates to capture inclinations of local asperity interactions. If instead written in local coordinates, the configurational dilatancy term produces a rotating conical yield surface. To produce realistic cyclic response, Stupkiewicz and Mroz [162] propose the following dilation function:

$$w = a_g \tanh\left[\frac{\sqrt{(s\tan\alpha_0)^2 + g_0^2} - g_0}{a_g}\right] \tag{2.40}$$

where α_0 is the initial dilation angle and g_0 is a model parameter describing the sharpness of the dilation curve at $s = 0$. Wear damage is introduced by assuming the aggregate size diminishes with frictional work.

Lastly, Stupkiewicz and Mroz [162] introduce an additional rotation of the conical slip surface for dealing with the formation of a granular layer between the two interfaces. The rotating surface allows them to reproduce the sudden drop in dilation that occurs during shear reversal, attributed to rearrangement of rubble particles.

In all, the model of Stupkiewicz and Mroz [162] presents a thorough summary of cyclic interface behavior and provides a simple approach for producing most features of the behavior. In fact, features of the model have been recycled in later models, e.g., that of Puntel, et al. [142]. However, the model parameters are largely non-physical and have not been calibrated against experimental data.

Sequential Plasticity Model [91]

The plasticity model by Lin and Bazant [91] is notable for its approach to modeling yielding in compression. The model defines an initial yield stress in compression that is below the peak compression strength: $f'_{c,0} = 0.6f'_c$. Loading up to the initial yield limit is elastic, then hardening develops, driven by plastic work, until the current compression reaches the peak strength. Plastic work after reaching the peak strength leads to either hardening or softening, depending on the sign of the volumetric plastic strain increment.

In multiple dimensions the approach of Lin and Bazant is a closed, ellipsoid yield surface that grows (hardens) to an enclosing surface, which then takes over the plastic behavior when the two surfaces collide.

2.3.3 Other Approaches

Many interface models exist in the literature beyond those summarized above. The models discussed above provide direct inspiration for a novel crack model proposed in later Chapters of this thesis, and so were discussed in detail. Other notable interface models include:

- the damage mechanics approach of Serpieri, et al. [159], which uses a sawtooth-shaped representative interface area that repeats periodically. The constitutive relation at each micro-plane is derived from a potential function and damage is based on fracture energy terms;
- The thermodynamic approach of Chudoba, et al. [40] that, unlike all previously discussed models, is valid for cyclic fatigue loading and is general enough to also handle the behavior of interfaces between steel bars and concrete;

Chapter 3

A Relative Performance Framework for Earthquake Damage Assessment

This chapter is extensively based on the following publication:

W. Galik et al., "Relative Collapse Analysis to Determine Crack Width Limits of Squat RC Shear Walls," *Bulletin of Earthquake Engineering,* under review, 2026

Summary After an earthquake, the decision to repair or replace a damaged structure is influenced by crack width observations, which are used to classify damage levels. However, empirical crack width limits (note, a "limit" describes the crack width that bounds a damage state, commonly an undesirable state that requires some form of intervention) prescribed by current guidelines do not consider variations of crack width limits that may arise due to reinforcement configuration, axial load ratio and component size. Through the lens of squat RC walls, this Chapter adopts an existing simulation framework — called herein the relative performance framework — to assess which structural parameters affect crack widths that correspond to a "red-tag" damage state, with the end goal to identify whether a structure is at risk of collapse based solely on crack width measurements. The relative performance framework quantifies the influence of a damaging earthquake on the collapse probability of a structure in a future earthquake. In this Chapter, the framework is implemented for seven squat RC shear walls from the experimental literature, modeled with a popular macro-

modeling approach. The use of an existing model helps establish the ability of current tools to model existing cracking damage.

3.1 Case Study: Squat Shear Walls

This Chapter demonstrates crack-assessment within a risk framework for the case of squat, planar RC shear walls, relying on simulation to probabilistically relate crack width and post-earthquake safety. This strategy mirrors previous successful crack-assessment studies on RC columns [9] and beam-column joints [179]. Squat RC shear walls — having an aspect ratio less than about 2.0 — are common in nuclear plants, parking structures and low-rise buildings where architectural configurations limit wall slenderness, but high strength and stiffness are required for satisfactory earthquake performance. Under severe shaking, low-aspect-ratio walls develop diagonal cracks and are susceptible to undesirable brittle shear modes such as Diagonal Tension (DT), Diagonal Compression (DC), Shear Sliding (SS), or Bar Buckling (BB) and Reinforcement Fracture (RF) in the boundary element. Guidelines for seismic assessment of walls categorize damage into one of several possible damage states based on visual damage markers (see Table 3.1). Crack width is tightly woven into the damage state definitions because:

- an increase in crack width indicates high local reinforcement strains and reduced concrete strut effectiveness, hence an increase in damage;
- the effectiveness of repair is limited by crack width [72];
- residual crack width is easy to measure after an event[1].

Unfortunately, there is little agreement on what level of crack width should trigger a detailed inspection, how the structural, reinforcement and loading configurations affect the crack width limit-state, and about whether damage is better correlated to crack width in the residual state or at the peak state. The lack of consensus on crack width thresholds is apparent from

[1]Trandafir, et al. [169] note that traditional crack width measurements can exhibit non-smoothness near ultimate loads, while the less traditional vertical crack width gives a smoother, more reliable crack profile measurement

the strikingly different crack-width recommendations compiled in Table 3.1 for squat RC shear walls.

Table 3.1. Summary of recommendations for crack width limits corresponding to squat wall damage states

Guideline	Minor	Moderate	Severe	Notes
FEMA 306[a] [59]	< 6.3 mm	–	–	Residual flexural crack
	1.6 - 3.2 mm	3.2 - 9.5 mm	> 9.5 mm	Residual shear crack
JBDPA [81]	< 0.2 mm	0.2 - 1.0 mm	1.0 - 2.0 mm	Residual crack
FEMA P-58 [60]	0.5 - 3.0 mm	> 3.0 mm	–	Peak flexural crack
	0.5 - 3.0 mm	–	> 3.0 mm	Peak shear crack
Carillo & Alcocer [29]	0.1 mm	0.5 mm	2.5 mm	Residual crack
Jiang, et al. [82]	0.06 mm	0.31 mm	0.68 mm	Residual crack
Rivera & Whittaker [150]	> 0.5 mm	> 1.0 mm	> 3.2 mm	Residual crack

[a] values correspond to behavior mode RC1B (diagonal tension cracks) in isolated strong wall

To evaluate whether the "Severe" recommendations of Table 3.1 accurately reflect crack widths at or near wall failure, a dataset of RC squat wall experiments has been collected and summarized in Table 3.2. Only experiments that report both peak and residual crack widths are included. While large databanks of RC wall experiments exist, very few provide quality crack data and fewer still provide both peak and residual crack data. Table 3.2 shows that peak widths of shear cracks tend not to exceed 5 mm, and often are much lower, with an average shear crack width of 2.34 mm at failure. Residual crack widths at failure are even smaller, with an average residual-to-peak crack width ratio of 0.44 as shown in Fig. 3.1. This echoes growing evidence [121, 137] that the residual crack widths proposed by FEMA 306 ($>$ 9.5 mm at failure) are significant overestimates, and are therefore unconservative.

Table 3.2. Collection of squat shear wall experiments for which peak and residual crack width data are available

Specimen	f'_c	M/VL	**ALR**	ρ_h	ρ_l	**Mode**	w_{res}	w_{peak}
Lowes, et al. [94]								
PW2	40.3	2.10	15.0	0.28	0.28	BC,BB	1.14	1.78
PW3	34.3	2.00	10.0	0.28	0.28	DC,BB	1.67	1.78
PW4	29.5	2.00	10.0	0.28	0.28	BC,BB	0.81	–
Tran & Wallace [167]								
RW-A20-P10-S38	48.0	2.00	7.3	0.27	0.27	DT	1.25	–
RW-A20-P10-S63	48.0	2.00	7.3	0.61	0.61	DC,BB	1.00	3.50
RW-A15-P10-S51	48.0	1.50	7.7	0.32	0.32	DT,RF	0.80	3.00
RW-A15-P10-S78	56.0	1.50	6.4	0.73	0.73	SS	1.25	3.00
RW-A15-P2.5-S64	56.0	1.50	1.6	0.61	0.61	DC	–	3.00
Jiang, et al. [82]								
SW7	28.0	2.0	30.0	0.66	0.66	BB	0.35	1.8
Rivera, et al. [149]								
SW1	25.0	0.94	0.0	0.67	0.67	SS	0.5	2.9
SW2	48.2	0.54	0.0	1.00	1.00	DC	2.0	2.1
SW3	53.8	0.54	0.0	0.67	0.67	SS	0.9	1.3

SW4	28.9	0.54	0.0	0.33	0.33	SS	2.0	5.0
SW5	29.6	0.33	0.0	1.00	1.00	SS,DC	0.7	0.9
SW6	26.2	0.33	0.0	0.69	0.63	SS	1.6	3.5
SW7	26.2	0.33	0.0	0.38	0.34	–	0.5	3.2
SW8	24.1	0.54	0.0	1.50	1.50	SS,DC	0.2	1.0
SW9	28.9	0.54	0.0	0.67	1.50	SS	1.5	6.4
SW10	31.7	0.54	0.0	0.33	1.50	DC	6.4	6.4
SW11	34.5	0.54	0.0	0.69	0.63	SS	0.3	0.9
SW12	34.5	0.54	0.0	0.38	0.34	DT	1.5	1.5
Alwashali, et al. [5]								
SC-13-D0	40.2	0.29	1.2	1.32	1.32	DC	0.5	1.2
Pizarro, et al. [137, 138]								
SW01	34.6	0.43	4.3	0.53	0.53	SS	0.43	1.06
SW02	28.5	0.43	10.5	0.53	0.53	DC	0.91	3.25
SW03	35.9	0.43	4.2	0.33	0.33	SS	0.66	1.80
SW04	42.4	0.43	4.7	0.39	0.53	DT,RF	0.60	3.20
HSW01	37.5	0.43	4.0	0.53	0.53	SS	1.00	3.07
HSW02-1.75	37.5	0.43	8.0	0.53	0.53	–	0.13	0.65
HSW02-2.00	37.5	0.43	8.0	0.53	0.53	–	0.36	2.50
HSW02-2.75	37.5	0.43	8.0	0.53	0.53	DC	–	4.89
Min	24.1	0.29	0.0	0.27	0.27	–	**0.13**	**0.65**
Max	56.0	2.00	30.0	1.50	1.50	–	**6.4**	**6.4**
Avg	–	–	–	–	–	–	**0.79**	**2.34**
St. Dev.	–	–	–	–	–	–	**1.18**	**1.49**

Some of the discrepancy between experimental crack widths and the FEMA guidelines may derive from the lack of dynamic, full-scale tests, which are often un-economical or infeasible. In fact, limited results indicate that quasi-static tests underestimate peak crack widths relative to dynamic excitations [137, 138] and that reduced-scale experiments develop smaller

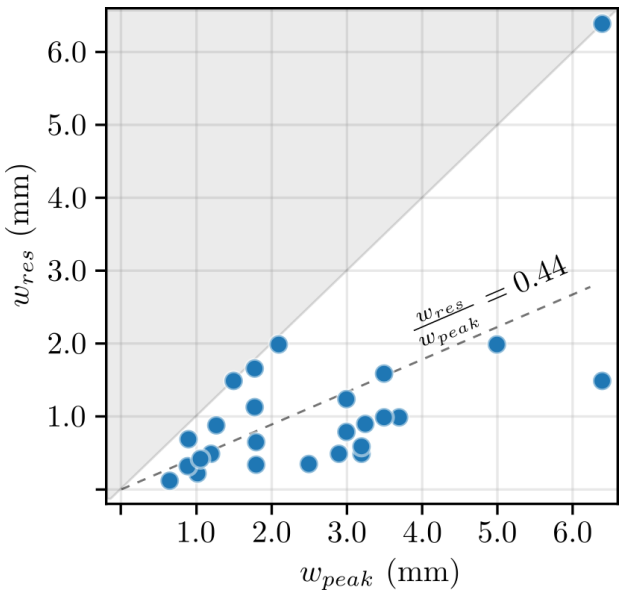

Figure 3.1. Empirical relationship between residual crack width and peak crack width for planar reversed-cyclic squat wall experiments

cracks than their full-scale companions due to tighter reinforcement and smaller bars. As full-scale, dynamic tests are unlikely to become available in numbers sufficient for developing improved crack-width guidelines, this Chapter turns toward numerical simulation to augment the existing database and provide a framework for developing preliminary guidelines for identifying acceptable crack widths. Section 3.2 describes an existing framework for assessing the effects of pre-existing damage on future earthquake performance. Section 3.3 then describes the numerical modeling scheme that is incorporated into the relative performance framework in order to assess the effect of cracking damage on future earthquake performance of squat RC walls, which is done in Section 3.4.

3.2 Relative Performance Framework

Burton & Deierlein [22] proposed a relative performance framework extending that of FEMA 306 [59] (discussed in Chapter 2) by supplanting the simplified SDOF pushover technique with nonlinear-time-history analyses.

For a building of interest, their relative collapse procedure first calls for the development of a collapse fragility curve to describe the probability that an undamaged building will collapse, conditioned on the ground motion intensity measure (IM). The lognormal collapse fragility curve (see Fig. 3.2) is fit to a significant set of Incremental Dynamic Analyses (IDA) and the scale factor required to collapse the structure (χ^i) is recorded for each i^{th} IDA for all ground motions in the ground motion set. In a separate analysis, earthquake damage is imposed by subjecting the initially undamaged building to a damaging ground motion j with a scale factor less than χ^j. Each unique combination of damaging ground motion and scale factor is referred to as a *damage instance* throughout the remainder of this Chapter.

After inducing damage, a collapse fragility curve is developed for the damaged wall instance and compared to its undamaged counterpart. The damage-induced leftward shift at the mean collapse probability is an indication of the likely relative performance of the damaged wall, and is measured as the mean collapse intensity ratio κ_{col}:

$$\kappa_{col} = \frac{I\hat{M}_{j/0.XX}}{I\hat{M}} \tag{3.1}$$

where $I\hat{M}$ indicates the mean collapse intensity for the undamaged building and the subscript $j/0.XX$ indicates that damage was induced by the jth ground motion scaled to XX% of the collapse scale factor for that ground motion χ^j.

An overview of the framework is provided in Fig. 3.2. Figure 3.2a shows a schematic of an undamaged collapse fragility curve and a damaged collapse fragility curve for a single damage instance. For each such pair, the relative performance index (κ_{col}) is calculated as in Eq. (3.1) and plotted in Fig. 3.2b against an engineering demand parameter (EDP) that is measured following the damaging ground motion. Repeating the analysis for many damage instances produces the idealized sketch of Fig. 3.2b wherein an increase of the EDP is correlated with a reduction in collapse performance. The κ_{col}-EDP plot is used to define a threshold damage value, i.e., an EDP measurement that, if observed after an EQ would indicate a higher-than-acceptable collapse vulnerability for future quakes. Various suggestions have been proposed for defining the cutoff EDP; Burton & Deierlein [22] suggest that the EDP corresponding to a κ_{col} value below 0.8 or 0.9 represents a

significant reduction in collapse performance, whereas Galvis, et al. [70] place the cutoff EDP at a kinking point of the κ_{col}-EDP curve.

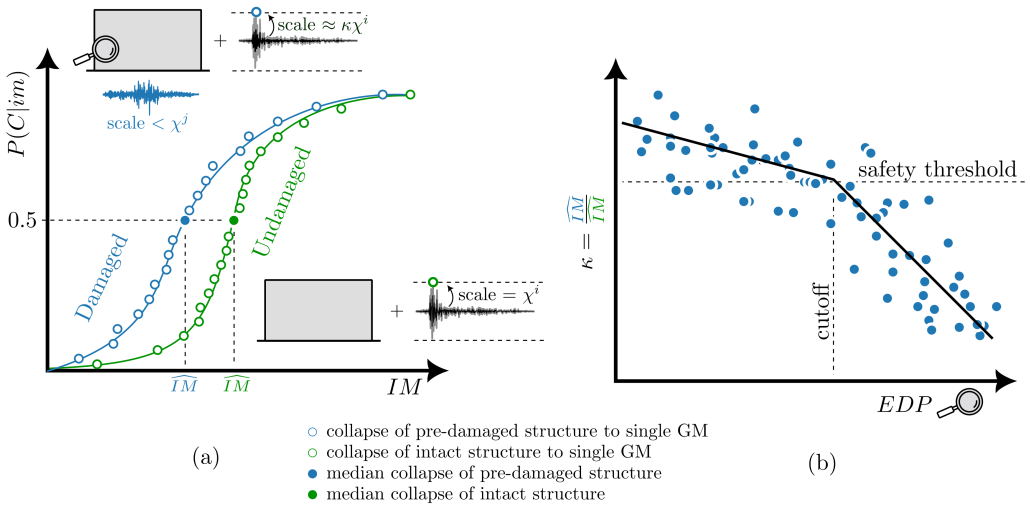

Figure 3.2. a) Damaged and undamaged collapse fragility curves composed of many IDAs for a single damage instance; b) schematic of relative collapse performance κ_{col} against damage measure

The modeling approach that is used within the relative collapse framework should avoid non-simulated failure modes, as any omission of damage mechanisms from the numerical model may lead to an overestimation of the collapse capacity of earthquake-damaged structures.

In the subsequent Sections the relative collapse framework is applied to squat, planar RC shear walls with crack width used as the primary damage measure. This approach builds on the crack-based assessment approaches summarized in Chapter 2 and the choice of crack-width as the EDP is rooted in the practical needs filled by crack-based assessment, discussed in Chapter 1. It is noted that criteria for choosing an efficient EDP for the relative collapse procedure are discussed elsewhere, e.g., [70].

3.3 Modeling Squat Walls with MVLEM Elements in OpenSees

The assessment framework outlined in Section 3.2 involves many sequential incremental dynamic analyses yet requires a sophisticated numerical model to capture local response quantities (namely, crack width) and replicate multiple failure modes (e.g., concrete crushing, reinforcement fracture). The computational burden of running even a single IDA with traditional finite-element approaches effectively rules out that approach. Instead, this work adopts a computationally efficient macro-modeling strategy available within the OpenSees software [109] that captures local response quantities. In this approach, a wall is meshed into an assemblage of RC panel elements (see Figure 3.3c). Each panel behaves according to the Fixed Strut Angle Model (FSAM) [128], which simplifies state-of-the-art panel theories (e.g., [174]) to be compatible with the standard uniaxial material models characteristic of OpenSees. The FSAM idealizes each RC panel as an assemblage of two diagonal concrete struts perfectly bonded to an orthogonal grid of x-y distributed reinforcement. The orientation of the concrete struts is fixed to align with the principal strain directions upon first cracking, and each strut follows the uniaxial hysteretic rules of the `ConcreteCM` model [35], calibrated according to Bernardini, et al. [19]. Concrete struts of the wall boundary elements are assigned augmented properties according to confinement factors suggested by Priestley, et al. [139] for rectangular wall sections. Cyclic concrete damage follows the rules of Mansour & Hsu [102].

Cracks, though not directly included in the numerical scheme, are considered in an ad-hoc fashion by: (i) reducing the strength of the uniaxial concrete struts to account for biaxial softening [174], (ii) incorporating tensile offsets in the uniaxial concrete law to capture the misalignment of cracks after simultaneous sliding and opening, and (iii) adding a component of frictional shear along each of the panel's crack faces [128]. The FSAM bounds the crack shear stress below a plastic limit, equal to the product of a friction coefficient (μ) and the compression crossing the crack (σ_{cr}) as shown in Eq. (3.2). Below the plastic friction limit, shear stresses in the crack reference frame (noted by the prime symbols in Eq. (3.2)) are elastic, with the crack shear modulus taken as 0.4 times the concrete modulus $D_{ts} = 0.4E_c$. According to the model, crack shear stress vanishes if the

crack-perpendicular strut is strained in tension.

$$v_{ci} = D_{ts}\gamma_{x'y'} \leq \mu\sigma_{cr} \tag{3.2}$$

While simplified, the FSAM crack shear model approximates experimental sliding behavior of a smooth crack [165] or a heavily damaged crack [143] for which protrusions are deteriorated and aggregate interlock is limited. This corresponds to the post-earthquake scenario.

Reinforcement strains in each RC panel are directly obtained from the panel strains ε_{xx} and ε_{yy}, consistent with the perfect bond assumption of the FSAM. Reinforcement axial stresses follow the `Steel02` uniaxial model of OpenSees. Dowel forces are approximated via an ad-hoc factor α_d that scales the panel shear strain and are added to the total shear resistance of the RC panel. Massone, et al. [107] recommend α_d values of 0.005 for flexure-controlled walls and 0.0001 for squat walls. The real behavior of reinforcement that crosses cracks is considerably more complicated, with mutual reductions in axial and dowel capacity of bars based on the crack opening and sliding trajectory [99]. However, these complexities can be safely ignored for reinforcement ratios less than about 2%, which is typical for wall web reinforcement.

Reinforcement fracture, which may occur at a diagonal tension crack [137] or at buckling-prone boundary elements [121], significantly reduces a wall's stability and must be modeled lest the collapse capacity of a damaged wall be overpredicted. As cumulative fatigue measures have been shown to be well correlated to reinforcement rupture during earthquake loading [103], the `DuctileFracture` material in OpenSees [185] is herein wrapped around the base-level `Steel02` reinforcement material law in OpenSees. The `DuctileFracture` material calculates a fracture index that tracks the cumulative effect of load history on the low-cycle fatigue life of a reinforcement bar. Reinforcement buckling is indirectly captured through a slenderness parameter ψ that has been calibrated for RC walls [32]. Resistance of a reinforcement element vanishes when the calculated fracture index exceeds 1.0.

The `Efficient-Shear-Flexure-Interaction` (E-SFI) beam-column element [107] of OpenSEES ties multiple FSAM panel elements together horizontally, enforcing a kinematic relation between horizontal panel strain and panel shear strain that is valid for squat and slender walls alike. A wall (Figure 3.3a) is vertically meshed with E-SFI line elements. An objective

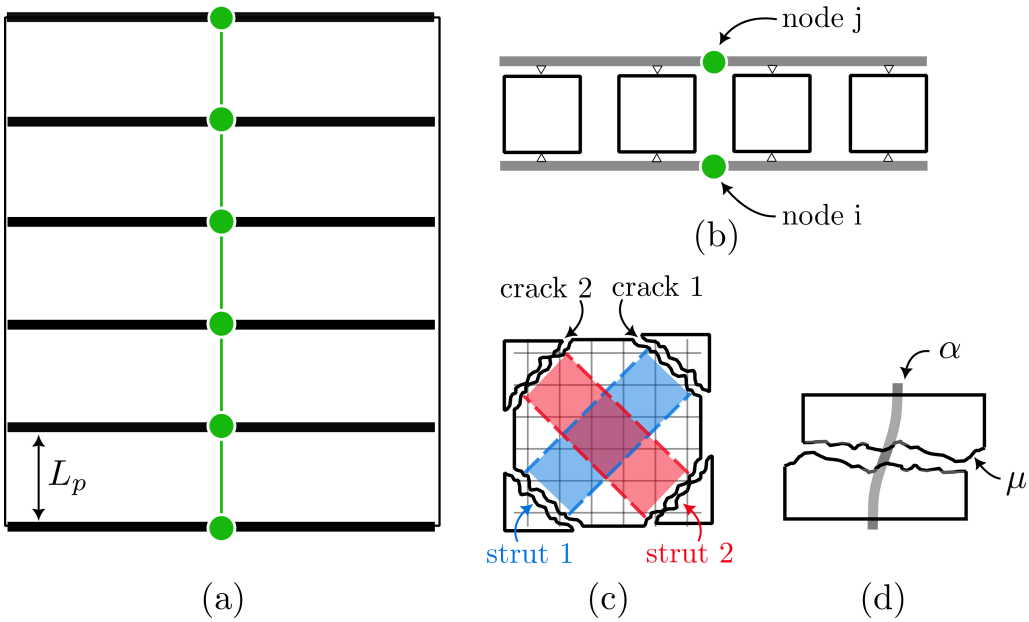

Figure 3.3. Macro-modeling approach: (a) wall macro-assembly, (b) E-SFI element, (c) FSAM panel with two concrete struts tied to a reinforcement grid, (d) ad-hoc crack parameters within the FSAM model

post-peak response is obtained if the height of the fixed-end line element equals the length of the plastic hinge region (L_p), or about twice the wall thickness for squat walls [107]. Strain penetration at the base of the wall is not included in the modeling approach of this Chapter.

3.3.1 Validating Modeling Approach: Global and Local Response

The `FSAM` panel material and the `E-SFI` line element have been previously verified against panel tests [128] and squat RC wall experiments [93], respectively. Massone, et al. [107] suggest values for the ad-hoc friction and dowel parameters as $\mu = 0.35$ and $\alpha_d = 0.0001$ for squat walls, though calibration against individual panel tests by Orakcal, et al. [128] revealed that a friction coefficient between 0.1-0.2 produced the best match for local panel strains, which are related to crack widths through Eq. (3.3).

This Chapter, being focused on crack width estimation, adopts Orakcal's suggestion of $\mu = 0.2$. Finally, the equivalent slenderness ratio ψ of reinforcing bars, used to calculate the `DuctileFracture` material and to predict reinforcement damage due to buckling, is taken as 0.5.

The modeling approach described above is validated against experimental results in the literature. Comparisons between experimentally measured response (gray) and numerically predicted response (blue) are shown in Fig. 3.4 for four squat RC wall specimens from the experimental literature – RW5-S1.75 [121], H60 [36], NF1T-B [11] and SWC1 [83] – shown in Fig. 3.4a-d, respectively. Specimen RW5-S1.75, with an aspect ratio of 1.75 and light boundary-element reinforcement, failed due to concrete crushing and buckling of longitudinal reinforcement. This failure mode was predicted by the numerical model in the final displacement cycle, leading to a sudden loss in load-carrying capacity. Similarly, the numerical model captured the sudden failure of the highly compressed (20% ALR) specimen SWC1 due to concrete crushing after 1% drift. Post-peak behavior of specimen H60 is replicated well by the model up until failure at a 3% drift ratio. Specimen NF1T-B, with an aspect ratio of 1.0 and heavily reinforced well-confined boundary elements, failed by diagonal tension. The numerical model predicts pinched loops relative to the experiment, but still captures the peak strength and initial stiffness.

Validation of crack width prediction is reported in Fig. 3.5. Simulation of the monotonic specimen W1 of Fathalla, et al. [58] confirms that the numerical model can capture the crack formation pattern by overlaying the simulated pattern on top of DIC measured pattern from the experiment in Fig. 3.5d. The simulated peak crack width of 2.39 mm is a reasonable estimate of the experimentally measured peak crack of 2.00 mm. The hybrid specimen HSW02 tested by Pizarro, et al., [138] is simulated and compared to the experimental response in Figure 3.5a-b. The simulated crack width evolution is remarkably accurate, though *residual crack widths are not captured by the numerical model.*

Crack width is obtained via Eq. (3.3) as the product of principal tensile strain (ε_1) and a crack spacing parameter ($s_{m\theta}$) for each of the panel's two crack systems (index i):

$$w_i = \varepsilon_{1,i} s_{m\theta} \tag{3.3}$$

The $s_m\theta$ term approximates the average crack spacing from the rein-

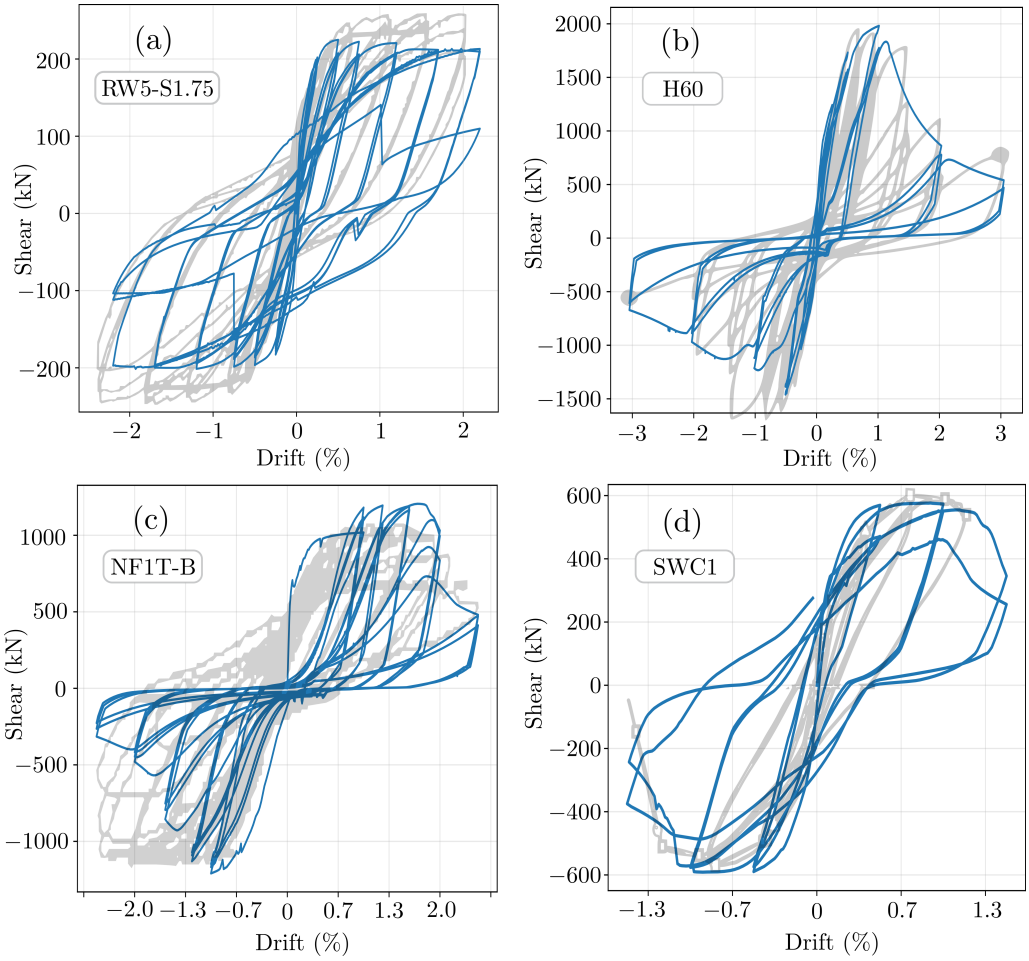

Figure 3.4. Validation of modeling approach for capturing load-deformation response, crack width evolution and crack pattern

forcement layout [42]. Large reinforcement diameter, small reinforcement ratio and large bar spacing all contribute to increased crack width. Average principal strains (ε_1,ε_2) can be obtained from the average panel strains (ε_{xx},ε_{yy},γ_{xy}) via solution of the eigenvalue problem in Eq. (3.4).

$$\det(\boldsymbol{\varepsilon} - \lambda_i \boldsymbol{I} = \mathbf{0}) \tag{3.4}$$

where $\boldsymbol{\varepsilon}$ is the strain tensor from the `FSAM` panel, λ_i holds the principal strains and $\boldsymbol{I}$ is the identity tensor. In the model, a crack is assumed to fully

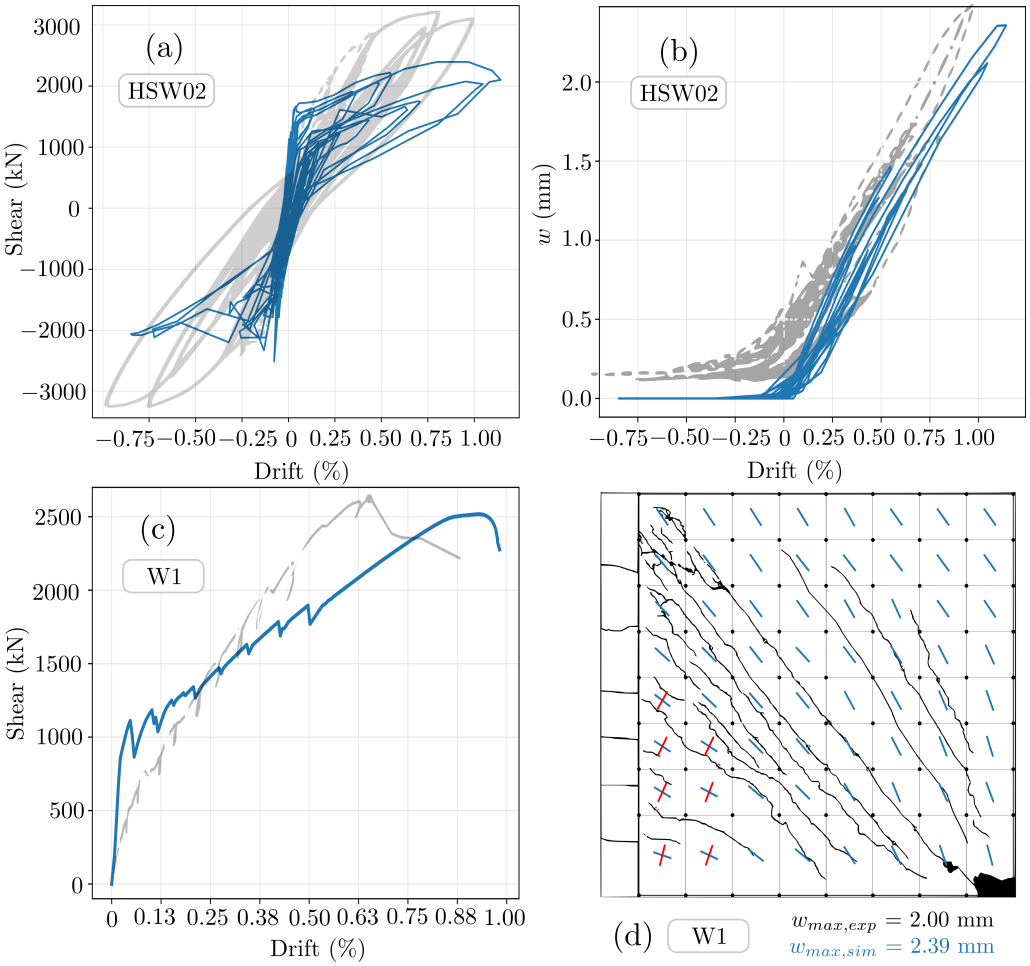

Figure 3.5. Validation of crack width prediction approach

close when the crack-perpendicular strain becomes compressive. In reality, non-zero compression is required to overcome wedging forces between rubble particles and laterally offset aggregates [153]. However, more realistic crack closure models do little to improve the residual crack width prediction, due to the perfect bond assumption (i.e., no local pullout) built into the `FSAM`. *Consequently, peak crack width is the damage indicator used in this Chapter.* While peak width is not directly measured after an earthquake, it has been reliably linked with damage [56]. Empirical relationships between peak and residual crack width (e.g., Fig. 3.1) can translate one measure to the other

as needed for use in post-earthquake inspections.

3.4 Effect of Wall Configurations on Crack Width Limits

Using the relative collapse procedure outline in Section 3.2, the effect of peak EQ-sustained shear-crack widths on subsequent collapse risk is analyzed for seven squat, planar RC walls from the experimental literature. The walls encompass a broad swath of design parameters, specifically: concrete strength, axial load ratio, aspect ratio, web reinforcement ratio and boundary element reinforcement ratio. Of these, only axial load ratio is currently considered in the acceptance criteria of shear-controlled RC walls [6]. The case-study walls are grouped to evaluate whether axial load ratio, transverse reinforcement ratio and wall scale (i.e., size effect) may also affect the critical crack widths. The case-study walls are summarized in Table 3.3.

Table 3.3. Summary of case-study wall parameters[a]

ID	f'_c	t_w	L_w	M/VL_w	ALR	m_{seis}	$V_n/A_{cv}\sqrt{f'_c}$	ρ_h	ρ_l	$\rho_{h,be}$	$\rho_{l,be}$
HSW02	37.5	200	3000	0.425	8.0	180	0.67	0.53	0.53	0.53	0.53
NFI1T-B	52.9	200	1500	1.00	7.0	277	0.47	0.40	0.54	2.57	2.98
RW-A15-P2.5-S64	56.0	150	1220	1.50	1.6	175	0.53	0.61	0.61	0.86	6.06
H60	44.0	200	2000	1.00	0.0	750	0.78	0.82	0.82	1.10	6.70
SW8	24.1	200	3050	0.54	0.0	650	0.90	1.50	1.50	1.50	1.50
SWC1	34.0	120	1200	1.25	20.0	150	0.72	0.58	0.65	0.92	2.82
SWC1-2[b]	34.0	240	2400	1.25	20.0	600	0.72	0.58	0.65	0.92	2.82

[a] units in MPa, mm (metric ton). Reinforcement ratios provided in percentages

[b] geometrically scaled up 2x relative to SWC1

Specimens NF1T-B [11], RW-A15-P2.5-S64 [167] and SWC1 [83] are grouped to assess how crack width damage depends on axial load ratio (between 0-20%). Specimen NF1T-B has well-confined boundary elements, was tested in single curvature, and subjected to an axial load ratio of 0.07. Specimen RW-A15-P2.5-S64 contains heavy longitudinal boundary reinforcement and a low axial-load ratio of 0.016. Wall SWC1 has a thin cross section, largely spaced transverse reinforcement and a high axial load ratio of 20%.

Specimens RW-A15-P2.5-S64 [167], H60 [36] and SW8 [150] are grouped to evaluate the effect of transverse reinforcement ratio. Specimen H60 has high reinforcing ratios, was designed with a high nominal shear strength, and supported no axial load. Specimen SW8 carried high web shears and failed in a combined sliding/crushing mode.

Walls NF1T-B [11] and HSW02 [138] are grouped to assess the difference between shear-critical and flexure-dominated walls. Unlike the other studied walls, HSW02 is shear-critical with $V_n < V_{@Mn}$. The wall lacks boundary elements, is tested in double curvature, and carries an axial load ratio of 0.08. The web reinforcement ratio (0.53%) and ALR are similar to that of wall NF1T-B.

Finally, wall SWC1 [83] is grouped with a geometrically-similar wall that is scaled-up by a factor of 2, to identify any size effect on crack width – damage evolution. The upscaled wall, named here SWC1-2, has no physical counterpart in the experimental literature, as full-scale experiments are scarce. To maintain the reinforcement ratio, the bar spacing of wall SWC1 is retained in wall SWC1-2, but the bar diameters are increased by a factor of $\sqrt{2}$.

Each wall is assumed to be the primary seismic force resisting system of a simple 1-story building. To provide a uniform baseline (i.e., undamaged) performance level, seismic masses are proportioned to each wall such that the ASCE-7 [7] MCE_R ground motion corresponds to a roughly 10% collapse probability, where the MCE_R spectrum is constructed assuming a risk category II building on site class B soil in Seattle, Washington (according to publicly available data from King County). A uniform baseline is necessary because – as pointed out by Galvis et al. [70] – the relative collapse framework implicitly assumes that the risk associated with the undamaged structure is acceptable to stakeholders.

For each case-study wall, incremental dynamic analysis is performed

for all the 44 ground motion records in the ATC-63 far-field ground motion dataset. The spectral acceleration at the building's fundamental period is recorded at collapse, which occurs when a small increase in the ground motion scale factor produces a large increase in peak horizontal displacement, as shown in Fig. 3.6 for wall SWC1-2.

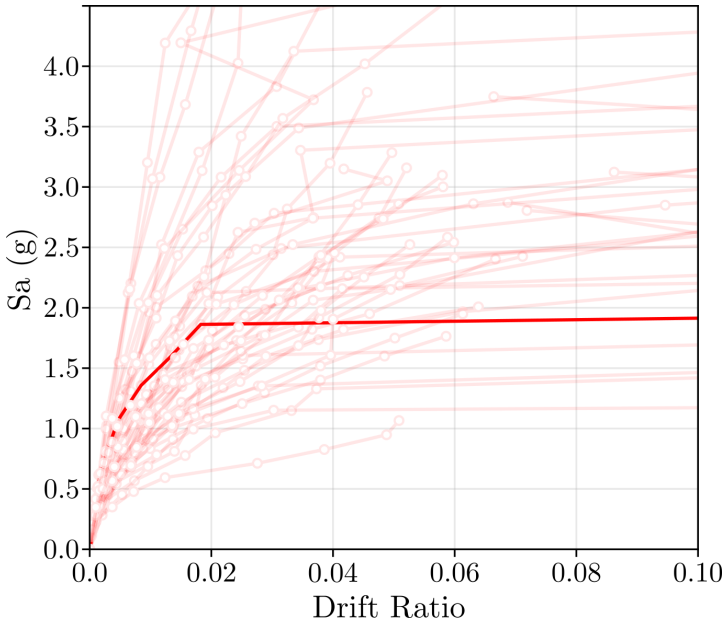

Figure 3.6. Identification of collapse drift

Collapse fragility curves are constructed for each as-designed, undamaged wall building by fitting a cumulative lognormal distribution to the simulated collapse spectral accelerations. The undamaged collapse fragility curves are plotted in Fig. 3.7. The short-period MCE_R acceleration ($S_{MS} = 1.07$) is overlayed on top of the fragility curves to indicate that the undamaged case-study walls approximate the ASCE 07-22 collapse risk target of 10% for new buildings [7].

Having established the baseline collapse performance, each of the case-study walls from Table 3.3 is submitted to sequential ground motion simulations to determine the effect of prior damage on the collapse behavior, as described in Section 3.2 and as depicted in Fig. 3.2. Damaged collapse fragility curves are constructed for various damage instances (i.e., combination of damaging ground motion and damaging scale factor) and

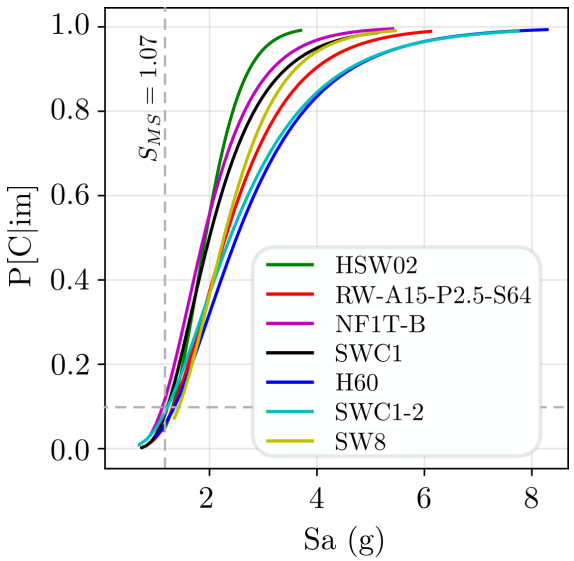

Figure 3.7. Collapse fragility curves for undamaged case-study wall buildings

relative collapse indices (κ_{col}) are calculated according to Eq. (3.1). Values of κ_{col} range between 0 and 1, with a particularly damaging earthquake resulting in a low κ_{col} value whereas an insignificant quake will produce κ_{col} near 1. Because κ_{col} is calculated using the fundamental-period spectral acceleration as the IM, Eq. (3.1) can be rewritten as:

$$\kappa_{col} = \frac{\hat{SA}(T_1)_{j/0.XX}}{\hat{SA}(T_1)} \tag{3.5}$$

To keep the number of nonlinear time history analyses manageable, 7 damaging ground motions are selected from the ground-motion dataset. The damaging ground motions are listed in Table 3.4 with the ID numbers provided by the ATC far field dataset [61].

Each i^{th} damaging ground motion is scaled between $0.2\chi_i$ and $0.95\chi_i$. In total, 28 damage instances (4 damage scale factors for each of 7 damaging motions) are simulated for each of the seven case-study walls. This results in 196 data points for κ_{col} by comparing the damaged collapse fragility for each damage instance with the collapse fragility of the associated intact wall shown in Fig. 3.7. In Fig. 3.8 - Fig. 3.11, κ_{col} is plotted against the peak simulated shear-crack experienced during the damaging EQ. Horizontal lines

Table 3.4. Ground motions used for damage input

EQ ID	M_w	PGA	Name	Station	Year
120111	6.7	0.52	Northridge	Beverly hills - Mulhol	1994
120821	7.5	0.22	Kocaeli, Turkey	Arcelik	1999
120911	7.3	0.24	Landers	Yermo Fire Station	1992
121322	7.0	0.55	Cape Mendocino	Rio Dell Overpass	1992
121411	7.6	0.35	Chi-Chi, Taiwan	CHY101	1999
121511	6.6	0.21	San Fernando	LA - Hollywood Stor	1971
121711	6.5	0.35	Friuli, Italy	Tolmezzo	1976

at $\kappa_{safe} = 0.8$ indicate the safety threshold suggested by Burton & Deierlein [22]. Data points below the safety threshold represent a significant reduction in mean collapse IM due to the damaging quake.

Fig. 3.8 plots the simulated $\kappa_{col} - w_{max}$ relationship for three walls with increasing axial load ratio from 1-20%. Axial load constrains crack opening. As a result, highly compressed walls fall below the collapse-safety threshold after having developed relatively small cracks. For example, a 0.6 mm crack corresponds to near-collapse of the heavily compressed wall SWC1 whereas the same crack width induces negligible damage in the lightly compressed wall RW-A15-P2.5-S64. Fig. 3.8 also shows that walls with low axial load possess residual collapse safety (κ_{col}) near the safety threshold even for crack widths up to 7 mm, indicating that pre-quake performance can be easily restored for low-axial-load-ratio walls.

Fig. 3.9 plots the collapse safety simulations for shear-critical wall HSW02 and flexural-limited wall NF1T-B. Both specimens have moderate axial load ratios and similar web reinforcement layouts. The collapse safety of the shear critical wall plunges below the safety threshold for crack widths that induce minimal damage in the more ductile NF1T-B specimen. Therefore, shear-critical walls fail not only more suddenly, but at crack widths that would otherwise be unremarkable for modern flexurally-limited walls.

Fig. 3.10 compares the collapse safety of three walls with similar axial load but different transverse reinforcement ratios. Wall H60 has a web

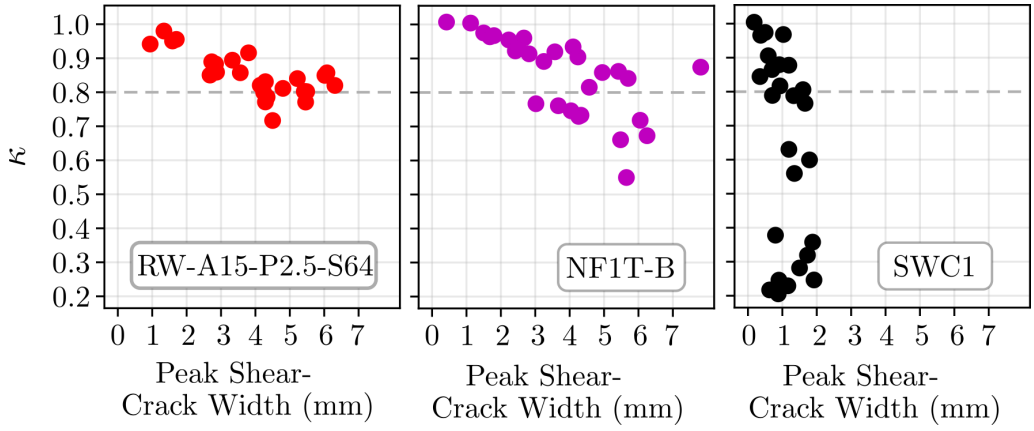

Figure 3.8. Effect of axial load ratio on $\kappa_{col} - w_{max}$ simulations. (axial load ratio increasing left to right)

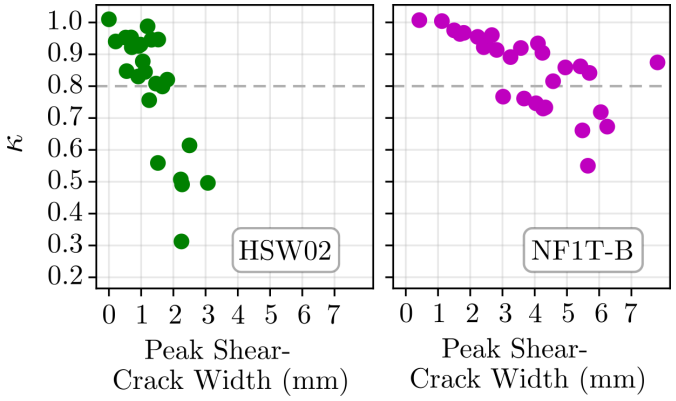

Figure 3.9. Effect of shear-critical or flexure-critical design on $\kappa_{col} - w_{max}$ simulations. (shear-critical wall on left)

transverse reinforcement ratio of 0.82 compared to 0.61 for wall RW-A15-P2.5-S64 and 1.50 for wall SW8. The simulation results would indicate that differences in transverse reinforcement ratio do little to differentiate critical crack width magnitudes. All three walls sustain minimal damage for crack widths up to 4-5 mm and tend to retain a residual collapse safety level that plateaus near the limit $\kappa_{safe} = 0.8$ for larger crack widths.

Fig. 3.11 compares the collapse safety of two geometrically similar specimens. Specimen SWC1 was tested by Jin, et al. [83] while SWC1-2 is geometrically scaled up 2 times while maintaining the reinforcement

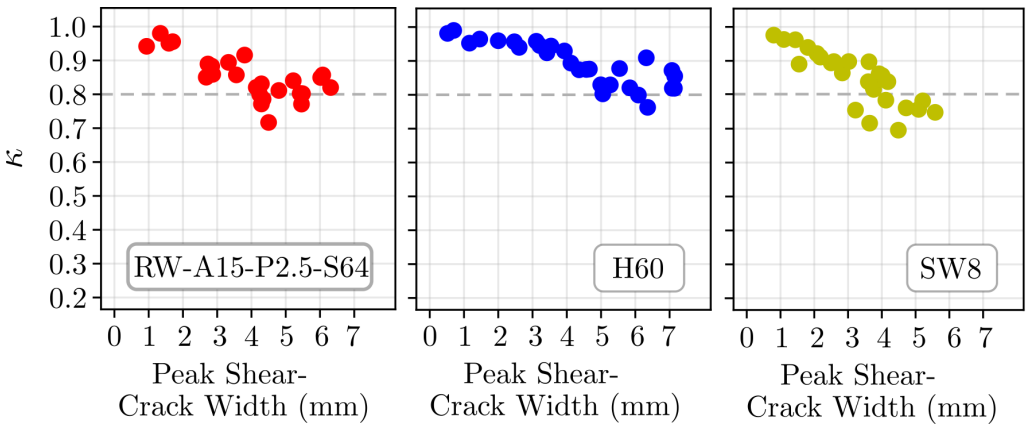

Figure 3.10. Effect of transverse reinforcement ratio on $\kappa_{col} - w_{max}$ simulations. (ρ_h increasing to the right)

ratio and spacing. The scaled-up specimen sustains crack widths up to 3.5 mm whereas no cracks develop beyond 2 mm before total collapse of the reduced-scale wall SWC1.

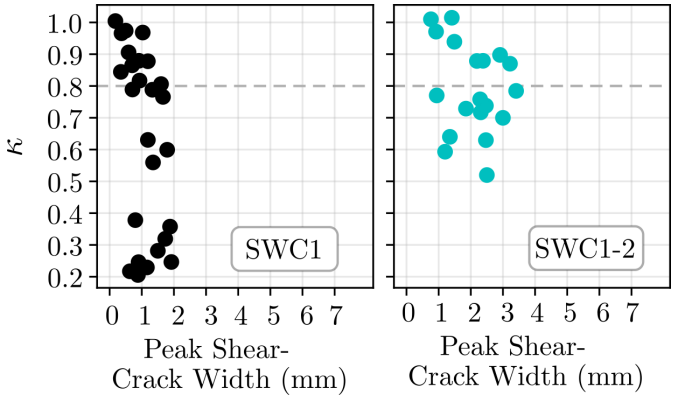

Figure 3.11. Effect of wall scaling on $\kappa_{col} - w_{max}$ simulations. (size increasing to the right)

Irrespective of axial load ratio, reinforcement layout or specimen size, Fig. 3.8 - Fig. 3.11 demonstrate that an increase in crack width is strongly correlated with a reduction in collapse safety. Therefore, maximum crack width is a useful index for earthquake damage of squat RC walls. Furthermore, a crack width threshold w_{lim} can be defined to represent an upper limit of acceptable damage. A structure experiencing a crack wider

than w_{lim} during an EQ would be assigned a red tag (i.e., unsafe structure). Conversely, peak crack widths below w_{lim} would indicate sufficient residual collapse safety ($\kappa_{col} > \kappa_{safe}$) and would garner a green tag. Due to the inability of a single EDP to perfectly capture the structural response, a non-zero false-tagging rate is inevitable. The goal, then, in setting w_{lim}, is to minimize the false-tag rate. As can be seen in the tagging schematic of Fig. 3.12, true green tags lie above κ_{safe} and to the left of w_{lim}. True red tags fall below κ_{safe} and to the right of w_{lim}. Thus, a true tag is one for which the prediction based on the observed crack width matches the real state – in this case, the simulation result.

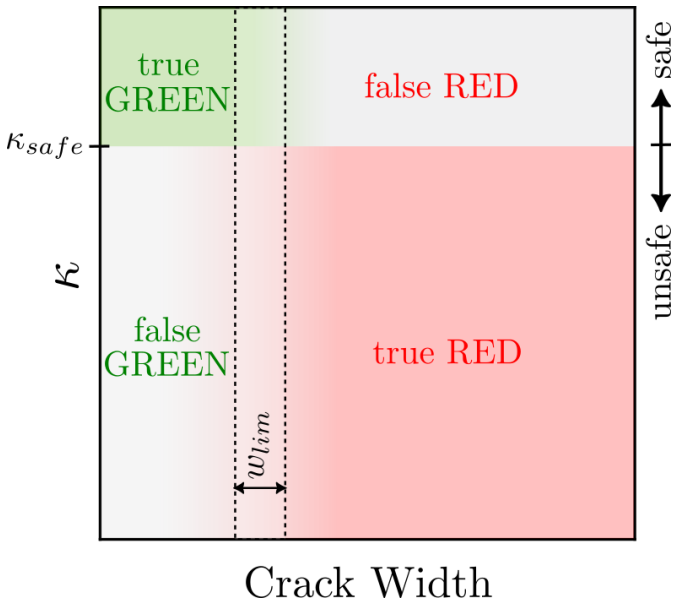

Figure 3.12. Tagging schematic

The simulation results shown in Fig. 3.8 - Fig. 3.11 represent truth models for each wall in Table 3.3. Thus, a w_{lim} can be identified for each wall by iteratively choosing w_{lim} until the true tag rate is maximized.

Fig. 3.13 shows, for each case-study wall, a solid dark gray line that measures tagging success rate for a continuous range of trial crack width inspection limits $w_{lim,tr}$. The tagging success rate at any $w_{lim,tr}$ is calculated as the percentage of the 28 "truth" simulations (which are overlayed in each subplot) that lie in the top-left or bottom-right rectangle formed by the horizontal line at $\kappa_{safe} = 0.8$ and the vertical line at $w_{lim,tr}$. The best crack

width inspection limit (w_{lim}) is the crack width corresponding to the highest true-tag rate for each wall. A dashed vertical line is plotted at these values in Fig. 3.13.

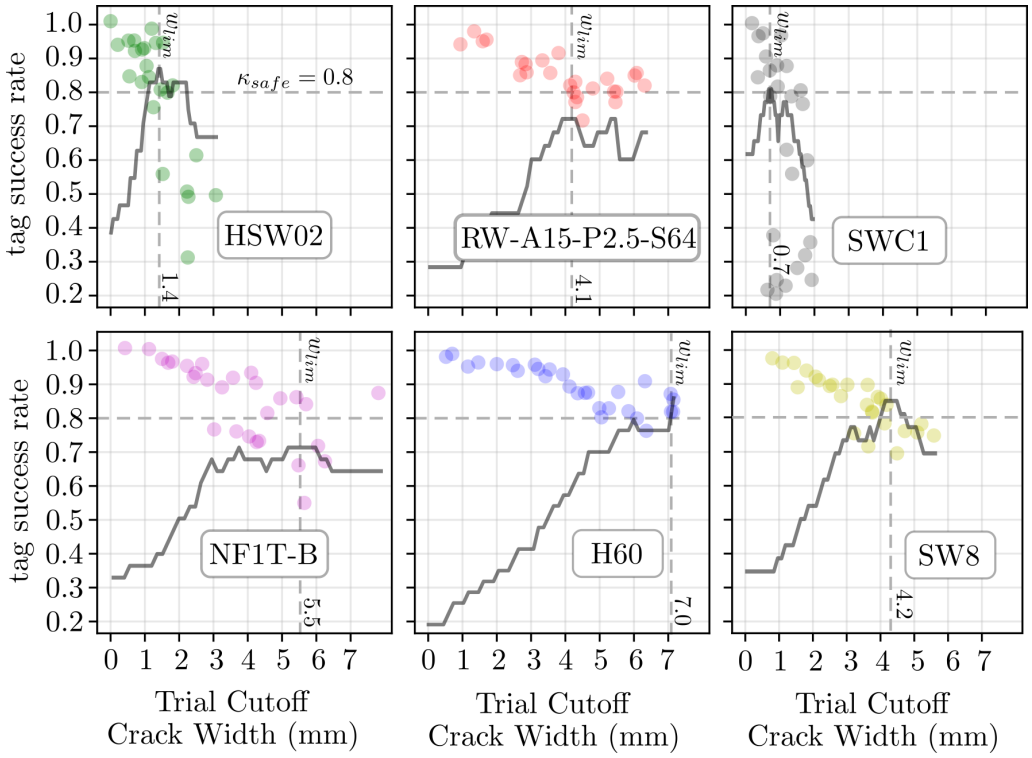

Figure 3.13. Tagging success rate as a means of establishing most reliable guideline for maximum allowable peak crack width

Calculated values of cutoff crack widths (w_{lim}) range from 0.7 mm for wall SWC1 to 7.0 mm for wall H60. It is therefore clear that *crack width inspection triggers cannot be invariant with respect to structural configuration*, as is the case in existing guidelines (see Table 3.1). This same sentiment has been echoed elsewhere [181, 12]. Based on the specimens studied here, it is evident that acceptance criteria for crack widths should, at a minimum, include the effect of axial load ratio. As axial load ratio is already a distinguishing parameter in the ASCE-41 protocol for shear wall drift limits [6], this would be a reasonable first step in advancing visual crack-based inspections.

3.5 Discussion and conclusions

Crack width is easy to measure after damaging earthquakes, and as such, is an obvious proxy for the residual health of a damaged RC component. Yet existing guidelines, which are based on limited experimental observations, disagree about the crack widths corresponding to discrete damage states.

Through simulation, the post-EQ collapse safety of damaged, squat-wall, one-story RC buildings has been assessed as a function of the maximum crack width. Peak shear-crack width experienced during the damaging EQ was shown to be an efficient predictor of collapse safety reduction, and this was leveraged to provide guidance for selecting post-EQ inspection crack width limits. The relative performance framework is general and can be extended to the assessment of various structural configurations in future work.

However, the adopted numerical modeling approach possesses various limitations, not the least of which is the inability to capture residual crack widths or bar pullout. Residual crack width is the damage measure directly observed after a quake, and would ideally be included into a direct crack-based assessment framework in order to represent built-in bar strains, reduced bar fatigue capacity and reduced shear-carrying capacity in the concrete.

Chapter 4

Description of a New Multi-Surface Crack Plasticity Model

This chapter is partially based on the following publication:

W. Galik et al., "A Multi-Surface Plasticity Model for Reinforced Concrete Cracks with Applications to Crack-Based Assessment," *Earthquake Engineering and Structural Dynamics*, 2026. DOI: 10.1002/eqe.70143

Chapter 2 summarized the experimental behavior of individual cracks in plain and reinforced concrete. A review of the testing literature showed that the primary dissipation mechanisms of a crack loaded in mixed-mode conditions are aggregate interlock and friction, both of which degrade with load cycles. In the case of cracks crossed by reinforcement, crack sliding and opening influenced the reinforcement response, which in return, influenced the crack behavior. Also in Section 2.2, existing approaches for modeling individual cracks were briefly reviewed. No single model was found to fully describe the experimental reversed-cyclic crack behavior, in particular with regard to the presence of initial non-zero crack widths and crack-crossing reinforcement. However, the previous modeling attempts demonstrated that convenient mathematical techniques such as damage mechanics and plasticity can be wielded with some success to describe the mechanics at play.

In this Chapter, inspiration is drawn from both damage mechanics and plasticity to propose a novel model for crack behavior that captures pressure-dependency, sliding-induced dilation, stiffness degradation due to

shearing of aggregate particles, strength reduction due to crack widening and loss of effective contact, and configuration-dependent dissipation mechanisms. A multi-surface plasticity approach is adopted to distinguish the yield mechanisms for tensile cracks, shear cracks and mixed-mode cracks, as well as to differentiate the loading behavior from the unloading behavior, whose distinction helps predict the correct pinched hysteresis, as demonstrated in Section 2.2. The aim of the crack model is to describe a crack having:

- a rough, damaged interface, typical of a naturally formed crack;
- a residual crack width (not necessarily zero, as many other models assume);
- non-zero residual stresses;

that is subject to arbitrary loading, of which some useful cases include:

- pure tensile, shear, or compressive loading;
- mixed-mode loading;
- non-proportional loading;
- single-sided cyclic or reversed-cyclic loading;
- arbitrary load reversals.

Scope The model, called henceforth multi-surf-crack-2D, is limited to two-dimensional cracks, and has been developed with rough, natural cracks in mind, though nothing in the formulation precludes its eventual extension to handle smooth or keyed interfaces. Likewise, the model is developed and calibrated for low-cycle, high-damage behavior that is representative of earthquake damage. Little attention is given to high-cycle fatigue, though the eventual incorporation of this behavior could be useful for applications to structures subject to traffic loading.

A note on sign convention Though previous works on the topic treated crack compression stresses as positive, this work adopts a consistent tension-positive and crack-widening-positive sign convention. This helps maintain a consistent formulation, particular when "vectorized". One exception to the rule is that compressive strength is kept as a positive value, so that negative signs do not have to be introduced wherever $\sqrt{f'_c}$ appears, which is often.

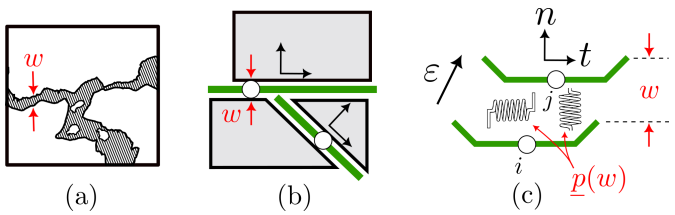

Figure 4.1. (a) real crack with locally varied width and orientation; (b) idealized crack with locally varied width, but global orientation; (c) material point schematic, with parameter group $\boldsymbol{p}$ calibrated in terms of crack width

The multi-surf-crack-2D model is formulated with crack-based assessment in mind so that the model can be initialized from an observation of residual crack width, and the user-input parameters are calibrated in terms of crack width. A schematic of the process for translating a real crack to a numerical model is sketched in Fig. 4.1. All stresses and displacements refer to the crack reference frame, which aligns with global crack orientation. Local variations in the crack contact angle are lumped into semi-physical material parameters, calibrated in a later chapter as a function of crack width. The length of a crack element should be small enough to approximate a uniform interfacial stress state; long cracks, as might form at the base of a shear wall, can be analyzed by meshing many crack elements together. Previous work on crack measurements [168] suggests a discretization no smaller than the maximum aggregate size a_g and up to 4 times the aggregate size to capture random variations of crack geometry.

The remainder of this Chapter develops the material-point description (i.e., constitutive law) for the multi-surf-crack-2D model. The scope of the crack constitutive law—and any constitutive law in general—is limited to calculating the stress increment for a given strain increment; whether or

not the stress increment satisfies equilibrium is managed elsewhere, outside the scope of the material description. In the sections that follow, however, a simple example is developed in tandem with the constitutive law. The example problem consists of a crack crossed perpendicularly by an elastic reinforcement element that is locally de-bonded across the crack. This simple structural assembly (Fig. 4.2) approximates the "real" condition at a crack, where crack formation leads to bond degradation. By weaving the example problem into the presentation of the material law formulation, this Chapter emphasizes that crack response and reinforcement are strongly linked. Additionally, closed-form equations of the simple example problem give insight into the expected effect of the model parameters.

A more formal and condensed description of the consitutive model is provided in Chapter 5, where the finite element implementation is emphasized.

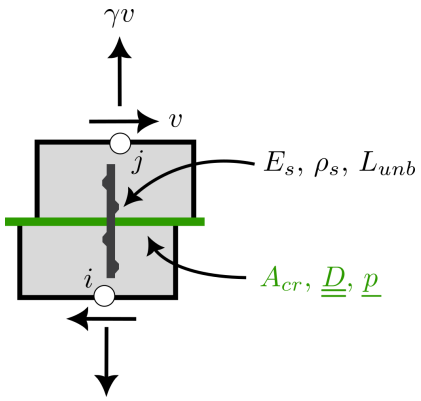

Figure 4.2. Simple example problem, consisting of crack (with stiffness tensor $\boldsymbol{D}$ and parameter set $\boldsymbol{p}$) crossed perpendicularly by locally unbonded reinforcement (with reinforcement ratio ρ_s and Young's modulus E_s), and subjected to shear-proportional loading via load ratio γ

4.1 Crack Model for Monotonic Behavior

Plasticity theory foresees a yield surface that bounds the allowable stress states for each plastic dissipation mechanism. Any stress state exceeding

the threshold cannot be sustained by the material and is returned to the surface boundary in a plastic-strain-inducing process that simultaneously morphs, or hardens, the yield surface. The restriction of material stresses to lie on or within the permissible surface is called the yield criterion and is written formally as:

$$F \leq 0 \tag{4.1}$$

where the yield function F is unique to each material (and process).

In the following subsections, a multiple-yield surface is proposed that is composed of yield surfaces for aggregate interlock, concrete crushing, tensile de-cohesion and sliding activation. Then, a standard state-determination algorithm is implemented for the combined yield surface in parallel with an elastic bar. This simple structural assembly, shown in Fig. 4.2, provides a simple, closed-form "sandbox" for exploring the features of the multi-surf-crack-2D model. More advanced reinforcement laws and configurations can be accommodated (without changing the proposed crack material formulation) by implementing the proposed material model into analysis software. The finite-element implementation of a material point is provided in Chapter 5.

In the following subsections, a naming convention is adopted whereby: plastic variables are indicated by the superscript p; elastic loading and elastic unloading are denoted by the superscripts e and unl; aggregate interlock, tension and compression are indicated by the superscripts lok, t and c. A hat symbol denotes the union of interlock, tension and compression surfaces, which defines generic mixed-mode loading conditions. Activated frictional sliding (more colloquially called "free" sliding) is assigned the superscript act.

4.1.1 Elastic Loading

According to the assumptions of plasticity, a crack develops elastic stress increments for any arbitrary strain increment if the stress state after the imposed deformation lies inside the yield-surface domain. For the crack-bar assembly of Fig. 4.2, a displacement increment $\boldsymbol{\varepsilon} = [\Delta w, \Delta s]$ is imposed between nodes j and i. Assuming, for the simplified problem, rigid concrete between cracks, the imposed nodal displacements correspond identically to the local crack deformation. The elastic deformation is linearly mapped

onto the crack stress vector via the stiffness matrix, as described by Eq. (4.2):

$$\begin{Bmatrix} \Delta\sigma_n \\ \Delta v_{ci} \end{Bmatrix} = \begin{bmatrix} D_{nw} & D_{ns}\text{sgn}(s) \\ D_{tw}\text{sgn}(s) & D_{ts} \end{bmatrix} \begin{Bmatrix} \Delta w^e \\ \Delta s^e \end{Bmatrix} \tag{4.2}$$

Crack stiffness terms are measured in Stress/Length units and have subscripts for mapping onto the normal or tangential stresses the crack width or slip increments. Off-diagonal stiffness terms carry a sgn(s) factor to account for the possibility of load reversals, discussed later. Available expressions for crack shear stiffness D_{ts} indicate a dependence on both crack width and concrete strength [49]. Existing expressions, however, are concerned with initial stiffness and typically do not consider the degradation of shear stiffness with increasing slip. A simple expression for shear stiffness can be constructed so that shear stiffness vanishes if imposed slip exceeds the material roughness scale (in this case the maximum aggregate diameter a_g):

$$D_{ts} = D_{ts,0}\left(1 - \frac{s_{max}}{a_g}\right) \tag{4.3}$$

where the initial stiffness $D_{ts,0}$ is left as a user-input parameter.

Crack normal stiffness D_{nw} depends on whether the crack is opening or closing. In this work, which aims to be valid for cyclic behavior for which a crack may both open and close, an agile definition of normal stiffness is sought. The crack closure model of Ruggiero [153], discussed already in Section 2.3.1, appears suitable. From the crack closure model, the crack normal stiffness can be approximated as (see Section 5.2.1 for a detailed discussion):

$$D_{nw} \approx \frac{f_{cl}}{w_{max}} \tag{4.4}$$

where f_{cl} is the magnitude of compression stress required to close a crack, and w_{max} is the maximum previously experienced crack width throughout the crack's load history.

Inclusion of off-diagonal coupling terms D_{ns} and D_{tw} in Eq. (4.2) is precedented by the contact density model [89], discussed in Section 2.3.1. Physical interpretations of the coupling terms are shown in Figure 4.3.

The stiffness D_{tw} is related to the horizontal projection of the average contact traction, and so its magnitude should increase with crack lateral offset and should vanish if the crack faces are perfectly mated. Conversely, the coupling stiffness D_{ns} describes the flattening of crack interfaces during sliding, which shifts the contact angle into a more vertical orientation.

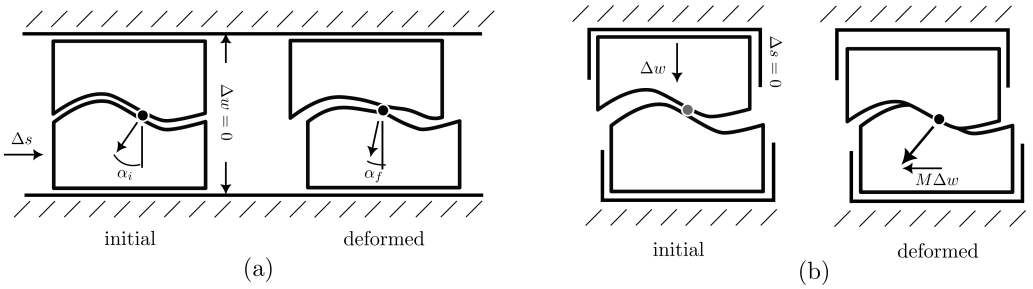

Figure 4.3. Off-diagonal stiffness terms: (a) D_{ns} describes change of crack inclination angles; (b) D_{tw} describes compaction-induced amplification of contact stresses

The plastic nature of the mechanisms sketched in Fig. 4.3 provides an intuitive argument for setting D_{ns} and D_{tw} to zero. Further interpretation of the coupling stiffness terms, including cases for which they should be non-zero, is given in Section 4.2.1.

Enforcing global equilibrium Having obtained in Eq. (4.2) the increment of crack local stresses corresponding to an elastic displacement step (a trivial example of crack-state determination), the material's scope ends and global equilibrium of the crack-bar assembly must be checked/enforced. Equilibrium perpendicular to the crack follows from Calvi et al. [26]:

$$\Delta f_x = \Delta\sigma_n + \rho_s \Delta f_s \tag{4.5}$$

where Δf_x is the increment in applied normal stress, Δf_s is the increment in reinforcement stress and $\Delta\sigma_n$ is the increment in crack-perpendicular traction during the displacement step. For the shear-proportional load configuration of the toy problem, a load ratio γ is defined as the ratio of applied normal-to-shear stress in the crack-aligned axes. Following Calvi et al. [26] and Trost [171], the tensile or compressive sense of the applied normal force does not switch when the applied shear changes sign:

$$\gamma = \text{sgn}(v_{ci}) \frac{\Delta f_x}{\Delta v_{ci}} \tag{4.6}$$

Elastic bar stresses accumulate linearly with crack width according to the following equation, where E_s is the bar stiffness and L_{unb} is the local unbonded reinforcement length, commonly estimated from crack width and bar strain [153]:

$$\Delta f_s = \frac{E_s}{L_{unb}} \Delta w \tag{4.7}$$

Plugging into Eq. (4.2), the "external" crack-perpendicular load corresponding to the imposed displacement is:

$$\Delta f_x = \left(D_{nw} + \frac{\rho_s E_s}{L_{unb}} \right) \Delta w^e + D_{ns} \text{sgn}(v_{ci}) \Delta s^e \tag{4.8}$$

and, in the absence of reinforcement dowel-shear contributions, the required shear stress is:

$$\Delta v = D_{tw} \text{sgn}(v_{ci}) \Delta w^e + D_{ts} \Delta s^e \tag{4.9}$$

The above equations are valid as long as the crack remains elastic. Crack yielding is now introduced.

4.1.2 Onset of Plasticity: Interlock "Yielding"

A crack plastifies when its stresses probe any surface that composes the multiple-surface $\hat{F} = 0$, shown in Fig. 4.4. Depending on the elastic stress path, the onset of plasticity may invoke either tensile-dominated, sliding-dominated, or crushing-dominated deformations. The combined surface $\hat{F}$ is constructed to smoothly transition between the tensile (red), shear (green), and compressive (purple) domains. Each sub-surface is parameterized by v_{cimax}, which serves as a link between each domain. The stress-like term v_{cimax} was defined in Section 2.2.1 as the peak shear transferable by a rough crack. The parameter, which is a function of crack width, sits at the peak of the combined yield surface, effectively controlling its size. This point is labeled the *critical point* in Fig. 4.4. As v_{cimax} evolves during a crack deformation process, the size of the shear yield surface changes, and the adjacent tensile and compressive surfaces are tugged along for the ride. As

can be noted in Fig. 4.4, the overall shape of the combined yield surface may elongate or compress, because the effect of v_{cimax} is different for each sub-surface.

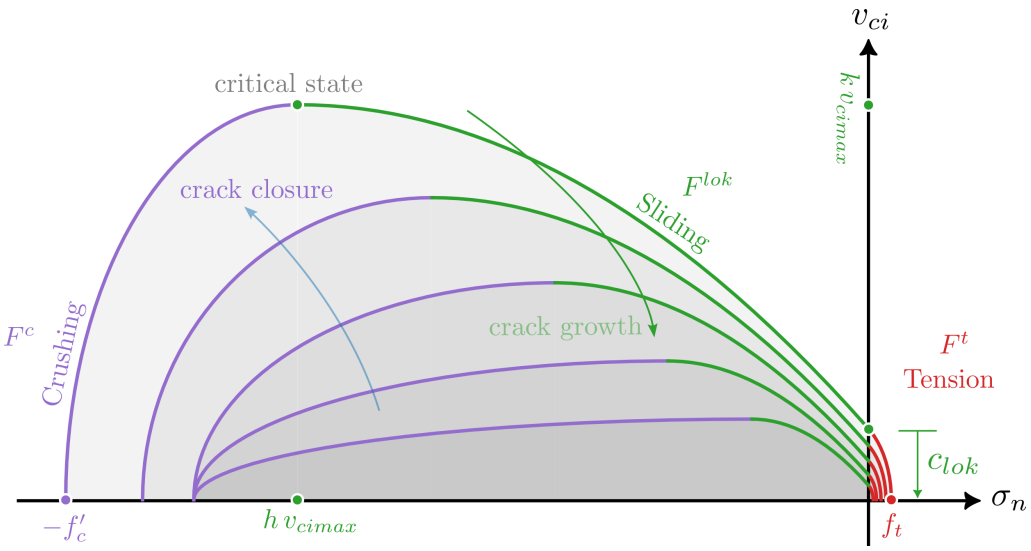

Figure 4.4. Hardening of combined strength criterion $\hat{F}$, which is symmetric about σ_n axis (Note: the sensitivity of f'_c to crack width is exaggerated for illustrative purposes)

The yield function in the sliding domain (green curve in Fig. 4.4) is characterized by Eq. (4.10), which is simply a generalization of Eq. (2.5) to reveal the parabola vertex $(h,\ k)$ in normalized stress space. The superscript *lok* indicates that this function corresponds to classical interlocking behavior, and is restricted to the compressive region $hv_{cimax} \leq \sigma_n \leq 0$:

$$F^{lok} = 4d\left(\frac{|v_{ci}|}{v_{cimax}} - k\right) + \left(\frac{\sigma_n}{v_{cimax}} - h\right)^2 = 0 \tag{4.10}$$

The choice $d = 0.305$ and $(h = -1.0,\ k = 1.0)$ corresponds to Eq. (2.5), the parabola proposed in the original MCFT paper [174] with a cohesion of $c_{lok} = 0.18 v_{cimax}$. Different cohesion values and other critical points can be accomodated by altering d as follows:

$$d = \frac{h^2}{4(k - \chi_{lok})} \tag{4.11}$$

where

$$\chi_{lok} = \frac{c_{lok}}{k\, v_{cimax}} \tag{4.12}$$

is a normalized measure of cohesion.

The tension-dominated (F^t) and compression-dominated (F^c) partial ellipses of Fig. 4.4 are constrained to transition smoothly from the bounds of F^{lok} to the uniaxial strength intercepts, f_t and $-f'_c$ (see Chapter 5 for details of the smoothing process). This constraint is useful for ensuring uniqueness of the multi-surface return-mapping algorithm and leads to the definition of a semi-elliptical strength domain (i.e., "cap") for concrete crushing,

$$F^c = \left(\frac{v_{ci}}{k\, v_{cimax}}\right)^2 + \left(\frac{\sigma_n - h\, v_{cimax}}{-f'_c - h\, v_{cimax}}\right)^2 - 1 = 0 \tag{4.13}$$

and a partial elliptical limit surface governing crack tension:

$$F^t = \frac{2x_c}{c_{lok}}\frac{d}{h}\left(\frac{v_{ci}}{f_t - x_c}\right)^2 + \left(\frac{\sigma_n - x_c}{f_t - x_c}\right)^2 - 1 = 0 \tag{4.14}$$

The center of F^t is horizontally located at $x_c = f_t^2/[2(c_{lok}d/h + f_t)]$.

The uniaxial strengths are weakened by the presence of a crack [21] and can be approximated from experimental data for compressed cracks [122] or tensile cracks [148] as a function of crack width. Together, F^{lok}, F^t and F^c form a continuous and smooth yield surface $\hat{F}$ that shrinks for crack growth and expands for crack closure, as dictated by the hardening parameter $v_{cimax}(w)$. For clarity, Fig. 4.4 omits compressive post-peak behavior, for which the elliptical compression surface F^c would be expected to shrink after reaching f'_c. Crushing and its implications on the combined yield surface $\hat{F}$ are discussed later in Section 4.1.3.2. Strategies for including sliding damage into the yield surface are discussed in Section 4.1.3.1.

4.1.2.1 Plastic Stress Determination Algorithm

When plastic deformations take place, the plastic stresses must be "returned" to the yield surface, which may simultaneously morph as a function

of plastic displacements, or "flow". Standard iterative schemes, called return maps, allow to consistently hit this moving target. As before, the algorithm is demonstrated for the simple crack-bar system of Fig. 4.2.

In the plastic stress-determination algorithm, an elastic trial step is first assumed. Here, a slip increment (Δs) is imposed and the equilibrium crack opening (Δw) of the simple system is approximated from a rearrangement of Eqs. (4.2), (4.6) and (4.8), which assume elasticity of crack and bar:

$$\Delta w^e = \frac{\gamma D_{ts}\text{sgn}(v_{ci}) - D_{ns}\text{sgn}(s)}{D_{nw} + \frac{\rho_s E_s}{L_{unb}} - \gamma D_{tw}\text{sgn}(s)\text{sgn}(v_{ci})}\Delta s \tag{4.15}$$

Eq. (4.15) has the global elastic equilibrium equations already built in, and so corresponds to a linear approximation of equilibrium from the previous converged solution. The objective of the stress-determination algorithm is to determine whether the displacement pair $(\Delta w, \Delta s)$ does indeed produce an elastic stress increment, and if not, identify the stress increment that corresponds to the displacement increment. (Note: in a larger finite element solution, an analogous coordinate pair will be iteratively passed to the material's `setTrialStrain()` subroutine until a global equilibrium solution is found).

Using the elastic prediction, trial stresses are obtained from Eq. (4.2) and $\hat{F}$ is evaluated from Eqs. (4.10), (4.13) or (4.14), depending on which domain σ_n lives in. If $\hat{F} < 0$, the elastic stress assumption was correct and the stress-determination algorithm is trivially completed. Else, the assumption of elastic-only stresses was errant and the stress state must be returned to the yield surface boundary. The return process induces plastic strains (Δw^p, Δs^p) that affect both the material stress state and the yield surface boundary. By defining rules for plastic strain evolution, the plastic incremental strain can be solved such that the material stress "finds" the yield surface boundary at the end of the displacement step. This special balanced state is called the consistency condition: $\hat{F} = 0$.

The material stress, even in a plastic step, is still calculated from Eq. (4.2) using elastic strains, but the elastic strain is no longer identical to the total strain. Elastic and plastic strain components are assumed to be additive, leading to a more general definition of the stress-inducing strain vector as:

$$\begin{Bmatrix} \Delta w^e \\ \Delta s^e \end{Bmatrix} = \begin{Bmatrix} \Delta w - \Delta w^p \\ \Delta s - \Delta s^p \end{Bmatrix} \tag{4.16}$$

Plastic strains are calculated as the product of a flow ratio and a non-negative flow multiplier ($\Delta\lambda$):

$$\begin{aligned} \Delta w^p &= \Delta\lambda \frac{\partial \hat{G}}{\partial \sigma_n} \\ \Delta s^p &= \Delta\lambda \frac{\partial \hat{G}}{\partial v_{ci}} \end{aligned} \tag{4.17}$$

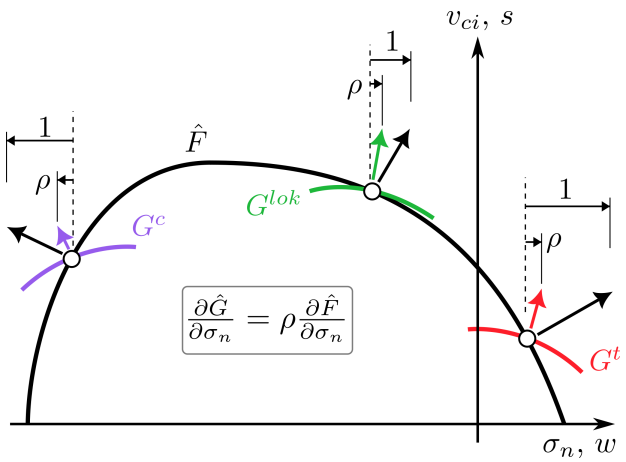

Figure 4.5. Non-associative dilation reduction factor (Note: yield surface and plastic potential surfaces are illustrative)

where $\hat{G}$ is the plastic potential surface corresponding to the combined yield surface $\hat{F}$. Because $\Delta\lambda$ is a scalar, the gradient of $\hat{G}$ indicates the direction of plastic strain accumulation, or the flow direction. The use of $\hat{G}$ in the flow rule indicates that this model is non-associative. Practically, non-associativity aligns with experimental observations—demonstrated in Fig. 2.12—that crack dilation angle diminishes with cyclic loading. Here $\hat{G}$ is assigned the same form as $\hat{F}$ but with a dilation-proportionality factor $\hat{\rho}$ to scale the plastic crack opening. Effectively, $\hat{G}$ is a vertically squashed counterpart to $\hat{F}$. This is written in Eq. (4.18) and sketched in Fig. 4.5.

Note that a single value of $\hat{\rho}$ is assumed to reflect the interlock, compression and tension plastic processes, but could be distinguished for each sub-surface if deemed necessary by future experiments. Note also that $\hat{\rho}$ is related to, but not equal to, the ratio α/ψ plotted in Fig. 2.12, which is defined in terms of the total crack strain increments, whereas $\hat{\rho}$ is defined in terms of plastic crack strain increments.

$$\begin{bmatrix} \frac{\partial \hat{G}}{\partial \sigma_n} & \frac{\partial \hat{G}}{\partial v_{ci}} \end{bmatrix} = \begin{bmatrix} \hat{\rho}\frac{\partial \hat{F}}{\partial \sigma_n} & \frac{\partial \hat{F}}{\partial v_{ci}} \end{bmatrix} \tag{4.18}$$

The plastic multiplier $\Delta\lambda$ is identified by solving the active consistency condition, from among Eqs. (4.10), (4.13) and (4.14). The resulting nonlinear equation for $\Delta\lambda$ is solved iteratively, and permits the calculation of the plastic displacement increments from Eq. (4.17). The stress increments from the partially plastic step, then, are obtained as:

$$\begin{Bmatrix} \Delta\sigma_n \\ \Delta v_{ci} \end{Bmatrix} = \begin{Bmatrix} D_{nw}(\Delta w - \Delta w^p) + D_{ns}(\Delta s - \Delta s^p)\mathrm{sgn}(s) \\ D_{tw}(\Delta w - \Delta w^p)\mathrm{sgn}(s) + D_{ts}(\Delta s - \Delta s^p) \end{Bmatrix} \tag{4.19}$$

The material stress vector after the imposed step lies on the yield surface (as enforced by the consistency condition) and is stored as a temporary solution, relative to the last converged stress $\boldsymbol{\sigma}^{cnvg}$:

$$\begin{Bmatrix} \sigma_n \\ v_{ci} \end{Bmatrix} = \begin{Bmatrix} \sigma_n^{cnvg} + \Delta\sigma_n \\ v_{ci}^{cnvg} + \Delta v_{ci} \end{Bmatrix} \tag{4.20}$$

The material scope terminates by returning the current, temporary stress to the equilibrium manager, where equilibrium is checked. If equilibrium is satisfied, the temporary solution is committed and the analysis advances to the next load or displacement step. If the structure is out of equilibrium, the temporary solution is wiped, and the trial crack width increment is revised and passed to the material's `setTrialStrain()` routine again. For the single crack-bar system, the equilibrium update is given by Eq. (4.21), which follows from combining the flow rule into the crack-perpendicular equilibrium condition. For larger assemblies or more general problems, the elastoplastic stiffness developed later in Section 5.3 should be used for equilibrium iterations.

$$\Delta w = \Delta w^e + \frac{(D_{nw} - \gamma D_{tw}\mathrm{sgn}(s)\mathrm{sgn}(v_{ci}))\frac{\partial \hat{G}}{\partial \sigma_n} - (\gamma D_{ts}\mathrm{sgn}(v_{ci}) - D_{ns}\mathrm{sgn}(s))\frac{\partial \hat{G}}{\partial v_{ci}}}{D_{nw} + \frac{\rho_s E_s}{L_{unb}} - \gamma D_{tw}\mathrm{sgn}(s)\mathrm{sgn}(v_{ci})}\Delta\lambda \tag{4.21}$$

The trial state converges once equilibrium and consistency are simultaneously satisfied. A flowchart for the iterative state-determination is summarized in Fig. 4.6.

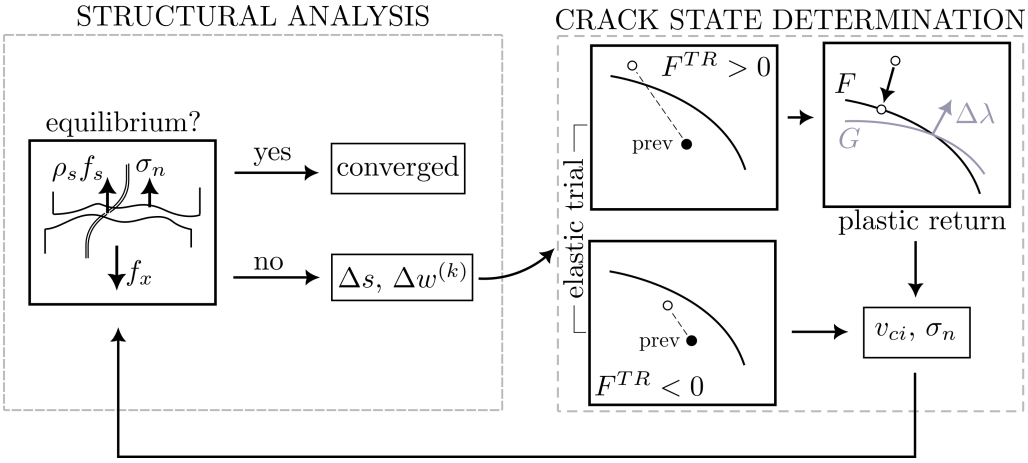

Figure 4.6. Solving a displacement step by simultaneously satisfying equilibrium and consistency

4.1.3 Modifications to MCFT-based Yield Surface

4.1.3.1 Incorporating Sliding Damage

While the form of the normalized yield surface $\hat{F}$ is inspired by the Modified Compression Field Theory, which has been tried and tested for years, the normalizing parameter v_{cimax} can lead to non-sensical results when crack sliding damage is significant, particularly when a crack is completely restrained or clamped firmly: as originally formulated v_{cimax} is only a function of crack opening, and not of crack sliding. This omission seems to have little effect for cracks that simultaneously open and slide, as it is for these cracks that the stress-like hardening term v_{cimax} was calibrated.

In fact, for most cases, this "natural" crack behavior prevails and so little error can be expected. However, for predominantly sliding cracks or for heavily clamped cracks, the width-based hardening rule can overestimate peak strength and predict a prolonged, stiff elastic response.

To improve the predictive power of the crack model, v_{cimax} can be generalized to harden with both crack displacement components. Inspired by early damage mechanics approaches [84], this Thesis uses a scalarized equivalent strain $\tilde{\omega}$ (rather than a tensorial description). One of many possible expressions for the equivalent strain $\tilde{\omega}$ can be derived from observations in Section 2.3.1, where the elastic stiffness matrix of the Contact Density Model [89] was modified (by the Author) to preserve symmetry, required for thermodynamic admissibility of an elastic process. It was found that symmetry is preserved by introducing a sliding displacement term into Li and Maekawa's contact reduction factor K_a. The original formulation of the contact reduction factor, like v_{cimax}, included only a crack-width component. Given the analogy, the modified K_a proposed in Section 2.3.1 is taken as a basis for the equivalent hardening strain $\tilde{\omega}$, as follows:

$$\tilde{\omega} = w + \frac{8 \sin \tilde{\theta}}{3\pi} s_{max} \tag{4.22}$$

where s_{max} is a history variable for the maximum slip previously experienced in either direction, and $\tilde{\theta}$ represents the portion of contact angle between two crack faces that may degrade. The $8 \sin \tilde{\theta}/(3\pi)$ coefficient could be bundled into a new parameter, and in fact, that might be cleaner than what is written. However, retaining the angle in the parameter grouping provides a natural parameter range from 0 to $\pi/2$. That being said, the original meaning of $\tilde{\theta}$ in the Contact Density Model as a contact angle is lost, given the somewhat loose derivation of Eq. (4.22). Rather $\tilde{\theta}$ is treated as a phenomenological parameter.

Equipped with a more complete damage measure, the stress-like hardening parameter v_{cimax} can be re-written by substituting Eq. (4.22) for w, and the form of the yield surface $\hat{F}$ remains unchanged:

$$v_{cimax}(w, s, \tilde{\theta}) = \frac{\sqrt{f'_c}}{0.31 + \frac{24\tilde{\omega}}{a_g + 16}} \tag{4.23}$$

The material parameter $\tilde{\theta}$ can be set to 0 to recover the initial definition

of $v_{cimax}(w)$, or can be calibrated to experimental observations (see Chapter 6).

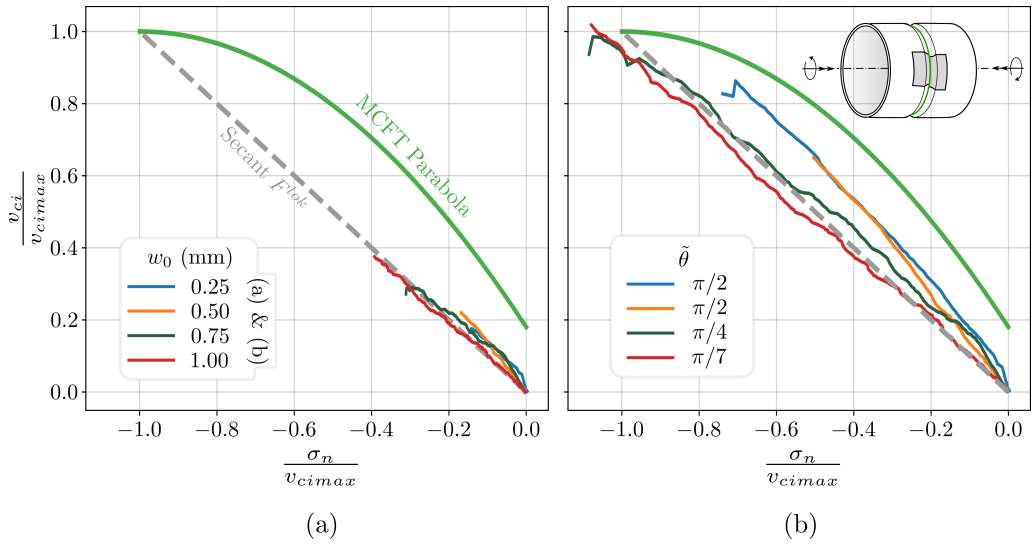

(a) (b)

Figure 4.7. Comparison of v_{cimax} against constant width tests by Becks, et al.: (a) with sliding damage and (b) without sliding damage

The effectiveness of the modified v_{cimax} at predicting the peak interface shear strength is compared to that of the original v_{cimax} in Fig. 4.7 for a series of constant-width experiments performed by Becks, et al. [18]. When the experimental crack stresses are normalized by v_{cimax} without including sliding damage, the F^{lok} surface (which assumes sliding failure to occur at the parabola vertex) overpredicts the shear strength by more than 2.5 times, as seen in Fig. 4.7a. When sliding damage is included according to Eq. (4.23), the shear strength prediction is much closer to reality, as seen in Fig. 4.7b. The average contact angle $\tilde{\theta}$ that gives the best prediction depends on the crack separation.

Inspection of Fig. 4.7 also reveals that the MCFT choice of cohesion $c_{lok} = 0.18k\,v_{cimax}$ contributes, for the specific experimental campaign reported in the Figure, to an over-prediction of the shear for a given clamping stress. A later section investigates the effect of the parabola shape – including the cohesion intercept – on the multi-surf-crack-2D predictions.

4.1.3.2 Incorporating Crushing Damage

An additional modification is made to v_{cimax} to give sensible behavior for plastic compression behavior. The total-width hardening term v_{cimax} predicts a crack to strengthen in shear upon closure. In shear, a narrower crack has more potential contact area, so the strength increase makes sense. The strength increase causes the sliding yield surface F^{lok} to expand (see Fig. 4.4) and, by virtue of continuity between F^{lok} and F^c, the semi-elliptical compression cap F^c is simultaneously tugged outward by crack closure. In the special case of pure compression, however, post-peak *softening* should accompany plastic crack closure (i.e., crushing). As a result, the compression cap surface should not grow, as would be predicted by v_{cimax}, but should shrink as shown in Fig. 4.8. The expected yield surface shrinking can be satisfied by introducing an additional history variable ν to track crushing deformations:

$$\Delta\nu = \frac{\min(0, \frac{\partial \hat{F}}{\partial \sigma_n})}{\frac{\partial \hat{F}}{\partial \sigma_n}} \Delta w \tag{4.24}$$

The crushing strain ν accumulates only when the compression cap F^c is engaged: the horizontal projection of the stress gradient of F^c is negative, and only in this case does Eq. (4.24) not vanish. The rate of post-peak compression softening E_{cp} can be calculated following Coleman and Spacone [41] after specifying the compressive fracture energy and a characteristic length l_{ch}. The compressive strength, reduced by crushing effects, is calculated as:

$$f'_{c,\nu} = f'_c + E_{cp}\,\nu \geq f'_{c,res} \tag{4.25}$$

where $f'_{c,res}$ is a residual (plateaued) compression strength, typically taken as $0.2f'_c$. Recall that f'_c and its variants are positive-valued by convention.

Building on Eq. (4.23), the stress-like hardening variable v_{cimax} is modified to account for crushing damage as:

$$v_{cimax}(\tilde{\omega}, \nu) = \frac{\sqrt{f'_{c,\nu}}}{0.31 + \frac{24\tilde{\omega}}{a_g+16}} \tag{4.26}$$

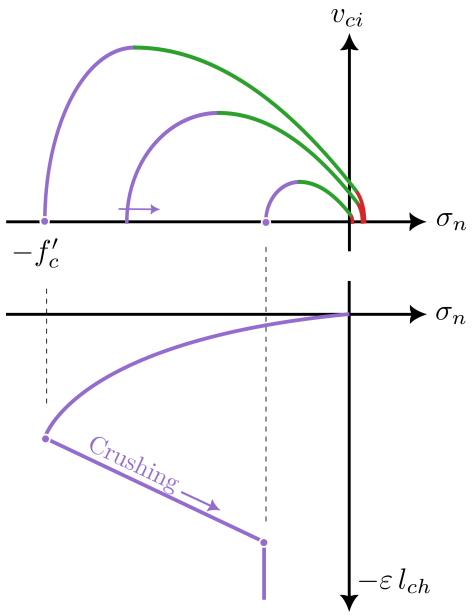

Figure 4.8. Schematic of crushing "hardening", which is active only when the compression-dominant yield surface F^c (purple) is engaged

4.1.4 Monotonic Parameter Study

The basic formulation of the multi-surf-crack-2D model adopted the MCFT parabola (Eq. (4.10)) as the sliding yield function F^{lok} and used the original MCFT v_{cimax} parameter as a stress-like hardening variable. The tension- and compression-dominant yield surfaces are tied to the sliding yield function without requiring any additional parameters. Formulated this way, the monotonic model only requires the selection of only one parameter, $\hat{\rho}$, and as such is user-friendly. Yet, more flexibility has been introduced to handle a wider range of problems, thereby "loosening" some assumptions that are baked into the MCFT parabola. One such assumption, that of width-only softening, was revisited in Section 4.1.3.1 by introducing the sliding damage variable $\tilde{\theta}$ and incorporating $\tilde{\theta}$ into an equivalent strain $\tilde{\omega}$. The parameter $\tilde{\theta}$, measured in radians between 0 and $\pi/2$, describes the degree to which inter-aggregate shearing drives damage.

A second additional model parameter, hinted at in Section 4.1.3.1, is the cohesion ratio $\chi_{lok} = c_{lok}/kv_{cimax}$. Modifying χ_{lok} from the original MCFT value of 0.18 is more aligned with cohesion values adopted by other authors,

making this term a suitable parameter to vary. The other parabola shape parameters h and k are fixed, though these too could be varied if further user-flexibility is desired (future studies on smooth or keyed cracks would likely require a different yield surface shape, which could be controlled by altering the parabola vertex).

This Section uses the simple crack-bar system previously discussed as a sandbox for investigating parameter sensitivity. The system consists of a rough, unit area crack ($f'_c = 40$ MPa, $a_g = 14$ mm, $w_0 = 0.2$ mm) crossed by an elastic reinforcing bar. The reinforcement has a reinforcement ratio ρ_s (fixed at 1%) and a non-zero local unbonded length L_{unb} (varied). The crack is subjected to a shear-proportional, monotonic load process, enacted in displacement (slip) control up to slip magnitude of 10 mm. Crack widths are not constrained, but are free to develop "naturally" to satisfy equilibrium with the clamping reinforcement. Dowel forces in the reinforcement are ignored. Analysis of the crack-bar system is performed using the model description of this Chapter, implemented within the OpenSees framework (For details of the implementation of the multi-surface-crack-2D model in OpenSees see Chapter 5). Throughout the parameter study, discussion is made with reference to crack-based assessment, which will be discussed thoroughly in Chapter 7.

In addition to studying the model parameters ρ, $\tilde{\theta}$ and χ_{lok}, the characteristics of the crack-bar system itself are varied so that the model is tested under a broad set of conditions, as may arise in diverse applications. The load ratio $\gamma = \frac{f_x}{v_{ci}}$ is varied, as is the reinforcement unbonded length. Loading ratios corresponding to pure shear, tension-shear and compression-shear are considered. Attention is also given to the sensitivity of crack response to the choice of elastic crack stiffness, as the crack normal and crack shear stiffness terms are less extensively characterized than for solid concrete. The initial shear stiffness $D_{ts,0}$ is directly accessed as a user parameter, whereas the crack normal stiffness is proxied by the crack closure stress magnitude f_{cl}.

Base Set of Parameters To perform the parameter study, a basic set of parameters is first established. That set of parameters is outlined in Table 4.1, and corresponds to a broad-strokes "best-fit" for a variety of problems, the validation of which can be found in Chapter 6.

In the parameter study, each parameter in the left-most ("Default")

Table 4.1. "Test" matrix for monotonic parameter study

	Default	Investigated Range	Figure
f_{cl}	1.0	$[1.0, 3.0, 5.0]$	Fig. 4.9
$D_{ts,0}$	10.0	$[0.1, 1.0, 10.0, 100.0]$	Fig. 4.10
$\hat{\rho}$	0.65	$[0.15, 0.30, 0.65, 1.00]$	Fig. 4.11
χ_{lok}	0.05	$[0.05, 0.10, 0.15]$	–
$\tilde{\theta}$	0.0	$[0.0, 0.26, 0.52, 0.78]$	Fig. 4.12
γ	0.0	$[-0.5, 0.0, 0.5, 5.0]$	Fig. 4.13
L_{unb}	250	$[100, 250, 500]$	Fig. 4.14

column of Table 4.1 is varie, one at a time. If a parameter is not being varied it assumes its default value. For each investigated parameter a 2-by-2 grid of response outputs is plotted: crack dilation is plotted in the top-left, shear stress vs slip is shown in the bottom-right, stress space in the bottom-right and normal stress vs width in the top-right. Within each subplot three or four curves are plotted that correspond to the values in the right-most column of Table 4.1. The basic parameter set appears as a reference (blue curve) in each each plot.

Sensitivity to crack stiffness The effect of crack normal stiffness D_{nw} is investigated by varying the model parameter f_{cl}, the crack closure stress. According to Eq. (4.4), the closure stress magnitude is proportional to the crack normal stiffness. Ruggiero [153] suggested a closure stress value that increases linearly with crack width, having a minimum value of 2.0 MPa. Figure 4.9 shows that any crack closure stress beyond about 3 MPa has little to no effect of the predicted monotonic crack response. Though not shown, the same trend holds for different load ratios and unbonded reinforcement lengths, meaning that the choice of crack normal stress has little effect on monotonic model predictions as long as a minimum closure stress is enforced. The minimum value suggested by Ruggiero is reasonable. (note: sensitivity of unloading behavior will be discussed in a later section)

The initial crack shear stiffness $D_{ts,0}$ is directly varied between 0.1 and 100.0 MPa/mm. A value of 90 MPa/mm corresponds to the calibration

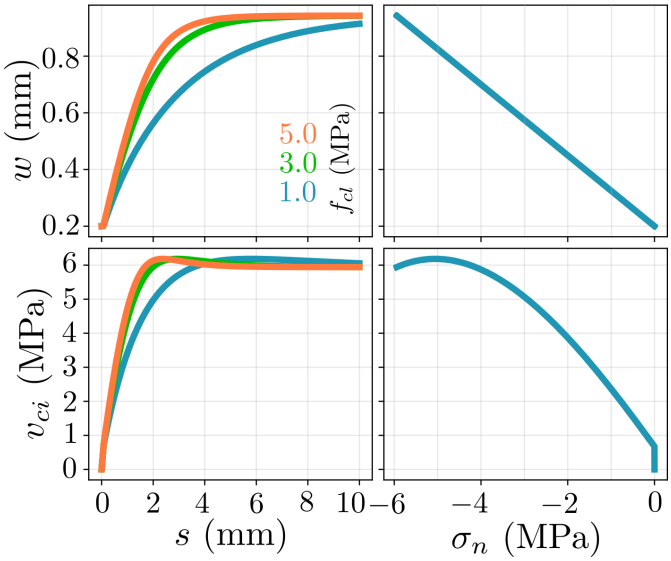

Figure 4.9. Effect of crack normal stiffness

performed by Jacobsen [78] for small cracks, while the equation proposed by Divakar [49] predicts shear stiffness at or below 1 MPa/mm for crack widths exceeding 1 mm. As for the crack normal stiffness it is seen in Fig. 4.10 that the effect of increasing crack shear stiffness saturates beyond about $D_{ts,0} = 10$ MPa/mm. Therefore, a choice between $D_{ts,0} = 1$ and $D_{ts,0} = 10$ seems reasonable.

Sensitivity to material model parameters First, the model parameter $\hat{\rho}$ is investigated. The dilation coefficient indicates how much plastic crack width accumulates, relative to the plastic crack width that would accumulate for an associated flow rule. In essence, $\hat{\rho}$ is a dilation "knockdown" factor. Because concrete typically has a flatter plastic potential surface than yield surface, the dilation coefficient $\hat{\rho}$ assumes values less than 1.0. Four values are considered in Fig. 4.11 where it can be observed that decreasing $\hat{\rho}$ slows frictional dilation, which tempers reinforcement clamping and limits shear accumulation.

The effect of the model parameter $\tilde{\theta}$ is shown in Fig. 4.12 for angles ranging from 0 to 0.78 radians, or 0 to 45 degrees, in 15 degree increments. Sliding damage produces a response that was not apparent in the previous figures. In the blue reference curve without sliding damage, the crack shear

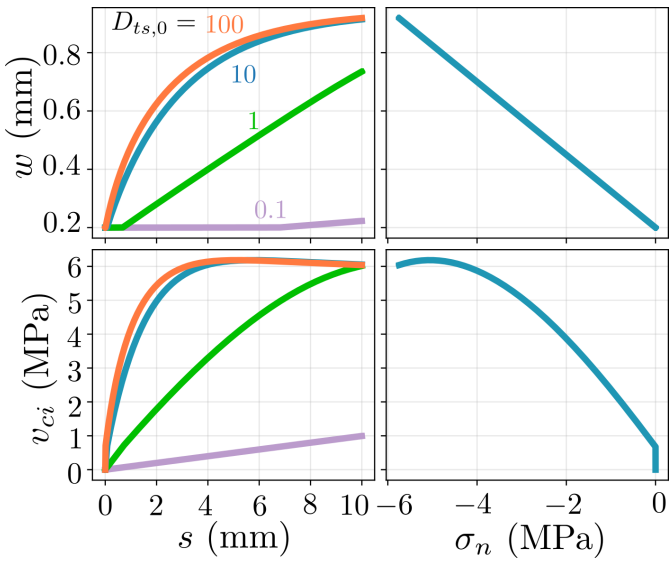

Figure 4.10. Effect of crack shear stiffness

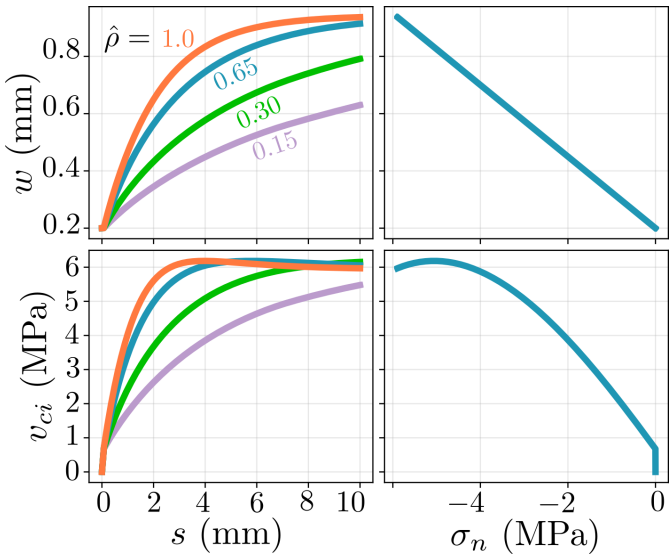

Figure 4.11. Effect of interlock dilation ratio

response is ductile because the crack width accumulation – which drives softening via v_{cimax} – flattens out near the critical point, where the stress gradient approaches vertical. However, when sliding damage is introduced, the yield surface size can shrink even if the crack width is saturated. This

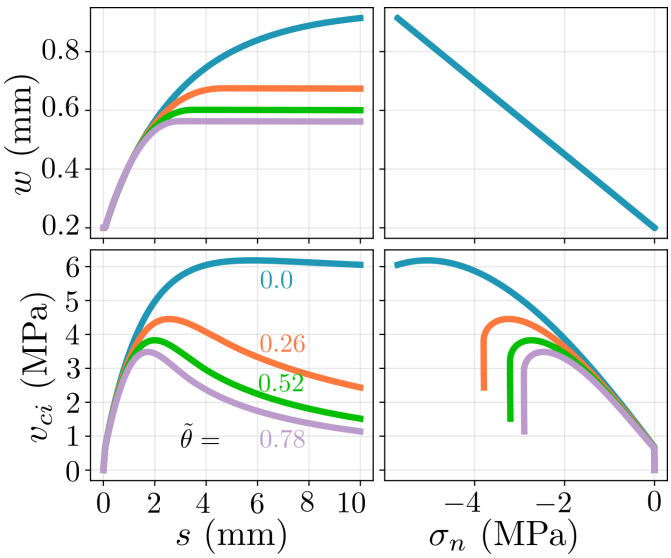

Figure 4.12. Effect of average contact angle. Note 1 radian = 57.3 degrees

effect is notable for the orange, green and pink curves with non-zero $\tilde{\theta}$, which saturate in the dilation plot but continue to soften in stress space. Thus, $\tilde{\theta}$ should be set to a non-zero value if significant post-peak softening response is expected.

While softening behavior commonly arises in constant crack-width tests it is unclear whether it is expected in the field. Being able to estimate $\tilde{\theta}$ will eventually be important for predicting the critical crack that was discussed in Chapter 3. This is clear from Fig. 4.12 for which the inclusion of sliding damage reduces the crack width associated with peak shear capacity.

Sensitivity to load ratio γ As discussed earlier, a primary motivation for developing a new crack model was the desire to unify crack behavior for flexure cracks and shear cracks and to provide a rational basis for developing new crack width guidelines. Accordingly, the response of the crack-bar system is tested for various load ratios. It is noted that the load ratio is not "known" by the crack model, but is rather a helpful construct used here to categorize various load scenarios.

The crack response is plotted in Fig. 4.13 for various load ratios ranging from quite tensile ($\gamma = 5.0$) to pure shear ($\gamma = 0.0$) to slightly compressive ($\gamma < 0$). As expected, a higher load ratio contributes to extra crack opening,

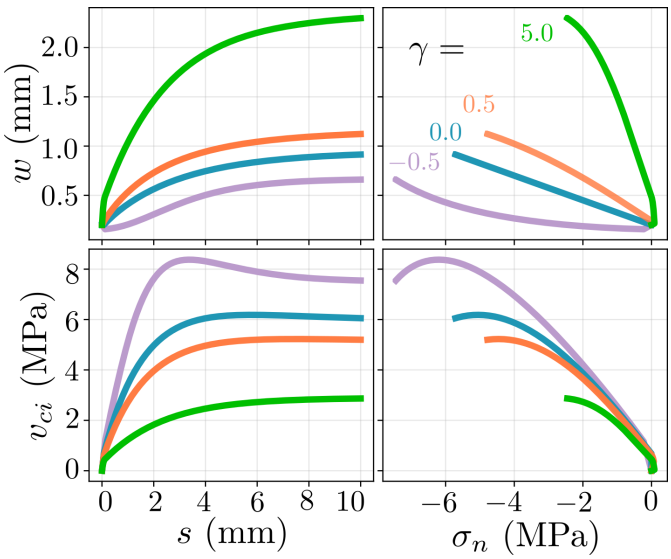

Figure 4.13. Effect of external load ratio

but perhaps unintuitively, even a crack with a primarily tensile external load (see curve for load ratio of 5.0) can develop compressive traction. The compression arises from the clamping part of reinforcement action and vanishes as the load ratio approaches ∞. A second observation from Fig. 4.13 is that cracks crossed by compression are stronger in shear than tensile cracks, but show signs of post-peak softening. Contextualizing in terms of crack-based assessment, it is important to know both the residual crack state as well as the expected loading scenario in order to define rational guidelines for safe crack limits.

Effect of reinforcement unbonded length Upon formation of a crack, local reinforcement bond slip occurs, producing a non-zero unbonded length. In Chapter 2.2, common estimations of L_{unb} were presented for bonded reinforcement. In other applications, reinforcement may intentionally be de-bonded. The crack behavior is similar for the two cases, but less clamping stress is produced for large unbonded lengths. This leads to weaker interfaces. The effect of L_{unb} is shown in Fig. 4.14.

Note: the crack material model does not rely on any inputs for reinforcement properties. Rather, the effect is calculated from equilibrium conditions within the finite-element solver. This does mean that, if directly

modeling cracks, reinforcement in the vicinity of the crack should also be modeled directly, taking care to define the nodal connectivity so that local unbonded length is properly captured. Sophisticated modeling approaches that account for both crack and bar are outlined in Chapter 6.

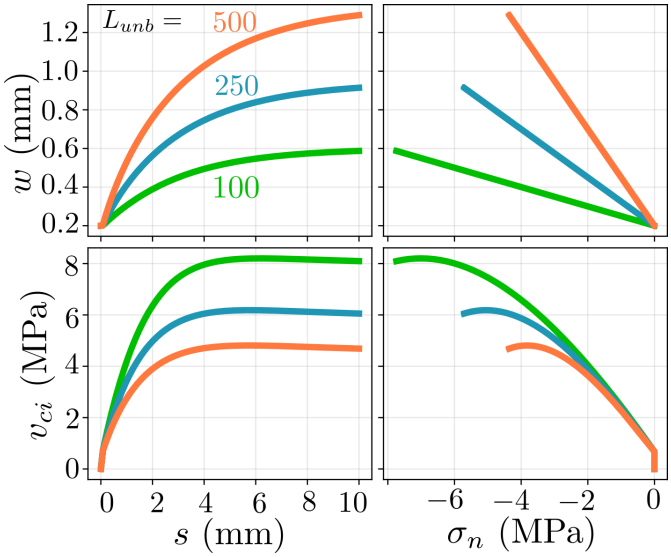

Figure 4.14. Effect of reinforcement unbonded length

Effect of reinforcement yielding To demonstrate the effect of reinforcement yielding on the crack response, Fig. 4.13 is replicated, but the reinforcing bar that crosses the crack is assigned a yield strength of 400 MPa (perfectly-plastic). The result, plotted in Fig. 4.15 demonstrates that shear capacity softens significantly after bar yielding, and that crack widths can grow quite large, even an order of magnitude larger than for the elastic reinforcement case (for the case of slip excursion to 10 mm investigated in this Section).

The crack widths reported for the toy example with yielding are still within the crack width limits suggested by FEMA 306 [59] for shear walls. Since this level of crack width is unlikely to occur without some bar yielding, it will be important to be able to invert the multi-surf-crack-2D model to handle yielded residual bar states when performing crack-based assessment: see Chapter 7.

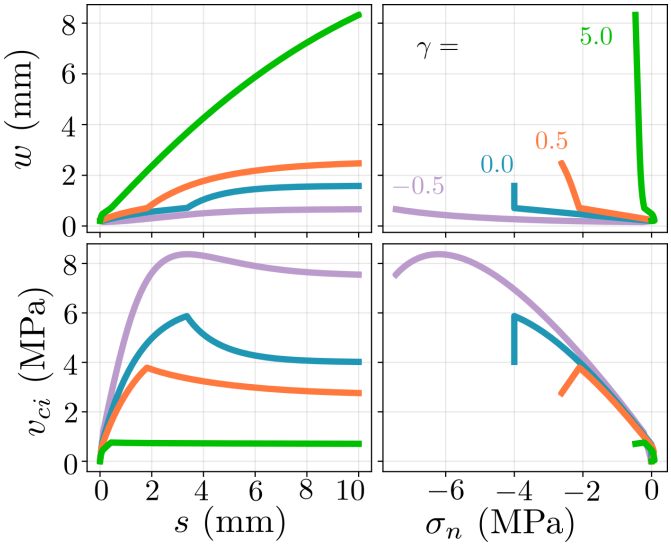

Figure 4.15. Effect of reinforcement yielding

Effect of non-proportional loading and path dependency The cases considered above were all loaded monotonically and proportionally. That is, the load ratio γ was held constant. Here, a particular case of non-proportional loading is considered wherein the interface is clamped or otherwise compressed prior to shear loading. The loading path in stress space, which is shown as Path 2 in Fig. 4.16, starts and ends at the same stress coordinates as the default path (Path 1); yet, Path 2 exhibits a much different response, completely undercutting the yield surface and arriving at the destination in a purely elastic process. While some experimental tests carried out with a Path-2-like protocol exhibit softened nonlinear hardening prior to reaching peak shear strength [165, 49], other experiments remain linear, as predicted by the multi-surf-crack2D model.

Path dependency is studied in more detail in Chapter 6, where the multi-surf-crack2D model is validated against test specimens subjected to various imposed displacement paths.

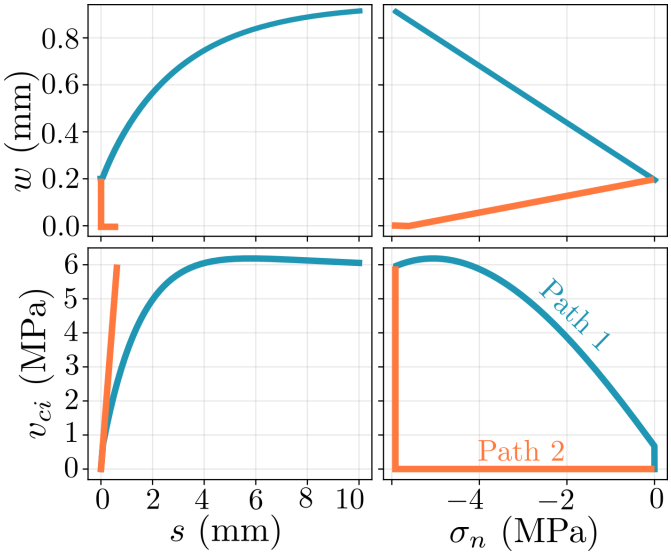

Figure 4.16. Effect of stress path

4.2 Extended Crack Model for Cyclic Behavior

The model presented in Section 4.1 serves as a suitable description of monotonic crack behavior, as it captures dilation, de-cohesion, sliding damage and pressure sensitivity. To extend the applicability of the multi-surf-crack-2D model into the realm of earthquake engineering, cyclic behavior is now introduced.

4.2.1 Elastic Unloading

A crack unloads elastically from the yield surface if an imposed displacement produces an elastic trial stress that lies within the yield surface. Elastic stress increments are calculated from Eq. (4.2), just as for loading, though the unloading stiffness components may differ from their loading counterparts due to asperity mismatch [162]. In particular the shear stiffness in unloading D_{ts}^{unl} does not tend to degrade. Additionally, a non-zero coupling term D_{ns}^{unl} captures the crack's predisposition to close during slip reversal, observed even in the absence of external clamping forces. That the coupling term need be included to reproduce elastic crack closure ($w^e < 0$)

can be seen from inspection of Eq. (4.15) with $\gamma = 0$.

It is noted that, in multiple dimensions, inward motion from the boundary of the yield surface is not sufficient to determine whether the crack is "unloading". For example, a number of possibile load steps exist that bring the stress pair inward from the yield surface, but for which shear increases. For the discussion here, it is assumed that unloading is driven by slip reversal, and corresponds to a decrease in shear magnitude. A more formal treatment of the "loading" and "unloading" cases is discussed in Section 5.6.

4.2.2 Sliding Reversal "Activation"

Elastic unloading, driven by sliding reversal, continues until applied shear forces overcome interface frictional resistance. Typically, shear must reverse beyond zero before initiating plastic slip reversal, hence the name "activation". As can be seen in Fig. 2.12, the activation shear is approximately linear with clamping stress. The proportionality constant between the clamping stress magnitude and the activation shear is derived by Nielsen [124] and shown in Eq. (4.27), where the concrete friction coefficient μ and secant dilation angle α are lumped into a net friction coefficient for the activation process μ^{act}. This effective friction parameter is taken as an independent user-input for the multi-surf-crack2D model. It assumes values lower than the classic concrete friction coefficient μ.

$$\mu^{act} = \frac{\mu - \tan(\alpha)}{1 + \mu \tan(\alpha)} \tag{4.27}$$

As a crack closes during slip reversal, rubble buildup slightly impedes sliding and provides a non-zero cohesion c_{act}. For lack of experimental characterization, c_{act} is assumed proportional to v_{cimax} via a proportionality factor χ_{act} as shown in Eq. (4.28):

$$c_{act} = \chi_{act} k v_{cimax} \tag{4.28}$$

Together, the frictional behavior characterized by μ^{act} and the cohesive limit behavior of Eq. (4.28) define a hyperbolic yield surface for activation of plastic reversal (F^{act}), given in Eq. (4.29).

$$F^{act} = \frac{|v_{ci}|}{\sqrt{1 + \left(\frac{\mu^{act}}{c_{act}}\sigma_n\right)^2}} - c_{act} = 0 \tag{4.29}$$

While the proportionality factor χ_{act} is not necessarily equal to the cohesion proportionality factor χ_{lok} for interlocking, if the two are equated, the activation surface is tied to both the interlock surface F^{lok} and the tensile surface F^t at the cohesion point. This case is depicted in Fig. 4.17. (Note that unloading from the positive interlock surface from Fig. 4.4 will skip over the positive activation surface shown in Fig. 4.17 and instead engage with its mirror image. Again, this is due to the "activation" nature of reversal. Rules for loading/unloading behavior will be provided in Section 5.6).

Because crack unloading typically involves crack closure, the reinforcement clamping stress decreases during the activation process and the crack normal stress σ_n grows less compressive during the reversal process. Simultaneously, a gradual "lifting" of the cohesion intercept takes place due to proportionality of cohesion with v_{cimax}, which increases for crack closure. The result in stress space is a curve that evolves between the two (orange) bounding curves of Fig. 4.17. The exact process evolution depends on the plastic flow accumulation.

Plastic flow, written in Eq. (4.30), develops perpendicular to the plastic potential surface G^{act}:

$$\begin{aligned} \Delta w^p &= \Delta\lambda \frac{\partial G^{act}}{\partial \sigma_n} \\ \Delta s^p &= \Delta\lambda \frac{\partial G^{act}}{\partial v_{ci}} \end{aligned} \tag{4.30}$$

The plastic potential function for activation, analogous to Eq. (4.18), is proportional to the activation yield surface F^{act} by a dilation factor $-\rho^{act}$ that scales the yield surface vertically. However, unlike the interlock plastic potential function, the activation plastic potential function is a mirrored version of the yield function. The mirror operation introduces a negative sign in Eq. (4.31) that marches the plastic stress state toward the origin of the hyperbolic yield surface. The opposite "sense" of activation flow also shows up experimentally, e.g., Fig. 2.12b.

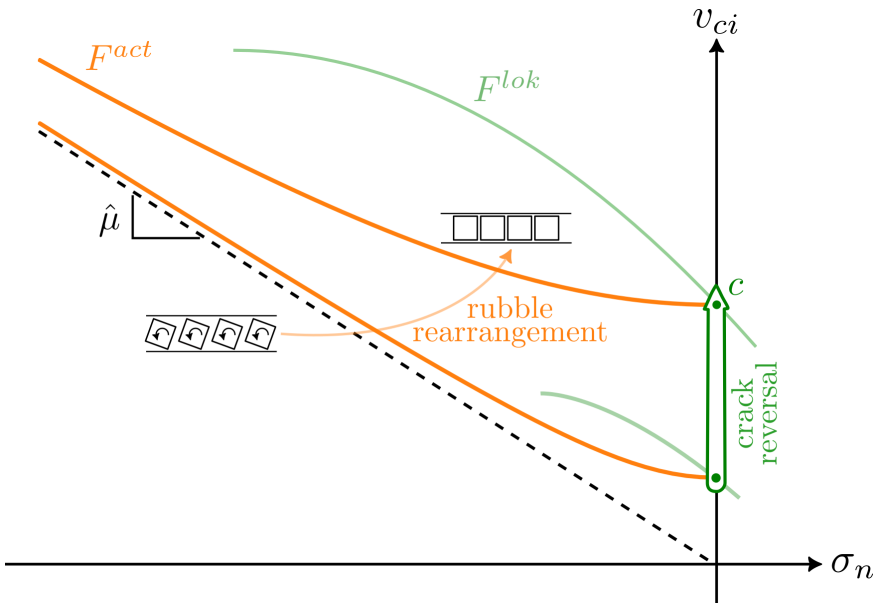

Figure 4.17. Strength criterion for activation reversal F^{act} (symmetric about σ_n axis). Note that the top half of the activation surface shown corresponds to reloading from interlocking in the negative direction

$$\left[\frac{\partial G^{act}}{\partial \sigma_n} \quad \frac{\partial G^{act}}{\partial v_{ci}}\right] = \left[-\rho^{act}\frac{\partial F^{act}}{\partial \sigma_n} \quad \frac{\partial F^{act}}{\partial v_{ci}}\right] \tag{4.31}$$

The plastic potential surface for reversal activation is shown in Fig. 4.18 for a converged state $\boldsymbol{\sigma}^{(n)}$. The figure also demonstrates how the plastic flow direction (orange arrow) favors a forward marching process.

The plastic reversal process continues marching down the activation surface until aggregate particles re-engage in the opposite direction.

As was done for interlocking, a nonlinear solution algorithm (see Return Mapping Algorithm in Section 5.7) can be implemented to find the plastic flow magnitude $\Delta\lambda$ that returns the plastic stress state to the yield surface for a given displacement step. If many reversal steps occur sequentially, a plastic process develops, that terminates when the combined interlocking surface is breached or when the crack reloads elastically away from the hyperbolic activation yield surface.

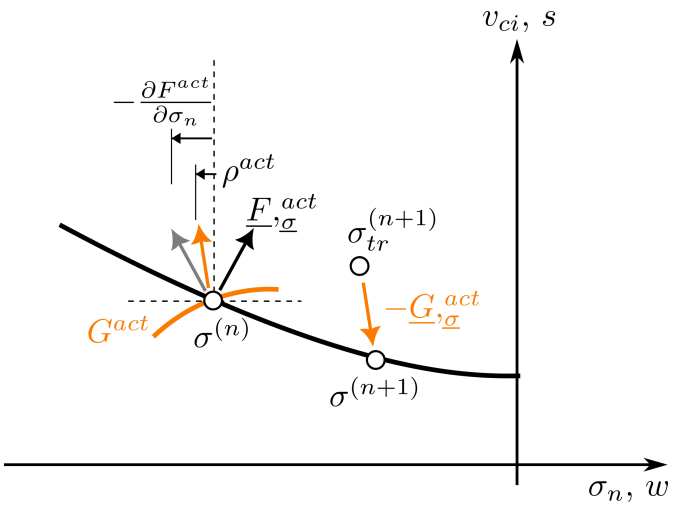

Figure 4.18. Plastic potential surface (orange curve) for activation, defined so that its gradient, the flow direction $\frac{\partial G^{act}}{\partial \boldsymbol{\sigma}}$, favors a forward return direction

4.2.2.1 "Activation" Parameter Study

The effect of model parameters for the unloading phase are examined for the same crack-bar system investigated in Section 4.1.4. The crack-bar assembly (with default monotonic parameters from Table 4.1) is first loaded in sliding control up to a slip offset of 10 mm. During the loading phase, the unloading parameters have no effect and the curve is identical to the blue curve in Figs. 4.9-4.15. Then, the crack is unloaded to zero residual slip. The initial shear stiffness $D_{ts,0}$ is assumed to be undamaged during the unloading process and the effects of model parameters ρ^{act}, μ^{act} and χ^{act} are investigated. Additionally, various choices of the off-diagonal stiffness terms are studied, based on the aforementioned observation that their omission leads to unrealistic dilation loops (it will be demonstrated in Section 5.5 that including the off-diagonal terms during unloading can lead to a more thermodynamically-robust unloading process). The off-diagonal stiffness terms are constrained to equal one another in the elastic domain so that a symmetric elastic stiffness matrix is retained and the model does not generate energy during elastic cycles.

In plotting the results of the parameter study in the following figures, the loading portion of the curve, corresponding to the default set of parameters

Table 4.2. "Test" matrix for activation parameter study

	Default	Investigated Range	Figure
ρ^{act}	1.0	$\left[0.5, 1.0, 3.0, 5.0\right]$	Fig. 4.19
μ^{act}	0.4	$\left[0.1, 0.2, 0.4, 0.6\right]$	Fig. 4.20
χ^{act}	0.05	$\left[0.01, 0.05, 0.10, 0.15\right]$	–
$D_{ns} = D_{tw}$	-1.0	$\left[0.0, -1.0, -2.0, -5.0\right]$	Fig. 4.21

in Table 4.1, is overlaid in grey.

Effect of activation dilation parameter ρ^{act} The primary effect of changing the dilation parameter ρ_{act} is to change the amount of crack width that is recovered during the sliding reversal process, as shown in Fig. 4.19. This also changes the shape of the dilation loop. Evidently, a value of ρ^{act} that is too high will create an un-naturally fat loop, while a low dilation leads to very little width-recovery. Also from Fig. 4.19 there appears to be a saturated amount of crack width recovery that cannot be exceeded. This value depends on unloading stress $\boldsymbol{\sigma}$ and the crack compliance $\boldsymbol{C}$. A final observation is that larger values of ρ^{act} accelerate the stress state toward the cohesion intercept. Physically, the tendency of large ρ^{act} to alleviate residual stresses and close the crack aligns with the expected effect of rubble consolidation. Whether or not the value of ρ^{act} is positively correlated with the amount of inter-crack rubble will need to be borne out of future experiments.

Effect of unloading friction μ^{act} The primary effect of altering the unloading friction coefficient μ^{act} is to alter the shear stress at which plastic reversal initiates. A secondary effect is to alter the rate at which crack width recovers with each slip reversal increment. Evidently a large unloading friction leads to increased crack closure and significant alleviation of residual stresses. This is similar to the effect of the dilation parameter in displacement space, but leads to a fuller path in stress space.

Effect of unloading cohesion χ_{act} Like χ_{lok}, there is nearly no effect from changing χ_{act}.

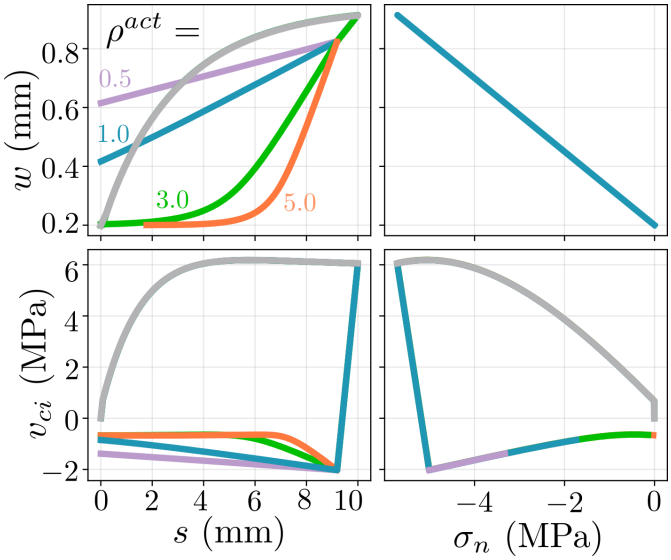

Figure 4.19. Effect of activation dilation parameter on unloading

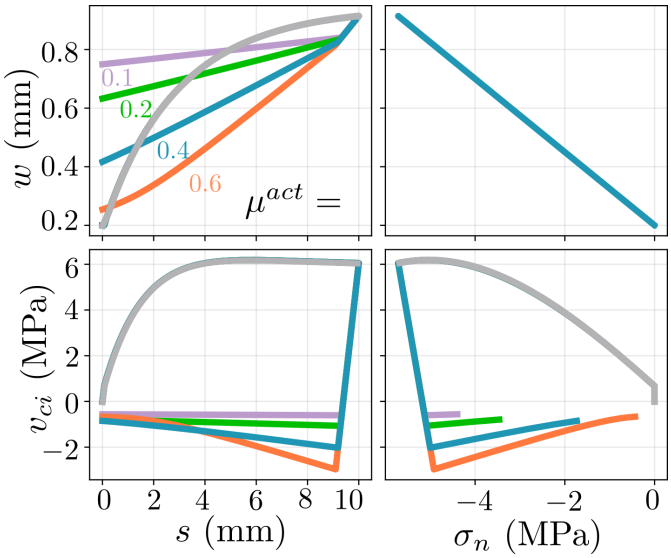

Figure 4.20. Effect of unloading friction coefficient on unloading

Effect of off-diagonal stiffness Inclusion of the off-diagonal stiffness terms during unloading serves the main purpose of creating realistic unloading displacement loops. For the pure shear case shown in Fig. 4.21, the omission of D_{ns} (pink curve) leads to a flat elastic portion of the

unloading loop, which is not observed experimentally. The addition of minimal coupling stiffness appears to resolve the issue. As the off-diagonal terms grow in magnitude, the stress-space portion of the response becomes unrealistically shallow (compared with experimental results from Chapter 2.2), even risking overshooting the activation yield surface altogether. In light of this, very small values are recommended for D_{ns} and D_{tw}. More precise recommendations are given in Chapter 6 after validation against specific examples.

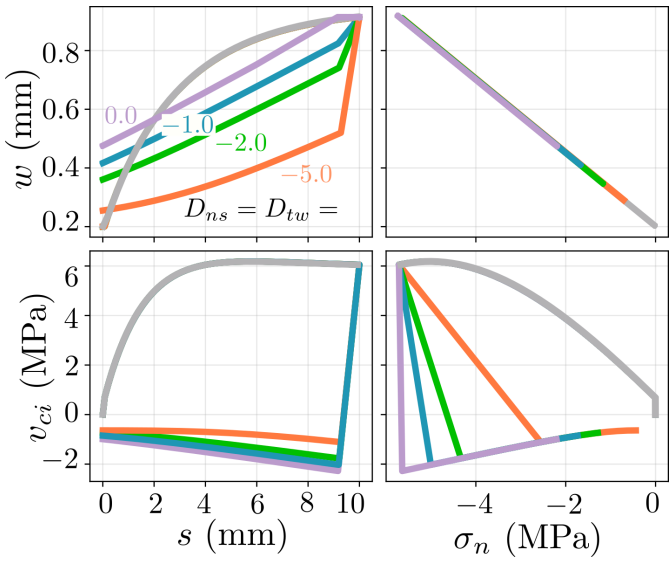

Figure 4.21. Effect of off-diagonal stiffness

4.2.3 Continued Cycling

Some attention is now given to the effect of repeated cycling on the crack behavior.

4.2.3.1 Cyclic Sliding Damage

Some cyclic sliding damage is already built into the stress-like hardening parameter v_{cimax}, which captures the effects of crack separation (both sliding and opening are captured by the $\tilde{\omega}$ parameter) and crack crushing (through the ν parameter) on the *size* of the multiple-yield surface. For instance,

if crack width does not fully recover after a cycle, as is typically the case, a strength reduction is natively reflected in v_{cimax}, which normalizes the combined yield surface. However, being a size parameter, v_{cimax} by itself is insufficient to capture the *shape* change induced by cycles, evident in the experimental review of Chapter 2.2: repeated cycles lead to severely pinched hysteresis loops that also exhibit ratcheting as cyclic displacement magnitudes grow. Both pinching and ratcheting are incorporated into the model subsequently.

Ratcheting Results from the testing literature indicate that aggregate interlock does not re-commence until crack slip has reversed beyond $s = 0$. The re-engagement slip increases with cycling and contributes to the ratcheting phenomenon that is characteristic of cyclic crack sliding. Inspiration is taken from the phenomenological Ibarra-Medina-Krawinkler model [77] to model the engagment point (or "break" point, as it is called by Ibarra, Medina and Krawinkler) as being proportional to the maximum experienced plastic slip, s^p_{max}:

$$s_{brk} = \zeta s^p_{max} \tag{4.32}$$

where ζ is a model parameter indicating how much aggregate re-engagement is delayed due to previous sliding damage and particle breakage.

Pinching To reflect the cycling-induced shape change of the combined interlock yield surface, the $\hat{F}$ parabola can be generalized so that shape parameters k (shear strength) and χ_{lok} (cohesion) are functions of a cyclic roughness parameter r that ranges between 0 for a smooth crack and 1 for a rough crack, independently in the forward (+) and reverse (−) directions. The crack roughness varies throughout loading as a function of crack slip, according to the hypothesis that a crack will be "rough" if it is excavating new territory and will be "smooth" if it is repeating slip magnitudes already covered. In other words, if a crack is pushed to a larger slip than previously experienced ($s \geq s_{max}$, where s_{max} is calculated independently for the forward and reverse directions), protruding aggregates engage with new particles and the crack effectively roughens (i.e., $r \to 1$). An interpolation function is defined in Eq. (4.33) to calculate the roughness r as a function of a user-input κ, which controls the rate at which roughness recovers with

increasing slip. The family of functions described by Eq. 4.33 is shown in Fig. 4.22a.

$$r^{\pm} = \frac{\frac{s}{s^{\pm}_{max}}(1-\kappa)}{\kappa - 2\kappa\frac{s}{s^{\pm}_{max}} + 1} \tag{4.33}$$

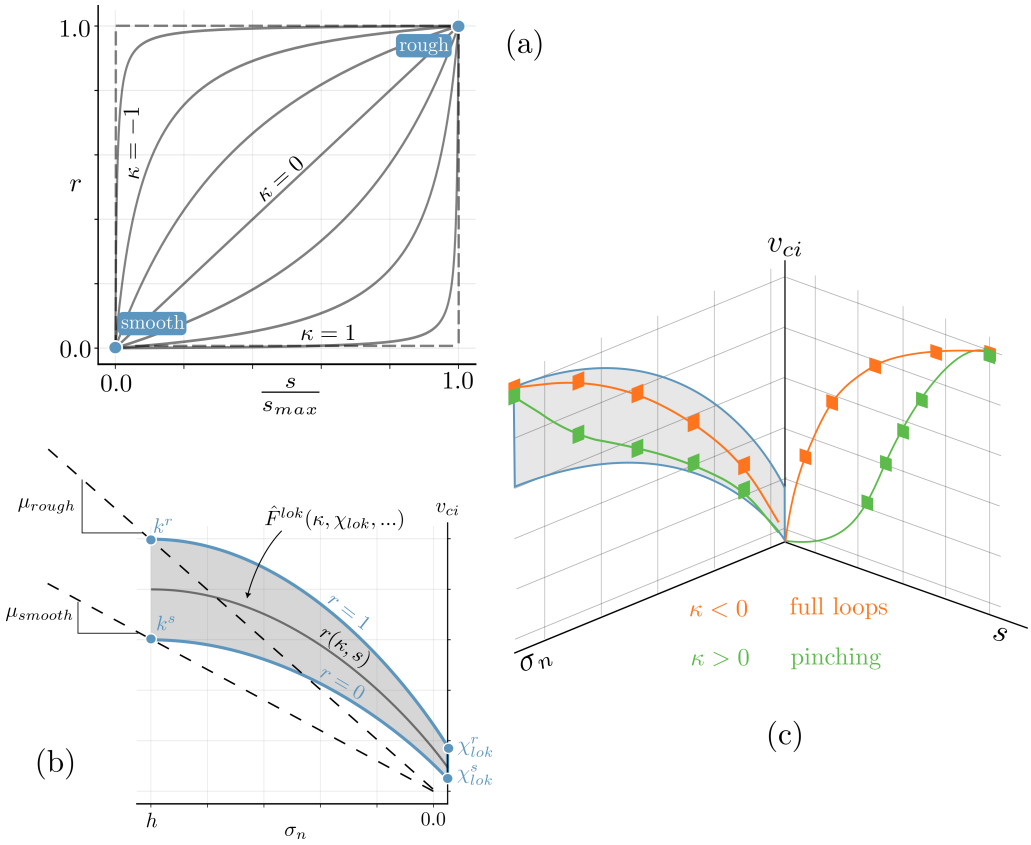

Figure 4.22. Crack roughness interpolation function for simulating pinched response throughout cyclic loading

Physically, r reduces the cohesion and shear strength magnitude during sub-critical cycles. The strength and cohesion are linearly interpolated between smooth and rough bounding values via the roughness parameter:

$$k = k^r\, r(\kappa) + k^s\,(1 - r(\kappa)) \tag{4.34}$$

$$\chi_{lok} = \chi^r_{lok} r(\kappa) + \chi^s_{lok}(1 - r(\kappa)) \tag{4.35}$$

where k^r and χ^r_{lok} characterize the rough, undamaged crack, and k_s and χ^s_{lok} characterize the smooth, damaged crack. Reasonable choices for k^r and k^s are 1.0 and 0.6, to align with the secant friction coefficients of the ACI code [2]. Meanwhile, χ^r_{lok} equals the user-input value for χ_{lok} and χ^s_{lok} can be taken as the user-input for χ_{act}, which is constant. This choice helps prevent overlap of the combined interlock surface $\hat{F}$ and the activation surface F_{act}.

The bounding parabolas of Fig. 2.12 are recovered with the values: $k_r = 1$, $\chi^r_{lok} = 0.18$, $k^s = 0.6$ and $\chi^s_{lok} = 0$, also noting that d is updated as a function of the three independent shape parameters in Eq. (4.11). For sub-critical cycling the generalized parabola F^{lok} is bounded by these equations and lives within the shaded region of Fig. 4.22b, based on the current value of $r(\kappa)$. From Fig. 4.22b, it is evident that the form of the sub-critical interlocking parabola does not change, but is merely scaled by the intermediate interpolation function. In this way, the model describes the apparent shape change without unnecessary modifications to the basic form of the yield surface. Figure 4.22c shows that severe pinching can be obtained for high κ values and full hysteresis loops can be obtained for low κ values. The κ parameter is bounded by -1 and 1.

It is noted that, while the preceding discussion focused on the shear-dominated parabolic yield surface, the cap surfaces $F^c(k, ...)$ and $F^t(\chi_{lok}, ...)$ are also scaled to maintain continuity with F^{lok}, thereby preserving the smoothness of the multi-yield surface.

4.2.3.2 Cyclic Parameter Study

To visualize the effect of the two cyclic parameters ζ and κ during repeated cycles, the two parameters are systematically varied wihtin the context of the toy problem previously discussed, while the remaining model parameters are held constant at their default values defined in Tables 4.1 and 4.2. The considered cyclic protocol, representative of many experimental programs, consists of 3 repeated cycles at a slip magnitude of 5 mm. The κ parameter, which controls the fullness of the shear hysteresis loops, is varied from -1 to 1. The ζ parameter, which has a recommended value of 0.5 [77] is varied from 0.2 to 0.6.

Table 4.3. "Test" matrix for cyclic parameter study

	Default	Investigated Range	Figure
ζ	0.4	$[0.2, 0.4, 0.6]$	Fig. 4.23
κ	-1.0	$[-1.0, 0.0, 1.0]$	Fig. 4.24

Effect of engagement slip ratio ζ The slip re-engagement parameter ζ serves to prolong the activation process, which delays the onset of aggregate interlock, evident in the plot of shear stress vs slip in Fig. 4.23. An unexpected consequence of large ζ values is that crack closure continues during activation, even after slip has switched sign and begun to increase. The result is significant flattening of the crack trajectory for repeated cycles. This effect was previously observed, though it was muted, in the experimental review of Chapter 2.2.

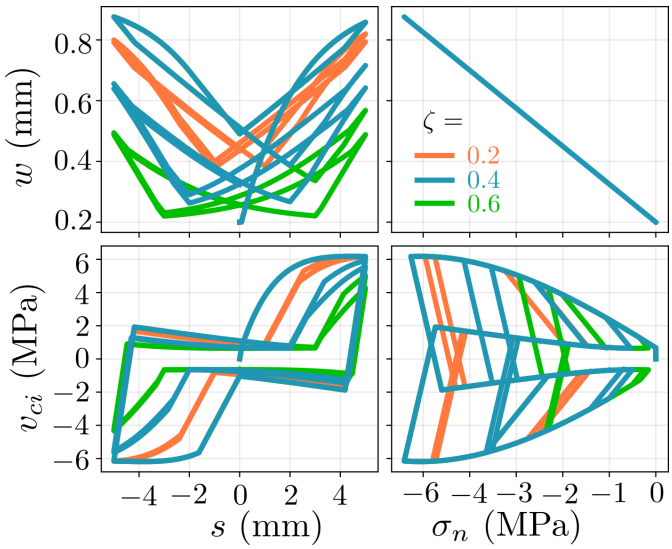

Figure 4.23. Effect of crack re-engagment parameter

Effect of shape change parameter κ The shape parameter alters the fullness of the hysteresis loops for repeated cycles, as shown for the full range of κ values in Fig. 4.24. As κ increases away from its default value of

−1, less shear is mobilized by aggregate interlock. This result mirrors the trend observed by the experiments of Tassios [165].

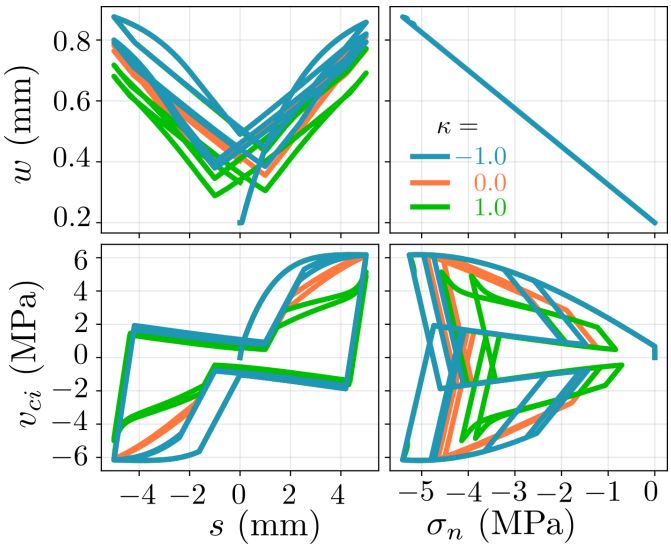

Figure 4.24. Effect of shape parameter

Though each model parameter has been varied in a systematic manner in Sections 4.1.4, 4.2.2.1 and 4.2.3.2, the parameter studies have been done against the backdrop of a default parameter group, selected because it produces reasonable, recognizable crack behavior. Many other behaviors can be obtained with the multi-surf-crack2D model, but have not been explored here because the full parameter space is far too vast to permit a complete characterization. Later, in Chapter 6, more tangible guidance is provided for selecting the parameters of the multi-surf-crack2D model, based on results of an extensive validation program.

4.3 Discussion and conclusions

The multi-surf-crack2D model described in this Chapter has been developed for arbitrarily loaded cracks, and as such provides a general basis for applications that require an agile crack model. Indeed, the model is ideally suited for one such application, crack-based assessment, as the model is completely parameterized by v_{cimax} which itself is a function of

the crack residual deformations. Thus, along with a small number of user-defined parameters, the difficult-to-determine residual crack state can be established, from visual observations alone. In order to analyze more full-scale structural damage with the multi-surf-crack2D model—and to establish the effect of cracking damage on future structural performance—the model must be implemented into a finite element environment. The details of the implementation are described in Chapter 5. But first, the model parameters are summarized and some limitations and future enhancements are discussed.

Summary of multi-surf-crack2D model parameters

The model parameters are summarized in Table 4.4.

Table 4.4. Summary of model parameters

Parameter	Description	Unit	Equation
Monotonic			
$\hat{\rho}$	Interlocking dilation "knockdown"	–	Eq. (4.18)
χ_{lok}	Interlocking cohesion ratio	–	Eq. (4.12)
$\tilde{\theta}$	Contact angle for sliding damage	rad.	Eq. (4.22)
Reversal			
ρ_{act}	Reversal dilation factor	–	Eq. (4.31)
μ_{act}	Unloading friction constant	–	Eq. (4.27)
χ_{act}	Rubble buildup cohesion	–	Eq. (4.28)
Cycling			
ζ	Aggregate re-engagment factor	–	Eq. (4.32)
κ	Cyclic roughness factor	–	Eq. (4.33)
Elastic Stiffness			
f_{cl}	Crack closure magnitude	MPa	Eq. (4.4)
$D_{ts,0}$	Initial shear stiffness	MPa/mm	Eq. (4.3)

Comments, limitations and future improvements of the mult-surf-crack2D model

Initial crack width Currently, a residual crack width is incorporated in the multi-surf-crack2D model by adding a "free" strain offset. Future work will deal with the possibility of residual stress states corresponding to a non-zero built-in crack width.

Fatigue damage Because elastic stiffness is constant, the multi-crack-surf2D model does not capture energy dissipation for sub-critical elastic cycles, and is therefore not suited to high-cycle fatigue damage. This feature could be incorporated by improving the elastic stiffness approximation. This is discussed in Section 5.2.

Equivalent kinematic and isotropic hardening In theory, the multi-surf-crack2D model can be assigned equivalent kinematic and isotropic hardening springs, then framed within a more general framework. However, the hardening of v_{cimax} induces both isotropic hardening as the size of the interlocking parabola changes, and kinematic hardening as the vertex of the parabola translates. When untangled from one another, the kinematic and isotropic hardening laws are unwieldy. As such, the kinematic-isotropic hardening split, though present, proved an inconvenient basis for representing the plastic crack processes.

Stress locking A potential issue with the current form of v_{cimax} is that it predicts excessive shear strength for wide cracks. In the limit that the crack width approaches the aggregate diameter a_g, one would expect the interface to shed all shear-transfer capacity due to loss of contact. This limit behavior is not built into v_{cimax}, which was calibrated for small width specimens tested by Walraven [176]. For practical problems when the crack width remains small relative to the aggregate size, no issue is encountered. However, crack widths may in some cases approach the aggregate diameter, and for these cases a more realistic limit behavior would be desired.

Complicated stress paths It has been seen that the multi-surf-crack2D model may predict excessive elastic behavior for stress paths preceded by a compressive pre-load. In the particular case of pure compression

followed by pure shear, it was shown in Fig. 4.16 that the multi-surf-crack2D model could not predict post-yield hardening, even though some hardening is observed experimentally for these boundary conditions [165], [49]. A possible remedy would be to treat the current yield surface $\hat{F}$ as an enclosing limit surface, with an additional interior surface $\hat{F}_0$ that hardens non-linearly up to the bounding surface. This approach would mimic the two-staged hardening laws of Lin and Bazant [91].

A framework for handling two-staged hardening is sketched in Fig. 4.25. The interior surface represents the onset of nonlinearity and would need to be fit from experiments, such as shear friction tests performed at constant normal stress. Continued loading beyond $\boldsymbol{\sigma_0}(\psi)$ pushes the interior surface outward (with a hardening law that is left for future work) until the current stress point contacts the enclosing surface, at which moment the multi-surf-crack2D model reverts to the description outlined previously in this Chapter.

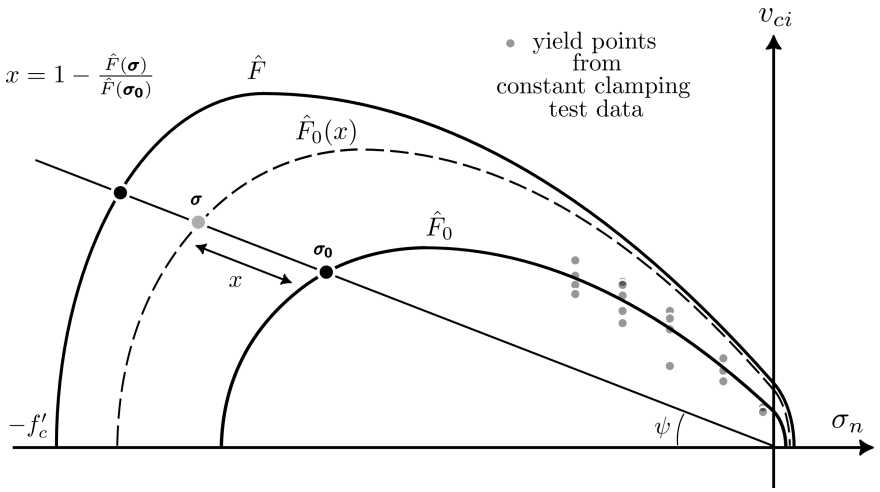

Figure 4.25. Initial stage of hardening in which inner surface grows to meet the enclosing surface (pictured test data is illustrative)

Chapter 5

Finite Element Implementation of Crack Plasticity Model

The previous Chapter presented an overview of the multi-surf-crack2D model, including the motivation for each modeling choice, based primarily on the collection of experimental observations built up in Chapter 2.2. Simultaneously, a toy problem was explored to show the typical behavior of the crack model in a simplified setting. However, some details of the crack constitutive model, particularly those that required a degree of formalism that might have disrupted the rhythm of Chapter 4, were brushed over. This Chapter is intended as a repository for the technical details that are crucial to the implementation of the multi-surf-crack2D model within a finite element setting but cumbersome to the story of this Thesis.

In Section 5.1, the derivation of each individual yield surface is provided, such that the resulting compound yield surface is smooth and well-behaved in the numerical sense. Section 5.2 provides details about the numerical implementation of the elastic stiffness tensor, with attention on distinguishing crack opening and closing behavior, and dealing with non-physical artifacts of the modeling approach, such as crack overlap. Section 5.3 derives in compact notation the elasto-plastic material tangent stiffness tensor and generalizes the formulation for all the yield surfaces so that the computer implementation is streamlined. Section 5.4 provides the derivatives, of which there are many, necessary for the implementation of the stiffness tensors. Section 5.5 justifies the validity of the material model from a thermodynamic perspective, while Section 5.6 treats the question of switching between yield surfaces and Section 5.7 provides the algorithm for

the return map.

Every detail laid out below has been included in the implementation of an `nDMaterial` within the OpenSees framework [109]. As of now, the constitutive law only exists within a local installation of OpenSees, so the source code is made available in Appendix B.

5.1 Smoothing the Combined Yield Surface

The yield surfaces F^t and F^c are tied to the surface F^{lok} at the cohesion point and the critical point, respectively, to form the combined surface for mixed-mode loading $\hat{F}$, sketched in Fig. 4.4. The surfaces F^t and F^c are constructed, starting from the assumption of an elliptical shape, to ensure that the combined surface is smooth so that problems of non-uniqueness are avoided in the return-mapping algorithm. This section provides the derivation for the two partial-elliptical surfaces. The yield surface for activation reversal, F^{act}, intersects the combined interlock surface and a separate routine is required for switching between the two.

In general, each yield surface is a function of stress variables (v_{ci} and σ_n), displacement variables (buried within v_{cimax} via $\tilde{\omega}$ and ν) and shape parameters h, k and χ_{lok}. While a fourth shape parameter d was used in the model description of Chapter 4, it is merely a linear combination of the other three independent shape parameters. Thus, in general, each yield surface can be written as:

$$F(\boldsymbol{\sigma}; \tilde{\omega}, \nu; h, k, \chi_{lok}) = 0 \tag{5.1}$$

This particular form is adopted below for each yield sub-surface, which results in slightly modified forms of the surfaces that were presented in Chapter 4. This form will be used consistently throughout the computer implementation, and will prove convenient for deriving the material plastic tangent.

Shear Yield Surface F^{lok}

The shear yield surface is the reference curve for the two partial elliptical surfaces F^t and F^c, as they must smoothly transition onto the shear-dominated strength limit curve, restated here for reference:

$$F^{lok} = 4d\left(\frac{|v_{ci}|}{v_{cimax}} - k\right) + \left(\frac{\sigma_n}{v_{cimax}} - h\right)^2 = 0 \tag{5.2}$$

The shear yield surface is now modified by expressing d in terms of h, k, and χ_{lok}, via Eq. (4.11). These three parameters are independent and have an intuitive physical interpretation: (h, k) is the location of the critical point in normalized stress space and χ_{lok} is the normalized cohesion. The transformation results in:

$$F^{lok} = \frac{h^2}{k - \chi_{lok}}\left(\frac{|v_{ci}|}{v_{cimax}} - k\right) + \left(\frac{\sigma_n}{v_{cimax}} - h\right)^2 = 0 \tag{5.3}$$

Constructing F^t

The tensile yield surface is assumed to have the form of a partial ellipse:

$$\frac{v_{ci}^2}{b^2} + \frac{(\sigma_n - x_c)^2}{(f_t - x_c)^2} - 1 = 0 \tag{5.4}$$

The tensile ellipse intersects the crack uniaxial tensile strength f_t, is centered on the σ_n axis at the horizontal position x_c and has a semi-minor axis of unknown length b in the v_{ci} direction. The two unknowns x_c and b must be solved to satisfy continuity and differentiability of the combined yield surface $\hat{F}$ at the cohesion point. The constructed ellipse is sketched in Fig. 5.1 and derived subsequently.

Enforcing continuity at the cohesion point where $(\sigma_n,\, v_{ci}) = (0, c_{lok})$ produces the following equation, which is specialized from Eq. (5.4):

$$\frac{c_{lok}^2}{b^2} + \frac{x_c^2}{(f_t - x_c)^2} - 1 = 0 \tag{5.5}$$

Differentiability of $\hat{F}$ at the cohesion point requires that the slope of F^t at the cohesion point equal the slope of F^{lok} at the cohesion point, which is:

$$\left(\frac{dv_{ci}}{d\sigma_n}\right)|_{\sigma_n=0} = \frac{h}{2d} \tag{5.6}$$

Isolating v_{ci} in the general form of the tensile ellipse (Eq. (5.4)), differentiating with respect to σ_n, evaluating at $\sigma_n = 0$ and equating

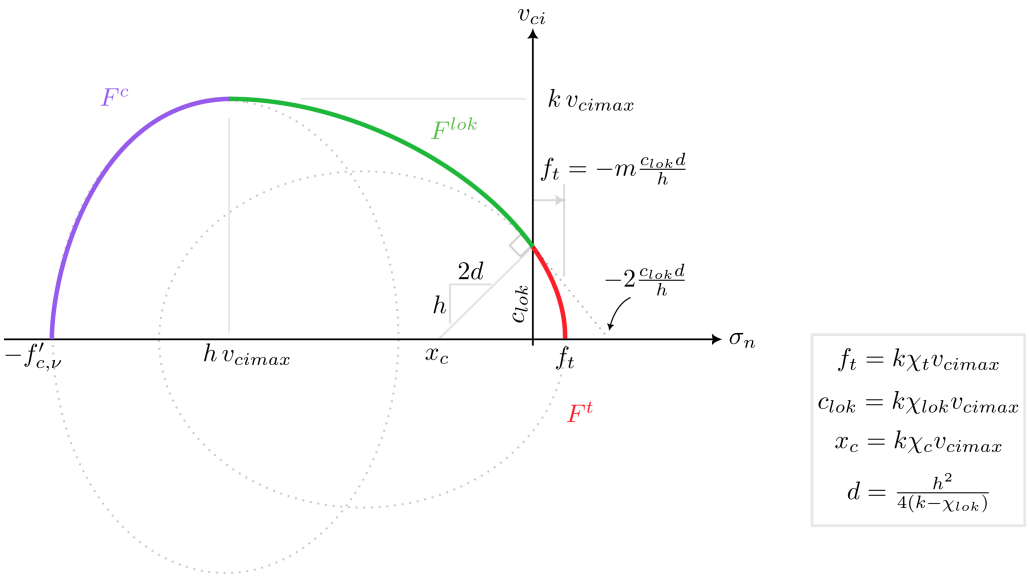

Figure 5.1. Construction of the tensile ellipse (red) to smoothly intersect the shear parabola (green) at the cohesion intercept, and the compressive ellipse (purple) to smoothly intersect the shear parabola at the critical point

the result with $h/(2d)$ gives the condition for differentiability of $\hat{F}$ at the cohesion point:

$$\frac{bx_c}{(f_t - x_c)^2\sqrt{1 - \frac{x_c^2}{(f_t - x_c)^2}}} = \frac{h}{2d} \tag{5.7}$$

The square root term in Eq. (5.7) is conveniently substituted by the continuity condition in Eq. (5.5) so that the continuity and differentiability conditions are written together as:

$$\frac{x_c}{c_{lok}}\frac{b^2}{(f_t - x_c)^2} = \frac{h}{2d} \tag{5.8}$$

Now, b (which is a distance and therefore positive) is solved in terms of x_c as:

$$b = (f_t - x_c)\sqrt{\frac{c_{lok}h}{2x_c d}} \tag{5.9}$$

Plugging b into the general definition of the tensile ellipse gives the form of the tensile ellipse presented in the previous chapter, written only in terms of x_c:

$$F^t = \frac{2x_c d}{c_{lok} h}\left(\frac{v_{ci}}{f_t - x_c}\right)^2 + \left(\frac{\sigma_n - x_c}{f_t - x_c}\right)^2 - 1 = 0 \tag{5.10}$$

where x_c, is identified by substituting b back into Eq. (5.5):

$$x_c = \frac{f_t^2}{2\left(\frac{c_{lok} d}{h} + f_t\right)} \tag{5.11}$$

From Fig. 5.1 it is seen that x_c must be negative to maintain compatibility with the slope of F^{lok} at the cohesion point. Enforcing this requires that the denominator of Eq. (5.11) be negative, which places an upper limit of the tensile strength

$$f_t < -\frac{c_{lok} d}{h} \tag{5.12}$$

Now, an approximation is made to allow the partial ellipse to be written in a form that is particularly convenient for computer implementation. By approximating the tensile strength f_t as a multiple of v_{cimax},

$$f_t = k\,\chi_t\,v_{cimax} \tag{5.13}$$

and recalling that $c_{lok} = k\,\chi_{lok}\,v_{cimax}$, the horizontal intercept of the tensile ellipse, x_c, can be simplified as:

$$x_c = k\,\chi_c\,v_{cimax} \tag{5.14}$$

where $\chi_c = \frac{\chi_t^2}{2\left(\chi_{lok}\frac{d}{h} + \chi_t\right)}$. It is noted that χ_t must be less than $|\chi_{lok}\frac{d}{h}|$ to ensure a negative-valued x_c, which is consistent with the slope at the cohesion point. Introducing a parameter m, the tensile strength ratio χ_t can be written as:

$$\chi_t = -m\chi_{lok}\frac{d}{h} \tag{5.15}$$

where it is noted that h is negative-valued and m must lie between 0 and 1. Now, writing d in terms of χ_{lok}:

$$\chi_t = -\frac{mh}{4}\frac{\chi_{lok}}{k-\chi_{lok}} \tag{5.16}$$

Plugging χ_t into χ_c gives:

$$\chi_c = \frac{m^2 h}{8(1-m)}\frac{\chi_{lok}}{k-\chi_{lok}} \tag{5.17}$$

Finally, by subbing Eqs. (5.13) and (5.14) into Eq. (5.10) and multiplying through by $(\chi_t - \chi_c)^2$, the tensile ellipse is parameterized by v_{cimax}:

$$F^t = \frac{2d}{h}\frac{\chi_c}{\chi_{lok}}\left(\frac{v_{ci}}{k\, v_{cimax}}\right)^2 + \left(\frac{\sigma_n}{k\, v_{cimax}} - \chi_c\right)^2 - (\chi_t - \chi_c)^2 = 0 \tag{5.18}$$

This feature proves quite handy for performing the partial derivatives that appear in the material tangent stiffness operator (see Section 5.3). To further ease the burden of derivative calculations, Eq. (5.18) is multiplied through by $k^2\, v_{cimax}^2$:

$$F^t = \frac{2d}{h}\frac{\chi_c}{\chi_{lok}}\, v_{ci}^2 + (\sigma_n - k\,\chi_c v_{cimax})^2 - \left[k\,(\chi_t - \chi_c) v_{cimax}\right]^2 = 0 \tag{5.19}$$

Now, the parameter d is eliminated in favor of parameters h, k and χ_{lok} via Eq. (4.11).

$$F^t = \frac{h}{2(k-\chi_{lok})}\frac{\chi_c}{\chi_{lok}}\, v_{ci}^2 + (\sigma_n - k\,\chi_c v_{cimax})^2 - \left[k\,(\chi_t - \chi_c) v_{cimax}\right]^2 = 0 \tag{5.20}$$

Lastly, the parameters χ_t and χ_c are substituted in terms of h, k and χ_{lok} via Eqs. (5.16) and (5.17), so that the yield surface is both parameterized by v_{cimax} and written in terms of the three independent shape parameters:

$$F^t = \frac{l}{2}\left[\frac{h}{k-\chi_{lok}} v_{ci}\right]^2 + \left[\sigma_n - l\frac{hk\chi_{lok}}{k-\chi_{lok}} v_{cimax}\right]^2 - \left[(n+l)\,\frac{hk\chi_{lok}}{k-\chi_{lok}} v_{cimax}\right]^2 = 0 \tag{5.21}$$

where two "survival algebra" parameters have been introduced to simplify the previous expression:

$$l = \frac{m^2}{8(1-m)} \tag{5.22}$$

$$n = \frac{m}{4} \tag{5.23}$$

Multiplying through by $(k - \chi_{lok})^2$ for convenience results in the form of the tensile ellipse that is used in the computer implementation:

$$F^t = \frac{l}{2}\big(hv_{ci}\big)^2 + \Big[(k-\chi_{lok})\sigma_n - lhk\chi_{lok}v_{cimax}\Big]^2 - \Big[(n+l)\,hk\chi_{lok}v_{cimax}\Big]^2 = 0 \tag{5.24}$$

Constructing F^c

The shear-compression yield surface F^c is, by inspection, a semi-ellipse centered horizontally at the critical point (i.e., vertex) of the F_{lok} parabola. For arbitrary $(h,\ k)$ values, the semi-elliptical yield surface in the compression regime is:

$$F^c = \left(\frac{v_{ci}}{k\,v_{cimax}}\right)^2 + \left(\frac{\sigma_n - h\,v_{cimax}}{-f'_{c,\nu} - h\,v_{cimax}}\right)^2 - 1 = 0 \tag{5.25}$$

where $f'_{c,\nu}$ is the compressive strength reduced by crushing damage.

Already, this surface forms a smooth, continuous transition with F^{lok}, as is sketched in Fig. 5.1.

Activation Surface F^{act}

The equation defining the activation yield surface is restated here, for completeness, in a form more suitable for computer implementation than that presented in Chapter 4:

$$F^{act} = v_{ci}^2 - (\mu_{act}\sigma_n)^2 - (k\chi_{act}v_{cimax})^2 = 0 \tag{5.26}$$

The user-input parameter χ_{act} is analogous to, but independent from χ_{lok}.

5.2 Elastic Stiffness Considerations

In Section 5.2.1, justification is provided for the approximate form of crack normal stiffness given in Eq. (4.4) and a penalty stiffness is defined for the case of non-physical crack overlap. Then, noting the similar "knockdown" form of the crack normal stiffness and the crack shear stiffness, an analogy is made between the multi-surf-crack2D and other damage-plasticity frameworks.

5.2.1 Crack Normal Stiffness

A precise description of the crack normal stiffness E relies on the loading direction, current crack width, maximum crack width, and crack closure stress, as described by the crack closure model of Ruggiero [153]. The computer implementation of the crack closure model is discussed here.

The cyclic crack traction-opening curve of Ruggiero is herein modified to match experimental observations that mixed-mode cracks can carry tensile stresses — even if crack width is large. It is recalled that the original crack closure curve of Ruggiero is constructed such that the crack normal stress vanishes once the current crack width meets or exceeds the maximum history crack width, w_{max}. Here, the crack normal stress at w_{max} is assumed to lie on the tensile cohesive curve $f_t(w)$. In context of the yield surface equations derived in Section 5.1, the cohesive curve corresponds to the uniaxial tensile strength intercept, i.e., Eq. (5.13), and describes how the tensile strength evolves with crack width. Equation (5.13) describes also a proportionality between tensile strength and v_{cimax}, which depends on crack width, average sliding contact angle $\tilde{\theta}$, maximum slip s_{max}, tensile size parameter χ_t and the shear size parameter k. Incorporating these dependencies, the closure/opening curve is modified as:

$$\sigma_n = q \ln(w + w^0) - f^0 + f_t(\chi_t, \tilde{\omega}_{max}, k) \tag{5.27}$$

where w^0 and f^0 are defined in Ruggiero's crack closure model in terms of the maximum crack width w_{max}, the crack closure stress f_{cl} and a rate parameter q. The rate parameter q can be assigned different values in opening and closing to produce loading/unloading hysteresis. The crack closure stress, which was originally defined in terms of crack width by Ruggiero [153], is here assumed constant. The effective closure stress

magnitude still increases with crack width as the cohesion vanishes. This is shown in Fig. 5.2, which also illustrates that the constant f_{cl} represents the closure stress for a wide crack that has no tension-carrying capacity.

Finally, the crack normal stiffness E is obtained by differentiating Eq. (5.27) with respect to crack width. Performing the differentiation results in:

$$E = \frac{q}{w + w^0}\left(1 + \frac{dw^0}{dw}\right) - \frac{df^0}{dw} + \frac{df_t(\tilde{\omega}_{max})}{dw} \tag{5.28}$$

Helpful derivatives $\frac{dw^0}{dw}$, $\frac{df^0}{dw}$ and $\frac{df_t(\tilde{\omega}_{max})}{dw}$ are provided in Section 5.4.

If $w < w_{max}$, the terms $\frac{dw^0}{dw}$, $\frac{df^0}{dw}$ and $\frac{df_t}{dw}$ all vanish, and the stiffness becomes:

$$E = \frac{q}{w + w^0} \leq E_{penalty} \tag{5.29}$$

For the case of negative crack width, a large penalty stiffness is placed on the closure stiffness to prevent excessive crack overlap, and to prevent numerical infinite stiffness as $w \to -w^0$. If, instead, a negative crack is re-opening, Eq. (5.29) is overridden and the compressive stress is constrained to reload to the origin of the crack closure law, i.e., the effective closure stress. This is shown in Fig. 5.2 along with the loading/unloading to/from the tensile cohesive curve.

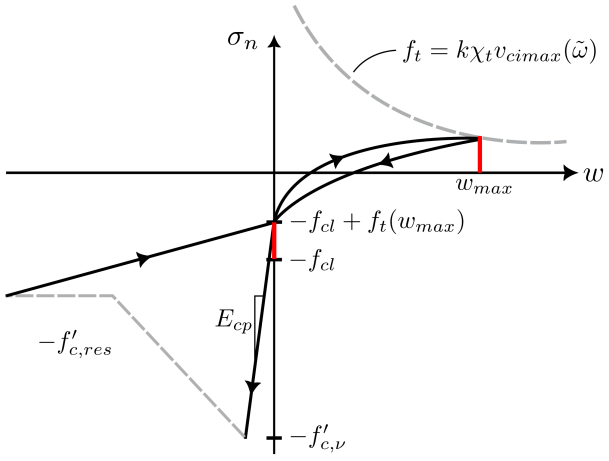

Figure 5.2. Crack normal stiffness schematic for a full cycle

Computer Implementation

For computer implementation of crack elastic normal stiffness, it is simplest to adopt a single value of q, regardless of loading or unloading. While it would make sense to adopt a value between $0.2 < q < 0.5$ as proposed by Ruggiero, a cruder approximation of the normal stiffness can be made by adopting a value of $q = \infty$. This produces a stiffness that is constant during elastic loading and unloading, but still degrades if w_{max} grows. For a positive crack width:

$$E = \frac{f_{cl}}{w_{max}} \tag{5.30}$$

If crack width is negative, the stiffness depends on the sign of crack opening. In closure, a large penalty stiffness prevents excessive non-physical crack overlap, and in opening the crack reloads to the closure state from the current point (w, σ_n):

$$E = \begin{cases} E_{penalty} & \Delta w < 0 \\ \frac{-f_{cl}+f_t(w_{max})-\sigma_n}{-w} & \Delta w > 0 \end{cases} \tag{5.31}$$

Also for computer implementation, an initial non-zero value of w_{max} must be specified. For a crack with measured residual width w^*, the maximum history width can be approximated as:

$$w_{max} = \frac{w^* f_{cl}}{\sigma^* + f_{cl}} > 0.04\text{mm} \tag{5.32}$$

where σ^* is the residual normal stress on the crack, estimated from Eq. (4.5) for an elastic bar with known reinforcement ratio and unbonded length. The w_{max} value should not be too low, to avoid overly stiff cracks. A cutoff value of 0.04mm was proposed by Divakar [49] for shear stiffness.

5.2.2 Crack Shear Stiffness

Like crack normal stiffness, crack shear stiffness D_{ts} is constant for elastic cycles but degrades with increased crack diplacement:

$$D_{ts} = D_{ts,0}\left(1 - \frac{s_{max}}{a_g/2}\right) \tag{5.33}$$

This leads to an analogy with standard damage-plasticity theories. One such class of models extends classic elasto-damage models by assuming that the intact (i.e., undamaged) material is elasto-plastic. This leads to the schematic shown in Fig. 5.3 in which plasticity and damage are coupled.

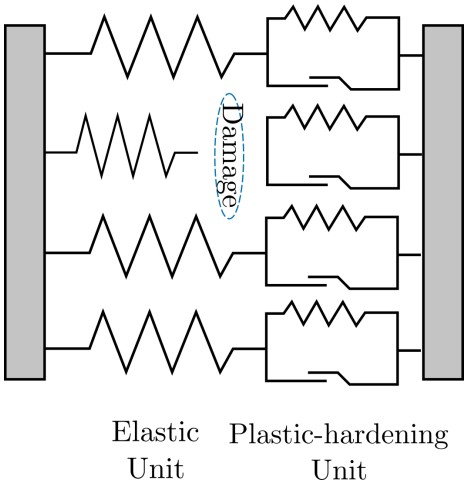

Figure 5.3. Schematic for one class of damage-plasticity models (adopted from [84])

The multi-surf-crack2D fits thematically into the damage-plasticity class of models, only that damage refers to loss of aggregate contact or aggregate rupture rather than continuum damage. Beyond making this analogy, no further effort has been dedicated to reconciling the elastic damage laws described above with a damage model. A simple scalar damage variable likely will not suffice, so a tensorial description will be required. This is left for future work.

5.3 Compact Elastoplastic Tangent Stiffness

This Section develops the elasto-plastic crack stiffness tensor $\boldsymbol{D}^{ep}$ for finite element implementation:

$$\Delta\boldsymbol{\sigma} = \boldsymbol{D}^{ep}\Delta\boldsymbol{\varepsilon} \tag{5.34}$$

Unlike in the previous chapter where component notation was adopted, compact notation is used here. One advantage of this approach is that

the equations describing aggregate interlocking and frictional reversal are unified, easing the finite element implementation. Bold capital letters denote 2nd order tensors and bold lowercase symbols or letters designate vectors. Vectors are column vectors unless transposed, in which case they are row vectors. Scalar quantities are non-bolded. It is noted that the organization of the vector equations is based on the choice that the crack element's local x-axis aligns with the crack-perpendicular (i.e., opening) direction.

The fundamental components of the crack plasticity model — (i) stress-strain law, (ii) plastic flow rule, (iii) yield surface, (iv) hardening evolution law and (v) consistency condition – are provided in Eqs. (5.35) - (5.41). Reorganization of those fundamental equations teases out the elasto-plastic stiffness.

The elastic stress law describes the transformation of an incremental elastic strain vector $\Delta\boldsymbol{\varepsilon^e} = \Delta\boldsymbol{\varepsilon} - \Delta\boldsymbol{\varepsilon^p}$ into a stress increment $\Delta\boldsymbol{\sigma}$ by the elastic material stiffness $\boldsymbol{D^e}$:

$$\Delta\boldsymbol{\sigma} = \boldsymbol{D^e}(\Delta\boldsymbol{\varepsilon} - \Delta\boldsymbol{\varepsilon^p}) \tag{5.35}$$

The total strain increment $\Delta\boldsymbol{\varepsilon}$ is typically prescribed whereas plastic incremental strains $\Delta\boldsymbol{\varepsilon^p}$ accumulate according to the plastic flow rule, generically described by Eq. (5.36), where $\boldsymbol{g_{,\sigma}}$ is shorthand for the stress gradient of the plastic potential surface G and $\Delta\lambda$ is the plastic multiplier.

$$\Delta\boldsymbol{\varepsilon^p} = \Delta\lambda\boldsymbol{g_{,\sigma}} \tag{5.36}$$

The flow direction adopted in this thesis is formalized in Eq. (5.37), where $\boldsymbol{f_{,\sigma}}$ is shorthand for the stress gradient of the yield surface F and ρ could take the place of the interlocking or activation dilation coefficient $\hat{\rho}$ or ρ_{act}, depending on the active surface:

$$\boldsymbol{g_{,\sigma}} = \mathrm{diag}(\boldsymbol{f_{,\sigma}}) \begin{bmatrix} \rho \\ 1 \end{bmatrix} \tag{5.37}$$

Though the multiple yield surface (both interlock and activation) evolves (i.e., hardens) with the stress-like hardening term v_{cimax}, it is often convenient to work with strain-like hardening terms. Here, v_{cimax} is telescoped down to its scalar strain components $\tilde{\omega}$ and ν (which are linear combinations of the crack displacement components w and s) to write total-strain

hardening laws in Eqs. (5.38) and (5.39) for effective crack opening and crushing, respectively:

$$\Delta\tilde{\omega} = \tilde{\boldsymbol{\omega}}_{,\boldsymbol{\varepsilon}}^{\boldsymbol{T}}\, \Delta\boldsymbol{\varepsilon} \tag{5.38}$$

$$\Delta\nu = \boldsymbol{\nu}_{,\boldsymbol{\varepsilon}}^{\boldsymbol{T}}\, \Delta\boldsymbol{\varepsilon} \tag{5.39}$$

The consistency condition requires that $\Delta F = 0$ during a plastic step. This means that a purely plastic step starts and ends on the plastic surface (for which $F = 0$). To evaluate the variation of F, the generalized yield surface is written in terms of all internal variables, so that the consistency condition becomes:

$$\Delta F(\boldsymbol{\sigma}; \tilde{\omega}, \nu; h, k, \chi_{lok}) = 0 \tag{5.40}$$

where, during a generic step, a change in F may originate from a change in: the stress components (within $\boldsymbol{\sigma}$), crack opening or sliding (within $\tilde{\omega}$), crushing (ν), or change in yield surface shape (through the 3 linearly independent parameters h, k and χ_{lok}). Taking the variation of F results in:

$$\Delta F = \boldsymbol{f}_{,\boldsymbol{\sigma}}^{\boldsymbol{T}}\, \Delta\boldsymbol{\sigma} + f_{,\tilde{\omega}}\, \Delta\tilde{\omega} + f_{,\nu}\, \Delta\nu + f_{,h}\, \Delta h + f_{,k}\, \Delta k + f_{,\chi_{lok}}\, \Delta\chi_{lok} = 0 \tag{5.41}$$

The yield surface change-of-shape driving terms Δh, Δk, $\Delta\chi_{lok}$ must be related to the strain vector $\Delta\boldsymbol{\varepsilon}$ so that the tangent stiffness can eventually be extracted, as already anticipated in Eq. (5.34). The equations describing the interpolation between rough and smooth parabolas that were presented in Chapter 4 can be formalized as:

$$\Delta h = 0 \tag{5.42}$$

$$\Delta k = \boldsymbol{k}_{,\boldsymbol{\varepsilon}}^{\boldsymbol{T}}\, \Delta\boldsymbol{\varepsilon} \tag{5.43}$$

$$\Delta\chi_{lok} = \boldsymbol{\chi_{lok}}_{,\boldsymbol{\varepsilon}}^{\boldsymbol{T}}\, \Delta\boldsymbol{\varepsilon} \tag{5.44}$$

Now, the plastic multiplier related to the total strain increment by inserting Eqs. (5.35)-(5.36), (5.38)-(5.39) and (5.42)-(5.44) into Eq. (5.41), as:

$$\Delta\lambda = \frac{\boldsymbol{f_{,\sigma}^T}\,\boldsymbol{D^e} + f_{,\tilde{\omega}}\,\boldsymbol{\tilde{\omega}_{,\varepsilon}^T} + f_{,\nu}\,\boldsymbol{\nu_{,\varepsilon}^T} + f_{,\chi_{lok}}\,\boldsymbol{\chi_{lok,\varepsilon}^T} + f_{,k}\,\boldsymbol{k_{,\varepsilon}^T}}{\boldsymbol{f_{,\sigma}^T}\,\boldsymbol{D^e}\boldsymbol{g_{,\sigma}^T}}\Delta\boldsymbol{\varepsilon} \tag{5.45}$$

Back-subbing the plastic multiplier into the flow rule and subsequently the flow rule into the incremental stress law, the elastoplastic material stiffness $\boldsymbol{D^{ep}}$ is found as:

$$\boldsymbol{D^{ep}} = \boldsymbol{D^e} - \left[\frac{(\boldsymbol{D^e}\boldsymbol{g_{,\sigma}})\otimes\left(\boldsymbol{f_{,\sigma}^T}\,\boldsymbol{D^e} + f_{,\tilde{\omega}}\,\boldsymbol{\tilde{\omega}_{,\varepsilon}^T} + f_{,\nu}\,\boldsymbol{\nu_{,\varepsilon}^T} + f_{,\chi_{lok}}\,\boldsymbol{\chi_{lok,\varepsilon}^T} + f_{,k}\,\boldsymbol{k_{,\varepsilon}^T}\right)}{\boldsymbol{f_{,\sigma}^T}\,\boldsymbol{D^e}\boldsymbol{g_{,\sigma}^T}}\right] \tag{5.46}$$

5.4 Helpful Derivatives

To implement the tangent stiffness, many partial derivatives must be obtained. Those calculations are provided below.

Stress gradient of yield surface:

$\boldsymbol{f_{,\sigma}}$ is evaluated differently for each portion of the multiple yield surface. If the combined interlock surface $\hat{F}$ is engaged, the evaluation depends on the current value of σ_n.

In the sliding regime ($-v_{cimax} \leq \sigma_n \leq 0$):

$$\left(\frac{\partial F^{lok}}{\partial\boldsymbol{\sigma}}\right)^T = \left[\frac{2}{v_{cimax}}\left(\frac{\sigma_n}{v_{cimax}} - h\right) \quad \frac{h^2}{v_{cimax}(k-\chi_{lok})}\mathrm{sgn}(v_{ci})\right] \tag{5.47}$$

Else, in the tensile regime ($0 < \sigma_n$):

$$\left(\frac{\partial F^{t}}{\partial\boldsymbol{\sigma}}\right)^T = \left[2(k-\chi_{lok})^2\left(\sigma_n - l\frac{hk\chi_{lok}}{k-\chi_{lok}}v_{cimax}\right) \qquad lh^2 v_{ci}\right] \tag{5.48}$$

And in the compressive regime ($\sigma_n < -v_{cimax}$):

$$\left(\frac{\partial F^c}{\partial \boldsymbol{\sigma}}\right)^T = \left[\frac{2(\sigma_n - h\, v_{cimax})}{(-f'_{c,\nu} - h\, v_{cimax})^2} \qquad \frac{2v_{ci}}{(k\, v_{cimax})^2}\right] \tag{5.49}$$

Lastly, if the activation surface is engaged:

$$\left(\frac{\partial F^{act}}{\partial \boldsymbol{\sigma}}\right)^T = \left[-2\mu_{act}^2\sigma_n \qquad 2v_{ci}\right] \tag{5.50}$$

Partial of yield surface with respect to v_{cimax}:

As all the yield surfaces are parameterized by v_{cimax} (see approximate form of F^t in Section 5.1), the partial derivative $\frac{\partial F}{\partial v_{cimax}}$ is a stepping stone to obtaining the partial derivatives $f_{,\tilde{\omega}}$ and $f_{,\nu}$.

In the sliding regime ($-v_{cimax} \leq \sigma_n \leq 0$):

$$\frac{\partial F^{lok}}{\partial v_{cimax}} = -\frac{1}{v_{cimax}^2}\left[\frac{h^2}{k - \chi_{lok}}|v_{ci}| + 2\sigma_n\left(\frac{\sigma_n}{v_{cimax}} - h\right)\right] \tag{5.51}$$

In the tensile regime ($0 < \sigma_n$):

$$\frac{\partial F^t}{\partial v_{cimax}} = -2(hk\chi_{lok})(k - \chi_{lok})\left[l\sigma_n + (n^2 + 2nl)\frac{hk\chi_{lok}}{k - \chi_{lok}}v_{cimax}\right] \tag{5.52}$$

In the compressive regime ($\sigma_n < -v_{cimax}$):

$$\frac{\partial F^c}{\partial v_{cimax}} = -\frac{2}{v_{cimax}}\left(\frac{v_{ci}}{kv_{cimax}}\right)^2 + 2h\frac{(\sigma_n - hv_{cimax})(f'_{c,\nu} + \sigma_n)}{(-f'_{c,\nu} - hv_{cimax})^3} \tag{5.53}$$

Lastly, if the activation surface is engaged:

$$\frac{\partial F^{act}}{\partial v_{cimax}} = -2k^2\chi_{act}^2 v_{cimax} \tag{5.54}$$

Contribution of $\tilde{\omega}$ to tangent stiffness: $f_{,\tilde{\omega}}\,\tilde{\boldsymbol{\omega}}_{,\boldsymbol{\varepsilon}}^{\boldsymbol{T}}$

The strain-like hardening parameter $\tilde{\omega}$, defined in Eq. (4.22), affects the peak-achievable crack shear stress through the stress-like term v_{cimax}. In light of the penalty stiffness approach described in Section 5.2, Eq. (4.22) is adjusted to prevent excessive hardening in the case of crack overlap (i.e., $w < 0$). The expression for effective crack width $\tilde{\omega}$ used in the computer implementation is:

$$\tilde{\omega} = \max(0, w) + \frac{8 \sin \tilde{\theta}}{3\pi} s_{max} \tag{5.55}$$

As $\tilde{\omega}$ only appears in v_{cimax}, which parameterizes all yield functions, $f_{,\tilde{\omega}}$ can be obtained from the chain rule as

$$f_{,\tilde{\omega}} = \frac{\partial F}{\partial v_{cimax}} \frac{\partial v_{cimax}}{\partial \tilde{\omega}} \tag{5.56}$$

The partials of the yield surface with respect to v_{cimax} have already been obtained in Eqs. (5.51)-(5.54). The second part of the chain is:

$$\frac{\partial v_{cimax}}{\partial \tilde{\omega}} = -\frac{\frac{24\sqrt{f'_{c,\nu}}}{a_g+16}}{\left(0.31 + \frac{24\tilde{\omega}}{a_g+16}\right)^2} \tag{5.57}$$

It is recalled that $\tilde{\omega}$ is a linear combination of the crack width w and a sliding history variable s_{max} that tracks the historical maximum sliding magnitude. Thus, crack opening damage is recoverable while the sliding part is non-recoverable. Both effects are captured by the strain-gradient term $\tilde{\boldsymbol{\omega}}_{,\boldsymbol{\varepsilon}}$:

$$\tilde{\boldsymbol{\omega}}_{,\boldsymbol{\varepsilon}}^{\boldsymbol{T}} = \begin{bmatrix} g_w & \frac{8 \sin \tilde{\theta}}{3\pi} g_s \end{bmatrix} \tag{5.58}$$

A toggle function g_w is needed for the case where the crack width becomes negative, which is permitted by the model's penalty stiffness approach to enforcing crack overlap. By toggling off the crack width participation, the tangent stiffness reflects that v_{cimax} is prevented from artificially hardening in the event of crack overlap.

$$g_w = \frac{\max(0, w)}{w} \tag{5.59}$$

The toggle function g_s is activated only if the current slip magnitude exceeds all previous slip magnitudes (note the use of the floor function $\lfloor \cdot \rfloor$):

$$g_s = \left\lfloor \frac{|s|}{s_{max}} \right\rfloor \tag{5.60}$$

Sliding damage can be turned off with the choice of the width-only hardening law originally posited by the MCFT, for which $\tilde{\boldsymbol{\omega}}_{\boldsymbol{\varepsilon}}^{\boldsymbol{T}} = [1 \quad 0]$.

Contribution of ν to tangent stiffness: $f_{,\nu}\, \boldsymbol{\nu}_{,\boldsymbol{\varepsilon}}^{\boldsymbol{T}}$

The crushing strain ν softens the concrete strength $f'_{c,\nu}$, which affects the shear-compression yield surface directly (see Eq. (5.25) for F^c) and affects the other yield surfaces indirectly through v_{cimax}. Accounting for both contributions:

$$f_{,\nu} = \frac{\partial F}{\partial v_{cimax}} \frac{\partial v_{cimax}}{\partial \nu} + \frac{\partial F^c}{\partial f'_{c,\nu}} \frac{\partial f'_{c,\nu}}{\partial \nu} \tag{5.61}$$

The partial of the yield surface with respect to v_{cimax} has already been obtained in Eqs. (5.51)-(5.54). The second partial is:

$$\frac{\partial v_{cimax}}{\partial \nu} = \frac{1}{2\sqrt{f'_{c,\nu}}} \frac{E_{cp}}{0.31 + \frac{24\tilde{\omega}}{a_g + 16}} \tag{5.62}$$

The effect of $f'_{c,\nu}$ on F^c is:

$$\frac{\partial F^c}{\partial f'_{c,\nu}} = 2\, \frac{\left(\sigma_n - h v_{cimax}\right)^2}{\left(-f'_{c,\nu} - h v_{cimax}\right)^3} \tag{5.63}$$

and the last partial describes the post-peak compression softening, which was assumed in Chapter 4 to be linear according to the Kent-Park model and zero if the residual crushing strength ($f'_{c,res} = 0.2 f'_c$) has been reached:

$$\frac{\partial f'_{c,\nu}}{\partial \nu} = \begin{cases} E_{cp} & \nu > \frac{f'_{c,res} - f'_c}{E_{cp}} \\ 0 & \nu \leq \frac{f'_{c,res} - f'_c}{E_{cp}} \end{cases} \tag{5.64}$$

The (negative-valued) crushing strain ν only accumulates if the shear-compression surface F^c is engaged. This condition is built into the strain gradient of ν, which describes how the total strain vector drives crushing hardening:

$$\boldsymbol{v}_{,\boldsymbol{\varepsilon}}^{\boldsymbol{T}} = [g_c \quad 0] \tag{5.65}$$

The toggle function g_c consents crushing damage (i.e. $g_c = 1$) only if the sub-surface F^c – which has a negative plastic crack opening component – is active. Formally:

$$g_c = \frac{\min(0, \frac{\partial \hat{F}}{\partial \sigma_n})}{\frac{\partial \hat{F}}{\partial \sigma_n}} \tag{5.66}$$

Crushing damage does not accumulate (i.e., $g_c = 0$) for elastic steps or if the activation surface is engaged.

Contribution of shape change to tangent stiffness: $f_{,\chi_{lok}}\,\boldsymbol{\chi_{lok}}_{,\boldsymbol{\varepsilon}}^{\boldsymbol{T}}$; $f_{,k}\,\boldsymbol{k}_{,\boldsymbol{\varepsilon}}^{\boldsymbol{T}}$

The shape of the yield surface is altered during sub-critical, cyclic sliding, through the parameters χ_{lok} and k. Note that variation of the shape parameter h could also be considered in the general case, but has no effect in the formulation outlined in Chapter 4 and so is here ignored.

→ Partial of yield surface with respect to shape parameter k: $f_{,k}$
The shape parameter k appears in all yield surfaces. Its effect is seen by differentiating the equations that describe those surfaces:

$$\frac{\partial F^{lok}}{\partial k} = -\frac{h^2}{k - \chi_{lok}} \tag{5.67}$$

$$\frac{\partial F^t}{\partial k} = 2(\sigma_n - lh\chi_{lok}v_{cimax})\Big[(k-\chi_{lok})\sigma_n - lhk\chi_{lok}v_{cimax}\Big] - 2\Big[(n+l)h\chi_{lok}v_{cimax}\Big]^2 k \tag{5.68}$$

$$\frac{\partial F^c}{\partial k} = -\frac{2}{k}\left(\frac{v_{ci}}{k\,v_{cimax}}\right)^2 \tag{5.69}$$

$$\frac{\partial F^{act}}{\partial k} = -2k\chi_{act}^2 v_{cimax}^2 \tag{5.70}$$

→ **Partial of yield surface with respect to shape parameter χ_{lok}:** $f_{,\chi_{lok}}$ The shape parameter χ_{lok} appears only in the shear and the shear-tension yield surfaces, F^{lok} and F^t. Its effect is seen by differentiating the equations that describe those surfaces:

$$\frac{\partial F^{lok}}{\partial \chi_{lok}} = \left(\frac{h}{k-\chi_{lok}}\right)^2 \left(\frac{|v_{ci}|}{v_{cimax}} - k\right) \tag{5.71}$$

$$\frac{\partial F^t}{\partial \chi_{lok}} = -2(\sigma_n + lhkv_{cimax})\Big[(k-\chi_{lok})\sigma_n - lhk\chi_{lok}v_{cimax}\Big] - 2\Big[(n+l)hkv_{cimax}\Big]^2 \chi_{lok} \tag{5.72}$$

$$\frac{\partial F^c}{\partial \chi_{lok}} = \frac{\partial F^{act}}{\partial \chi_{lok}} = 0 \tag{5.73}$$

→ **Strain gradient of shape parameters χ_{lok} and k:** $\boldsymbol{\chi_{lok,\varepsilon}}$, $\boldsymbol{k_{,\varepsilon}}$ Variations of the shape parameters depend on their strain gradients:

$$\boldsymbol{\chi_{lok,\varepsilon}^T} = [0 \quad \chi_{lok,s}\, g_d] \tag{5.74}$$

$$\boldsymbol{k_{,\varepsilon}^T} = [0 \quad k_{,s}\, g_d] \tag{5.75}$$

where the variation of the shape parameters with sliding is a chained derivative, due to the nesting of the user-input κ parameter within the roughness interpolation function $r^{\pm}(\kappa)$ (recall Eq. (4.33)):

$$\chi_{lok,s} = \frac{d\chi_{lok}}{dr}\frac{dr^{\pm}(\kappa)}{ds} \tag{5.76}$$

$$k_{,s} = \frac{dk}{dr}\frac{dr^{\pm}(\kappa)}{ds} \tag{5.77}$$

The derivatives of the shape parameters k and χ_{lok} with respect to the intermediate interpolating function r are:

$$\frac{d\chi_{lok}}{dr} = \chi^r_{lok} - \chi^s_{lok} \tag{5.78}$$

$$\frac{dk}{dr} = k^r - k^s \tag{5.79}$$

and the derivative of the interpolating function $r^{\pm}(\kappa)$ with respect to crack sliding is:

$$\frac{dr^{\pm}(\kappa)}{ds} = \frac{1}{s^{\pm}_{max}} \frac{1-\kappa^2}{\left[\kappa - 2\kappa\left(\frac{s}{s^{\pm}_{max}}\right) + 1\right]^2} \tag{5.80}$$

As none of the shape change variations default to zero when $s \to s^{\pm}_{max}$, a toggle function $g^{\pm}_d$ is defined to toggle off shape change when $s/s^{\pm}_{max} \geq 1$, using the floor function $\lfloor \cdot \rfloor$.

$$g^{\pm}_d = 1 - \left\lfloor \frac{s}{s^{\pm}_{max}} \right\rfloor \tag{5.81}$$

It is noted that, as formulated, shape change occurs for all subcritical loading and unloading, even if elastic.

Derivatives that appear in the elastic crack closure relationship

To avoid unnecessary complexity, the crack closure stress f_{cl} is assumed to remain constant in the following derivatives.

The terms $\frac{dw^0}{dw}$, $\frac{df^0}{dw}$ and $\frac{df_t(\tilde{\omega}_{max})}{dw}$ are only non-zero if $w = w_{max}$. They can be calculated in the general case as:

$$\frac{dw^0}{dw} = \left\lfloor \frac{w}{w_{max}} \right\rfloor \frac{\exp(-f_{cl}/q)}{1-\exp(-f_{cl}/q)} \tag{5.82}$$

$$\frac{df^0}{dw} = \left\lfloor \frac{w}{w_{max}} \right\rfloor \frac{q}{w_{max}} \tag{5.83}$$

$$\frac{df_t(\tilde{\omega}_{max})}{dw} = \left\lfloor \frac{w}{w_{max}} \right\rfloor k\chi_t \frac{\partial v_{cimax}}{\partial \tilde{\omega}} \tag{5.84}$$

where the term $\left\lfloor \frac{w}{w_{max}} \right\rfloor$ evaluates to zero if $w < w_{max}$ and 1 if $w = w_{max}$.

5.5 Thermodynamic Considerations

A material that undergoes load cycles must not generate energy, lest the laws of thermodynamics be violated. Formally, the work done during a complete stress loop must be non-negative:

$$\oint (\boldsymbol{\sigma} - \boldsymbol{\sigma}^*) \cdot d\boldsymbol{\varepsilon} \geq 0 \tag{5.85}$$

where $\boldsymbol{\sigma}$ is a plastically-admissible stress, $\boldsymbol{\sigma}^*$ is a stress within the yield surface and the $\oint$ indicates a closed stress loop that starts at $\boldsymbol{\sigma}^*$ then goes to $\boldsymbol{\sigma}$ before returning elastically to the starting point.

This thesis adopts a crack elastic stiffness description that does not dissipate energy elastically, so the work inequality of Eq. (5.85) simplifies to:

$$(\boldsymbol{\sigma} - \boldsymbol{\sigma}^*) \cdot d\boldsymbol{\varepsilon}^{\boldsymbol{p}} \geq 0 \tag{5.86}$$

Graphically, the stress vector $\boldsymbol{\sigma} - \boldsymbol{\sigma}^*$ points from any arbitrary stress point $\boldsymbol{\sigma}^*$ within the yield surface to any other arbitrary point $\boldsymbol{\sigma}$ on the yield surface. Meanwhile, the plastic flow vector $d\boldsymbol{\varepsilon}^{\boldsymbol{p}}$ points in the direction normal to the plastic potential surface that overlaps the yield surface at $\boldsymbol{\sigma}$. Figure 5.4 shows that the $d\boldsymbol{\varepsilon}^{\boldsymbol{p}}$ vector, at its shallowest and most restrictive for Eq. (5.86), approaches a purely vertical orientation in the limit case of $\rho \to 0$. The projection of the stress vector onto the flow direction is non-negative, and therefore thermodynamically admissible, only if the internal angle between the two vectors is less than $\pi/2$.

Figure 5.4 shows the two relevant vectors for the combined interlocking surface $\hat{F}$, which is built up from the shear surface F^{lok}, the tensile-shear surface F^t and the compression-shear surface F^c. By graphical reasoning, any stress increment with an increasing shear magnitude is guaranteed to satisfy the dissipation inequality for the combined interlock surface. Since the shear stiffness is always positive, it can be stated that any yielding process on $\hat{F}$ is guaranteed to be energetically admissible if the crack slip increment driving the stress change does not shrink. This rule is intuitive—after all, an unloading crack with $\Delta s < 0$ is not expected to provoke aggregate interlock—and will be implemented into the multi-surface "handling" algorithm in Section 5.6.

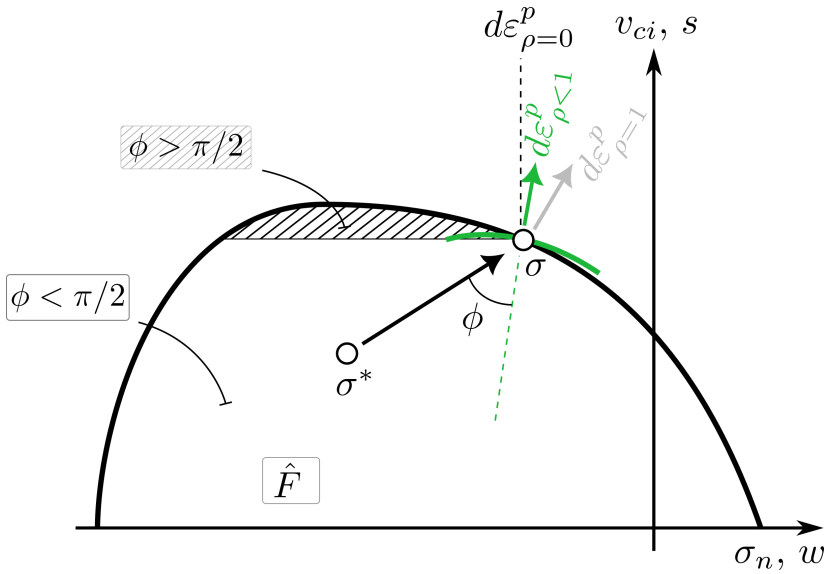

Figure 5.4. Graphical proof of thermodynamic admissibility of interlocking processes

A similar graphical proof for the thermodynamic admissibility of the plastic activation process is provided in Fig. 5.5. The dissipation criterion is satisfied if the elastic trial step has non-negative projection onto the plastic flow vector $d\varepsilon^p \propto \frac{\partial G^{act}}{\partial \boldsymbol{\sigma}}$. This criterion is indicated by the inclined dashed line in the figure: the component of the stress increment $(\boldsymbol{\sigma} - \boldsymbol{\sigma}^*)$ that is perpendicular to the inclined dashed line must point above the line. An additional constraint on the elastic trial step is enforced to ensure that the elastic normal stress increment increases during activation (see discussion in Chapter 4). This constraint is shown by the vertical dashed line: the horizontal projection of the stress increment $(\boldsymbol{\sigma} - \boldsymbol{\sigma}^*)$ must point to the right.

For the arbitrary stress point $\boldsymbol{\sigma}$ on the activation surface, the two constraints are satisfied by stress states $\boldsymbol{\sigma}^*$ that approach $\boldsymbol{\sigma}$ from the "permissible approach zone" wedge sketched in the figure. These permissible states must have an elastic trial step that satisfies the following inequality:

$$\gamma^{int} < \frac{1}{\mu^{act}\rho^{act}} \tag{5.87}$$

where

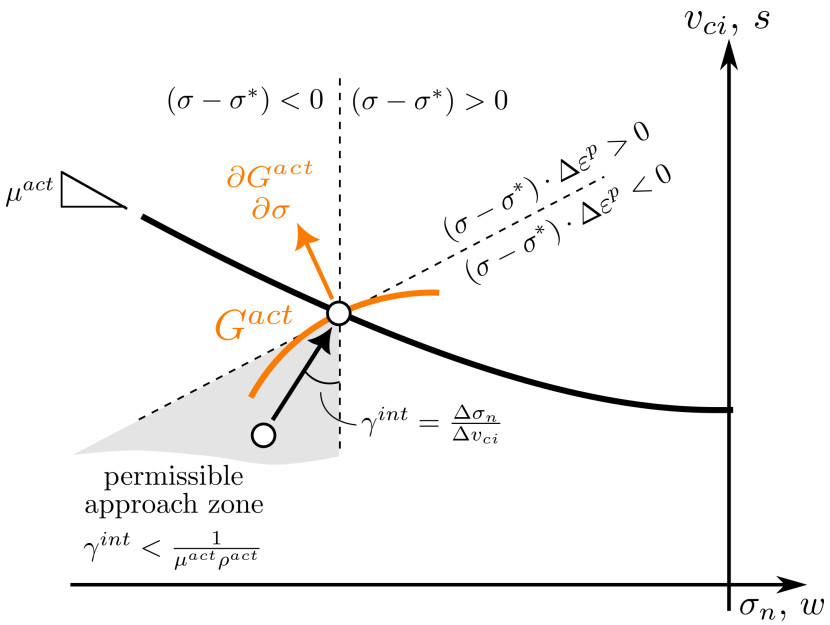

Figure 5.5. Graphical proof of thermodynamic admissibility of activation processes

$$\gamma^{int} = \frac{\Delta\sigma_n^{tr}}{\Delta v_{ci}^{tr}} \tag{5.88}$$

is defined as the internal load angle. Satisfaction of the approach zone inequality can be checked for various choices of crack stiffness and external load ratio γ. If the off-diagonal stiffness terms are set to zero, the approach zone inequality is satisfied for nearly all load conditions except for large γ (approaching the pure tensile state). When small amounts of off-diagonal stiffness are included, the approach zone criterion is improved.

5.6 Handling Loading and Unloading Yield Surfaces

This section describes the algorithm for switching between the combined interlock surface $\hat{F}$ and the activation surface F^{act}. In Section 5.5 it was shown that thermodynamic admissibility of the plastic interlock process can

only be guaranteed for increasing slip magnitude; therefore, the combined interlock surface is loosely termed the "loading" surface. Meanwhile, it was shown that the activation surface is active for steps with decreasing slip magnitude and offloading of residual stresses. As such, the activation surface is termed the "unloading" surface. By enforcing rules for when to switch from the loading surface to the unloading surface, a unique stress-return algorithm can be guaranteed.

Rule 1: The combined interlock surface must always be checked Though $\hat{F}$ has just been loosely called the loading surface (based on thermodynamic consequences of the non-associativity of aggregate interlock), some unloading scenarios may trigger the surface. For instance, shear-unloading paths could be constructed that cross the permissible stress threshold even when shear is decreasing. Accordingly, the yield surface is always enforced lest unrealistic compressive strength or tensile strength be predicted if the model ignores yield surface contact for these special cases. To ensure thermodynamic admissibility of these unloading paths, $\hat{\rho} = 1$ could be enforced in the tensile (F_t) and compressive (F_c) domains.

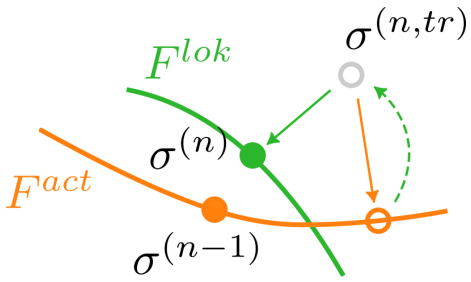

Figure 5.6. Handling of surface overlap during aggregate re-engagement near the cohesion point

Rule 2: The branches of the hyperbolic activation surface are direction-specific The conditions for engaging either branch are:

$$v_{ci}\,\Delta s > 0 \tag{5.89}$$

and

$$|s_{n+1}| - |s_n| < 0 \tag{5.90}$$

Equation (5.89) ensures that shear must flip sign before activation reversal can occur. For example, if Δs is negative, activation cannot occur unless the crack shear v_{ci} is also negative. For typical unloading, this means that the nearest activation branch is passed over in favor of the farther activation branch (e.g., see unloading branch 1-2 in Fig. 5.7).

Equation (5.90) further restricts activation to occur only if the crack slip decreases in magnitude from step n to step $n+1$. This restriction can be loosened if crack re-engagement is delayed via the ζ parameter (described in Chapter 4), in which case the activation surface is enforced—even if condition (5.90) is violated—when:

$$|s^{\pm}| < |s^{\pm}_{brk}| \tag{5.91}$$

The break point s_{brk} was defined in Eq. (4.32). This pre-engagement condition can induce small tensile tractions if the plastic stress point travels along the activation surface beyond the cohesion point. If the predicted tensile stresses grow beyond the tensile limit surface F^t, Rule 1 is enforced and activation is turned off, even if the break point has not yet been exceeded.

Rule 3: Single-sided fatigue does not trigger activation Inherently, the conditions in Eqs. (5.89) & (5.90) for plastic activation are not satisfied for single-sided load cycles or single-sided displacement cycles. This matches experimental trends, which do not show evidence of sliding activation under these conditions. The more lenient condition in Eq. (5.91), however, can lead to unrealistic behavior if subcritical single-sided cycling follows a large plastic excursion. To prevent such a response, a new history variable $\hat{v}^{unl}_{ci}$ is introduced to keep track of the last unloading point from the combined interlock surface $\hat{F}$, and the following condition is checked before the activation surface is engaged:

$$v_{ci}\,\hat{v}^{unl}_{ci} < 0 \tag{5.92}$$

In summary, the combined interlock surface $\hat{F}$ is always checked, while the activation surface is checked only if a crack is unloading or pre-engagement, and has been previously yielded in the opposite direction of current travel. If a stress state is returned to the activation surface but lies

outside of the combined interlock surface, the stress is returned instead to the interlock surface and the activation process is terminated.

The rules outlined above also capture premature overlap of F^{act} and $\hat{F}$ that may follow from the change of shape term κ, described in Chapter 4. An arbitrary stress path is sketched in Fig. 5.5 to summarize Rules 1-3.

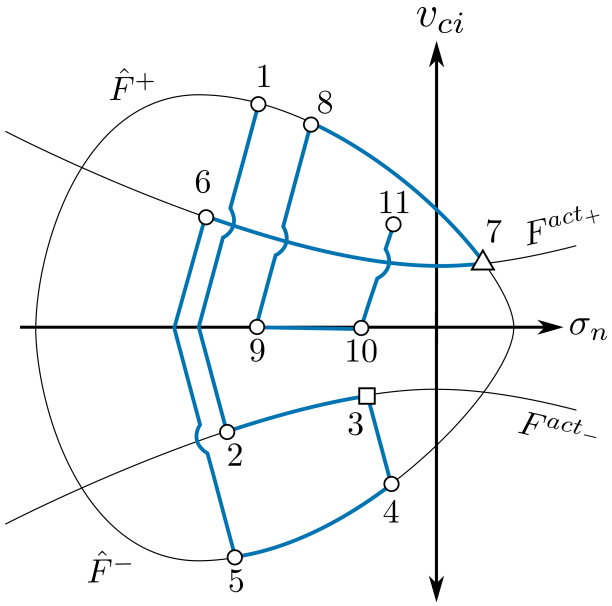

△ end of activation (surface overlap)
□ end of activation ($s = s_{brk}$)
) bypass activation surface (conditions not met)

Figure 5.7. Arbitrary stress path demonstrating onset and termination of activation surface, as well as when activation surface is bypassed (size and shape changes of yield surfaces omitted for clarity)

5.7 Return Mapping Algorithm

Chapter 4 introduced the elastic-trial plastic-correction algorithm for determining the stress increment corresponding to an arbitrary strain increment. For a prescribed strain vector increment, the algorithm consisted of first assuming that only elastic stresses would develop. If that assumption

produced a stress state outside of the controlling yield surface, a plastic-correction was applied to the elastic trial stress to "return" the trial stress to the yield surface. Section 5.6 described a routine for identifying which surface the trial stress should be returned to, and this Section describes the plastic-correction algorithm, also called the return map.

Graphically, the return process is simple. A trial stress is returned along a prescribed direction until the stress point lands on the controlling yield surface. The return direction is known a priori: by inspection of Eq. (5.35) the return direction is the plastic flow vector $d\boldsymbol{\varepsilon}^p = \left[\frac{\partial G}{\partial \sigma_n}, \frac{\partial G}{\partial v_{ci}}\right] = \boldsymbol{g}_{,\boldsymbol{\sigma}}$. The magnitude of the flow vector, and the unknown to be solved, is the plastic magnitude $\Delta\lambda$. (To avoid confusion, it is noted that the closed-form expression for $\Delta\lambda$ in Eq. (5.45) is a linearized approximation of the plastic magnitude based on the previous converged state. That expression is baked into the crack tangent stiffness, which is assembled into the global stiffness and tells the equilibrium-finding routine how to prescribe a trial displacement vector to satisfy global equilibrium (within a tolerance). A subset of the trial displacement vector is then passed to the corresponding crack element. Only at this stage does the crack stress-state determination routine, i.e. elastic-trial plastic correction algorithm, get called.)

In all but the simplest problems, the return mapping is an iterative process. The yield surface hardens, changing shape, during the plastic return step, requiring the return direction to update throughout the process, like a guided missile tracking a moving target. One simple algorithm for guiding the return direction is the generalized cutting plane algorithm, summarized neatly by Jirásek and Bazant [85].

The objective of the return map is represented mathematically by the consistency condition, which when satisfied describes a stress state that lies on the controlling yield surface, generically denoted as F:

$$F\left(\boldsymbol{\sigma}^{(tr)} - \Delta\lambda^{(n+1)}\boldsymbol{D}^e\boldsymbol{g}_{,\boldsymbol{\sigma}}^{(n)}\right) = 0 \tag{5.93}$$

The $(k+1)^{th}$ Newton-Raphson iteration to find the plastic magnitude at step $(n+1)$ that satisfies the consistency condition is:

$$\Delta\lambda^{(n+1,k+1)} = \Delta\lambda^{(n+1,k)} + \delta\lambda \tag{5.94}$$

where $d\lambda$ is the linear approximation of the increment of plastic magnitude needed to solve the consistency condition, based on the current

error $F^{(n+1,k)}$ and the "stiffness" of the yield condition with respect to an increment of plastic magnitude:

$$\delta\lambda = -\frac{F^{(n+1,k)}}{\frac{\partial F^{(n+1,k)}}{\partial(\Delta\lambda)}} \tag{5.95}$$

The "stiffness" of the yield function is identified by taking the partial of F (see Eq. (5.41)), where it is helpful to note that the strain hardening terms $\tilde{\omega}$ and ν and the shape change terms h, k and χ_{lok} are constructed in terms of total strains instead of plastic strains. Those terms vanish and the following stiffness is obtained:

$$\frac{\partial F^{(n+1,k)}}{\partial(\Delta\lambda)} = -\boldsymbol{D}^{\boldsymbol{e}}\boldsymbol{g}_{,\boldsymbol{\sigma}}^{(n+1,k)} \tag{5.96}$$

Substituting, the incremental update $\delta\lambda$ becomes

$$\delta\lambda = \frac{F^{(n+1,k)}}{\boldsymbol{f}_{,\boldsymbol{\sigma}}^{(n+1,k)}\,\boldsymbol{D}^{\boldsymbol{e}}\boldsymbol{g}_{,\boldsymbol{\sigma}}^{(n+1,k)}} \tag{5.97}$$

The crucial ingredient of the generalized cutting plane algorithm described above is that the flow direction $\boldsymbol{g}_{,\boldsymbol{\sigma}}$ is updated with each iteration. For crack plasticity, which is described in this Thesis by a non-associative model, the updating flow direction guides the trial stress state toward the target yield surface, even if the initial return direction is askew. This is sketched in Fig. 5.8.

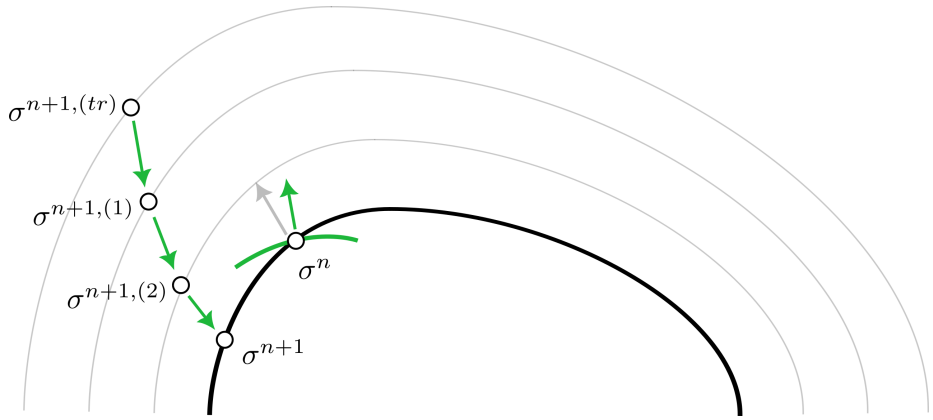

Figure 5.8. General cutting plane algorithm, with updating return direction at each iteration

Chapter 6

Validating the multi-surf-crack2D Model

The crack material model formulated in Chapters 4 and 5 is validated in this Chapter, first for single crack experiments (without reinforcement in Section 6.1.1 and with reinforcement dowel action in Section 6.1.2), then for structural components in Section 6.2. In order to properly handle the interaction between reinforcement and concrete—necessary to simulate realistic crack behavior in the general case—a brief overview of the modeling approach is given below. There, the crack constitutive model from the previous Chapters is augmented with a simplified model for including the reinforcement effects (such as those that were discussed in Section 2.2.4).

In the previous Chapters, a constitutive model for a crack was introduced, intended for use within discrete analysis of crack systems – i.e., direct inclusion of individual cracks in a finite element model of a structure. The crack constitutive law indirectly captures effects of reinforcement via pressure-sensitive yield surfaces, but the crack element itself does not "know" that its nodal forces are partially imparted by adjacent reinforcement elements. Thus, it is necessary to model the reinforcement elements separately. A simple reinforcement model that captures yielding in flexure, bearing against concrete, bond slip, and the interaction of these effects with interfacial shear resistance is described in detail in Appendices A and D. The approach, wherein reinforcement is modeled with fiber elements and is discretized along its length so that zero-length node-to-node interaction elements can be placed at the bar-concrete

interface, is summarized in Fig. 6.1. The zero-length interface elements capture dowel action (pictured in the figure) as well as bond slip (not pictured), which is important for predicting the clamping stress transmitted to the crack.

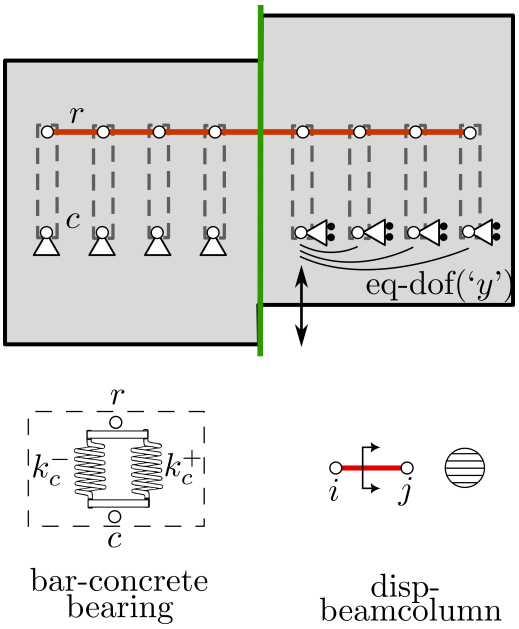

Figure 6.1. Simplified geometric model of the "crack influence zone" for dowel action problems. Boundary conditions and loads shown for pure sliding action

The modelling approach summarized in Fig. 6.1 is valid in the so-called "crack-influence zone", which extends about 5 bar diameters on either side of the crack. Within this region, each reinforcement node is attached to adjacent concrete by multiple interaction elements. In the bar-perpendicular direction, a `Series` material was developed to simulate local bearing stiffness of reinforcement against concrete. In the bar-parallel direction, a macro-element was developed that captures the mechanical and frictional aspects of bond slip. For the simplified modeling of bar-crack effects, the interaction of the two directions was not considered. Future models may seek to include this effect, whereby bar pullout weakens the bearing stiffness.

6.1 Crack Model Calibration

The primary goal of this Section is to demonstrate the versatility of the multi-surf-crack2D model by reproducing a large number of experiments. A heap of high-quality data has been gathered for cracks tested both monotonically and cyclically, representing a broad range of load conditions, reinforcement layouts, initial crack widths and material properties.

In Section 6.1.1, 26 aggregate interlock specimens are simulated and compared with the reported experimental data. Each simulation is repeated many times within the quoFEM [110] framework until a set of model parameters is found that minimizes the error between measured and simulated response. In this manner (see Appendix C for more details on utilizing quoFEM), the multi-surf-crack2D model is calibrated.

From the best-fit results of the calibration dataset, simple relationships are proposed that link the best-choice model parameters with the measured crack width. These relationships are statistical curve-fits over the entire calibration dataset and seek to be broadly applicable. Ideally, most cracks "in the wild" will fall within the confines of the proposed relationships. Though this Thesis deals primarily with isolated cracks, it is envisioned that the multi-surf-crack2D model could eventually be used within meshes of diffusely cracked structures, in which case simple rules for establishing the model parameter values at each material point will be imperative.

6.1.1 Aggregate Interlock Calibration

As a first calibration step, experimental tests of plain concrete interfaces are replicated with the multi-surf-crack2D model. Monotonic tests are simulated in Section 6.1.1.1 and reversed-cyclic tests are simulated in Section 6.1.1.2.

6.1.1.1 Monotonic Tests

Though many experiments have been performed monotonically on individual cracks, only those that report detailed crack data are included in the calibration dataset. In addition to shear and slip data, which are standardly reported, the crack width and normal stress response are included in each calibration, as a unique replication of shear-slip behavior cannot

be guaranteed without them. In other words, any number of boundary conditions and model parameters may produce identical sliding response. With this restriction in mind, only experiments that report width, slip, shear and normal stress are simulated, to encourage unique calibrations.

The experimental campaigns reporting both stresses and both displacement components are summarized in Table 6.1. The Table reports the researcher who performed the experiments, whether the experiments were performed in load or displacement control and the Table briefly describes the boundary conditions. The Table also lists the total number of aggregate interlock specimens tested by the researcher as well as the subset of those specimens that have been validated in this Thesis. Specimens tested by Walraven [176] and Tirassa [166] were not simulated in this work, but could eventually be included. More detailed interpretation of the listed experiments can be found in Chapter 2.2.

Table 6.1. Summary of monotonic aggregate-interlock experiments

Researcher	No.	Control	Boundary Conditions
Calvi [25]	6/6	Load	shear-proportional with tensile load ratio $\gamma \leq 1$
Becks [18]	4/4	Displacement	constant width
	1/1	Displacement	linear increasing width
Tassios [165]	1/5	Displacement	constant clamping stress
Jacobsen [78]	3/16	Displacement	constant forced dilation angle
Hassanzadeh [74]	5/15	Displacement	parabolic crack path
	1/2	Displacement	stair-step path
Walraven [176]	–	Displacement	"natural" crack opening
Tirassa [166]	–	Displacement	constant forced dilation angle

The experimental campaigns by Calvi, et al. [25] and Becks, et al. [18] examine crack behavior up to large slips. Given the context of this thesis in earthquake engineering, where cracks may undergo significant sliding and may open substantially (ostensibly developing widths up to 9 mm for certain wall shear cracks), these experiments are given the most attention, and in fact, all tested specimens from these two groups are simulated. A

handful of specimens are validated from the remaining test groups so that the calibration set represents a variety of boundary conditions and test parameters.

Calvi Validation Tests The specimens PC3, PC4, PC12, PC16, PC17 and PC18 were tested by Calvi, et al. [25] under single-sided cyclic loading. The "cyclic" specimens are taken here to be representative of monotonic crack behavior because the cycles were not repeated, but merely unloaded/reloaded at select load stages and the crack response did not vary from the monotonic backbone. It is also noted that reinforcement across the primary crack was de-bonded across a large length to prevent any dowel contribution to the total shear. Thus, the cyclic, reinforced tests of Calvi can be classified as monotonic aggregate interlock specimens.

The six specimens were modeled in OpenSees adopting the simple crack-bar configuration sketched in Figure 4.2. The model consists of two overlapping nodes connected by two zero-length elements. The first element is a 2-dimensional element (`zeroLengthND`) that is assigned the `multi-surf-crack2D` material to represent the crack multi-dimensional force-displacement behavior. A second `zeroLength` element describes the uniaxial reinforcement force-displacement response ($\rho_s = 0.01085$, $f_{sy} = 618$ MPa) with a simple elastic-perfectly-plastic (`ElasticPP`) material law. Node 1 is fixed and node 2 is passed a reference load vector $[\gamma v \; v]$ corresponding to the particular experimental load ratio ($0 < \gamma < 1$) adopted for each test. It is noted that the initial cracked state is represented in OpenSees without having to model physical nodal separation; initial crack width is carried as an internal variable within the crack constitutive law and initial strain is passed to the reinforcement element.

The OpenSees analysis is performed in displacement control, even though the actual experiments were load controlled; displacement control facilitated a point-by-point comparison of the predicted and actual responses, required for evaluating the validation error function within the quoFEM workflow. Each OpenSees model was simulated repeatedly until a set of model parameters was found that minimized the calibration error function, as described above and in Appendix C. Results of the optimization are plotted in Fig. 6.2 for the Calvi test series. Best-fit stiffness parameters ($D_{ts,0}$, f_{cl}) and best-fit monotonic model parameters ($\hat{\rho}$, χ_{lok}, $\tilde{\theta}$) are reported in Table 6.2.

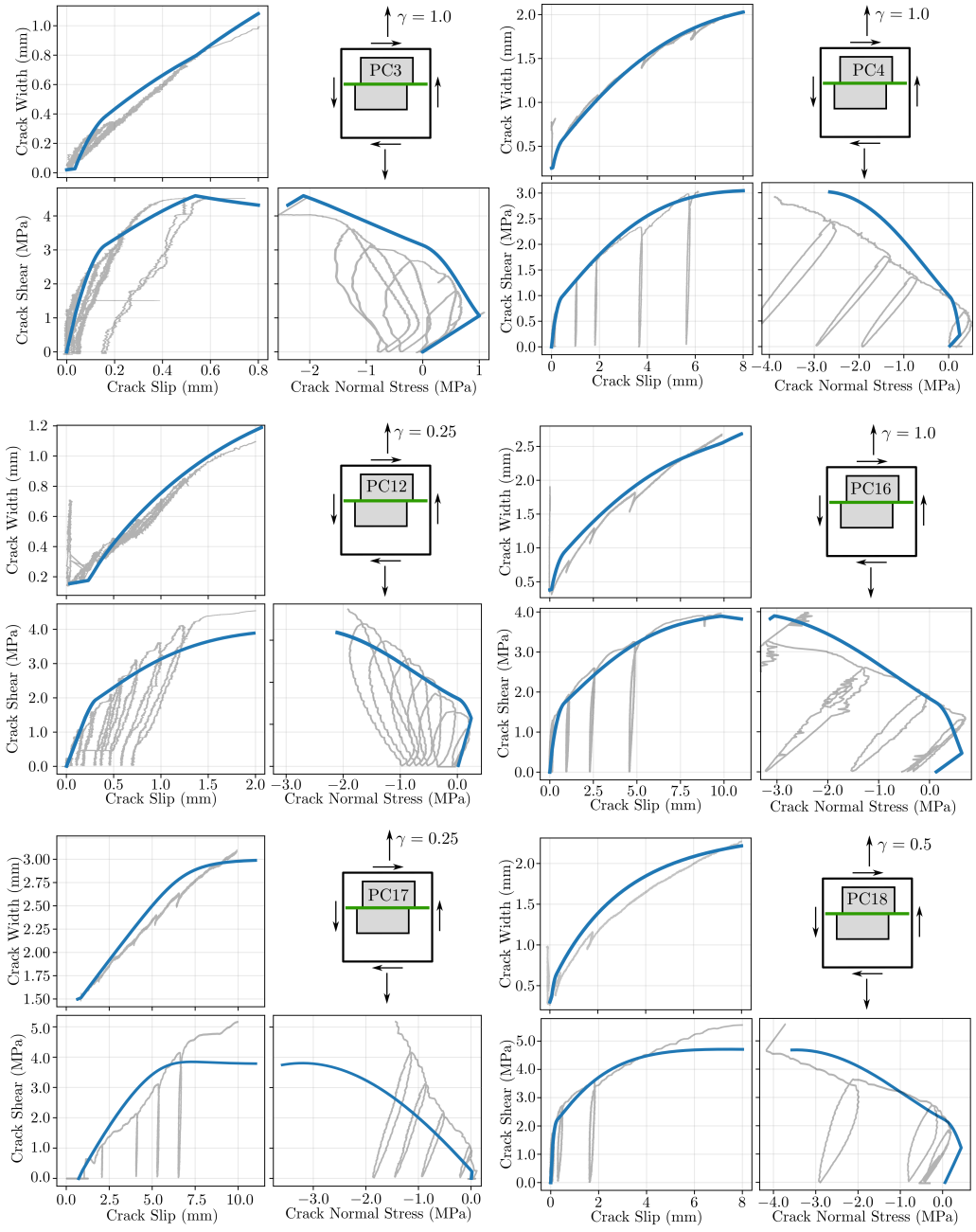

Figure 6.2. Optimal model parameters for matching Calvi cyclic experiments

The Calvi tests were "natural" cracks, the simulations of which are evaluated and updated based on errors in predicted shear stress and crack width. Indeed, for each specimen in Fig. 6.2, the crack dilation and the shear-slip backbone are replicated remarkably well. Minor errors in the shear-slip curves for specimens PC12, PC17 and PC18 seemingly arise from the tendency of the multi-surf-crack2D model to saturate as v_{ci} approaches v_{cimax}. If in the future, it becomes apparent that the multi-surf-crack2D model systematically underpredicts peak shear, the shape parameter k, which vertically scales the vertex of the yield surface, could be included as a user parameter.

It is emphasized that the best-fit simulation curves follow the experimental clamping stress rather closely, even though the crack normal stress was not included in the calibration cost function. This inspires confidence that the mechanics underlying the pressure-sensitivity of the shear strength are sufficiently captured by the yield surfaces that were proposed in Chapter 4 to govern aggregate interlocking.

Becks Monotonic Tests Each of the four constant-width cracks tested monotonically with the novel "TorAx" tester [18] are simulated here. Each crack was formed from the same batch of high-strength concrete with aggregate size of 4 mm. Because concrete strength was not specified in the original publication, a strength of 65 MPa is assumed here. The four tests were performed for crack widths of 0.25, 0.50, 0.75 and 1.00 mm. Given the small aggregate particles used, these crack widths represent "large" cracks.

Modeling of the Becks specimens was again done in OpenSees, with a single `zeroLengthND` crack element connecting two overlapping nodes. The crack element was assigned the `multi-surf-crack2D` material model and sliding displacements were imposed using the `sp()` command. The quoFEM parameter-determination scheme was again used, with the normal and shear stresses being fed to the error cost function, as crack width was held fixed. An added constraint was enforced that the stiffness should decrease with increasing crack width. Therefore, after identifying the stiffness for the narrowest crack, the allowable range for $D_{ts,0}$ was decreased for subsequent validations of larger crack widths. Following this approach, the curves of Fig. 6.3 were obtained. The corresponding material parameters are summarized in Table 6.2. It is noted that the same value of $\tilde{\theta}$ was obtained for each validation, corresponding to the extreme value of the range $(\pi/2)$.

A noteworthy trend from the outputs of Fig. 6.3 is that sliding damage participation $\tilde{\theta}$ is maxed out for the considered constant-width tests. Intuitively, the high sliding damage results from the forced ploughing of aggregate particles through the concrete matrix of the opposite crack face. Less intuitive is the prediction that cohesion χ_{lok} is predicted to vanish under constant-width conditions. One possible explanation is that the small aggregate diameter contributed little cohesive resistance to sliding due to the high w/a_g ratio.

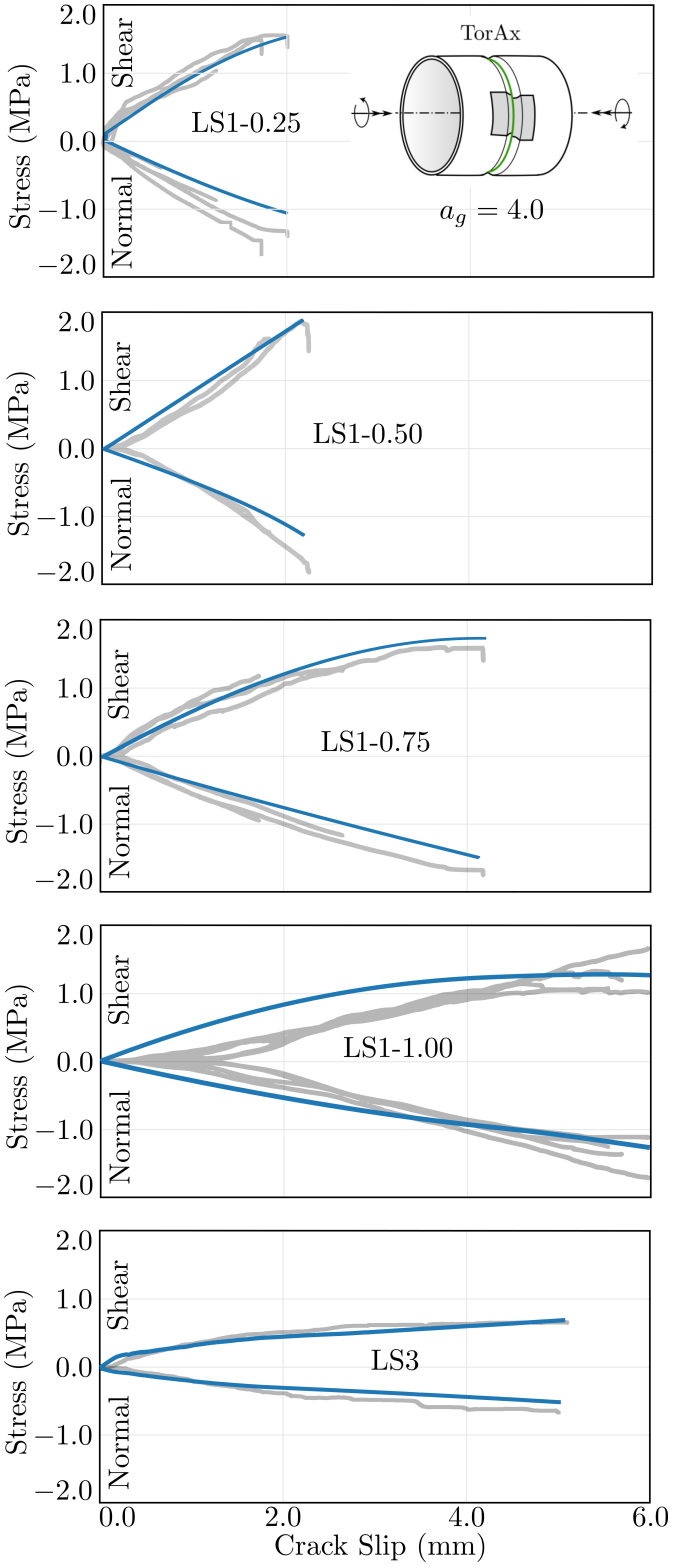

Figure 6.3. Optimal model parameters (model prediction in blue) for Becks constant-width monotonic experiments (LS1 series)

Jacobsen Forced-Dilation Tests The initially intact, double-notched specimens (see schematic in Fig. 6.4) of Jacobsen [78] were tested in a sequential displacement process. These tests represent the first verification of the multi-surf-crack2D model's path-dependency capabilities, all too important for earthquake-type loading.

In a first loading phase, a crack was formed at the weak section of the notched specimens, and the pure tensile load was sustained until a crack of desired width was obtained (the crack width at the end of phase I did not exceed 0.1 mm for any of the 15 tests). Then, in a second loading phase, a constant dilation angle was imposed between the crack faces without letting the phase-I crack unload.

While the constant-dilation-angle process is artificial and does not reflect crack dilation in "true" loading scenarios, the Jacobsen experiments provide a unique opportunity to demonstrate that the multi-surf-crack2D model can predict crack behavior for scenarios that deviate from expected behavior.

To avoid skewing the calibration dataset too far toward artificial dilation patterns that may not represent reality, only three specimens of the test group are calibrated here. The three specimens included in the calibration dataset all develop a phase-I crack width of 0.1 mm and are dilated at imposed angles of 40°, 45° and 50° up to crack slips near 0.5 mm. The OpenSees simulation using the `multi-surf-crack2D` material model is compared in Fig. 6.4 against the reported experimental data. Best-fit model parameters are summarized in Table 6.2, where it is seen that the sliding-damage participation factor $\tilde{\theta}$ is at the upper end of the parameter's range. Again, as for the pure-sliding tests of Becks, it appears that the ploughing parameter is necessary to capture shearing damage during forced sliding processes. It is also noted that the predicted shear stiffness of the Jacobsen specimens is significantly larger than the for cracks of Calvi or Becks, which were wider. Furthermore, the shear stiffness parameters obtained for the three Jacobsen cracks align with the value of 90 MPa/mm suggested by Jacobsen [78] for use with a simplified crack model that does not explicitly consider the surface topography.

Hassanzadeh Parabolic Path Tests The tests performed by Hassanzadeh on double-notched specimens include, like those of Jacobsen, tests with various imposed dilation paths, including linear, parabolic and non-proportional paths. The specimens forced along parabolic paths, deemed

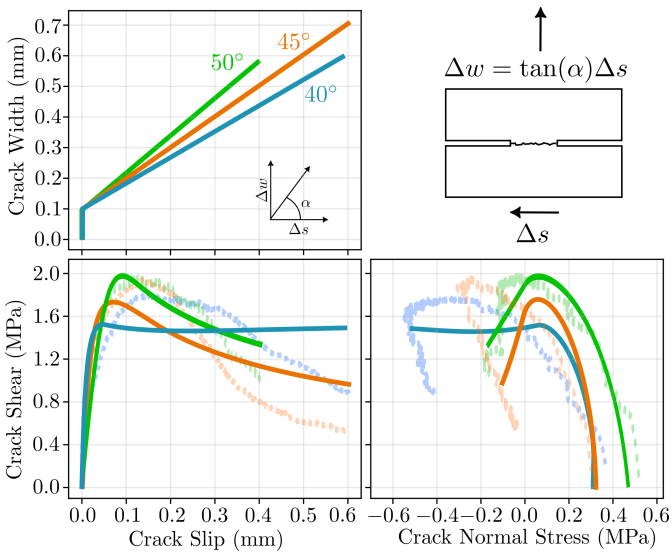

Figure 6.4. Optimal model parameters (model prediction in solid lines) for Jacobsen forced-dilation experiments with initial crack width of 0.1 mm)

more natural by Hassanzadeh, are simulated first. The testing protocol is nominally identical to that of Jacobsen save for the phase-II crack path, which is described by the family of curves: $w = \beta\sqrt{s}$ where β ranges from 0.4 to 0.9. The best-fit OpenSees simulations with the `multi-surf-crack2D` material law are shown for five of the Hassanzadeh specimens in Fig. 6.5a. The corresponding best-fit parameter sets are provided in Table 6.2. As the dilation path grows steeper, the best-fit values of $\hat{\rho}$, $D_{ts,0}$ and χ_{lok} decrease, as expected due to a decreasing fraction of contact area.

Next, the mixed displacement path shown in Fig. 6.5c is simulated. The mixed path consists of an initial linear segment, followed by a jaunt along the $\beta = 0.4$ parabola, which then transitions linearly up to the $\beta = 0.6$ parabola where the last leg of loading occurs. The experimental and simulated results are shown in Fig. 6.5b, along with reference results for the two parabolic loading paths. Along the initial linear branch, which is flatter than the parabolic paths for low slips, the crack shear accumulates rapidly. At the intersection of the linear path with the shallow parabola, the crack shear of the two paths is not equal due to concrete's path-dependent behavior. The subsequent loading branch along the $\beta = 0.4$ parabola is shallower than

the initial linear branch and causes a spike in the crack shear. The third loading branch consists of a linear jump from the shallow parabola to the steep parabola and sees the crack shed significant shear. The final branch of loading along the $\beta = 0.6$ parabola is accompanied by a gradual decay in shear resistance. It can be observed that the `multi-surf-crack2D` model prediction in blue captures the experimental path-dependent trends (gray) rather well. Notably, *the numerical crack model has a memory of previous damage* and does not revert to the reference $\beta = 0.6$ curve after the mixed displacement path merges to the $\beta = 0.6$ parabola.

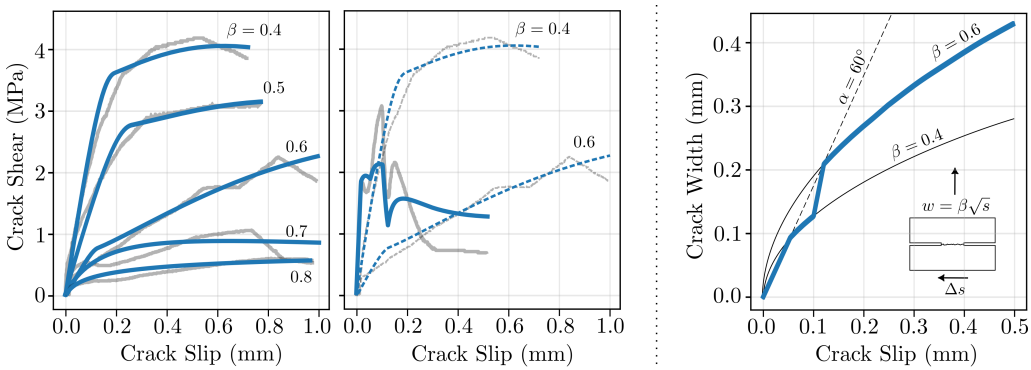

Figure 6.5. Best-fit simulations (solid blue) for Hassanzadeh test group (solid gray) with: (a) parabolic displacement path and (b) mixed linear-parabolic displacement path. Displacement paths shown in (c)

Tassios Constant Clamp Tests Tassios and Vintzeleou [165] tested rough cracks subjected to monotonic sliding displacement with a constant clamping stress imposed across the crack. Clamping pressures ranged from 0.5-2.0 MPa. Generally, the shear response exhibited an initial linear stage, followed by gradual hardening. One of the specimens, R-30,1.0/M, is simulated in OpenSees with the `multi-surf-crack2D` material model. The predicted response in shown and compared with the experimental response in Fig. 6.6. As already anticipated in the monotonic parameter study of Section 4.1.4, the crack material model tends to predict an extended elastic response when an initial pre-clamping load is followed by pure shear. The quoFEM optimization appears to find a solution that balances the error by softening significantly post-peak to compensate for the early over-estimation

of shear strength. This is not ideal and should be remedied in future releases of the material model. In the context of crack-based assessment, the crack model would errantly predict a brittle loss of shear capacity for any observed crack state beyond the yield point.

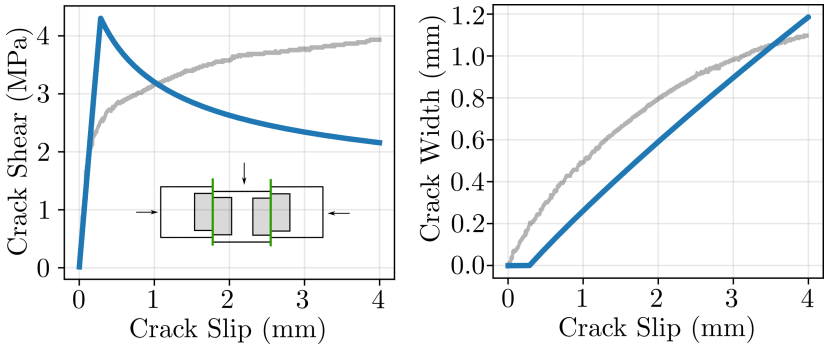

Figure 6.6. Best-fit simulation (solid blue) for Tassios test specimen R-30,1.0/M with constant clamping stress of 1.0 MPa

Monotonic Parameter Guidance The collection of calibrated monotonic aggregate-interlock tests are summarized in Table 6.2 as well as in Fig. 6.7. The Figure plots the trends of the initial shear stiffness ($D_{ts,0}$), the dilation parameter ($\hat{\rho}$) and the interlock cohesion (χ_{lok}) against the initial experimental crack width. Each of the three parameters decreases approximately linearly with increasing initial crack width, according to the following relationships:

$$D_{ts,0} = -45.4w_0 + 31.7 \geq 1.0 \tag{6.1}$$

$$\hat{\rho} = -0.84w_0 + 0.87 \geq 0.15 \tag{6.2}$$

$$\chi_{lok} = -0.43w_0 + 0.25 \geq 0.01 \tag{6.3}$$

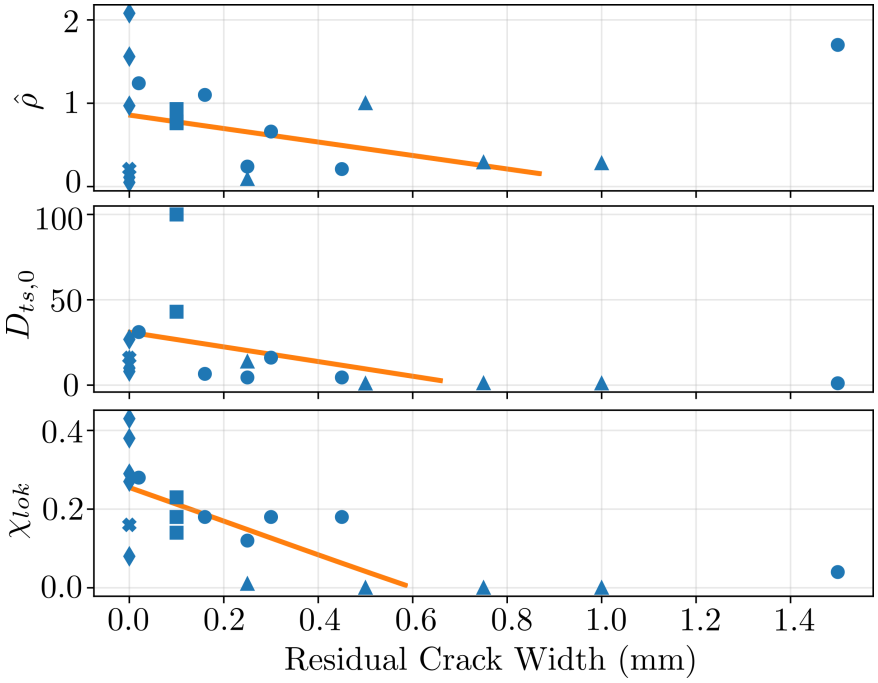

Figure 6.7. Best fit parameters for the monotonic calibration dataset
□: Jacobsen, △: Becks, ◯: Calvi, ◊: Hassanzadeh, X: Tassios

Table 6.2. Summary of best-fit parameters for monotonic aggregate-interlock experiments (units in MPa, mm)

Specimen	f'_c	a_g	w_0	$D_{ts,0}$	f_{cl}	$\hat{\rho}$	χ_{lok}	$\tilde{\theta}$
Calvi, et al. [25]								
PC3	44	14	0.02	31.1	14.7	1.24	0.28	0.0
PC4	38	14	0.25	4.5	12.7	0.24	0.12	0.0
PC12	31	14	0.16	6.6	1.9	1.1	0.18	0.0
PC16	103	14	0.45	4.5	25.0	0.21	0.18	0.0
PC17	93	14	1.50	1.1	1.8	1.70	0.04	0.0
PC18	93	14	0.30	16.1	2.0	0.66	0.18	0.00
Becks, et al. [18]								
LS1	–	4	0.25	13.8	1.0	0.09	0.01	0.78
LS1	–	4	0.50	0.9	25.0	1.00	0.00	0.78
LS1	–	4	0.75	1.1	1.6	0.29	0.00	0.78
LS1	–	4	1.00	1.0	1.1	0.28	0.00	0.78
LS3	–	4	0.40	1.42	0.25	0.62	0.01	1.57
Jacobsen, et al. [78]								
$\alpha_{40}/w_{0.1}$	41	8	0.10	100	1.0	0.78	0.14	1.56
$\alpha_{45}/w_{0.1}$	41	8	0.10	100	0.5	0.76	0.18	0.78
$\alpha_{50}/w_{0.1}$	41	8	0.10	43	1.0	0.93	0.23	1.56
Hassanzadeh [74]								
$\beta_{0.4}$	50	8	0.00	26.8	1.0	2.08	0.43	0.0
$\beta_{0.5}$	50	8	0.00	14.7	1.0	1.56	0.38	0.0
$\beta_{0.6}$	50	8	0.00	8.0	1.0	0.97	0.08	0.0
$\beta_{0.7}$	50	8	0.00	10.0	1.0	0.11	0.27	0.0
$\beta_{0.8}$	50	8	0.00	10.0	1.0	0.05	0.29	0.0
α_{60}–$\beta_{0.4}$–α_{76}–$\beta_{0.6}$	50	8	0.00	100	0.5	0.61	0.22	1.57
Tassios and Vintzeleou [165]								
$R-30, 1.0/M$	30	–	0.0	16.0	1.0	0.21	0.16	0.0

6.1.1.2 Reversed-Cyclic Aggregate Interlock Tests

A set of detailed aggregate-interlock tests has previously been curated (see Table 2.1) representing twelve experimental campaigns. A pared down version of that table is replicated below as Table 6.3, which includes only the experiments that investigated aggregate interlock in isolation. Even with the small dataset, a variety of boundary conditions are represented: "natural" boundary conditions were adopted by both Calvi [25] and Gebreyouhannes [71], each of whom employed unbonded reinforcement to passively resist crack opening. Gebreyouhannes' test specimens were subjected to a constant amplitude of shear cycles until failure, while the Calvi specimens were subject to increasing shear amplitudes with three cycles at each amplitude. A rough crack subject to repeated 5 mm displacement cycles was tested by Tassios [165] under constant compression of 0.5 MPa. Puntel [143] also tested cracks under constant compressive stress but pushed the specimens to slip amplitudes from 10 to 40 mm. Lastly, Becks, et al [18] tested a crack with constant width of 0.25 mm under three cycles at increasing slip levels, up to a maximum slip of 3 mm.

In this Section, one specimen is simulated from each testing campaign from Table 6.3, using the `multi-surf-crack2D` material model that was described in Chapters 4 and 5 and implemented within the OpenSees framework. Unlike in the previous Section, the selection of best-fit parameters is done in this Section by manual trial-and-error, using as a guide the recommendations in Table 6.2 for monotonic parameters as well as the data provided in Fig. 2.12 for cyclic parameters.

Table 6.3. Summary of reversed-cyclic aggregate-interlock experiments

Researcher	**No.**	**Control**	**Boundary Conditions**
Calvi [25]	1/8	Load	shear-proportional tensile load ratio $\gamma \leq 1$ unbonded reinforcement 3 cycles each load lvl
Becks [18]	1/1	Displacement	constant width 1 cycle each slip lvl
Tassios [165]	1/1	Displacement	constant clamping stress 8 cycles at single slip lvl
Puntel [143]	1/5	Displacement	constant clamping stress large slip excursions 1 slip cycle at each slip lvl
Gebreyouhannes [71]	1/2	Load	shear-only load natural bc's w/ unbnd reinf repeated cycles at same shear lvl

Calvi PC9 Calvi [25] tested pre-formed cracks under combinations of shear and tensile load, to test crack behavior under realistic loading conditions expected at a naturally formed crack. Specimen PC9 was subject to loading cycles that were repeated at incrementally increasing shear magnitudes until failure, keeping steady a tension-to-shear load ratio of 0.5. Specimen PC9 was cycled first at low stress levels, progressively building in amplitude, three cycles at a time, to failure. Reinforcement was provided across the crack to resist crack opening in a natural manner, and was unbonded to avoid kinking action and dowel shear.

The test of Calvi was simulated in OpenSees using the `multi-surf-crack2D` material model in parallel with a `zeroLength` reinforcement element with an effective stiffness to match the experimental reinforcement configuration (ρ_s=0.01085, L_{unb} = 700 mm). The OpenSees modeling approach has been described in detail in an earlier Section. Initial guesses for monotonic model parameters were selected based on the residual crack width of specimen PC9 (w_0 = 0.2 mm), using the guidance of Fig. 6.7. Cyclic model parameters such as the breakaway dilation factor ρ_{act} and the breakaway friction μ_{act} were initially selected based on the review of experimental data in Chapter 2.2. Starting points for the roughness transition factor κ and the slip-engagement factor ζ were -1.0 and 0.3, respectively. The experiment was simulated and the model parameters were iteratively tweaked to arrive at a best-fit set of model parameters. This set reproduces the simulation presented in Fig. 6.8a and is provided also in Table 6.4.

Becks Becks [18] measured the shear and normal stresses transferred across a crack throughout 3 slip cycles of increasing amplitude. The LS2 crack specimen was constrained to maintain a constant width of 0.25 mm throughout the test. This constraint was applied in OpenSees via the `sp()` command, along with an imposed sliding history via a `Path timeSeries`, passing the array of crack slip history also to an `sp()` command.

Model parameters were chosen based on the results of the monotonic tests of the LS1 series, also performed by Becks and team, as well as the experimental data summarized in Chapter 2.2. The parameters used to generate the model simulation of Fig. 6.8b are summarized in Table 6.4. The best-fit set of parameters proves quite accurate in predicting the crack hysteresis for the constant-width test, but does slightly undershoot the free

slip portion of the later cycles. This seems to follow from the restriction that each model parameter is held constant. In reality, the process may evolve, as discussed in regards to Fig. 2.12, and a future model improvement will be to incorporate such evolution laws, particularly for ρ_{act}.

Tassios R-30,0.5/2.0 Tassios [165] measured the shear-capacity degradation of a pre-formed, narrow crack during 8 repeated slip excursions between ±5 mm, carried out under constant compression. The specimen R-30,0.5/2.0 ($f'_c = 30$ MPa, $\sigma_n = -0.5$ MPa) is taken as a representative specimen for rough, normal strength cracks under light compression, cycled at post-peak displacements. The measured shear-slip hysteresis, shown in gray in Fig. 6.8c, indicates that dissipated energy decreases at a decreasing rate for repeated cycles. In other words, the first cycle causes the most damage, and then damage eventually stabilizes in subsequent cycles at the same displacement level.

A numerical simulation of specimen R-30,0.5/20 is overlayed in blue on the experimental shear-slip curve of Fig. 6.8. To perform the analysis in OpenSees, the constant compressive stress is applied in a first load stage, then shear loads are applied in a second load stage (using displacement control). The best-fit cyclic parameters include a breakaway friction constant of 0.20, an interlock dilation knockdown of 0.15, an activation dilation knockdown of 1.0, a κ value of 0.75 and a ζ value of 0.0. The simulation reproduces the peak shear and the subsequent decay of shear strength with additional cycles.

Puntel Puntel [143] tested the frictional behavior of large lift-joints, typical of joints found in concrete dams. The "Test 3" specimen was compressed to a constant clamping stress of 0.37 MPa and pushed to slips of ±35 mm. Interestingly, the experimental response of Test 3 under constant clamping (see Fig. 6.8d) varies slightly from that of Tassios. Instead of the gradual hardening observed in the first cycle of the Tassios experiment, Test 3 decays drastically after attaining the initial peak. This behavior is replicated by the simulation. Slight differences in the breakaway friction and residual loading resistance are artifacts of modeling choices described in Chapter 5. Namely, the activation cohesion is restrained to less than the interlock cohesion. Were these two de-coupled the experimental shear-slip response of Test 3 could be improved.

The dilation behavior of the lift joint is significantly over-predicted by the model. Again, this indicates that both $\hat{\rho}$ and ρ_{act} should be given evolution laws. Were $\hat{\rho}$ to decrease with damage, the excessive over-prediction of crack widening could be avoided for large slips.

Gebreyouhannes NSC-RCL1 Gebreyouhannes [71] tested the fatigue performance of rough, moderate-width cracks under low- and high-cycle fatigue. The low-cycle fatigue response of specimen NSC-RCL1, which had an initial crack width of 0.61 mm and underwent load cycles between ± 2.26 MPa until failure, is reproduced in Fig. 6.8e. The cyclic load magnitude corresponded to 70% of the specimen's monotonic failure load, and led to substantial stiffness degradation in the reversed sliding direction. The numerical prediction does not capture this trend, though the shape of individual hysteresis loops is promising. Furthermore, the dilation prediction significantly under-predicts the experimentally measured dilation. The experimental pattern indicates bar pullout, though no such mention was made by Gebreyouhannes in the original publication.

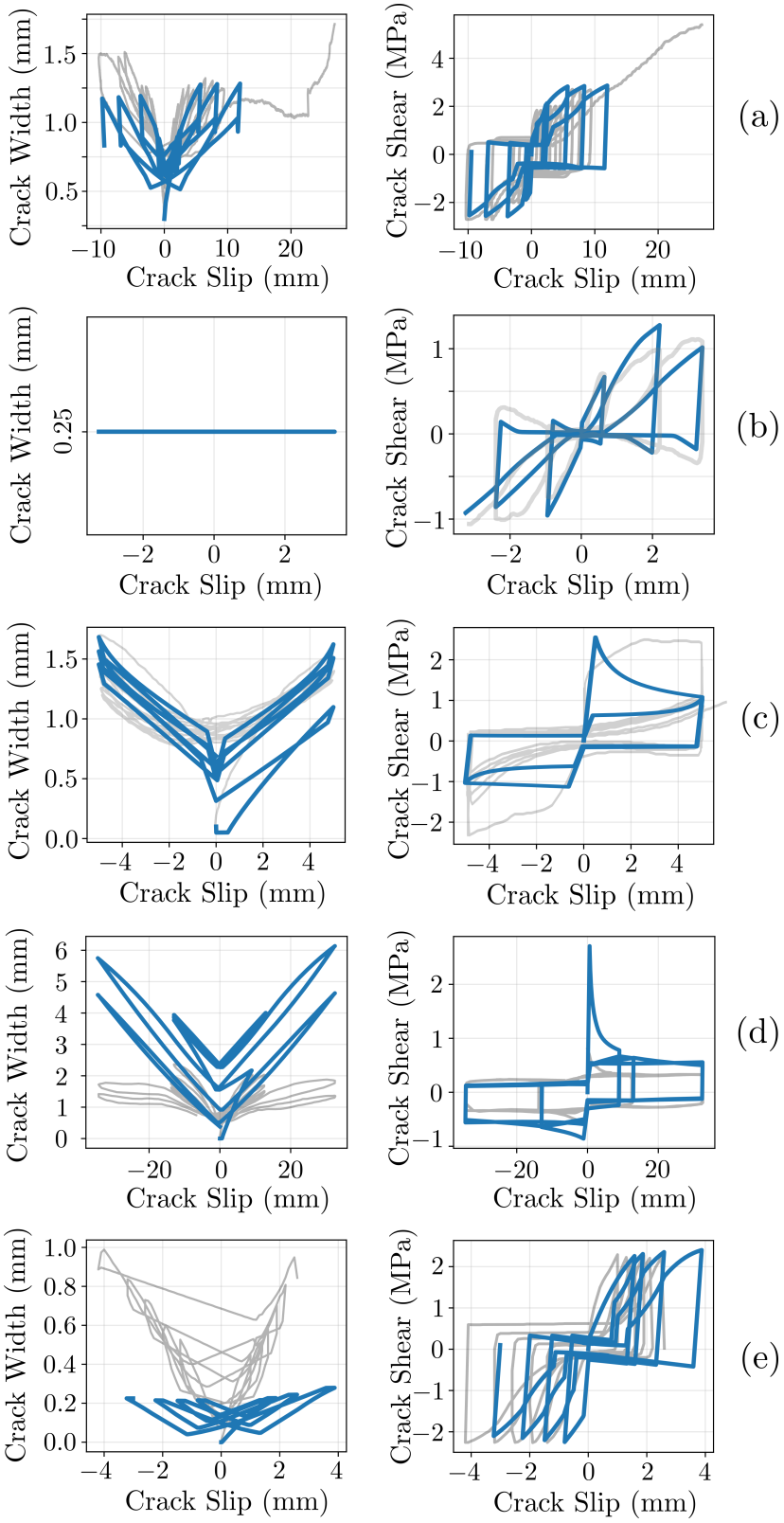

Figure 6.8. Validation of `multi-surf-crack2D` model against suite of reversed-cyclic aggregate interlock experiments: (a) PC9 [25], (b) LS2 [18], (c) R-30,0.5/2.0 [165], (d) Test 3 [143], (e) NSC-RCL1 [71]

The best-fit model parameters for the reversed-cyclic aggregate interlock experiments are summarized in Table 6.4, where it is seen that there is remarkable unlformity across the 5 experiments, which covered different boundary conditions, crack widths and slip amplitudes.

Table 6.4. Summary of best-fit parameters for reversed-cyclic aggregate-interlock experiments (units in MPa, mm)

Specimen	$D_{ts,0}$	f_{cl}	$\hat{\rho}$	χ_{lok}	$\tilde{\theta}$	ρ_{act}	μ_{act}	χ_{act}	κ	ζ
PC9	8.0	1.0	0.30	0.08	0.0	1.5	0.22	0.08	0.65	0.30
LS2	7.0	0.5	0.15	0.01	1.57	1.0	0.20	0.01	0.45	0.30
R-30,0.5/2.0	5.0	1.0	0.15	0.15	0.55	1.0	0.20	0.05	0.75	0.0
Test 3	5.0	0.5	0.15	0.15	0.05	1.25	0.20	0.15	0.0	0.0
NSC-RCL1	10.0	1.0	0.5	0.03	0.5	1.5	0.25	0.03	0.5	0.5

6.1.2 Rebar Dowel Action

The suitability of the modeling approach (described in Appendix D) for simulating rebar dowel action is assessed in this Section by replicating the reversed-cyclic dowel response of two representative experimental specimens, one tested by Vintzeleou and Tassios [175] and the other by Moradi [120]. The two experimental campaigns adopted a similar testing setup, with minor differences. Each setup foresaw the formation of smooth, non-contacting interfaces (by virtue of plexiglass sheets placed between the two concrete pours) to preclude any aggregate interlock and isolate the dowel effect. A schematic of the two beam-type setups is shown in Fig. 6.9. Though the overall deformation of the two setups is different (Moradi specimen rotates, Vintzeleou specimen does not), the deformations in the beam local coordinate frame (i.e., axes aligned with the beam) are identical. Therefore the same modeling approach can be used for each experiment.

Because the shear resistance at the interface is solely provided by the reinforcement, it is sufficient to model only the reinforcement elements, taking care to also model the interaction between reinforcement and surrounding concrete. This permits the use of a geometrically simplified model that

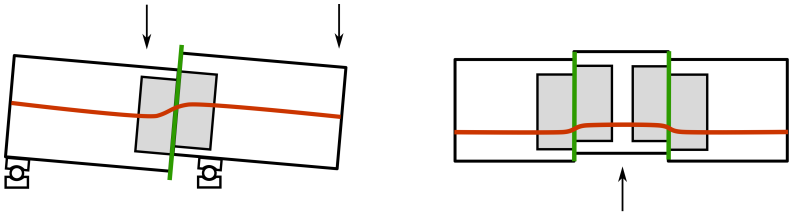

(a) Moradi Setup (b) Vintzeleou Setup

Figure 6.9. (a) Morandi beam-type test, and (b) Vintzeleou push-off style test

consists of a row of fixed concrete nodes and a row of reinforcement nodes, each occupying the same y-coordinate and having the same discretization in the x direction. Solid concrete elements are omitted without loss of predictive power. Reinforcement elements are modeled with `dispBeamColumn` elements and assigned fiber sections. The model geometry is summarized in Fig. 6.1. A `zeroLength` element, containing the material description of the concrete-bearing interaction, connects each pair of concrete and reinforcement nodes. To account for reversed-cyclic loading, the bearing element is modeled in each of the two directions perpendicular to the bar axis. Bond-slip interaction is not modeled, as its contribution was not noted in the experimental campaigns. In OpenSees, the same concrete node is used for each `zeroLength` element, and the directionality is manually assigned via the `-orient` keyword with the appropriate direction vector. By assigning different properties (e.g., concrete cover via Eq. (D.1)) to the two `zeroLength` elements at a node, an asymmetric response can be obtained. The model schematic is shown in Fig. 6.1 within the crack damage zone (gray region cut by green interface). Each spring in the bar-concrete bearing assemblage shown in the figure is described by the `Series` material outlined in Appendix D. Additionally, were bond slip to be modeled, the macro-element would contain additional springs in the crack-parallel direction.

Model parameters to be chosen or calibrated include: (s_{1p}, e_{1p}), (s_{2p}, e_{2p}), (s_{3p}, e_{3p}) and (s_{1n}, e_{1n}), (s_{2n}, e_{2n}), (s_{3n}, e_{3n}) to define the hysteretic backbone of Fig. D.1, as well as β_{ops} to regulate the rate of concrete unloading decay with plastic indentation. The pinching and damage options of the `Hysteretic` material are set to zero to reduce the number of modeling decisions.

The choice of the backbone points is done to match the semi-analytical

model of Pejatovic and Muttoni [135], for the range of dowel bearing displacement expected during the experiment. An estimate of the transverse bar deflection at the free crack can be obtained as half the crack slip ($\delta_\perp = s/2$). For the two specimens, each with 14 mm diameter reinforcement and slips s approaching 2 mm, the expected transverse displacement of a spring at the crack face is less than 1 mm, or $0.07d_b$. Bar transverse displacement will be even less farther away from the crack face. Since the bearing stiffness model of Pejatovic and Muttoni [135] is constant up to $0.02d_b$, a reasonable choice for the `Hysteretic` material backbone points is to set them at strain values $0.02d_b$, $0.04d_b$, and $0.07d_b$. The corresponding forces for each displacement are obtained from the secant stiffness of Eq. (D.1).

Lastly, the unloading stiffness damage rate β_{ops} must be calibrated. Typical values range between 0 and 0.5, with a value of 0 corresponding to pure plasticity (i.e., no reduction in elastic stiffness) and values greater than 0 corresponding to damaged unloading. Intuitively, a value of 0 corresponds to a more severe pinching shape, as the gap is larger and the material reloads more steeply. This was shown for a single material point in Fig. D.2. For the two specimens considered here, a choice of 0.2 produces the correct pinching shape near the origin, as shown in Fig. 6.10, where the numerically simulated dowel responses are overlayed on the experimental curves. It is noted that the experimental specimens unloaded nearly vertically (steeper than the initial loading stiffness), which leads to more pronounced loops than those that are predicted numerically. The choice of β_{ops} was controlled by this observation, as a higher value led to smaller loops, but a lower value led to over-exaggerated pinching. Even with a reduced hysteresis loop, the numerical analyses still predict residual, unloaded slips somewhat well. This feature is important for future applications in crack-based assessment routines.

In all, the simplified modeling approach provides a reasonable approximation of the dowel peak strength and pinching response. Inaccuracies in the initial unloading should be colored by observations that dowel action constitutes a relatively small portion of total crack shear resistance, particularly for small crack slips.

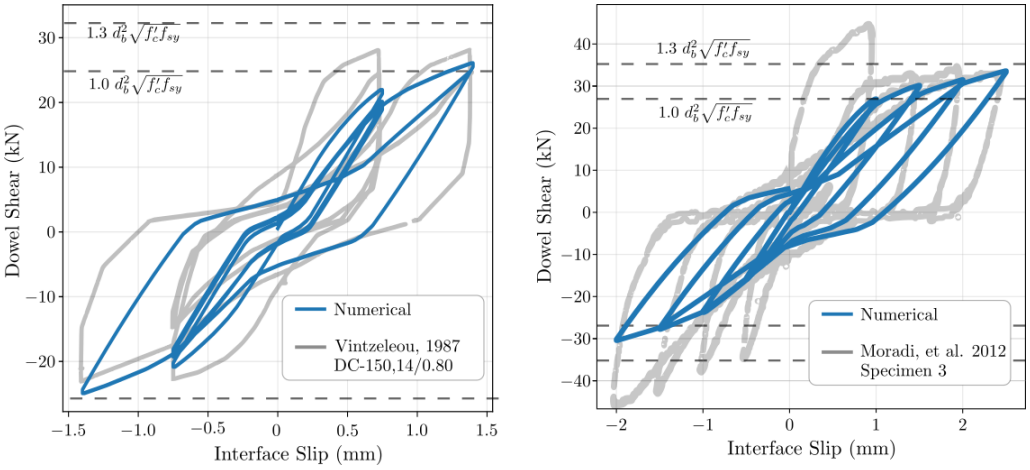

Figure 6.10. Simulated response of two dowel action laboratory specimens tested under fully reversed cyclic loading

6.1.3 Combined Interlock + Dowel Actions

A final step in the component-level verification involves simulations of aggregate interlock and dowel action simultaneously active, to confirm that the recommendations of Sections 6.1.1 and 6.1.2 produce reasonable predictions of combined (generalized) crack behavior. One well-instrumented specimen from the experimental campaign of Oikonomopoulou, et al. [125] is simulated to demonstrate the performance of the modeling approach. The experimental program of Oikonomopoulou is the only campaign that (to the Author's knowledge) provides measurements of both crack stresses and reinforcement deformations near the crack.

Oikonomopoulou, et al. [125] tested the cyclic response of long concrete interfaces crossed by post-installed screws. Post-installed screws are a common retrofit solution when external layers are added to existing concrete. This reinforcement configuration is characterized by a short embedment length and serves here to verify the effect of bar pullout on the effective clamping stress that can be transferred across an interface. In particular, specimen LR-23-G/65/01 is simulated.

Specimen LR-23-G/65/01 consists of an intentionally roughened interface that is 1200 mm long and 300 mm wide, crossed by 10 mm high-strength ($f_{sy} = 690$ MPa) post-installed anchors spaced at 100 mm and embedded to a depth of 65 mm. The average concrete strength is 25 MPa, the maximum

aggregate diameter is 32 mm and the surface roughness is 2.66 mm. Cyclic shear slips were imposed to the interface up to a maximum imposed slip of 5 mm, with three cycles performed at each slip magnitude. Strain gauges were placed on the extreme fibers of each dowel (2 gauges per dowel) to allow the separation of average axial clamping stress from dowel action. These measurements provide rare experimental data for the crack clamping stress in tests with bonded reinforcement.

In modeling specimen LR-23-G/65/01, a single anchor is modelled along its length, using fiber elements as outlined in Section 6.1.2. A 5 mm discretization is adopted for the reinforcement. Each reinforcement node along the length of the anchors is connected to a concrete node via uncoupled `zeroLength` elements for reinforcement bond slip and reinforcement bearing action. The nodal configuration resembles that of Fig. 6.1 with the addition of `zeroLength` springs oriented parallel to the bar to cacpture bond slip.

The approach for modeling bond slip is discussed in Appendix A whereby bond slip is simulated with `zeroLength EPPGap` elements. A bond strength of $1.0\sqrt{f'_c}$ is assigned to the reinforcement interface element with a secant stiffness of 20 MPa/mm at peak bond strength.

In the bar-perpendicular direction, a macro element is modeled at each node (see approach for modeling dowel action in Appendix D) to simulate the bearing action of reinforcement against solid concrete. A `Hysteretic` material is defined using experimental relationships [135] for reinforcement bearing. A β value of 0.2 is used for the `Hysteretic` material definition, based on results from Section 6.1.2.

At the crack interface, a `zeroLengthND` element is placed to represent the aggregate interlock resistance, passing the `multi-surf-crack-2d` material to the element. Values of the crack plasticity model parameters are chosen using judgement and guidance from the results summarized in Table 6.4 to simulate the expected cyclic behavior of the roughened crack in the LR-23-G/65/01 specimen. The set of parameters that best simulates the experimental test — arrived at by trial and error — is summarized in Table 6.5.

The simulation results are overlayed in blue on the experimental data in Fig. 6.11. The results show that the proposed crack model is capable of replicating the shear-slip and width-slip response, even when bar pullout is significant, as was the case for specimen LR-23-G/65/01. It is noted, however, that the simulated average cross-sectional bar strain tends not

Table 6.5. Model parameters passed to the `multi-surf-crack2d` model to simulate the aggregate interlock contribution to the shear resistance of specimen LR-23-G/65/01 (units in MPa, mm)

Specimen	$D_{ts,0}$	f_{cl}	$\hat{\rho}$	χ_{lok}	$\tilde{\theta}$	ρ_{act}	μ_{act}	χ_{act}	κ	ζ
LR-23-G/65/01	8.0	2.0	0.20	0.10	0.0	2.0	0.20	0.01	0.65	0.50

to recover as much as the experimental measurements, particulary during small amplitude slip cycles. This suggests premature flexural yielding of the reinforcement in the numerical model, possibly due to an underestimation of the bearing spring stiffness. The result in stress space (bot-left plot of Fig. 6.11) is a general over-prediction of clamping stresses passed to the crack interface. The simulation could be adjusted by increasing ρ_{act}, but values of ρ_{act} that improve the simulation of specimen LR-23-G/65/01 seem unrealistically high compared to those suggested in Section 6.1.2. It is also noted that the activation reversal region in the experiments (solid gray line) is much more gradual that predicted by the model, commencing even before the applied shear reverses sign. The `multi-surf-crack-2d` model cannot currently capture this phenomenon, as the activation yield surface is inactive until the sense of the applied shear switches.

6.2 Structural Components

Cracks in structural components may not exhibit the idealized behavior that is measured in laboratory specimens [1]. This is partly due to the inadequacy of the uniform-stress assumption (typically true in the lab) for describing "real" specimens, which are larger and subject to less controlled environments. This Section ensures that the material-point description of the `multi-surf-crack2d` model is generalizable via finite elements to capture variations of stress and damage along a crack, thereby reproducing complex behavior of cracks within common structural components. A novel coupling beam solution is modeled with the `multi-surf-crack2d` material in Section 6.2.1.

In modeling the medium size structural components, all intentions are

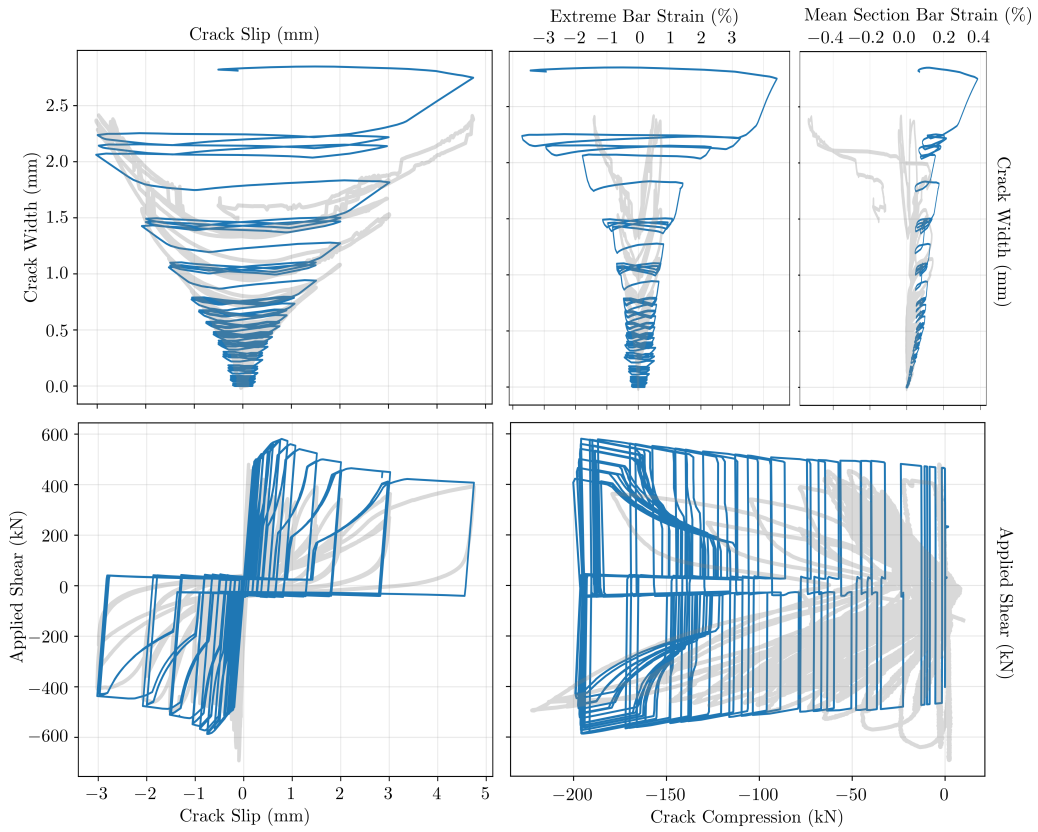

Figure 6.11. Simulation (solid blue) of specimen LR-23-G/65/01 overlayed on experimental measurements (gray)

to retain ease-of-modeling while capturing the important sources of non-linearity in the behavior of the structural component.

6.2.1 Double-Beam Coupling Beams

The double-beam coupling beam (DBCB) is a novel coupling beam solution that promotes and exploits the formation of a single, well-placed crack to ensure satisfactory earthquake performance in terms of strength and ductility [39], [38]. As a bonus, the reinforcement layout of the DBCB is less cluttered than a traditionally reinforced diagonal coupling beam, uses less reinforcement to achieve a similar performance, and improves repairability by shifting damage away from the beam-wall junction.

The DBCB solution consists of two reinforcing cages separated vertically by a through-thickness unreinforced concrete strip (UCS) at the mid-height of the beam. This layout is shown in Fig. 6.12. Initially, the beam resists seismic action monolithically as a traditional coupling beam, attracting large shear due to the low slenderness that is typical of coupling beam construction. During this initial elastic phase, the cross-sectional stress distribution in the uncracked concrete follows the classical distribution sketched in Fig. 6.12. Because the peak of the stress distribution aligns with the position of the unreinforced concrete strip at mid-height, a well-defined crack plane forms between the upper and lower reinforcement cages. The crack initiates at mid-span, farthest away from the built-in ends, and progresses towards the beam-wall interface. As the crack progresses, the DBCB resists load by means of the two increasingly de-coupled sub-beams that remain, each with twice the slenderness of the original coupling beam. With the increased slenderness, the beams respond in a controlled flexural manner that is consistent and predictable, thus ensuring the desired "weak-beam" yield mechanism.

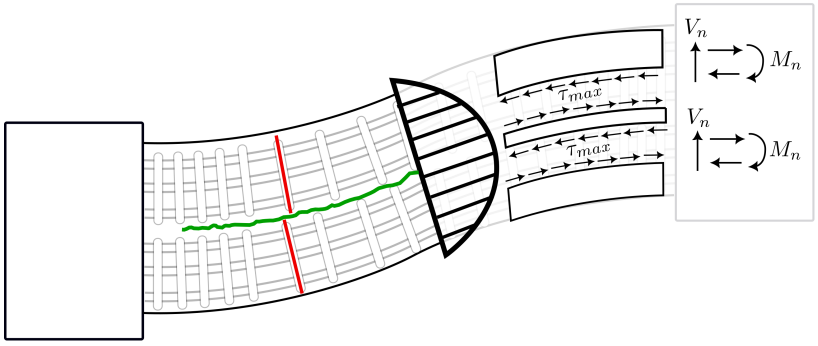

Figure 6.12. Transfer of forces at the mid-height crack of the double-beam coupling beam (adapted from [39])

The DBCB cannot fully separate into two isolated beams while simultaneously satisfying the continuity condition at the built-in ends. In fact, [38] estimates that the crack forms only along 90% of the beam span, leaving short intact portions near the ends. It can be reasoned that even the cracked span length is in firm contact, particularly at the crack front where the clamping stress is highest. Figure 6.12 also shows that the touching crack

faces slide in opposite directions to preserve plane-sections-remain-plane kinematics in each beam. This relative sliding action produces shear along the interface, which (see free-body diagram of Fig. 6.12) unburdens the top and bottom beams from some flexural demand. In experiments, the crack shear contributed between 10-25% of the total DBCB shear resistance [38].

To see the crack shear contribution, the nominal shear strength of each slender beam is de-componsed into a flexural contribution V_F and a crack-shear contribution V_{UC}:

$$V_n = V_F + V_{UC} \tag{6.4}$$

The effective crack contribution V_{UC} is obtained from moment equilibrium as $V_{UC}l' = V_{UCS}h_b/4$. Writing the shear stress at the crack as $v_{ucs} = V_{UCS}/(l'b_w)$, the nominal DBCB shear is composed as:

$$2V_n = \left(\frac{M_{pr}}{l} + \frac{v_{ucs}h_b b_w}{4}\right) \tag{6.5}$$

Proper design of the DBCB thus relies on an accurate estimation of the crack shear contribution to the total shear resistance; if the crack shear transfer is under-estimated or ignored, the coupling beam design may possess excessive overstrength. Choi and Chao [38] propose a conservative design shear strength of 2.1 MPa at the crack.

Initial testing [38] indicates that the amount of usable crack shear depends on the thickness of the unreinforced concrete strip. Conceptually, the mode of crack behavior depends on the inclination of the compression-resisting struts that form between adjacent hoops that protrude into the unreinforced concrete strip. A large gap promotes inclined compression struts for which the concrete crushes and forms a loose rubble. This crack mode is desirable, as the rubble layer acts like rollers and the two beams approach the de-coupled, pure-flexure idealization. However, the ability to increase the UCS thickness is limited, given that an increase in UCS thickness reduces the internal lever, and hence the strength, of the individual beams. On the other hand, small cage separation leads to significant aggregate interlock, which is trickier to predict and leads to incomplete cracking along the length of the UCS. Incomplete crack formation can delay the beam separation, risking the formation of inclined shear cracks and brittle failure of the DBCB. A lower limit of 38 mm was proposed for the UCS thickness [38].

Simulating the double-beam coupling beam The double-beam coupling beam is a simple, yet "real" earthquake-engineering application, playground for validating the crack material model proposed in Chapters 4 and 5 on the structural component scale. A model of the DBCB has been constructed in OpenSees (see Fig. 6.13). Each individual beam is modeled with a center-line "stick" model, i.e., displacement-based, beam-column fiber-section elements. Material characterization of the fibers is based on strength values reported in [39], using a 25% overstrength on top of the design reinforcement yield strength. The `multi-surf-crack2d` model is fed to `zeroLengthND` elements to simulate the shear transfer along the crack interface, placing 9 node-to-node crack elements along the span. With this mesh, the crack tributary areas do not count the small lengths near the beam-wall juncture ($0.05l$ on each side) that remain clamped by the built-in constraint. Rotational `rigidLink` elements cover the distance between the beam centerlines and the crack plane. It is noted that a change of spatial dimensions is required to link the nodes of the `zeroLengthND` elements – which have no rotational dof – with the beam-column nodes. This is done via an `equalDOF()` constraint (not shown in Fig. 6.13).

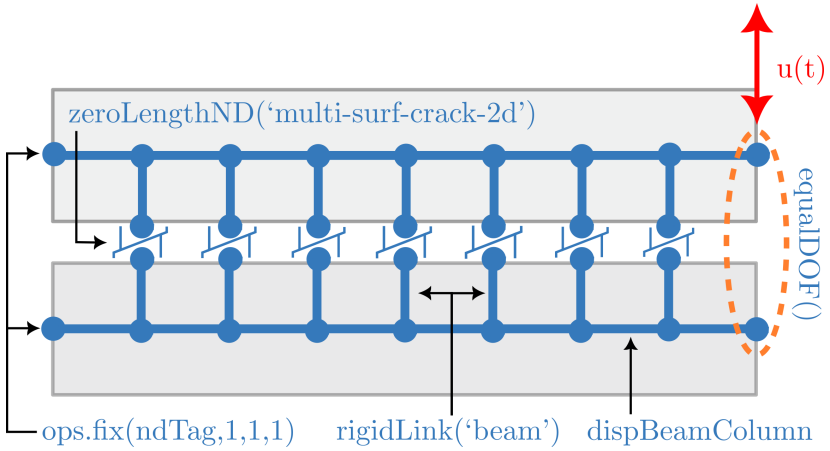

Figure 6.13. Schematic of OpenSees "stick" model for the double-beam coupling beams (note grayed out beams for visualization only)

As no detailed crack data is reported aside from v_{ucs} (which itself was not directly measured, but was back-calculated from Eq. (6.5)) the model parameters of the `multi-surf-crack2d` constitutive law are assigned based on the calibration results obtained in Section 6.1.1.2. All instances of the

`multi-surf-crack2d` material are assigned the same set of parameters, though it may eventually be logical to assign different parameters to crack elements depending on their proximity to the mid-span or beam-ends (crack lengths near the beam ends are more heavily clamped and may experience excessive ploughing, i.e., large $\tilde{\theta}$). Table 6.6 summarizes the adopted model parameters, where are based on the 5 best-fit parameter sets in Table 6.4 for reversed-cyclic tests on individual cracks.

Table 6.6. Model parameters passed to the `multi-surf-crack2d` model at the mid-height crack of a double-beam coupling beam (units in MPa, mm)

Specimen	$D_{ts,0}$	f_{cl}	$\hat{\rho}$	χ_{lok}	$\tilde{\theta}$	ρ_{act}	μ_{act}	χ_{act}	κ	ζ
DBCB	7.0	1.0	0.30	0.10	0.5	1.5	0.20	0.10	0.50	0.30

Validation is performed for two DBCB specimens: R-2.4-SC-1 and R-2.4-SC-2-W. Both specimens have a span-to-depth ratio of 2.4 but differ in the thickness of the unreinforced concrete strip. The first specimen has a strip thickness of 1 in. (25.4 mm) and the second specimen has a strip thickness of 2 in. (50.8 mm). The second beam is also wider. Results of the OpenSees simulation (using a simplified loading protocol with only 1 cycle per drift level) of specimens R-2.4-SC-1 and R-2.4-SC-2-W are shown in Figs. 6.14 and 6.15, respectively. It is seen that the simulated crack contribution slightly underestimates the back-calculated crack shear for the 1 in. gap, but is nearly identical for the 2 in. gap. This suggests that for large enough cracks (i.e., cracks for which the reinforcement protrusions do not affect force transfer mechanisms) the peak shear predicted by the `multi-surf-crack2d` model is quite accurate. Unfortunately more detailed DBCB crack data is not available for a truly thorough investigation of the cyclic performance.

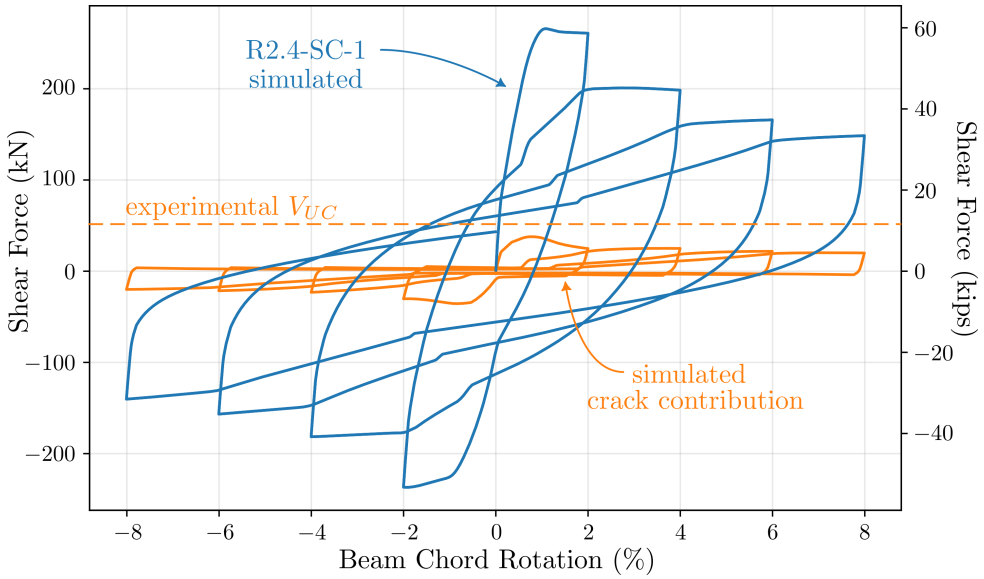

Figure 6.14. Simulation of double-beam coupling beam with 1" unreinforced concrete strip and span-depth ratio of 2.4 (experimental details can be found in [39])

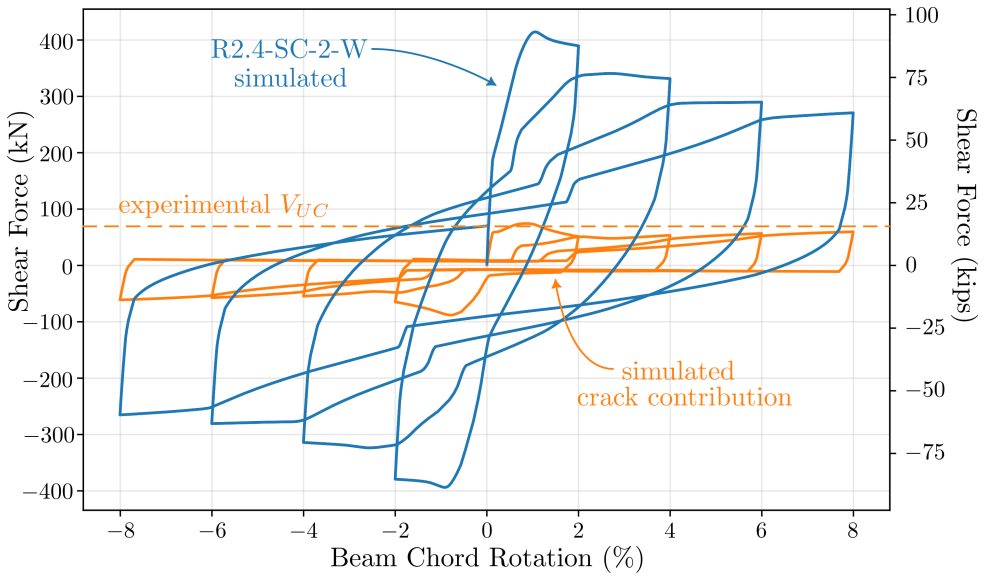

Figure 6.15. Simulation of wide double-beam coupling beam with 2" unreinforced concrete strip and span-depth ratio of 2.4 (experimental details can be found in [38])

6.3 Discussion and conclusions

This Chapter has sought to demonstrate the ability of the proposed crack constitutive model to replicate a variety of experimental observations. Significant effort went into calibrating the monotonic version of the crack model, as most available high-quality data lies within this realm. Suggestions were made, based on simulations of both proportional and non-proportional experimental loading paths, for the monotonic model parameters. Curve-fits were proposed for each parameter using linear regressions against the residual crack width. Additionally, five reversed-cyclic aggregate interlock specimens were simulated, where it was seen that shear-slip behavior was well reproduced across the board, but some difficulty was had replicating the dilation behavior for large slip excursions. Model predictions may be improved in the future by incorporating non-constant parameters, to account for evolution of the crack surface with sliding damage.

Briefly, the suitability of a simplified approach for modeling dowel action was assessed, so that the performance of the crack model could be tested under general conditions — representative of an arbitrary crack in an RC component.

Lastly, a novel coupling beam solution was modeled using the proposed crack model, to show that medium-scale analyses can be modeled without too much numerical burden.

Chapter 7

Conclusions: Towards Crack-Based Assessment

This Thesis sought to provide a tool capable of filling a gap in the existing approaches for crack-based assessment; namely, the ability (or inability) to accurately describe the stress-deformation response of a crack under *arbitrary* loading conditions, with a focus on reversed-cyclic shear-controlled behavior.

The crack-centric viewpoint adopted in this work was justified in Chapter 3, where crack information was shown to be strongly correlated with useful post-EQ evaluation metrics such as collapse risk, by incorporating advanced modeling into an existing framework for collapse risk assessment. While demonstrating the potential utility of crack width as an engineering demand parameter, some deficiencies with existing smeared crack approaches were highlighted. Particularly of note is the difficulty in predicting residual crack widths using simplified finite-element models that are currently available in common software. This observation led to the development (Chapter 4) and implementation (Chapter 5) of a novel crack model, based in plasticity theory and intended for use within discrete crack analyses. This approach is well-suited for crack-based assessment and was preliminary calibrated and validated in Chapter 6 against single-crack and component-level experiments. Key takeaways regarding the novel plasticity crack model (coined `multi-surf-crack2D`) include:

- the crack model is completely parameterized by crack width, making the `multi-surf-crack2D` model unique among interface models and

well-positioned between computational-mechanics theory and practical applications;

- the `multi-surf-crack2D` model unifies the description of shear and flexural cracks through a combined yield surface that builds on a functional form for combined shear-normal strength proposed in the Modified Compression Field Theory. The unification of crack behavior reduces the need to interpret visual evidence, hopefully leading to reduced reliance on "engineering judgement" in future damage assessment protocols;

- loading and unloading are described in the `multi-surf-crack2D` model by different yield surfaces to reflect the different resisting mechanisms during forward sliding (aggregate interlock) and sliding reversal (frictional "breakaway");

- plasticity yield surfaces inspired by the Modified Compression Field Theory provide a reasonable estimate of crack capacity, both for monotonic loading and for cyclic loading;

- the `multi-surf-crack2D` model provides users with significant modeling flexibility through 6 parameters, mainly used to control the dilation and damage evolution of crack interfaces. Default values for each parameter are based on thorough examination of existing monotonic and reversed-cyclic laboratory tests on pre-formed crack interfaces;

- the `multi-surf-crack2D` model parameters, though physically interpretable, are phenomenological in nature. This means that they can be tuned to provide accurate descriptions of long crack segments. Thus, meshes of structural elements with cracks represented by `multi-surf-crack2D` elements require relatively course meshes (hence, faster computation time) as compared with simpler constitutive models such as the rigid-plastic Contact Density model.

While significant calibration and validation efforts were undertaken in this Thesis (Chapter 6), some challenges remain before the model can be used within a generic crack-based-assessment framework. These are discussed briefly below.

Model Enhancements Before attempting to use the proposed crack plasticity model within crack-based assessment schemes, a more complete validation should be performed, ranging from the individual crack level to cracked components (such as panels or walls). Particular effort should be devoted toward calibrating the model on cracks that are crossed by bonded reinforcement, as this represents a realistic configuration in an arbitrarily cracked RC component. Currently, existing experimental data for the bonded case is limited.

Possible enhancements to the model include:

- the effect of material parameters on energy dissipation should be studied in detail, as proper prediction of energy dissipation is crucial in earthquake applications;
- alternative, more thermodynamically forgiving yield surfaces may be considered for the activation phase;
- the loading/unloading rules should be tested under arbitrary loading (e.g. white noise), rather than simplified experimental protocols, to ensure proper performance of the constitutive model under actual earthquake sequences;
- non-proportional load paths, such as those involving a pre-compression phase, should be studied in further detail;
- evolution laws for material parameters should be introduced to reflect the updated shape of crack interfaces, particularly relevant when large slips are expected;
- proposed modifications to the well-known v_{cimax} shear term should be verified experimentally;
- terms involving maximum aggregate diameter a_g could be generalized to also encompass intentionally roughened interfaces, whose roughness may not correlate to the aggregate size;
- the residual crack state could be improved by accounting for residual crack slip as well as residual crack width;

- a non-local enhancement could modify the residual damaged state by considering the crack spacing (or crack density) in the area of the crack-of-interest;
- a possible correlation between rubble buildup and model parameter values could be investigated via discrete-element models, as such a relationship would be useful for establishing model parameters based on visual observations.
- extension of the model to 3D, to handle torsion cracks or interfaces expected to undergo bi-directional sliding, e.g., [155].

Obtain Improved Experimental Data As always, additional experimental data would improve the ability to calibrate the proposed crack-plasticity model. A primary difficulty of crack-based assessment is mapping crack measurements from a single snapshot in time onto a parameter or set of parameters that represents the damage sustained due to an unknown load history. Solving this type of inverse problem typically requires auxiliary information to augment the original problem statement. Somewhat fortuitously, the problem of ill-posedness becomes slightly improved by the use of a total-width hardening strain in the crack-plasticity model (though the total-width choice was initially inspired by the MCFT stress-like normalizing term v_{cimax}). According to the crack-plasticity model, the yield surface can be completely sized based on the current crack width. Yet, information about the maximum slip history and input sliding energy could improve the model calibration. In order to fill this gap, and others, desirable data includes:

- crack experiments with bonded reinforcement, reporting also reinforcement strains, e.g., following the procedure of [125] which allows for the crack normal tractions to be deduced;
- tests of cracks crossed by large compression stresses;
- data for sub-critical loading, which can be used to determine if crack width data needs to be augmented by an energetic term when assigning values to the parameters of the crack-plasticity model;

- testing protocols that include cyclic loading followed by monotonic loading to failure, to determine if the monotonically-derived v_{cimax} term requires modifications for cyclic loading;

- a test program to establish if cracks possess an inherent "fracture energy" in sliding, and if such a term can be correlated to crack width.

Identify Bar Stresses The residual bar state is important to identify when assessing earthquake-damaged structures especially in regard to fatigue capacity [106]. This has been recognized in the yet-to-be finished ATC-145 document that governs post-earthquake assessment of RC buildings [8]. Difficulty, however, in inferring the maximum bar strains based on crack width measurements has been noted following the Canterbury EQ sequence of 2010 [55].

A comprehensive review on existing relationships between crack width and residual bar strains or residual fatigue life should be performed. If necessary, the experimental dataset should be augmented with bars under dowel actions, which are not considered in typical works on this topic, e.g., [43].

Meshing Routine This Thesis, though motivated by the goal of a general-purpose crack-based-assessment tool, maintained a narrow focus on individual cracks or components controlled by well-defined crack planes. The eventual extension to more general analyses will require a sophisticated meshing routine. Ideally, the mesher will take as input a linework image and discretize the cracked structure-of-interest. A promising tool for this task is Triangle [160]. Preliminary work has been done creating a scipt that augments meshes that are output from Triangle to handle the `zeroLength` elements required to build crack meshes using the `multi-surf-crack-2D` material model.

Eventually, a sensitivity study should be performed to identify mesh discretization sizes (along the length of the crack) that provide a balance between accuracy and computational effort. Unlike simpler crack constitutive laws such as the Contact Density Model, the `multi-surf-crack2D` provides enough flexibility to be able to capture the phenomenological effect of crack roughness without having to finely discretize the crack length. Future studies should bear out this finding.

Create a Crack Macro-Element that is Compatible with Line Elements One application of the proposed crack plasticity model – among many discussed in Chapter 1 – is the analysis of base-sliding walls. A possible extension of the crack material model is a macro element that can be used with line elements that are common in earthquake engineering. Inspiration can be taken from a similar macro-element that has been developed for capturing shear-flexure interaction in walls [86]. Work on this task is currently underway so that earthquake engineers are not shoehorned into expensive solid-element analyses whenever they want to include sliding along an interface.

Produce Rational Guidelines for Severe Crack Widths Finally, it is hoped that the proposed crack plasticity model can eventually serve as a basis for producing general-purpose crack-width guidelines.

References

[1] S. Abdullah, J. Wallace, W. Ghannoum, G. Hagen, M. Talaat, and L. Lowes, "Shear-friction strength of rc structural walls," in *18th World Conference on Earthquake Engineering, Milan Italy*, WCEE, Ed., 2024.

[2] ACI318-19, *Building code requirements for structural concrete*, 2019.

[3] A. Alhashmi and F. Oudah, "Structural assessment of cracked concrete members by digital image random nonlinear finite element," *ACI Structural Journal*, vol. 122, pp. 57–69, 5 2025. DOI: 10.14359/51746792

[4] G. Almasabha and S. Chao, "A new reinforcing configuration for achieving high-ductility and high-strength rectangular squat structural walls," *ACI Structural Journal*, vol. 120, pp. 253–268, 1 2023. DOI: 10.14359/51737144

[5] H. Alwashali, M. Maeda, Y. Ogata, N. Aizawa, and K. Tsuragai, "Residual seismic performance of damaged reinforced concrete walls," *Engineering Structures*, vol. 243, 2021. DOI: 10.1016/j.engstruct.2021.112673

[6] ASCE-41, *Seismic evaluation and retrofit of existing buildings*, 2017.

[7] ASCE-7, *Minimum design loads and associated criteria for buildings and other structures*, 2022.

[8] ATC-145, *Resilient repair guide source report: Post-earthquake assessment of reinforced concrete buildings*, 2021.

[9] B. Aydin, B. Binici, S. Aktas, M. Hendriks, and K. Tuncay, "Maximum Drift Demands of Earthquake Damaged Reinforced Concrete Columns Based on Residual Flexure Cracks," *Bulletin of Earthquake Engineering*, vol. 22, pp. 4055–4081, 2024. DOI: 10.1007/s10518-024-01922-z

[10] S. Azhari and M. Hamidia, "Probabilistic Postearthquake ASCE 41-17 Compliant Performance Level Identification for Shear-Dominated RC Shear Walls via Crack Image Analysis," *Journal of Structural Engineering*, vol. 151, no. 1, 2025. DOI: 10.1061/JSENDH.STENG-12895

[11] J. Baek, H. Park, J. Lee, and C. Bang, "Cyclic Loading Test for Walls of Aspect Ratio 1.0 and 0.5 with Grade 550 MPa (80 ksi) Shear Reinforcing Bars," *ACI Structural Journal*, vol. 114, no. 4, pp. 969–982, 2017. DOI: 10.14359/51689680

[12] A. Bahnamiri and T. Hrynyk, "Toward crack-based assessment of existing reinforced concrete structures," *ACI Structural Journal*, vol. SP-365 Shear in Structural Concrete, pp. 148–164, 2025.

[13] A. Baktheer and M. Classen, "A review of recent trends and challenges in numerical modeling of the anisotropic behavior of hardened 3D printed concrete," *Additive Manufacturing*, vol. 89, 2024. DOI: 10.1016/j.addma.2024.104309

[14] A. Baktheer, C. Goralski, J. Hegger, and R. Chudoba, "Stress configuration-based classification of current research on fatigue of reinforced and prestressed concrete," *Structural Concrete*, vol. 25, no. 3, pp. 1765–1781, 2024. DOI: 10.1002/suco.202300667

[15] Z. Bazant and P. Gambarova, "Rough Cracks in Reinforced Concrete," *Journal of the Structural Division*, vol. 106, no. 4, 1980. DOI: 10.1061/JSDEAG.0005400

[16] F. Bazzucchi, L. Restuccia, and G. Ferro, "Considerations over the italian road bridge infrastructure safety after the polcevera viaduct collapse: Past errors and future perspectives," *Fratture ed Integrità Strutturale*, vol. 46, pp. 400–421, 2018. DOI: 10.3221/IGF-ESIS.46.37

[17] H. Becks and C. M., "Influence of coarse aggregates on the fatigue behavior of high-strength concrete under mode-II loading," *Construction and Building Materials*, vol. 491, 2025. DOI: 10.1016/j.conbuildmat.2025.142565

[18] H. Becks, M. Schmidt, S. Bosback, and C. M., "Large-scale combined torsional and axial loading system (TorAx) - A new perspective on multiaxial testing of fraction and stress transfer in plain and reinforced concrete," *Engineering Structures*, vol. 302, no. 1, 2024. DOI: 10.1016/j.engstruct.2023.117391

[19] D. Bernardini, D. Ruta, P. Di Re, and A. Paolone, "Calibration of material parameters for the chang-mander model for unconfined concrete," in *Proceedings of the 2022 Eurasion OpenSees Days, Turin Italy*, S. Nature, Ed., 2023.

[20] M. Blomfors, C. Berrocal, K. Lundgren, and K. Zandi, "Incorporation of pre-existing cracks in finite element analyses of reinforced concrete beams without transverse reinforcement," *Engineering Structures*, vol. 229, 2021. DOI: 10.1016/j.engstruct.2020.111601

[21] J. Bochman, M. Curbach, and F. Jesse, "Influence of artificial discontinuities in concrete under compression load - A literature review," *Structural Concrete*, vol. 19, no. 2, pp. 559–567, 2018. DOI: 10.1002/suco.201700041

[22] H. Burton and G. Deielein, "Integrating visual damage simulation, virtual inspection and collapse capacity to evaluate post-earthquake structural safety of buildings," *Earthquake Engineering and Structural Dynamics*, vol. 47, no. 2, pp. 294–310, 2018. DOI: 10.1002/eqe.2951

[23] G. Calvi, M. Moratti, G. O'Reilly, N. Scattarreggia, R. Monteiro, and P. Calvi, "Once upon a time in italy: The tale of the morandi bridge," *Structural Engineering International*, vol. 29, pp. 198–217, 2 2019. DOI: 10.1080/10168664.2018.1558033

[24] P. Calvi, G. Proestos, and D. Ruggiero, "Towards the development of direct crack-based assessment of structures," *ACI Structural Journal*, vol. SP-328 Shear in Structural Concrete, pp. 9.1–9.20, 2018.

[25] P. Calvi, E. Bentz, and M. Collins, "Reversed Cyclic Experiments on Shear Stress Transfer across Cracks in Reinforced Concrere Elements," *ACI Structural Journal*, vol. 113, no. 4, 2016. DOI: 10.14359/51688926

[26] P. Calvi, E. Bentz, and M. Collins, "Pure Mechanics Crack Model for Shear Stress Transfer in Cracked Reinforced Concrete," *ACI Structural Journal*, vol. 114, no. 2, 2017. DOI: 10.14359/51689460

[27] P. Calvi, E. Bentz, and M. Collins, "Model for assessment of cracked reinforced concrete membrane elements subjected to shear and axial loads," *ACI Structural Journal*, vol. 115, pp. 501–509, 2 2018. DOI: 10.14359/51701093

[28] M. Cao, Q. Ren, and P. Qiao, "Nondestructive Assessment of Reinforced Concrete Structures Based on Fractal Damage Characteristic Factors," *Journal of Engineering Mechanics*, vol. 132, no. 9, pp. 924–931, 2006. DOI: 10.1061/(ASCE)0733-9399(2006)132:9(924)

[29] J. Carillo and S. Alcocer, "Acceptance limits for performance-based seimic design of RC walls for low-rise housing," *Earthquake Engineering and Structural Dynamics*, vol. 41, pp. 2273–2288, 2012. DOI: 10.1002/eqe.2186

[30] J. Carillo, D. Dominguez, and N. Prado, "Seismic Damage Index Based on Fractal Dimension of Cracking on Thin Reinforced Concrete Walls," *ACI Structural Journal*, vol. 114, no. 6, pp. 1649–1658, 2017. DOI: 10.14359/51700919

[31] I. Carol, P. Prat, and C. López, "Normal/Sehar Cracking Model: Application to Discrete Crack Analysis," *Journal of Engineering Mechanics*, vol. 123, no. 8, pp. 765–773, 1997. DOI: 10.1061/(ASCE)0733-9399(1997)123:8(765)

[32] J. Carranza, G. Deierlein, and K. Zhong, "Simulation of longitudinal reinforcing steel bar fracture in reinforced concrete walls," *Bulletin of Earthquake Engineering*, vol. 23, pp. 517–551, 2025. DOI: 10.1007/s10518-024-02078-6

[33] S. Cattaneo, G. Zorzato, and A. Bonati, "Assessing method of shear strength between old to new concrete interface under cycling loading," *Construction and Building Materials*, vol. 309, 2021. DOI: 10.1016/j.conbuildmat.2021.125160

[34] F. Cavagnis, M. Fernandez Ruiz, and A. Muttoni, "A mechanical model for failures in shear of members without transverse reinforcement based on development of a critical shear crack," *Engineering Structures*, vol. 157, pp. 300–315, 2018. DOI: 10.1016/j.engstruct.2017.12.004

[35] G. Chang and J. Mander, "Seismic energy based fatigue damage analysis of bridge columns," NCEER, Technical Report NCEER-94-0006, 1994.

[36] M. Cheng, S. Hung, R. Lequesne, and A. Lepage, "Earthquake-Resistant Squat Walls Reinforced with High-Strength Steel," *ACI Structural Journal*, vol. 113, no. 5, pp. 1065–1076, 2016. DOI: 10.14359/51688825

[37] A. Chhabra and R. V. Jensen, "Direct determination of the f(α) singularity spectrum," *Phys. Rev. Lett.*, vol. 62, pp. 1327–1330, 12 Mar. 1989. DOI: 10.1103/PhysRevLett.62.1327

[38] Y. Choi and S. Chao, "Analysis and Design of Double-Beam Coupling Beams," *ACI Structural Journal*, vol. 117, no. 5, pp. 79–95, 2020. DOI: 10.14359/51725985

[39] Y. Choi, P. Hajyalikhani, and S. Chao, "Seismic Performance of Innovative Reinforced Concrete Coupling Beam — Double-Beam Coupling Beam," *ACI Structural Journal*, vol. 115, no. 1, pp. 113–125, 2018. DOI: 10.14359/51700951

[40] R. Chudoba, M. Vorechovsky, M. Aguilar, and A. Baktheer, "Coupled sliding-decohesion-compression model for a consistent description of monotonic and fatigue behavior of material interfaces," *Computer Methods in Applied Mechanics and Engineering*, vol. 398, 2022. DOI: 10.1016/j.cma.2022.115259

[41] J. Coleman and E. Spacone, "Localization issues in force-based frame elements," *Journal of Structural Engineering*, vol. 127, pp. 1257–1265, 11 2001. DOI: 10.1061/(ASCE)0733-9445(2001)127:11(1257)

[42] M. Collins and D. Mitchell, in *Prestressed Concrete Structures*. Prentice Hall, 1991.

[43] E. Corres and A. Muttoni, "Estimation of the bar stress based on crack width measurements in reinforced concrete structures," *Structural Concrete*, vol. 25, no. 6, pp. 4454–4479, 2024. DOI: 10.1002/suco.202400210

[44] E. Corres and A. Muttoni, "Local bond-slip model based on mechanical considerations," *Engineering Structures*, vol. 314, 2024. DOI: 10.1016/j.engstruct.2024.118190

[45] O. Davaadorj, P. Calvi, and J. Stanton, "Experimental response of headed stud connections subjected to combined shear and bending actions," *PCI Journal*, vol. 65, no. 5, pp. 38–50, 2020. DOI: 10.15554/pcij65.5-02

[46] O. Davaadorj, P. Calvi, and J. Stanton, "Shear stress transfer across concrete-to-concrete interfaces: Experimental evidence and available strength models," *PCI Journal*, vol. 65, no. 4, pp. 87–111, 2020. DOI: 10.15554/pcij65.4-04

[47] R. Davoudi, G. Miller, P. Calvi, and J. Kutz, "Computer vision-based damage and stress state estimation for reinforced concrete and stell fiber-reinforced concrete panels," *Structural Health Monitoring*, vol. 19, 6 2019. DOI: 10.1177/1475921719892345

[48] A. Demir, N. Caglar, and H. Ozturk, "Parameters affecting diagonal cracking behavior of reinforced concrete deep beams," *Engineering Structures*, vol. 184, pp. 217–231, 2019. DOI: 10.1016/j.engstruct.2019.01.090

[49] M. Divakar, A. Fafitis, and S. Shah, "Constitutive Model for Shear Transfer in Cracked Concrete," *Journal of Structural Engineering*, vol. 113, no. 5, 1987. DOI: 10.1061/(ASCE)0733-9445(1987)113:5(1046)

[50] A. Ebrahimkhanlou, A. Athanasiou, T. Hyrnyk, O. Bayrak, and S. Salamone, "Fractal and Multifractal Analysis of Crack Patterns in Prestressed Concrete Girders," *Journal of Bridge Engineering*, vol. 24, no. 7, 2019. DOI: 10.1061/(ASCE)BE.1943-5592.0001427

[51] J. Echegaray-Oviedo, J. Navarro-Gregori, E. Cuenca, and P. Serna, "Modified push-off test for analysing the shear behavior of concrete cracks," *Strain*, vol. 53, no. 6, 2017. DOI: 10.1111/str.12239

[52] R. Eligehausen, E. Popov, and V. Bertero, "Local bond stress-slip relationships of deformed bars under generalized excitations," Earthquake Engineering Research Center, University of California, Report No. UCB/EERC-83/23, 1983.

[53] K. Elwood, "Performance of Concrete Buildings in the 22 February 2011 Christchurch Earthquake and Implications for Canadian Codes," *Canadian Journal of Civil Engineering*, vol. 40, 2013.

[54] K. Elwood, "Impact of prior shaking on earthquake response and repair requirements for structures - studies from atc-145," in *NZSEE 2021 Annual Conference, Christchurch, New Zealand*, 2021.

[55] K. Elwood et al., "Draft framework for assessing residual capacity of earthquake-damaged concrete buildings," in *NZSEE Conference, Christchurch, New Zealand*, 2016.

[56] A. Farhidzadeh, E. Dehghan-Niri, A. Moustafa, S. Salamone, and A. Whittaker, "Damage Assessment of Reinforced Concrete Structures Using Fractal Analysis of Residual Crack Patterns," *Experimental Mechanics*, vol. 53, pp. 1607–1619, 2013. DOI: 10.1007/s11340-013-9769-7

[57] E. Fathalla and B. Mihaylov, "Comprehensive approach for examining shear-critical rc walls using detailed experimental measurements," *Structural Concrete*, vol. 25, pp. 4780–4794, 6 2024. DOI: 10.1002/suco.202400276

[58] E. Fathallah, B. Ringeisen, M. Lenges, and B. Mihaylov, "Shear Behavior of Full-Scale Squat Shear Walls with and without Precast Pre-walls," *Journal of Advanced Concrete Technology*, vol. 22, no. 2, pp. 86–102, 2024. DOI: 10.3151/jact.22.86

[59] FEMA-306, *Evaluation of earthquake damaged concrete and masonry wall buildings: Basic procedures manual*, 1998.

[60] FEMA-P58, *Seismic performance assessment of buildings: Volume 1 - methodology, 2nd edition*, 2018.

[61] FEMA-P695, *Quantification of building seismic performance factors: Appendix a*, 2009.

[62] G. Ferro, L. Restuccia, D. Falliano, A. Devitofraceschi, and A. Gemelli, "Collapse of existing bridges: From the lesson of la reale viaduct to the definition of a partial safety coefficient of variable traffic loads," *Journal of Structural Engineering*, vol. 148, 11 2022. DOI: 10.1061/(ASCE)ST.1943-541X.0003458

[63] D. Figueira, C. Sousa, R. Calçada, and A. Neves, "Push-Off Tests in the Study of Cyclic Behavior of Interfaces between Concretes Cast at Different Times," *Journal of Structural Engineering*, vol. 142, no. 1, 2015. DOI: 10.1061/(ASCE)ST.1943-541X.0001364

[64] L. Fronteddu, P. Léger, and R. Tinawi, "Static and Dynamic Behavior of Concrete Lift Joint Interfaces," *Journal of Structural Engineering*, vol. 124, no. 12, pp. 1418–1430, 1998. DOI: 10.1061/(ASCE)0733-9445(1998)124:12(1418)

[65] C. Fujiyama, X. Tang, K. Maekawa, and X. An, "Pseudo-cracking approach to fatigue life assessment of rc bridge decks in service," *Journal of Advanced Concrete Technology*, vol. 11, pp. 7–21, 1 2013. DOI: 10.3151/jact.11.7

[66] W. Galik and P. Calvi, "Corrosion and Fatigue Coupling: Assessment of a Prestressed Concrete Cable Stay," *Journal of Performance of Constructed Facilities*, vol. 38, no. 1, 2024. DOI: 10.1061/JPCFEV.CFENG-4307

[67] W. Galik, P. Calvi, and G. Andreotti, "Discrete modeling of reinforced concrete crack interfaces: A crack-based assessment perspective," in *18th World Conference on Earthquake Engineering, Milan Italy*, WCEE, Ed., 2024.

[68] W. Galik, P. Calvi, and G. Andreotti, "A Multi-Surface Plasticity Model for Reinforced Concrete Cracks with Applications to Crack-Based Assessment," *Earthquake Engineering and Structural Dynamics*, 2026. DOI: 10.1002/eqe.70143

[69] W. Galik, Y. Waktola, and P. Calvi, "Relative Collapse Analysis to Determine Crack Width Limits of Squat RC Shear Walls," *Bulletin of Earthquake Engineering,* under review, 2026.

[70] F. Galvis, A. Hulsey, J. Baker, and G. Deierlein, "Simulation-based methodology to identify damage indicators and safety thresholds for post-earthquake evaluation of structures," *Earthquake Engineering and Structural Dynamics*, vol. 52, no. 11, pp. 3455–3476, 2023. DOI: 10.1002/eqe.3876

[71] E. Gebreyouhannes, T. Kishi, and K. Maekawa, "Shear Fatigue Response of Cracked Concrete Interface," *Journal of Advanced Concrete Technology*, vol. 6, no. 2, pp. 365–376, 2008. DOI: 10.3151/jact.6.365

[72] C. Gulec, A. Whittaker, and J. Hooper, "Fragility functions for low aspect ratio reinforced concrete walls," *Engineering Structures*, vol. 32, no. 9, pp. 2894–2901, 2010. DOI: 10.1016/j.engstruct.2010.05.008

[73] M. Hamidia, A. Ganjizadeh, and K. Dolatshahi, "Peak drift ratio estimation for RC moment frames using multifractal dimensions of surface crack patterns," *Engineering Structures*, vol. 255, 2022. DOI: 10.1016/j.engstruct.2022.113893

[74] M. Hassanzadeh, "Behaviour and fracture process zones in concrete influenced by simultaneously applied normal and shear displacements," Doctoral Thesis, Division of Building Materials, Lund University, 1992.

[75] A. Hillerborg, M. Modeer, and P. Petersson, "Analysis of crack formation and crack growth in concrete by means of fracture mechanics and finite elements," *Cement and Concrete Research*, vol. 6, pp. 773–781, 1976.

[76] IAEA, *Guidebook on non-destructive testing of concrete structures*, 2002.

[77] L. Ibarra, R. Medina, and H. Krawinkler, "Hysteretic models that incorporate strength and stiffness deterioration," *Earthquake Engineering and Structural Dynamics*, vol. 34, no. 12, pp. 1489–1511, 2005. DOI: 10.1002/eqe.495

[78] J. Jacobsen, P. Poulsen, and J. Olesen, "Characterization of mixed mode crack opening in concrete," *Materials and Structures*, vol. 45, no. 1-2, pp. 107–122, 2012. DOI: 10.1617/s11527-011-9754-5

[79] J. Jacobsen, P. Poulsen, J. Olesen, and K. Krabbenhoft, "Constitutive mixed mode model for cracks in concrete," *Engineering Fracture Mechanics*, vol. 99, pp. 30–47, 2013. DOI: 10.1016/j.engfracmech.2013.01.004

[80] D. Jansen and S. Shah, "Effect of length on compressive strain softening of concrete," *Journal of Engineering Mechanics*, vol. 123, pp. 23–35, 1997.

[81] JBDPA, *Guideline for post-earthquake damage evaluation and rehabilitation*, 2001.

[82] H. Jiang, B. Wang, and X. Lu, "Experimental Study on Damage Behavior of Reinforced Concrete Shear Walls Subjected to Cyclic Loads," *Journal of Earthquake Engineering*, vol. 17, no. 7, pp. 958–971, 2013. DOI: 10.1080/13632469.2013.791895

[83] C. Jin, Y. Su, Z. Pan, and S. Meng, "Experimental Study and Finite Element Modelling of Squat Shear Walls under Combined Cyclic Loads and High Axial Loads," *Buildings*, vol. 13, no. 2104, 2023. DOI: 10.3390/buildings13082104

[84] M. Jirásek, in *Numerical Modeling of Concrete Cracking: CISM Courses and Lectures, vol. 532*. Springer, 2011, ch. Damage and Smeared Crack Models, pp. 1–49, ISBN: 978-3-7091-0896-3.

[85] M. Jirásek and Z. Bazant, in *Inelastic Analysis of Structures*. Wiley, 2002, ch. Numerical Methods in Plasticity, pp. 391–422, ISBN: 978-0-471-98716-1.

[86] K. Kolozvari, K. Kalbasi, K. Orakcal, L. Massone, and J. Wallace, "Shear-flexure-interaction models for planar and flanged reinforced concrete walls," *Bulletin of Earthquake Engineering*, vol. 17, pp. 6391–6417, 2019. DOI: 10.1007/s10518-019-00658-5

[87] S. Kono, H. Tanaka, and F. Watanabe, "Interface shear transfer for high strength concrete and high strength shear friction reinforcement," in *High Performance Materials in Bridges*, pp. 319–328. DOI: 10.1061/40691(2003)28

[88] M. Leblouba, S. Barakat, M. Ahmed, and S. Al-Toubat, "Shear strength at the interface of precast bridge concrete decks and girders subjected to cyclic loading with varying speeds," *Engineering Structures*, vol. 196, 2019. DOI: 10.1016/j.engstruct.2019.109296

[89] B. Li and K. Maekawa, "Contact Density Model for Cracks in Concrete," *IABSE Colloquium*, vol. 54, pp. 51–62, 1997.

[90] Y. Li, Y. Yang, Q. Wang, and S. Feng, "Cyclic shear loading test for grout-sleeve joints in precast concrete shear wall structure," *Journal of Building Engineering*, vol. 82, 2024. DOI: 10.1016/j.jobe.2023.108329

[91] F. Lin, Z. Bazant, J. Chern, and A. Marchertas, "Concrete Model with Normality and Sequetial Identification," *Computers and Structures*, vol. 26, no. 6, pp. 1011–1025, 1987. DOI: 10.1016/0045-7949(87)90118-0

[92] J. Liu, A. Wan, X. Chen, H. Zheng, X. Huang, and Q. Wu, "Effect of Fatigue Loading and Precracking on the Interface Shear Transfer of Cold Joints," *KSCE Journal of Civil Engineering*, vol. 28, pp. 5137–5150, 2024. DOI: 10.1007/s12205-024-1455-z

[93] C. Lopez, L. Massone, and K. Kolozvari, "Validation of an efficient shear-flexure interaction model for planar reinforced concrete walls," *Engineering Structures*, vol. 252, 2022. DOI: 10.1016/j.engstruct.2021.113590

[94] L. Lowes, D. Lehman, A. Birely, D. Kuchma, K. Marley, and C. Hart, "Earthquake response of slender planar concrete walls with modern detailing," *Engineering Structures*, vol. 43, pp. 31–47, 2012. DOI: 10.1016/j.engstruct.2012.04.040

[95] L. Lowes, J. Moehle, and S. Govindjee, "Concrete-Steel Bond Model for Use in Finite Element Modeling of Reinforced Concrete Structures," *ACI Structural Journal*, vol. 101, no. 4, pp. 501–511, 2004. DOI: 10.14359/13336

[96] X. Lv, Z. Yu, and Z. Shan, "Bond stress-slip model for rebar-concrete interface under monotonic and cyclic loading," *Structures*, vol. 34, pp. 498–506, 2021. DOI: 10.1016/j.istruc.2021.07.093

[97] K. Maekawa, H. Okamura, and A. Pimanmas, in *Nonlinear Mechanics of Reinforced Concrete*. CRC Press, 2003, ISBN: 978-0415271264.

[98] K. Maekawa and J. Qureshi, "Computational Model for Reinforcing Bar Embedded in Concrete under Combined Axial Pullout and Transverse Displacement," *Journal of the Japanese Society of Civil Engineers*, vol. 31, no. 538, pp. 227–239, 1996. DOI: 10.2208/jscej.1996.538_227

[99] K. Maekawa and J. Qureshi, "Embedded Bar Behavior in Concrete under Combined Axial Pullout and Tranverse Displacement," *Journal of the Japanese Society of Civil Engineers*, vol. 30, no. 532, pp. 183–195, 1996. DOI: 10.2208/JSCEJ.1996.532_183

[100] K. Maekawa and J. Qureshi, "Stress Transfer Across Interfaces in Reinforced Concrete due to Aggregate Interlock and Dowel Action," *Journal of the Japanese Society of Civil Engineers*, vol. 34, no. 557, pp. 159–172, 1997. DOI: 10.2208/jscej.1997.557_159

[101] J. Maffei, K. Telleen, and Y. Nakayama, "Probability-based seismic assessment of buildings, considering post-earthquake safety," *Earthquake Spectra*, vol. 24, pp. 667–699, 3 2008. DOI: 10.1193/1.2950066

[102] M. Mansour and T. Hsu, "Behavior of Reinforced Concrete Elements under Cyclic Shear. II Theoretical Model," *Journal of Structural Engineering*, vol. 131, no. 1, 2005. DOI: 10.1061/(ASCE)0733-9445(2005)131:1(54)

[103] I. Mantawy, T. Thonstad, D. Sanders, J. Stanton, and M. Eberhard, "Reinforcing steel fracture identification for a high-performance bridge system," *Structures*, vol. 19, pp. 58–67, 2019. DOI: 10.1016/j.istruc.2018.11.017

[104] K. Marder, K. Elwood, C. Motter, and G. Clifton, "Post-earthquake assessment of moderately damaged reinforced concrete plastic hinges," *Earthquake Spectra*, vol. 36, no. 1, pp. 299–321, 2020. DOI: 10.1177/8755293019878192

[105] P. Marti, M. Alvarez, W. Kaufmann, and V. Sigrist, "Tension Chord Model for Structural Concrete," *Structural Engineering International*, vol. 8, no. 4, pp. 287–298, 1998. DOI: 10.2749/101686698780488875

[106] L. Massone and P. Herrera, "Experimental study of the residual fatigue life of reinforcement bars damaged by an earthquake," *Materials and Structures*, vol. 52, no. 61, 2019. DOI: 10.1617/s11527-019-1361-x

[107] L. Massone, C. López, and K. Kolozvari, "Formulation of an efficient shear-flexure interaction model for planar reinforced concrete walls," *Engineering Structures*, vol. 243, 2021. DOI: 10.1016/j.engstruct.2021.112680

[108] A. H. Mattock, "Cyclic Shear Transfer and Type of Interface," *Journal of the Structural Division*, vol. 107, no. 10, 1981. DOI: 10.1061/JSDEAG.0005795

[109] F. Mckenna, M. Scott, and G. Fenves, "Nonlinear Finite-Element Analysis Software Architecture Using Object Composition," *Journal of Computing in Civil Engineering*, vol. 24, no. 1, 2010. DOI: 10.1061/(ASCE)CP.1943-5487.0000002

[110] F. McKenna et al., *Quofem*, https://doi.org/10.5281/zenodo.10443180, v3.5.0, 2023.

[111] B. Mihaylov, E. Bentz, and M. Collins, "Behavior of large deep beams subjected to monotonic and reversed cyclic shear," *ACI Structural Journal*, vol. 107, pp. 726–734, 6 2010. DOI: 10.14359/51664021

[112] B. Mihaylov, E. Bentz, and M. Collins, "Two-parameter kinematic theory for shear behavior of deep beams," *ACI Structural Journal*, vol. 110, pp. 447–456, 3 2013. DOI: 10.14359/51685602

[113] B. Mihaylov, E. Fathalla, and A. Trandafir, "Rapid crack-based assessment of deep beams based on a single crack measurement," *Engineering Structures*, vol. 322, 2025. DOI: 10.1016/j.engstruct.2024.119054

[114] B. Mihaylov, P. Hannewald, and K. Beyer, "Three-parameter kinematic theory for shear-dominated reinforced concrete walls," *Journal of Structural Engineering*, vol. 142, 7 2016. DOI: 10.1061/(ASCE)ST.1943-541X.0001489

[115] B. Mihaylov, B. Hunt, E. Bentz, and M. Collins, "Three-parameter kinematic theory for shear behavior of continuous deep beams," *ACI Structural Journal*, vol. 112, pp. 47–57, 1 2015. DOI: 10.14359/51687180

[116] S. Millard and R. Johnson, "Shear transfer across cracks in reinforced concrete due to aggregate interlock and to dowel action," *Magazine of Concrete Research*, vol. 36, no. 126, pp. 9–21, 1984. DOI: 10.1680/macr.1984.36.126.9

[117] D. Mitchell, J. Marchand, P. Croteau, and W. Cook, "Concorde overpass collapse: Structural aspects," *Journal of Performance of Constructed Facilities*, vol. 25, pp. 545–553, 6 2011. DOI: 10.1061/(ASCE)CF.1943-5509.0000183

[118] J. Moehle, in *Seismic Design of Reinforced Concrete Structures*. McGraw-Hill, 2015, ch. Axially Loaded Members, pp. 109–139, ISBN: 978-0-07-183944-0.

[119] H. Momeni and K. Dolatshahi, "Predictive equations for drift ratio of RC shear walls using surface crack patterns," *Engineering Structures*, vol. 190, pp. 410–421, 2019. DOI: 10.1016/j.engstruct.2019.04.018

[120] A. Moradi, M. Soltani, and A. Tasnimi, "A Simplified Constitutive Model for Dowel Action across RC Cracks," *Journal of Advanced Concrete Technology*, vol. 10, pp. 264–277, 2012. DOI: 10.3151/jact.10.264

[121] J. Moscoso, M. Hube, and H. Santa Maria, "Residual Seismic Capacity of Reinforced Concrete Walls with Unconfined Boundaries," *ACI Structural Journal*, vol. 118, no. 5, pp. 205–220, 2021. DOI: 10.14359/51732830

[122] H. Nakamura, T. Nanri, T. Miura, and S. Roy, "Experimental investigation of compressive strength and compressive fracture energy of longitudinally cracked concrete," *Cement and Concrete Composites*, vol. 93, pp. 1–18, 2018. DOI: 10.1016/j.cemconcomp.2018.06.015

[123] K. Nakano and Y. Matsuzaki, "Design method and compound effect considering deformation of shear transfer elements in precast concrete connections," in *13th World Conference on Earthquake Engineering, Vancouver, B.C.*, 2004.

[124] M. Nielsen, in *Limit Analysis and Concrete Plasticity*, ch. The Crack as a Joint, pp. 730–740. DOI: 10.1201/b10432

[125] E. Oikonomopoulou, V. Palieraki, E. Vintzileou, and G. Genesio, "Cyclic Behavior of Long Concrete Interfaces Crossed by Steel Screws," *Applied Sciences*, vol. 14, 2024. DOI: 10.3390/app14188246

[126] E. Opabola and K. Elwood, "Flexure-axial-shear interaction of ductile beams with single-crack plastic hinge behaviour," *Earthquake Engineering and Structural Dynamics*, vol. 52, pp. 2115–2134, 2023. DOI: 10.1002/eqe.3873

[127] E. Opabola and K. Elwood, "Seismic design of concrete structures for damage control," *Earthquake Spectra*, vol. 40, pp. 2038–2058, 3 2024. DOI: 10.1177/87552930241235487

[128] K. Orakcal, L. Massone, and D. Ulugtekin, "A Hysteretic Constitutive Model for Reinforced Concrete Panel Elements," *International Journal of Concrete Structures and Materials*, vol. 13, no. 51, 2019. DOI: 10.1186/s40069-019-0365-9

[129] C. Pagni and L. Lowes, "Predicting earthquake damage in older reinforced concrete beam-column joints," Pacific Earthquake Engineering Research Center (PEER), Report 2003/17, 2004.

[130] V. Palieraki, E. Oikonomopoulou, G. Genesio, and E. Vintzileou, "Experimental cyclic behavior of concrete interfaces with postinstalled reinforcing bars or alternative connectors," *Structural Concrete*, vol. 24, pp. 5265–5283, 2023. DOI: 10.1002/suco.202201034

[131] V. Palieraki, E. Oikonomopoulou, E. Vintzileou, and G. Genesio, "Cyclic behavior of long concrete interfaces crossed by short postinstalled reinforcement," *Engineering Structures*, vol. 326, 2025. DOI: 10.1016/j.engstruct.2024.119537

[132] V. Palieraki and E. Vintzileou, "Calculation of the interface resistance in rc construction using different codes," in *Life-Cycle of Structures and Infrastructure Systems, 2023*, pp. 2253–2260. DOI: 10.1201/9781003323020-275

[133] V. Palieraki, E. Vintzileou, and S. J.F., "Behavior of RC interfaces subjected to shear: State-of-the art review," *Construction and Building Materials*, vol. 306, 2021. DOI: 10.1016/j.conbuildmat.2021.124855

[134] V. Palieraki, E. Vintzileou, and S. J.F., "Modeling Reinforced Interfaces – Cold Joints Subjected to Cyclic Shear," *ACI Structural Journal*, vol. 119, no. 4, pp. 225–238, 2022. DOI: 10.14359/51734521

[135] M. Pejatovíc and A. Muttoni, "Steel stresses and shear forces in reinforcing bars due to dowel action," *Structural Concrete*, vol. 25, no. 6, pp. 4956–4974, 2024. DOI: 10.1002/suco.202400322

[136] M. Petracca, G. Camata, E. Spacona, and L. Pelà, "Efficient constitutive model for continuous micro-modeling of masonry structures," *Internation Journal of Architectural Heritage*, vol. 17, 1 2023. DOI: 10.1080/15583058.2022.2124133

[137] D. Pizarro, M. Kovarbasic, and B. Stojadinovic, "Cyclic Tests Performed on Real-Scale Squat Reinforced Concrete Shear Walls: Transition between Diagonal Shear and Sliding Shear Controlled Behavior Modes," *Journal of Structural Engineering*, vol. 151, no. 4, 2025. DOI: 10.1061/JSENDH.STENG-14025

[138] D. Pizarro, M. Kovarbasic, and B. Stojadinovic, "Hybrid Simulation Tests of Real-Scale Squat Reinforced Concrete Shear Wall Specimens," *Journal of Structural Engineering*, vol. 151, no. 4, 2025. DOI: 10.1061/JSENDH.STENG-14251

[139] M. Priestley, F. Seible, and G. Calvi, in *Seismic Design and Retrofit of Bridges*. Wiley & Sons, 1996, ISBN: 9780471579984. DOI: 10.1002/9780470172858

[140] M. di Prisco, M. Colombo, and P. Martinelli, "Structural aspects of the collapse of a rc half-joint bridge: Case of the annone overpass," *Journal of Bridge Engineering*, vol. 28, 11 2023. DOI: 10.1061/JBENF2.BEENG-6063

[141] M. Pundir, M. Tirassa, M. Fernandez Ruiz, A. Muttoni, and G. Anciaux, "Review of fundamental assumptions of the Two-Phase model for aggregate interlocking in cracked concrete using numerical methods and experimental evidence," *Cement and Concrete*

Research, vol. 125, p. 105 855, 2019. DOI: 10.1016/j.cemconres.2019.105855

[142] E. Puntel, G. Bolzon, and V. Saouma, "Fracture Mechanics Based Model for Joints under Cyclic Loading," *Journal of Engineering Mechanics*, vol. 132, no. 11, 2006. DOI: 10.1061/(ASCE)0733-9399(2006)132:11(1151)

[143] E. Puntel and V. Saouma, "Experimental Behavior of Concrete Joint Interfaces under Reversed Cyclic Loading," *Journal of Structural Engineering*, vol. 134, no. 9, 2008. DOI: 10.1061/(ASCE)0733-9445(2008)134:9(1558)

[144] P. de Quevedo Iñarritu, N. Sipcic, M. Kohrangi, and P. Bazzurro, "Effects of pre-existing damage on fragility of urm and rc frame buildings," in *Energy-Based Seismic Engineering, Lecture Notes in Civil Engineering 155*. 2021. DOI: 10.1007/978-3-030-73932-4_2

[145] RAIU, "Malahide viaduct collapse on the dublin to belfast line on the 21st august 2009," Railway Accident Investigation Unit - Railway Safety Commission, Investigation Report No. 2010 - R004, 2010.

[146] N. Randl, "Design recommendations for interface shear transfer in *fib* model code 2010," *Structural Concrete*, vol. 14, pp. 230–241, 3 2013. DOI: 10.1002/suco.201300003

[147] M. Rasoolinejad and Z. Bazant, "Size Effect of Squat Shear Walls Extrapolated by Microplane Model M7," *ACI Structural Journal*, vol. 116, no. 3, pp. 75–84, 2019. DOI: 10.14359/51714478

[148] H. Reinhardt, "Fracture Mechanics of an Elastic Softening Material like Concrete," *Heron*, vol. 29, no. 2, 1984.

[149] J. Rivera, B. Luna, and A. Whittaker, "Seismic damage assessment of low aspect ratio reinforced concrete shear walls," MCEER, Technical Report MCEER-18-0003, 2018.

[150] J. Rivera and A. S. Whittaker, "Damage and Peak Shear Strength of Low-Aspect-Ratio Reinforced Concrete Shear Walls," *Journal of Structural Engineering*, vol. 145, no. 11, 2019. DOI: 10.1061/(ASCE)ST.1943-541X.0002364

[151] J. Rots and J. Blaauwendraad, "Crack models for concrete: Discrete or smeared? fixed multi-directional or rotating?" *Heron*, vol. 34, pp. 3–59, 1 1989.

[152] D. Ruggiero, E. Bentz, G. Calvi, and M. Collins, "Shear Response under Reversed Cyclic Loading," *ACI Structural Journal*, vol. 113, no. 6, pp. 1313–1324, 2016. DOI: 10.14359/51689033

[153] D. Ruggiero, E. Bentz, G. Calvi, and M. Collins, "The General Crack Component Model for reversed cyclic shear," *Structural Concrete*, vol. 25, no. 4, pp. 2571–2590, 2024. DOI: 10.1002/suco.202300266

[154] J. Sagaseta and R. Vollum, "Influence of aggregate fracture on shear transfer through cracks in reinforced concrete," *Magazine of Concrete Research*, vol. 63, no. 2, pp. 119–137, 2011. DOI: 10.1680/macr.9.00191

[155] M. Salehi, P. Sideris, and A. Liel, "Experimental testing of hybrid sliding-rocking bridge columns under torsional and biaxial lateral loading," *Earthquake Engineering and Structural Dynamics*, vol. 50, pp. 2817–2837, 10 2021. DOI: 10.1002/eqe.3474

[156] P. Santos and E. Júlio, "A state-of-the-art review on shear-frction," *Engineering Structures*, vol. 45, pp. 435–448, 2012. DOI: 10.1016/j.engstruct.2012.06.036

[157] N. Scattarreggia, R. Salamone, M. Moratti, D. Malomo, R. Pinho, and G. Calvi, "Collapse analysis of the multi-span reinforced concrete arch bridge of caprigliola, italy," *Engineering Structures*, vol. 251, 2022. DOI: 10.1016/j.engstruct.2021.113375

[158] M. Scott and T. Haukaas, "Software Framework for Parameter Updating and Finite-Element Response Sensitivity Analysis," *Journal of Computing in Civil Engineering*, vol. 22, no. 5, 2008. DOI: 10.1061/(ASCE)0887-3801(2008)22:5(281)

[159] R. Serpieri, G. Alfano, and E. Sacco, "A mixed-mode cohesive-zone model accounting for finite dilation and asperity degradation," *International Journal of Solids and Structures*, vol. 67-68, pp. 102–115, 2015. DOI: 10.1016/j.ijsolstr.2015.04.005

[160] J. R. Shewchuk, "Triangle: Engineering a 2D Quality Mesh Generator and Delaunay Triangulator," in *Applied Computational Geometry: Towards Geometric Engineering*, ser. Lecture Notes in Computer Science, M. C. Lin and D. Manocha, Eds., vol. 1148, From the First ACM Workshop on Applied Computational Geometry, Springer-Verlag, May 1996, pp. 203–222.

[161] Y. Shinohara, "Shear behavior in fracture process zone of concrete," in *Fracture Mechanics of Concrete Structures*, de Borst et al (eds), Ed., 2001.

[162] S. Stupkiewicz and Z. Mroz, "Modelling of friction and dilatancy effects at brittle interfaces for monotonic and cyclic loading," *Journal of Theoretical and Applied Mechanics*, vol. 3, pp. 707–739, 39 2001.

[163] T. Takeda, M. Sozen, and N. Nielsen, "Reinforced concrete response to simulated earthquakes," *Journal of the Structural Division*, vol. 96, 12 1970. DOI: 10.1061/JSDEAG.0002765

[164] Y. Tanaka and J. Murakoshi, "Reexamination of Dowel Behavior of Steel Bars Embedded in Concrete," *ACI Structural Journal*, vol. 108, no. 6, pp. 659–668, 2011.

[165] T. Tassios and E. Vintzeleou, "Concrete-to-concrete friction," *Journal of Structural Engineering*, vol. 113, no. 4, 1987. DOI: 10.1061/(ASCE)0733-9445(1987)113:4(832)

[166] M. Tirassa, M. Ruiz, and A. Muttoni, "Influence of cracking and rough surface properties on the tranfer of forced in cracked concrete," *Engineering Structures*, vol. 225, 2020. DOI: 10.1016/j.engstruct.2020.111138

[167] T. Tran and J. Wallace, "Experimental study of nonlinear flexural and shear deformations of reinforced concrete structural walls," in *15th World Conference on Earthquake Engineering, Lisboa*, 2012.

[168] A. Trandafir, D. Palipana, G. Proestos, and B. Mihaylov, "Framework for crack-based assessment of existing lightly reinforced concrete deep members," *ACI Structural Journal*, vol. 119, pp. 255–266, 1 2022. DOI: 10.14359/51733143

[169] A. Trandafir, D. Palipana, G. Proestos, and B. Mihaylov, "The importance and use of vertical crack displacements for the assessment of existing reinforced concrete deep beams," *Engineering Structures*, vol. 316, 2024. DOI: 10.1016/j.engstruct.2024.118635

[170] A. Trandafir, G. Proestos, and B. Mihaylov, "Detailed crack-based assessment of a 4-m deep beam test specimen," *Structural Concrete*, vol. 24, pp. 756–770, 1 2023. DOI: 10.1002/suco.202200149

[171] B. Trost, "Interaction of sliding, shear and flexure in the seismic response of squat reinforced concrete shear walls," Doctoral Thesis, ETH Zurich, 2017.

[172] B. Trost, H. Schuler, and B. Stojadinovic, "Experimental investigation of sliding on compact sliding specimens under cyclic loads," in *Second European Conference on Earthquake Engineering and Seismoology, Istanbul*, 2014.

[173] F. Vecchio, "Analysis of Shear-Critical Reinforced Concrete Beams," *ACI Structural Journal*, vol. 97, no. 1, 2000. DOI: 10.14359/839

[174] F. Vecchio and M. Collins, "The Modified Compression-Field Theory for Reinforced Concrete Elements Subjected to Shear," *ACI Structural Journal*, vol. 83, no. 2, pp. 219–231, 1986. DOI: 10.14359/10416

[175] E. Vintzeleou and T. Tassios, "Behavior of Dowels under Cyclic Deformations," *ACI Structural Journal*, vol. 84, no. 1, pp. 18–30, 1987. DOI: 10.14359/2749

[176] J. Walraven, "Fundamental Analysis of Aggregate Interlock," *Journal of the Structural Division*, vol. 107, no. 11, pp. 2245–2270, 1981. DOI: 10.1061/JSDEAG.0005820

[177] J. Woods, Y. Yang, P. Chen, D. Lau, and J. Erochko, "Automated Crack Detection and Damage Index Calculation for RC Structures Using Image Analysis and Fractal Dimension," *Journal of Structural Engineering*, vol. 147, no. 4, 2021. DOI: 10.1061/(ASCE)ST.1943-541X.0002970

[178] Y. Yoshida, T. Kisaku, and C. Fujiyama, "Pseudo-cracking approach in reinforced concrete beam with horizontal crack," *Structural Concrete*, 2025. DOI: 10.1002/suco.70045

[179] O. Yurdakul, C. Del Vecchio, M. Di Ludovico, L. Routil, and O. Avsar, "Crack width-based fragility curves for repairability of substandard beam-column joints," *Bulletin of Earthquake Engineering*, vol. 19, pp. 6081–6111, 2021. DOI: 10.1007/s10518-021-01218-6

[180] J. Zaborac, A. Athanasiou, S. Salamone, O. Bayrak, and T. Hrynyk, "Evaluation of structural cracking in concrete," Center for Transportation Research, Rep. No. FHWA/TX-19-0-6919-1, 2019.

[181] J. Zaborac, A. Athanasiou, S. Salamone, O. Bayrak, and T. Hrynyk, "Crack-based shear strength assessment of reinforced concrete members using a fixed- crack continuum modeling approach," *Journal of Structural Engineering*, vol. 146, 4 2020. DOI: 10.1061/(ASCE)ST.1943-541X.0002564

[182] J. Zaborac, B. Perez, T. Hrynyk, and O. Bayrak, "Structural performance assessment of a 60-year-old reinforced concrete bent cap," *Structural Concrete*, vol. 21, pp. 2549–2564, 6 2020. DOI: 10.1002/suco.202000033

[183] P. Zamani, S. Azhari, M. Hamidia, and N. Hassani, "Crack image-based FEMA P-58 compliant fragility models for automated earthquake-induced loss estimation in non-ductile RC moment frames," *Structures*, vol. 60, 2024. DOI: 10.1016/j.istruc.2024.105873

[184] E. Zewdie, C. Fujiyama, and K. Maekawa, "Dowel Bar Contribution to Bond Deterioration under Cyclic Loading," *ACI Structural Journal*, vol. 121, no. 5, 2024. DOI: 10.14359/51740858

[185] K. Zhong, "Influence of reinforcing steel fracture on seismic performance of concrete structures: Fracture simulation, earthquake duration effects, and design strategies," Doctoral Thesis, Stanford University, 2020.

Appendix A

A simple macro-element for modeling interface behavior

This Appendix is partially based on the following publication:

W. Galik et al., "Discrete modeling of reinforced concrete crack interfaces: A crack-based assessment perspective," in *18th World Conference on Earthquake Engineering, Milan Italy*, WCEE, Ed., 2024

This appendix presents a simplified approach for modeling interfaces with existing tools. In some cases, high-fidelity crack models may not be worth the effort required to model and deal with convergence issues. For these cases, a simpler macro-element has been developed. The macro-element is useful for modeling 1-dimensional interfacial behavior, such as crack sliding or bond-slip of reinforcement elements.

Crack Sliding The reversed-cyclic hysteretic shear-slip behavior of concrete cracks consists of four distinct behavioral phases, each of which can be approximated with the gap element (elastic-plastic or hyperbolic) that is available in OpenSees. The phases are:

1. Rapid shear stress accumulation characterized by a softening stiffness. Depending on the initial crack width, an initial "engagement" slip (i.e., gap) δ_{ci}^{+} may be required to mate aggregate particles of opposing crack faces. Shear stress accumulation begins after the aggregates interlock;

2. Rapid shear stress reversal upon unloading. This progresses until

an activation load V_{act}^{-} (negative magnitude) is attained, at which point the crack slip reverses suddenly with little increase in shear load magnitude. Plastic slip reversal continues until aggregate particles mate in the negative direction;

3. Shear accumulation with continued unloading beyond V_{act}^{-} begins at an engagement slip δ_{ci}^{-}. The trend in this region mirrors that of the initial loading phase, though is not necessarily symmetric;

4. Rapid shear stress reversal upon reloading. Sudden slip reversal at an activation stress V_{act}^{+} (positive magnitude). This behavior resembles that of the unloading phase.

Each behavior phase is modeled by a gap element (see Fig. A.1) that is characterized by a direction (i.e., compression-only or tension-only), a slip δ at which load begins to accumulate, and a peak strength V_{max}^{i}. A hyperbolic shear force-slip backbone is adopted for each i^{th} gap element:

$$V^{i}(s) = \frac{s - \delta^{i}}{\frac{1}{G} + \frac{s-\delta^{i}}{V_{max}^{i}}} \tag{A.1}$$

where s is the interfacial relative slip, δ^{i} is the element-specific slip offset, and G is the interface shear stiffness. The signs of δ^{i} and V_{max}^{i} determine whether the gap element is compression-only or tension-only.

Arranging the four gap elements in parallel produces a macro-element that can represent the reversed-cyclic behavior of cracked concrete (or other interfaces such as bar-concrete bond behavior). A schematic of the macro-element is shown in Fig. A.1.

The V_{max}^{i} values depend on the interface characteristics and the crack stresses. Calvi, et al [26] provide an expression for the activation stress. Assuming interfacial contact is not lost:

$$V_{act} = \pm f_{ci} A_c \frac{\left(\mu \cos\frac{w}{s} - \sin\frac{w}{s}\right)}{\left(\cos\frac{w}{s} + \mu \sin\frac{w}{s}\right)} \tag{A.2}$$

The maximum shear force in the loading phases (1 and 3) can be estimated with Eq. (2.4), which estimates the maximum shear stress that can be transferred between two opposite crack faces with a fixed width. Note that Eq. (A.2) captures the evolution of V_{act} with dilation

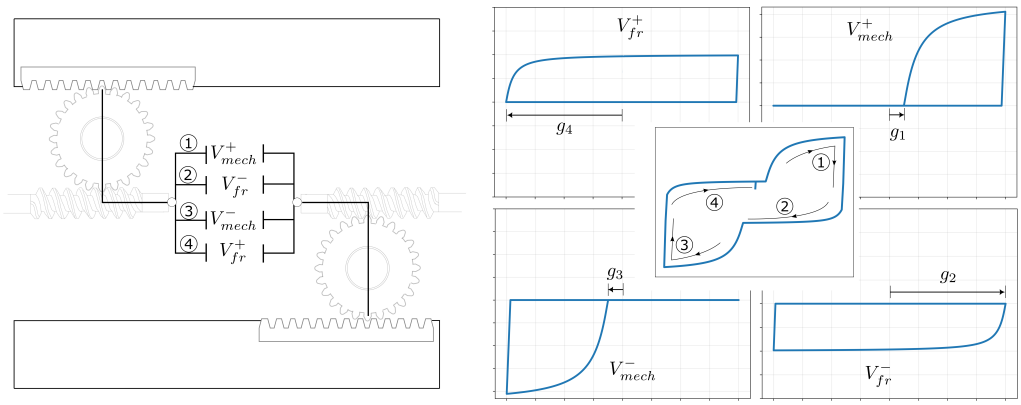

Figure A.1. (a) parallel arrangement of interface macro-element, which gives rise to (b) characteristic reversed-cyclic interface response

and local crack compression. Strictly, a parameter update routine (Scott and Haukaas [158]) should be implemented to model this dependency in OpenSees. However, the parameter update functionality is not available for all materials in OpenSees, so a cruder analysis can be performed in OpenSees with a constant shear value based on characteristic values of α and f_{ci}.

An example of the crack sliding macro-element can be found in the conference paper [67].

Reinforcement Bond Slip Cyclic bond, discussed briefly in Section 2.2.4, may be single-sided or fully-reversed, depending on the application, and resists pullout by an interlocking mechanism (reinforcement lugs ploughing through concrete matrix) and by frictional means. In loading, both mechanisms are active, while only friction is counted on during reversal. Overall, the cyclic bond-slip behavior resembles that of cyclic crack sliding, where reinforcement lugs play the role of aggregate interlock. The analogy is exploited by adapting a simple macro-element, developed originally for crack sliding by the Author [67], to model bond-slip. The macro-model for interface behavior is summarized in Fig. A.1.

The macro-model consists of a directional `hyperbolicGap` material in parallel with an `EPPGap` material. Putting this configuration in both directions results in a 4-component macro-element. The `hyperbolicGap`

materials define the mechanical sliding resistance and the `EPPGap` materials describe friction. The model is fully defined by a mechanical strength, a frictional strength and an initial sliding stiffness.

Bar pullout strength, though affected by numerous factors including confinement pressure, bar diameter, concrete strength and number of load cycles (all briefly discussed in Section 2.2.4), can be reasonably approximated at each material point as $1.0\sqrt{f'_c}$, which is the upper end of the expected average bond stress along a length of bar [118]. This strength is assigned to each `hyperbolicGap` material. Frictional strength is taken as 10% of the mechanical resistance to sliding and is assigned to the `EPPGap` elements. Together, the total resistance in loading is $1.1\sqrt{f'_c}$. The initial sliding stiffness of the `hyperbolicGap` element is chosen so the peak mechanical bond (i.e., $0.9V_{mech} + V_{fr}$) is attained at a secant stiffness of 20 MPa/mm, corresponding to the suggestion of Lowes, et al [95].

The use of a hyperbolic loading function for bond slip does not capture the loss of bond strength at large slips. This in theory limits the usefulness of the macro-element for when large slips are not expected. However, the model mimics the Tension Chord Model [105] which uses rigid-plastic bond slip laws and captures a wide range of phenomena in cracked structural concrete. An alternative approach would be to replace the `HyperbolicGap` components with `ElasticPPGap` elements having a negative post-peak stiffness.

Appendix B

Source code for OpenSees implementation of 2D crack material

The C++ source code for the implementation of a new nD crack material is reproduced here, following the guide for implementing new materials in OpenSees: guide for adding new material. Eventual updates to the source code can be followed at the github repository: BillGalik/multi-surf-crack2d

The code is broken into a header file, `MultiSurfCrack2D.h`, which defines the variables and methods used by the material model, as well as a body file `MultiSurfCrack2D.cpp`, which provides the implementation of the methods. Some methods are required within the OpenSees framework and are called by other routines. These include the constructor, the trial strain method, the commit method, as well as various getters and setters. Additionally, a slew of private "helper" functions have been defined to visually simplify the OpenSees methods. This aids both in readability of the code and in debugging.

The header file is reproduced in Source Code B.1, while the implementation is partially shown in Source Code B.3. Some OpenSees specific methods—such as the parsing method, printing methods, sending methods and receiving methods—have been removed for conciseness and readability of the implementation file. The full source code is maintained at the above github repository.

The big picture of the implementation is in the `setTrialStrain()` method, which, although already included in Source Code B.3, is isolated in Source Code B.2 as a quick reference. All the helper subroutines can be

traced back to the `setTrialStrain()` method.

Source Code B.1: header file for material model

```
#pragma once
#include <string>
#include <stdio.h>
#include <stdlib.h>
#include <math.h>
#include <algorithm>
#include <cstdlib>

#include "Vector.h"
#include "Matrix.h"
#include <ID.h>
#include <NDMaterial.h>

class MultiSurfCrack2D: public NDMaterial
{
public:

// FUNCTIONS REQUIRED BY OTHER OPENSEES ROUTINES
// ---------------------------------------------
// empty constructor
MultiSurfCrack2D();

// full constructor
MultiSurfCrack2D(int tag,
   Matrix De,            // elastic loading stiffness
   matrix (MPa/mm)
   Matrix DeU,           // elastic unloading stiffness
   matrix (MPa/mm)
   double user_fc,       // concrete strength (MPa)
   double user_ag,       // max aggregate diameter (mm)
   double user_fcl,      // crack closure stress magnitude
   (MPa)
   double user_Acr,      // nominal crack area (thickness *
    element discretization length)
   double user_rho_lok,  // interlock dilation parameter
   double user_chi_lok,  // cohesion ratio for interlock
   surface
   double user_rho_act,  // rubble dilation parameter
   double user_mu,       // unloading friction coefficient
   double user_chi,      // unloading cohesion ratio (c/
   vcimax)  -- activation surface
```

```
    double user_zeta,      // slip break point (pinching)
    double user_kappa,     // roughness transition parameter
    double user_theta,     // average contact angle (radians)
    double user_w,         // initial crack width (mm)
    int cPath);            // 1 if load path is width-
    constant, else 0

// destructor
~MultiSurfCrack2D();

// clone the material
NDMaterial* getCopy();
NDMaterial* getCopy(const char* type);

int getOrder() const { return 2; }
const char* getType() const { return "MultiSurfCrack2D"; }

int commitState();
int revertToLastCommit();
int revertToStart();

//get the strain
int setTrialStrain(const Vector& strainFromElement);

//send back the strain
const Vector& getStrain();

//send back the stress
const Vector& getStress();

//send back the tangent
const Matrix& getTangent();
const Matrix& getInitialTangent();

void Print(OPS_Stream& s, int flag);
int sendSelf(int commitTag, Channel& theChannel);
int recvSelf(int commitTag, Channel& theChannel,
    FEM_ObjectBroker& theBroker);


void PrintState();

private:

// INTERNAL "HELPER" FUNCTIONS
```

```
79 // -----------------------------------------------
80 void setLoadingDirection();
81 void setDamagedStiffness();
82 void trialTangentStiffness();
83 void takeElasticTrialStep();
84 void checkActiveYieldSurface();
85 void checkActiveYieldSurface(std::string&
       controlling_surface);
86 int overlapYieldSurface();
87 double getF_interlock();
88 double getF_activation();
89 void plasticReturn();
90 double incrementPlasticMultiplier();
91 void trialStressReturn();
92 void updateFlowDir();
93 void updateInterlockFlowDir();
94 void updateActivationFlowDir();
95 void initializeSurfacesShape();
96 void updateInterlockShape();
97 void updateDerivedShapeParameters();
98 double get_w_tilde();
99 void setvcimax();          // set vcimax, and drag rest of
       yield surfaces along with MCFT surface
100 double d_vcimax_d_w_tilde();
101 double d_vcimax_dnu();
102 double d_F_dvcimax();
103 double d_F_dfcc();
104 double d_F_dw();
105 double d_F_dnu();          // partial of yield surface w/rsp
        crush strain
106 double d_F_dchi();
107 double d_F_dk();
108 Vector strain_gradient_w_tilde();
109 Vector strain_gradient_nu();
110 Vector strain_gradient_chi();
111 Vector strain_gradient_k();
112 double d_r_ds();
113 double get_postPeakCompressionSoftening();
114
115
116 // CLASS MEMBERS
117 // -----------------------------------------------
118 // input elastic properties (initial) ..............
119 const Matrix tangent_elastic_loading_initial;
120 const Matrix tangent_elastic_unloading_initial;
```

```
121
122
123 // committed state ..................................
124 Vector strain_committed;
125 Vector strain_plastic_committed;
126 Vector stress_committed;
127 Matrix tangent_committed;
128 double sMAX;      // maximum (positive) plastic slip
129 double sMIN;      // maximum (negative) plastic slip
130 double sDAM;      // maximum (pos or neg) total slip --
    used for sliding damage calculations
131 double wMAX;
132
133 // current state ....................................
134 Matrix tangent_elastic_damaged;
135 Matrix tangent_current;         // Stress/length, for
    internal calculations
136 Matrix tangentF;                // Force/length, for
    handing off to element
137 Vector strain_increment;
138 Vector strain_current;          // strain from element (not
     counting initial residual strain)
139 Vector strain_plastic_current;
140 Vector stress_current;          // crack stresses used for
    internal calculations
141 Vector force_current;           // crack forces, passed to
    zeroLengthND element
142 double vcimax;                  // peak attainable shear
    stress (positive valued)
143 double crushing_strain;         // accumulated crushing
    strain (crack closure, therefore negative) while F_c^lok
     is active
144 double dLambda;
145
146 // crack properties .................................
147 double fc;     // concrete strength (MPa)
148 double ag;     // max aggregate diameter (mm)
149 double fcl;    // closure stress magnitude (MPa)
150 double Acr;    // area of this crack section (thickness x
    discretization length)
151 double w_res;  // residual crack width at start of analysis
     (mm)
152
153 // MCFT aggregate interlock (lok) parabola ...........
154 double c_lok;         // cohesion
```

```
155 double chi_lok;        // cohesion ratio
156 double chi_lok_r;      // bounding value of chi_lok for
       rough surface
157 double chi_lok_s;      // bounding value of chi_lok for
       smooth surface
158 double d;              // parameters defining yield surface
       parabola
159 double h;              //   --
160 double k;              //   --
161 double k_rough;        // bounding value of k for rough
       surface
162 double k_smooth;       // bounding value of k for smooth
       surface
163 double rho_lok;        // dilation parameter for aggregate
       interlock
164 Vector dF_lok;         // flow direction for aggregate
       interlock
165 Vector dG_lok;         // non-associated flow direction for
       interlock
166 double kappa;          // roughness factor for interlock
167 double theta_tilde;    // average contact angle (radians)
       for sliding damage calculation
168 int criticalPath;      // 1 if loading path is constant-
       width, else 0
169 double shift;          // amount of tensile strength
       available for constant-width surface (i.e., horizontal
       shift from origin)
170
171 // partial Elliptical tension yield surface.............
172 double ft;            // peak traction
173 double chi_t;         // ratio of ft / vcimax
174 double xc;            // horizontal position of tensile
       ellipse center
175 double chi_c;         // ratio of xc / vcimax
176 double a_t;           // half horizontal axis length for
       tensile ellipse
177 double b_t;           // half vertical axis length for
       tensile ellipse
178 double m;             // parameter enforcing size of tensile
        ellipse (for real ellipse, need 0 < m < 1)
179 double l;             // survival algebra parameter
180 double n;             // survival algebra parameter
181
182 // semi-Elliptical compression yield surface............
183 double fcc;          // fc reduced to account for crushing
```

```
    damage (positive-valued)
double a_c;          // half horizontal axis length for
    compression ellipse
double b_c;          // half vertical axis length for
    compression ellipse

// Hyperbolic unloading activation (act) surface .....
double c_act;        // cohesion for activtion branch (may
    differ from c_lok)
double chi_act;      // cohesion ratio for activation branch
     (may differ from chi_lok)
double mu;           // friction ratio
double rho_act;      // dilation parameter for frictional
    unloading
Vector dF_act;       // flow direction for frictional
    unloading
Vector dG_act;       // non-associated flow direction for
    unloading
double zeta;         // break point (aka pinching point)

// crack stage ......................................
bool isElastic;
std::string dir;
double yield_criterion;
std::string active_surface;
double last_vci_lok;              // shear value of most
    recent stress point that converged to the combined
    interlock surface
double* rho_engaged;              // pointers to the
    currently engaged yield surface
Vector* dF_engaged;               //  --
Vector* dG_engaged;               //  --

};
```

Source Code B.2: `setTrialStrain()` method, isolated to provide a big-picture view of the implementation

```
// solve a trial displacement step
int MultiSurfCrack2D::setTrialStrain(const Vector&
    strainFromElement)
{
  strain_current = strainFromElement;
  strain_increment = strain_current - strain_committed;

  // update yield surface due to trial width
  setvcimax();

  // decide if crack is loading or unloading
  setLoadingDirection();

  // update elastic stiffness terms
  setDamagedStiffness();

  // get elastic trial stresses and check yield function
  takeElasticTrialStep();

  // plastic return if elastic trial violates yield surf
  if (yield_criterion > 0)
    plasticReturn();

  // check surface overlap after return to act. surface
  if (overlapYieldSurface())
  {
    // end activation process and reset stiffness
    dir = "loading";
    setDamagedStiffness();

    // return to previous converged state and redo elastic-
   trial, plastic correction
    takeElasticTrialStep();
    if (yield_criterion > 0)
      plasticReturn();
  }

  // tangent stiffness at trial stress that has been
   returned to yield surface
  trialTangentStiffness();

  return 0;     }
```

Source Code B.3: body file for material model

```
#include <cmath>
#include <iostream>
#include <string>
#include <vector>
#include <stdio.h>
#include <stdlib.h>
#include <math.h>
#include <algorithm>
#include <cstdlib>

#include <MultiSurfCrack2D.h>
#include <Channel.h>
#include <FEM_ObjectBroker.h>
#include <MaterialResponse.h>
#include <elementAPI.h>


// Parse user inputs and create material
void* OPS_MultiSurfCrack2D()
{
...
}

// Constructor
MultiSurfCrack2D::MultiSurfCrack2D(int tag,
        Matrix De,
        Matrix DeU,
        double user_fc,
        double user_ag,
        double user_fcl,
        double user_Acr,
        double user_rho_lok,
        double user_chi_lok,
        double user_rho_act,
        double user_mu,
        double user_chi,
        double user_zeta,
        double user_kappa,
        double user_theta,
        double user_w,
        int cPath = 0)
  : NDMaterial(tag, ND_TAG_MultiSurfCrack2D),
  tangent_elastic_loading_initial(De),
```

```
    tangent_elastic_unloading_initial(DeU),strain_committed
    (2),strain_plastic_committed(2),stress_committed(2),
    tangent_committed(De),sMAX(0.001),sMIN(-0.001),sDAM(0.),
    wMAX(0.1),tangent_elastic_damaged(De),tangent_current(De
    ),tangentF(2,2),strain_increment(2),strain_current(2),
    strain_plastic_current(2),stress_current(2),
    force_current(2),vcimax(15.),crushing_strain(0.),dLambda
    (0.),fc(user_fc),ag(user_ag),fcl(user_fcl),Acr(user_Acr)
    ,w_res(user_w),c_lok(0.),chi_lok(user_chi_lok),chi_lok_r
    (user_chi_lok),chi_lok_s(user_chi),h(-1.),k(1.),k_rough
    (1.),k_smooth(0.6),rho_lok(user_rho_lok),dF_lok(2),
    dG_lok(2),kappa(user_kappa),theta_tilde(user_theta),
    criticalPath(cPath),shift(0.005),m(0.5),fcc(user_fc),
    c_act(0.),chi_act(user_chi),mu(user_mu),rho_act(
    user_rho_act),dF_act(2),dG_act(2),zeta(user_zeta),
    isElastic(true),dir("loading"),yield_criterion(-1.),
    active_surface(""),last_vci_lok(0.0),
44  rho_engaged(&rho_lok),dF_engaged(&dF_lok),dG_engaged(&
    dG_lok)
45 {
46   // handling to ensure smooth yield surface
47   initializeSurfacesShape();
48
49   wMAX = std::max(wMAX, user_w);
50
51   // set initial size of MCFT parabola, cohesion and
     compression/tension ellipses
52   setvcimax();
53
54   // initialize flow directions
55   updateFlowDir();
56 }
57
58 // Destructor
59 MultiSurfCrack2D::~MultiSurfCrack2D()
60 {
61
62 }
63
64
65 void MultiSurfCrack2D::initializeSurfacesShape()
66 {
67   // activation cohesion not to exceed interlock cohesion
68   chi_act = std::min(chi_lok, std::max(chi_act, 0.0001));
69
```

```
70    // initialize "survival algebra variables"
71    l = m * m / (8 * (1 - m));
72    n = m / 4;
73
74    // calculate derived shape parameters
75    updateDerivedShapeParameters();
76  }
77
78
79  // solve a trial displacement step
80  int MultiSurfCrack2D::setTrialStrain(const Vector&
        strainFromElement)
81  {
82    strain_current = strainFromElement;
83    strain_increment = strain_current - strain_committed;
84
85    // update yield surface due to trial width
86    setvcimax();
87
88    // decide if crack is loading or unloading
89    setLoadingDirection();
90
91    // update elastic stiffness terms
92    setDamagedStiffness();
93
94    // get elastic trial stresses and check yield function
95    takeElasticTrialStep();
96
97    // plastic return if elastic trial violates yield surf
98    if (yield_criterion > 0)
99      plasticReturn();
100
101   // check for surface overlap after return to activation
        surface (if relevant)
102   int overlap = overlapYieldSurface();
103   if (overlap)
104   {
105     // end the activation process and reset loading
        stiffness
106     dir = "loading";
107     setDamagedStiffness();
108
109     // return to previous converged state and redo elastic-
        trial, plastic correction
110     takeElasticTrialStep();
```

```
111     if (yield_criterion > 0)
112       plasticReturn();
113   }
114
115   // tangent stiffness at trial stress that has been
       returned to yield surface
116   trialTangentStiffness();
117
118   return 0;
119 }
120
121
122 void MultiSurfCrack2D::setLoadingDirection()
123 {
124   // check direction of slip increment
125   double s = strain_current[1];
126   double vci = stress_current[1];
127   double s_prev = strain_committed[1];
128   double ds = strain_increment[1];
129   bool increasingSlipMagnitude = ((std::abs(s) - std::abs(
       s_prev)) > 0);
130
131
132   if (increasingSlipMagnitude)
133   {
134     // check if pinching point is exceeded
135     if ((s > zeta * sMAX) || (s < zeta * sMIN))
136       dir = "loading";
137
138     else
139     {
140       dir = "unloading";
141     }
142   }
143   else
144   {
145     if (ds == 0)
146     {
147       // case of pure mode-I loading
148       dir = "loading";
149     }
150     else
151     {
152       // slding reversal
153       dir = "unloading";
```

```
154     }
155   }
156 }
157
158
159 void MultiSurfCrack2D::setDamagedStiffness()
160 {
161   // crack stiffness in MPa/mm
162
163   double& sigTR = stress_committed[0];      // current
       normal stress (note, still haven't taken trial step)
164   double wCURR = strain_current[0] + w_res;   // current
       crack width
165   double& wInc = strain_increment[0];     // crack opening
       direction
166   double E_penalty = 1000.;         // penalty stiffness
       against crack overlap
167   double E_ruggiero;
168
169
170   // Update Crack Normal Stiffness -- Ruggiero model (
       simplified)
171   if (wCURR >= 0.0)   // separated crack nodes
172   {
173     E_ruggiero = std::min(E_penalty, fcl / wMAX);   //
       ruggiero model with q = infty
174   }
175   else    // overlapping crack nodes
176   {
177     if (wInc > 0)
178     {
179       // reload to closure point
180       double cohesive_stress = 0.0;
181       E_ruggiero = (-fcl + cohesive_stress - sigTR) / (-
      wCURR);
182     }
183     else
184     {
185       // penalty against further overlap
186       E_ruggiero = E_penalty;
187     }
188   }
189
190   tangent_elastic_damaged(0, 0) = E_ruggiero;
191
```

```
192   // Update Crack Shear Stiffness
193   double shearDamage = std::max(0.1, (1 - 2 * sMAX / ag));
194
195   if (dir == "loading")
196   {
197     tangent_elastic_damaged(1, 1) =
     tangent_elastic_loading_initial(1, 1) * shearDamage;
198     tangent_elastic_damaged(0, 1) =
     tangent_elastic_loading_initial(0, 1);
199     tangent_elastic_damaged(1, 0) =
     tangent_elastic_loading_initial(1, 0);
200   }
201   else
202   {   // undamaged stiffness if unloading
203     tangent_elastic_damaged(1, 1) =
     tangent_elastic_unloading_initial(1, 1);
204     tangent_elastic_damaged(0, 1) =
     tangent_elastic_unloading_initial(0, 1);
205     tangent_elastic_damaged(1, 0) =
     tangent_elastic_unloading_initial(1, 0);
206   }
207 }
208
209
210
211 void MultiSurfCrack2D::takeElasticTrialStep()
212 {
213   // clear any plastic residual from previous non-solution-
     path steps
214   isElastic = true;
215   strain_plastic_current = strain_plastic_committed;
216   stress_current = stress_committed;
217   dLambda = 0.0;
218   active_surface = "";
219
220   double& dwe = strain_increment[0];
221   double& dse = strain_increment[1];
222   double& s = strain_current[1];
223   double sign_s = (s > 0) ? 1 : ((s < 0) ? -1 : 0);
224
225   Matrix& De = tangent_elastic_damaged;
226   double dsig = De(0, 0) * dwe + De(0, 1) * dse * sign_s;
227   double dvci = De(1, 0) * dwe * sign_s + De(1, 1) * dse;
228   stress_current[0] = stress_committed[0] + dsig;
229   stress_current[1] = stress_committed[1] + dvci;
```

```
230
231   checkActiveYieldSurface();
232 }
233
234
235 void MultiSurfCrack2D::checkActiveYieldSurface()
236 {
237   double& ds = strain_increment[1];
238   double& vci = stress_current[1];
239
240   if (dir == "loading")
241   {
242     // check if interlock surface breached
243     yield_criterion = getF_interlock();
244     if (yield_criterion > 0)
245     {
246       isElastic = false;
247       active_surface = "interlock";
248       rho_engaged = &rho_lok;
249
250       updateInterlockFlowDir();
251       dF_engaged = &dF_lok;
252       dG_engaged = &dG_lok;
253     }
254   }
255   // else if (dir == "unloading" && (ds * vci > 0 && vci *
      last_vci_lok < 0))
256   else if ((dir == "unloading") && (ds * vci > 0))
257   {
258     // check if activation surface breached
259     yield_criterion = getF_activation();
260     if (yield_criterion > 0)
261     {
262       isElastic = false;
263       active_surface = "activation";
264       rho_engaged = &rho_act;
265
266       updateActivationFlowDir();
267       dF_engaged = &dF_act;
268       dG_engaged = &dG_act;
269     }
270
271   }
272   else
273   {
```

```
274     yield_criterion = -1.;
275   }
276 }
277 
278 
279 void MultiSurfCrack2D::checkActiveYieldSurface(std::string&
        controlling_surface)
280 {
281   if (controlling_surface == "interlock")
282     yield_criterion = getF_interlock();
283   else
284     yield_criterion = getF_activation();
285 }
286 
287 
288 int MultiSurfCrack2D::overlapYieldSurface()
289 {
290   int overlap = 0;
291   double& sigTR = stress_current[0];
292 
293   // check if activation surface overlaps with tensile de-
       cohesion surface
294   if ((active_surface == "activation") && (sigTR > 0))
295   {
296     // check if interlock surface breached for current
       stress state, which has already been returned to the
       activation surface
297     yield_criterion = getF_interlock();
298 
299     // signal if breached
300     if (yield_criterion > 0)
301       overlap = 1;
302   }
303 
304   else
305     overlap = 0;
306 
307   return overlap;
308 }
309 
310 
311 double MultiSurfCrack2D::getF_interlock()
312 {
313   double& sigTR = stress_current[0];
314   double& vciTR = stress_current[1];
```

```
315
316   double F_interlock;
317
318   if (!criticalPath)
319   {
320     // yield surface in tensile region
321     if (sigTR > 0)
322     {
323       double hkxv = h * k * chi_lok * vcimax;
324       F_interlock = 1 / 2 * std::pow(h * vciTR, 2) + std::
      pow((k - chi_lok) * sigTR - 1 * hkxv, 2) - std::pow((n +
      1) * hkxv, 2);
325     }
326
327     else if (sigTR < h * vcimax)
328     {
329       // yield surface in compressive region
330       F_interlock = std::pow((sigTR - h * vcimax) / a_c, 2)
     + std::pow(vciTR / b_c, 2) - 1;
331     }
332
333     else
334     {
335       // Parabolic (MCFT) yield surface
336       F_interlock = h * h / (k - chi_lok) * (std::abs(vciTR
     ) / vcimax - k) + std::pow((sigTR / vcimax - h), 2);
337     }
338   }
339
340   else
341   {
342     // Linear (constant crack width) yield surface
343     F_interlock = std::abs(vciTR) + (sigTR - shift * vcimax
     );
344   }
345
346   return F_interlock;
347 }
348
349
350 double MultiSurfCrack2D::getF_activation()
351 {
352   double& sigTR = stress_current[0];
353   double& vciTR = stress_current[1];
354
```

```
355   // Hyperbolic yield surface for cohesion-frictional
       sliding reversal
356   double F_activation = vciTR * vciTR - std::pow(k *
       chi_act * vcimax, 2) - std::pow(mu * sigTR, 2);
357
358   return F_activation;
359 }
360
361
362 // stress-return algorithm
363 void MultiSurfCrack2D::plasticReturn()
364 {
365   // if entering this method, FTR > 0, hence do-while loop
366
367   // newton-raphson method with updating flow direction (
       general cutting plane algorithm)
368   const double F_TOL = 1e-8;
369   int itercnt = 0;
370   const int CNT_MAX = 1000;
371
372   do
373   {
374     // update flow direction at each iteration
375     if (active_surface == "interlock")
376       updateFlowDir();
377
378     // estimate plastic multiplier to return stress state
       to yield surface
379     double dlam = incrementPlasticMultiplier();
380
381     // add the incremental flow to the accumulated flow
       during the current iterative plastic return step
382     dLambda += dlam;
383
384     // updated stresses (still trial)
385     trialStressReturn();
386
387     // check active yield function at new approximation
388     checkActiveYieldSurface(active_surface);
389
390     // emergency exit (non-convergence of newton-raphson
       solver)
391     itercnt += 1;
392     if (itercnt > CNT_MAX)
393     {
```

```
394       // PRINT opserr WARNING
395       break;
396     }
397   } while (std::abs(yield_criterion) > F_TOL);
398 }
399
400
401 double MultiSurfCrack2D::incrementPlasticMultiplier()
402 {
403   Matrix& De = tangent_elastic_damaged;
404   Vector& dF = *dF_engaged;
405   Vector& dG = *dG_engaged;
406
407   // generalized cutting plane algorithm
408   double dlam = yield_criterion / (dF ^ (De * dG));
409
410   return dlam;
411 }
412
413
414 void MultiSurfCrack2D::trialStressReturn()
415 {
416   // updated plastic strains
417   Vector depsP = dLambda * (*dG_engaged);
418   strain_plastic_current = strain_plastic_committed + depsP
      ;
419
420   // some shortcut parameters
421   double& s = strain_current[1];
422   double& ds = strain_increment[1];
423   double sgn_s = (s > 0) ? 1 : ((s < 0 ? -1 : 0));
424   double& dw = strain_increment[0];
425   double& dsP = depsP[1];
426   double& dwP = depsP[0];
427   Matrix& De = tangent_elastic_damaged;
428
429   // updated stress
430   double dsig = De(0, 0) * (dw - dwP) + De(0, 1) * (ds -
      dsP) * sgn_s;
431   double dvci = De(1, 0) * (dw - dwP) * sgn_s + De(1, 1) *
      (ds - dsP);
432   stress_current[0] = stress_committed[0] + dsig;
433   stress_current[1] = stress_committed[1] + dvci;
434 }
435
```

```
436
437 // get flow vectors
438 void MultiSurfCrack2D::updateFlowDir()
439 {
440   updateInterlockFlowDir();
441   updateActivationFlowDir();
442 }
443
444
445 void MultiSurfCrack2D::updateInterlockFlowDir()
446 {
447   double sigTR = stress_current[0];
448   double vciTR = stress_current[1];
449
450   // get sign of vci
451   double sign_vci = (vciTR > 0) ? 1 : ((vciTR < 0) ? -1 :
      1);
452
453   if (!criticalPath)
454   {
455     // override for tensile region
456     if (sigTR > 0)
457     {
458       dF_lok[0] = 2 * std::pow(k - chi_lok, 2) * (sigTR - l
      * h * k * chi_lok * vcimax / (k - chi_lok));
459       dF_lok[1] = l * h * h * vciTR;
460     }
461
462     // override for compressive region
463     else if (sigTR < h * vcimax)
464     {
465       dF_lok[0] = 2 * (sigTR - h * vcimax) / (a_c * a_c);
466       dF_lok[1] = 2 * vciTR / (b_c * b_c);
467     }
468
469     else
470     {
471       // parabolic MCFT yield parabola
472       dF_lok[0] = 2.0 / vcimax * (sigTR / vcimax - h);
473       dF_lok[1] = h * h / vcimax / (k - chi_lok) * sign_vci
      ;
474     }
475   }
476
477   else
```

```
478   {
479     // linear "critical path" parabola
480     dF_lok[0] = 1.0;
481     dF_lok[1] = sign_vci;
482 
483   }
484 
485   // also, non-associated flow
486   dG_lok[0] = rho_lok * dF_lok[0];
487   dG_lok[1] =           dF_lok[1];
488 }
489 
490 
491 void MultiSurfCrack2D::updateActivationFlowDir()
492 {
493   double sigTR = stress_current[0];
494   double vciTR = stress_current[1];
495 
496   // use current stresses to calculate flow direction
497   dF_act[0] = -2 * mu * mu * sigTR;
498   dF_act[1] = 2 * vciTR;
499 
500   // also non-associated flow
501   dG_act[0] = rho_act * dF_act[0];
502   dG_act[1] =           dF_act[1];
503 }
504 
505 
506 void MultiSurfCrack2D::setvcimax()
507 {
508   // update crushing damage to f'c
509   double Ecp = get_postPeakCompressionSoftening();
510   fcc = std::max(0.2*fc, fc + Ecp * crushing_strain);
511 
512   // get effective crack width, including sliding damage
513   double w_tilde = get_w_tilde();
514 
515   // update vcimax (both crushing and sliding damage)
516   vcimax = std::sqrt(fcc) / (0.31 + 24 * w_tilde / (ag +
      16));
517 
518   // update compression ellipse
519   a_c = -fcc - h * vcimax;
520   b_c = k * vcimax;
521 
```

```
522   // update interlock cohesion
523   c_lok = k * chi_lok * vcimax;
524
525   // update activation cohesion
526   c_act = k * chi_act * vcimax;
527
528   // update traction ellipse
529   ft = k * chi_t * vcimax;
530   xc = k * chi_c * vcimax;
531   a_t = ft - xc;
532   b_t = a_t * std::sqrt(h * c_lok / (2 * xc * d));
533 }
534
535
536 double MultiSurfCrack2D::get_w_tilde()
537 {
538   double w = strain_current[0] + w_res;
539   double pi = 2 * std::acos(0.0);
540   double w_tilde = std::max(0.0, w) + 8 / (3 * pi) * std::
      sin(theta_tilde) * sDAM;
541
542   return w_tilde;
543 }
544
545
546 double MultiSurfCrack2D::get_postPeakCompressionSoftening()
547 {
548   // Softening Modulus (MPa/mm) -- positive valued
549   double Ecp = 100.0;
550
551   return Ecp;
552 }
553
554
555 void MultiSurfCrack2D::trialTangentStiffness()
556 {
557   if (isElastic)
558   {
559     tangent_current = tangent_elastic_damaged;
560   }
561   else
562   {
563     Matrix& De = tangent_elastic_damaged;
564
565     // stress vector contributions
```

```
566     Vector dF = *dF_engaged;          // stress gradient
        for active yield surface
567     Vector dG = *dG_engaged;          // flow vector
568
569     // strain-hardening contributions
570     double f_w = d_F_dw();          // yield surface
        sensitivity to crack width
571     double f_nu = d_F_dnu();          // yield surface
        sensitivity to crushing -- contributes to elastoplastic
        tangent if...
572     Vector w_eps = strain_gradient_w_tilde();     // strain
         gradient of effective width, omega_tilde
573     Vector nu_eps = strain_gradient_nu(); // strain
        gradient of crushing strain, nu
574
575     // shape change contributions
576     double f_chi = d_F_dchi();        // variation of yield
         surface with shape parameter chi_lok
577     double f_k = d_F_dk();          // variation of yield
        surface with shape parameter k
578     Vector chi_eps = strain_gradient_chi(); // strain
        gradient of cohesion shape parameter chi_lok
579     Vector k_eps = strain_gradient_k();   // strain
        gradient of size shape parameter k
580
581     Vector Dg = De * dG;
582     Vector fD = De ^ dF;
583     Vector v_strain = w_eps * f_w + nu_eps * f_nu;
584     Vector v_shape = f_chi * chi_eps + f_k * k_eps;
585     tangent_current = De - (Dg % (fD + v_strain + v_shape))
        / (dF ^ (De * dG));
586   }
587 }
588
589
590 // partial derivative of yield surface w/rsp crack width
591 double MultiSurfCrack2D::d_F_dw()
592 {
593   double f_w = d_F_dvcimax() * d_vcimax_d_w_tilde();
594   return f_w;
595 }
596
597
598 // partial derivative of yield surface w/rsp crushing
        strain (nu in crack formulation paper)
```

```
599 double MultiSurfCrack2D::d_F_dnu()
600 {
601   double Ecp = get_postPeakCompressionSoftening();
602 
603   double f_nu = d_F_dvcimax() * d_vcimax_dnu() + d_F_dfcc()
      * Ecp;
604 
605   return f_nu;
606 }
607 
608 
609 // partial derivative of yield surface w/rsp size parameter
     d
610 double MultiSurfCrack2D::d_F_dchi()
611 {
612   double f_chi = 0.0;
613 
614   double& sigTR = stress_current[0];
615   double& vciTR = stress_current[1];
616 
617   if (active_surface == "interlock")
618   {
619     // compressive surface
620     if (sigTR < h * vcimax)
621     {
622       f_chi = 0.0;
623     }
624 
625     // tensile surface
626     else if (sigTR > 0)
627     {
628       double hkv = h * k * vcimax;
629       f_chi = -2 * (sigTR + l * hkv) * ((k - chi_lok) *
    sigTR - l * chi_lok * hkv) - 2 * chi_lok * std::pow((n +
     l) * hkv, 2);
630     }
631 
632     // MCFT surface
633     else
634     {
635       f_chi = std::pow(h / (k - chi_lok), 2) * (std::abs(
    vciTR) / vcimax - k);
636     }
637   }
638 
```

```
639   else if (active_surface == "activation")
640   {
641     f_chi = 0.0;
642   }
643 
644   return f_chi;
645 }
646 
647 
648 // partial derivative of yield surface w/rsp size parameter
      k
649 double MultiSurfCrack2D::d_F_dk()
650 {
651   double f_k = 0.0;
652 
653   double& sigTR = stress_current[0];
654   double& vciTR = stress_current[1];
655 
656   if (active_surface == "interlock")
657   {
658     // compressive surface
659     if (sigTR < h * vcimax)
660     {
661       f_k = -2 / k * std::pow(vciTR / (k * vcimax), 2);
662     }
663 
664     // tensile surface
665     else if (sigTR > 0)
666     {
667       double hxv = h * chi_lok * vcimax;
668       f_k = 2 * (sigTR - l * hxv) * ((k - chi_lok) * sigTR
      - l * k * hxv) - 2 * k * std::pow((n + l) * hxv, 2);
669     }
670 
671     // MCFT surface
672     else
673     {
674       f_k = -h * h / (k - chi_lok);
675     }
676   }
677 
678   else if (active_surface == "activation")
679   {
680     f_k = -2 * k * std::pow(chi_act * vcimax, 2);
681   }
```

```
682
683   return f_k;
684 }
685
686
687 // derivative of vcimax w/rsp effective crack width
688 double MultiSurfCrack2D::d_vcimax_d_w_tilde()
689 {
690   double w_tilde = get_w_tilde();
691
692   double denom = 0.31 + 24 * w_tilde / (ag + 16.0);
693   double deriv = -24.0 / (ag + 16.0) * std::sqrt(fcc) / (
       std::pow(denom, 2));
694
695   return deriv;
696 }
697
698
699 // derivative of vcimax w/rsp crushing strain
700 double MultiSurfCrack2D::d_vcimax_dnu()
701 {
702   double w_tilde = get_w_tilde();               //
       effective crack width
703
704   double denom = 0.31 + 24 * w_tilde / (ag + 16.0);
705   double Ecp = get_postPeakCompressionSoftening();
706   double deriv = 1. / 2. / std::sqrt(fcc) * Ecp / denom;
707
708   return deriv;
709 }
710
711
712 // derivative of yield surface w/rsp vcimax
713 double MultiSurfCrack2D::d_F_dvcimax()
714 {
715   double deriv;
716   double& sigTR = stress_current[0];
717   double& vciTR = stress_current[1];
718
719   if (active_surface == "interlock")
720   {
721     if (!criticalPath)
722     {
723       // override for compressive surface
724       if (sigTR < h * vcimax)
```

```
725       {
726         deriv = 2 * h * (sigTR - h * vcimax) * ((sigTR - h
    * vcimax) - a_c) / std::pow(a_c, 3) - 2 / vcimax * std::
    pow(vciTR / b_c, 2);
727       }
728
729       // override for tensile surface
730       else if (sigTR > 0)
731       {
732         double hkx = h * k * chi_lok;
733         double k_minus_x = k - chi_lok;
734         deriv = -2 * hkx * k_minus_x * (l*sigTR + (n*n + 2*
    n*l) * hkx/k_minus_x * vcimax);
735       }
736
737       else
738       {
739         // MCFT surface
740         deriv = -1 / std::pow(vcimax, 2) * (h * h / (k -
    chi_lok) * std::abs(vciTR) + 2 * sigTR * (sigTR / vcimax
     - h));
741       }
742     }
743
744     else
745     {
746       deriv = -shift;
747     }
748   }
749   else if (active_surface == "activation")
750   {
751     double radical = std::sqrt(1 + std::pow(mu * sigTR / (
    chi_act * vcimax), 2));
752     deriv = -2 * vcimax * std::pow(k * chi_act, 2);
753   }
754
755   return deriv;
756 }
757
758
759 // derivative of yield surface w/rsp reduced compression
    strength fcc
760 double MultiSurfCrack2D::d_F_dfcc()
761 {
762   double deriv = 0.0;
```

```
763
764   double& sigTR = stress_current[0];
765
766   // this derivative only non-zero when compression surface
        is active
767   if (active_surface == "interlock" && sigTR < h * vcimax)
768   {
769     deriv = 2 * std::pow(sigTR - h * vcimax, 2) / std::pow(
       a_c, 3);
770   }
771
772   return deriv;
773 }
774
775
776 // strain gradient of effective crack width omega_tilde
777 Vector MultiSurfCrack2D::strain_gradient_w_tilde()
778 {
779   Vector w_tilde_eps(2);
780
781   double w = strain_current[0] + w_res;   // total crack
       width
782   w += 0.0000001;                // avoid div.by.zero
783
784   double t_w = std::max(0., w) / w;     // toggle width
       part off if w < 0
785   w_tilde_eps[0] = t_w;
786
787   double& s = strain_current[1];
788   double t_s;
789   t_s = std::floor(std::abs(s) / (sDAM + 0.00001));   //
       toggle sliding part off if |s| < sDAM    (avoid div.by.
       zero)
790   t_s = std::min(1.0, std::max(0.0, t_s));
791
792   double pi = 2 * std::acos(0.0);
793   w_tilde_eps[1] = 8 / (3 * pi) * std::sin(theta_tilde) *
       t_s;
794
795   return w_tilde_eps;
796 }
797
798
799 // strain gradient of crushing strain nu
800 Vector MultiSurfCrack2D::strain_gradient_nu()
```

```
{
  Vector nu_eps(2);

  // toggle function (1 if compression surface engaged, else 0)
  double t_c;

  Vector dF = *dF_engaged;    // stress gradient for active yield surface

  dF[0] += 0.00000001;       // avoid div.by.zero
  t_c = std::min(0., dF[0]) / dF[0];    // ...outward normal points in negative crack direction (t_c = 1)
  t_c = (active_surface == "interlock") ? t_c : 0.0;    // ...and interlock surface is active

  nu_eps[0] = t_c;

  return nu_eps;
}


// strain gradient of shape parameter d
Vector MultiSurfCrack2D::strain_gradient_chi()
{
  Vector chi_eps(2);

  double d_chi_r = chi_lok_r - chi_lok_s;
  double d_chi_s = d_chi_r * d_r_ds();

  chi_eps[1] = d_chi_s;

  return chi_eps;
}


// strain gradient of shape parameter k
Vector MultiSurfCrack2D::strain_gradient_k()
{
  Vector k_eps(2);

  double k_r = k_rough - k_smooth;
  double k_sl = k_r * d_r_ds();

  k_eps[1] = k_sl;
```

```
842
843   return k_eps;
844 }
845
846
847 int MultiSurfCrack2D::commitState()
848 {
849   double& sP = strain_plastic_current[1];
850   double& sCurr = strain_current[1];
851   double wCurr = strain_current[0] + w_res;
852
853   // update pinching break points (aggregate re-engagment)
854   sMAX += (sP - sMAX) * (sP > sMAX);
855   sMIN += (sP - sMIN) * (sP < sMIN);
856
857
858   // update max crack width (for ruggiero stiffness update)
859   wMAX += (wCurr - wMAX) * (wCurr > wMAX);
860
861   // update max crack slip (for sliding damage calcs)
862   sDAM += (std::abs(sCurr) - sDAM) * (std::abs(sCurr) >
      sDAM);
863
864   // update crushing strain accumulation
865   if ((active_surface == "interlock") && (stress_current[0]
        < h * vcimax))
866   {
867     // use total strains so post-peak response isn't
      affected by user's choice of rho^lok
868     double& wPrev = strain_committed[0];
869     double crush_increment = wCurr - wPrev;
870     if (crush_increment < 0)
871     {
872       crushing_strain += crush_increment;
873     }
874   }
875
876   // update committed state
877   strain_committed = strain_current;
878   strain_plastic_committed = strain_plastic_current;
879   stress_committed = stress_current;
880   tangent_committed = tangent_current;
881   dLambda = 0.0;
882
883   // update shape of interlocking yield surface (only after
```

```
    committing state)
  if (sP && (!criticalPath))
  {
    updateInterlockShape();
  }

  // update yield surface (with updated sliding damage,
   updated crushing damage and updated interlock shape)
  setvcimax();

  // store last shear point converged to interlock surface
  if (active_surface == "interlock")
  {
    last_vci_lok = stress_committed[1];
  }


  return 0;
}


int MultiSurfCrack2D::revertToLastCommit()
{
...
}


void MultiSurfCrack2D::updateInterlockShape()
{
  double& vci = stress_committed[1];
  double& s = strain_committed[1];
  double& sP = strain_plastic_committed[1];

  double s_rough;

  if (vci > 0)
  {
    s_rough = 1.0 * sMAX;
  }
  else
  {
    s_rough = 1.0 * sMIN;
  }

  // intermediate slip variable
```

```
927   double x = std::abs(s / s_rough);
928   x = std::min(1.0, x);
929   x = std::max(0.0, x);
930 
931   // update Roughness parameter based on current slip
932   double r = (x - kappa * x) / (kappa - 2 * kappa * x + 1);
933 
934   // update shape of interlocking parabola, F^lok
935   k = k_rough * r + k_smooth * (1 - r);
936   chi_lok = chi_lok_r * r + chi_lok_s * (1 - r);
937   h = -1;
938 
939   // update dependent shape parameters (d, chi_t, chi_c)
940   updateDerivedShapeParameters();
941 }
942 
943 
944 
945 void MultiSurfCrack2D::updateDerivedShapeParameters()
946 {
947   // calculate derived shape parameters from updated k and
       chi_lok
948   d = h * h / 4 / (k - chi_lok);
949   chi_t = -m * h / 4 * chi_lok / (k - chi_lok);
950   chi_c = m * m * h / (8 * (1 - m)) * chi_lok / (k -
       chi_lok);
951 }
952 
953 
954 
955 double MultiSurfCrack2D::d_r_ds()
956 {
957   double& vci = stress_committed[1];
958   double& s = strain_committed[1];
959   double& sP = strain_plastic_committed[1];
960 
961   double s_rough;
962   if (vci >= 0)
963   {
964     s_rough = 1.0 * sMAX;
965   }
966   else
967   {
968     s_rough = 1.0 * sMIN;
969   }
```

```
970
971   // intermediate slip variable
972   double x = std::abs(s / s_rough);
973   x = std::min(1.0, x);
974   x = std::max(0.0, x);
975
976   // toggle off if s = s_rough
977   double t_d = 1 - std::floor(x);
978
979   // avoid div.by.zero if kappa = -1 or kappa = 1
980   x = std::min(0.999, x);
981   x = std::max(0.001, x);
982
983   double denom = kappa - 2 * kappa * x + 1;
984   double r_s = 1 / s_rough * (1 - std::pow(kappa, 2)) / std
       ::pow(denom,2);
985
986   return r_s * t_d;
987 }
988
989
990 const Vector& MultiSurfCrack2D::getStrain()
991 {
992   return strain_current;
993 }
994
995
996 const Vector& MultiSurfCrack2D::getStress()
997 {
998   // send force back to zLND element
999   force_current = stress_current * Acr;
1000
1001   return force_current;
1002 }
1003
1004
1005 const Matrix& MultiSurfCrack2D::getTangent()
1006 {
1007   // want units of Force/Disp for zLND element tangent, so
       multiply by this crack element's area
1008   tangentF = tangent_current * Acr;
1009
1010   return tangentF;
1011 }
1012
```

```
1013
1014 const Matrix& MultiSurfCrack2D::getInitialTangent()
1015 {
1016   // multiply by this crack element's area to get units of
       Force/Disp
1017   tangentF = tangent_elastic_loading_initial * Acr;
1018
1019   return tangentF;
1020 }
1021
1022
1023 int MultiSurfCrack2D::revertToStart()
1024 {
1025 ...
1026 }
1027
1028
1029 NDMaterial* MultiSurfCrack2D::getCopy(const char* type) {
1030
1031   // This crack model is limited to 2D and meant for use
       with zLND element -- warn users if type != "
       PlaneStrain2D", which comes from zeroLengthND element
       parsing
1032
1033   if (strcmp(type, "PlaneStrain2D") != 0)
1034   {
1035     opserr << "WARNING: element must be of type
       PlaneStrain2D to handle crack material " << endln;
1036   }
1037
1038   MultiSurfCrack2D* theCrackMaterial = new MultiSurfCrack2D
       (this->getTag(),
1039                     tangent_elastic_loading_initial,
1040                     tangent_elastic_unloading_initial,
1041                     fc,ag,fcl,Acr,rho_lok,chi_lok,
1042                     rho_act,mu,chi_act,zeta,kappa,
       theta_tilde,
1043                     strain_committed[0]+w_res,criticalPath)
       ;
1044   return theCrackMaterial;
1045 };
1046
1047
1048 int MultiSurfCrack2D::sendSelf(int commitTag, Channel&
       theChannel)
```

```
{
...
}


int MultiSurfCrack2D::recvSelf(int commitTag, Channel&
    theChannel, FEM_ObjectBroker& theBroker)
{
...
}
```

Appendix C

Utilizing quoFEM to identify parameters of the multi-surf-crack2D model

For each simulation in Chapter 6, the quoFEM software [110] is used to identify the ideal set of parameters to best match experimental data. In each "deterministic calibration" (this is one of many options available in the quoFEM tool) simulation, two response quantity time histories are evaluated in the cost function, though only one is needed. The second response quantity ensures that a certain response quantity is not weighted too heavily without regard to other quantities. Selection of which two response quantities should be considered depends on the boundary conditions for each particular test. A test performed in slip control with constant crack width uses shear stress and crack normal stress as the two response quantities, whereas a test in slip control with constant crack normal stress uses shear stress and crack width in the cost function. "Natural" cracks use shear stress and crack width. For each cost function, a scaling procedure is implemented before inputting the response quantity time histories into quoFEM such that each response quantity is weighted evenly in the error evaluation.

The set of model parameters that minimizes the cost function is the best-fit parameter set. Optimization of model parameters was performed using the deterministic calibration feature of the quoFEM tool. The optimization procedure was instructed to search the parameter space summarized in Table C.1. If the best-fit solution for a parameter was found at the boundary of that parameter's range, the range was extended (if determined to be reasonable).

Table C.1. Response quantities in the calibration error function

	v_{ci}	σ_n	w
Natural	✓		✓
Constant Width	✓	✓	
Constant Clamp	✓		✓
Imposed Dilation Path	✓	✓	

It is noted that to run quoFEM with the `multi-surf-crack2d` material model, which is not in the official OpenSees repository, OpenSeesPy is run locally and quoFEM is instructed to read the Python script that imports the local installation of OpenSees (including the user material model) and runs the numerical simulation. Results of the simulation are printed to .txt files that are specified to and read by quoFEM, comparing the results to input .txt files in order to evaluate the cost function. Instructions for using quoFEM and for formatting the input and output files can be found at the online documentation.

Appendix D

A simple approach for modeling dowel action

As described in Section 2.2.4, dowel action can provide a non-negligible contribution to crack shear, and cannot always be ignored. Additionally, yielding of extreme bar fibers that accompanies dowel action reduces the effectiveness of the reinforcement clamping stress across the interface for high-strength concrete, cracks crossed by large diameter reinforcement or cracks expected to undergo large slips. This means that ignoring dowel action can lead to overpredictions of interface capacity. Given these observations, the modeling scheme for dowel action must capture flexural deformations. Here, fiber elements are used for the crack-crossing reinforcement.

The approach for modeling dowel action must also be compatible with the discrete crack approach. To achieve this, the reinforcement within a short zone near the crack, called here the "crack influence zone" (also the "curvature influence zone" or the "bond degradation zone" by Maekawa and Qureshi [99]) is distinctly modeled to consider the interaction between reinforcement and surrounding concrete. The length of the crack influence zone can be approximated as 5 bar diameters in each direction away from the crack face [99]. A schematic of the discrete modeling approach is shown in Fig. 6.1.

At each reinforcement node within the crack influence zone, an interaction must be modeled between the reinforcement (nodes 'r' in Fig. 6.1) and concrete (nodes 'c' in Fig. 6.1) to ensure that the reinforcement displacement profile (from which curvature and axial stresses are derived)

is correctly captured. In OpenSees, such an interaction is typically modeled using `zeroLength` elements and `uniaxial` materials. For concrete bearing, which governs the strength and stiffness of dowel action, the dof of interest is perpendicular to the bar's axis.

Of the empirical expressions for the concrete bearing stiffness, that of Pejatovic and Muttoni [135] is the most comprehensive, accounting for effects of concrete strength, bar diameter, presence of cyclic loading, concrete cover, crack orientation, and bond slip. The description of the effective bearing stiffness was summarized in Eq. (2.11), and is repeated as Eq. (D.1):

$$k_c = 0.2\frac{E_c}{d_b}\eta_\theta\eta_\delta\eta_c\eta_{cast}\eta_{fc}\eta_{bond}\eta_{cyc} \tag{D.1}$$

As a first step toward creating a realistic material law for reinforcement bearing against concrete at a point, the backbone response outlined by the secant stiffness in Eq. (D.1) is passed to a `Hysteretic` uniaxial material in OpenSees, which requires 3 stress-strain pairs to be defined in the postive and negative direction. The first point can be taken at the onset of concrete nonlinearity in bearing, $\delta_\perp = 0.02d_b$ [135]. The third point can be taken when the bearing stiffness stabilizes, roughly around a bar indentation of $\delta_\perp = 0.25d_b$. An intermediate backbone point can be chosen between the onset and stabilized points depending on the expected deformation.

A schematic of the output from the `Hysteretic` material for a full cycle is shown in Fig. D.2a. While reasonable in the compressive regime (lower-left quadrant), the native symmetric version of the `Hysteretic` material also predicts that tensile stresses will develop. This is undesirable behavior at the interface between bar and concrete, which is not adhesive. Hence, a method is needed to eliminate the tensile part of the response. While no "compression-only" wrapper exists (to the author's knowledge in the public documentation), the same effect can be obtained by combining the `Hysteretic` backbone of Fig. D.2a in series (via the OpenSees `Series` wrapper) with a stiff `ENT` (elastic no tension) material. The schematic is sketched in Fig. D.1.

In compression, both springs carry the same force, and the stiff `ENT` material remains essentially undeformed. Upon loading into the tensile regime, the materials unload to zero, following the combined stiffness, until the materials are load free (see step 3-4 in Figs. D.1 & D.2). If the backbone

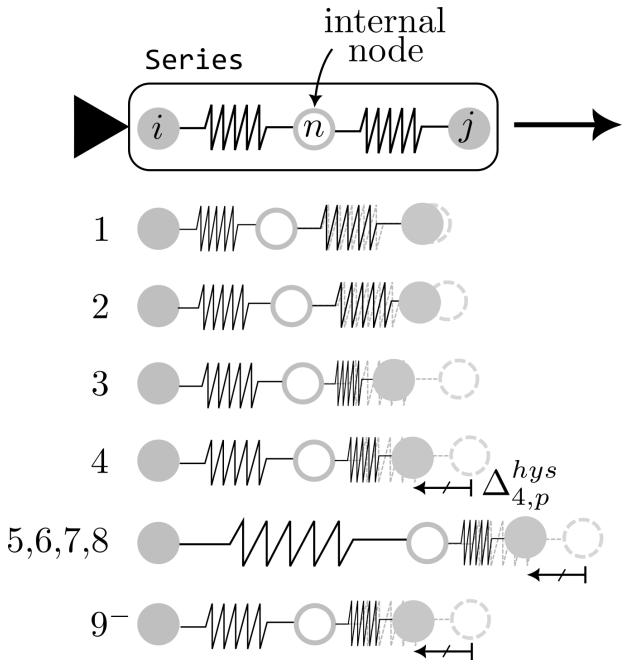

Figure D.1. Step by step nodal displacements of a `Hysteretic` material (right-most spring) in series with an `elastic-no-tension` material (left-most spring)

material had yielded prior to this point, the unloaded point $\Delta_{4,p}^{hys}$ will not correspond to zero displacement. As the series material is stretched further, all additional displacement will accrue in the `ENT` material – which has no tensile stiffness – and the built-in strain in the backbone material will remain. Upon reloading in compression, the `ENT` material has to completely shed the accumulated zero-stiffness strain before it stiffens and allows the backbone curve to carry more load. This force-displacement response in the `ENT` material is shown in Fig. D.2b.

The result of this series combination is the desired compression-only behavior that is expected at the interface with an indenting element. It is also noted that the series material simulates a gap behavior with damage accumulation. This replicates the expected behavior under cyclic indentation of concrete to retain some indentation. With each cycle the reinforcement must travel through a gap before re-contacting the concrete that has been damaged in previous load cycles. The gap corresponds to

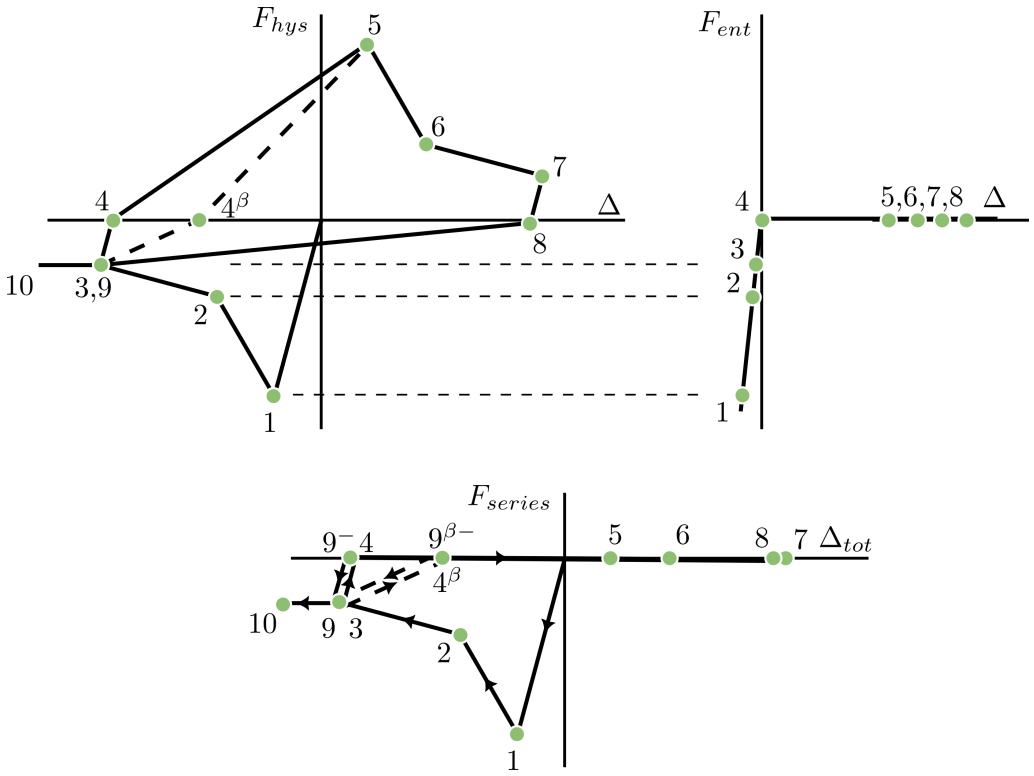

Figure D.2. Series combination of (a) `hysteretic` material and (b) `ENT` material to obtain (c) a compression-only, gap material with accumulating damage [Note: damaged unloading only shown in compression, for clarity]

the maximum plastic displacement in the concrete (at a point). It is noted that concrete is neither a true damage material nor a true plastic material. That is, the unloading stiffness degrades, but not so much that the material unloads to the origin. To account for this, the β_{ops} parameter (note *ops* subscript has been added herein to distinguish the notation from other notation in this Thesis) of the `Hysteretic` material can be set to a non-zero value. Values between 0.2-0.5 have been recommended in the literature [163]. The effect of the β_{ops} parameter is shown by dashed lines in Figure D.2. By varying β_{ops}, the dowel re-engagement displacement can be fine-tuned, which also affects the reloading stiffness. While the unloading/reloading rules for the single material-point response are assumed

to be linear, the complete dowel response for the full crack damage zone – which is composed of multiple bearing elements along the bar length – is non-linear, reflecting that each bearing spring along the bar length engages at a different point and with a different slope.

Finally, it is noted that a `zeroLength` element with the `Series` material is placed on either side of each reinforcement node within the crack influence zone to simulate the bilateral bearing against concrete.